2010

# Supported Mono And Bimetallic Platinum And Iron Nanoparticles Electronic, Structural, Catalytic, And Vibrational Properties

Jason Robert Croy
*University of Central Florida*

## STARS Citation

Croy, Jason Robert, "Supported Mono And Bimetallic Platinum And Iron Nanoparticles Electronic, Structural, Catalytic, And Vibrational Properties" (2010). *Electronic Theses and Dissertations, 2004-2019*. 1522.
https://stars.library.ucf.edu/etd/1522

# SUPPORTED MONO AND BIMETALLIC PLATINUM AND IRON NANOPARTICLES: ELECTRONIC, STRUCTURAL, CATALYTIC, AND VIBRATIONAL PROPERTIES

by

JASON ROBERT CROY

B.S. Ball State University, 2005

A dissertation submitted in partial fulfillment of the requirements
for the degree of Doctor of Philosophy
in the Department of Physics
in the College of Sciences
at the University of Central Florida
Orlando, Florida

Spring Term 2010

Major Professor: Beatriz Roldan Cuenya

# ABSTRACT

Catalysis technologies are among the most important in the modern world. They are instrumental in the realization of a variety of products and processes including chemicals, polymers, foods, pharmaceuticals, fuels, and fuel cells. As such, interest in the catalysts that drive these processes is ongoing, and basic research has led to significant advances in the field, including the production of more environmentally friendly catalysts that can be tuned at the molecular/atomic level. However, there are many factors which influence the performance of a catalyst and many unanswered questions still remain. The first part of this work is concerned with the factors that influence the catalytic properties (activity, selectivity, and stability) of supported Pt and Pt-M nanoparticles (NPs). These factors are a synergistic combination of size, composition, support, oxidation state, and reaction environment (i.e. adsorbates, temperature, pressure, etc.). To probe the catalytic properties of complex and dynamic NP systems we have used MeOH decomposition and oxidation reactions, each of which has significant environmental and economic potential. We have given some emphasis to the state of NP oxidation, and with the aid of X-ray photoelectron spectroscopy (XPS) and temperature programmed desorption (TPD), have followed the formation and temperature-dependent evolution of oxide species on Pt NPs. Further, we have explored how these species behave under the conditions of our probe reactions using a packed-bed mass flow reactor coupled to a quadrupole mass spectrometer (QMS).

To carry out our investigations we exploit a NP synthesis method which is rather novel to nanocatalysis, micelle encapsulation. Since most available experimental techniques give information on ensemble averages, control over size distributions in NP samples is critical if unambiguous results are to be obtained. Micelle encapsulation allows us this control with several unique, inherent

advantages. It is to this end that micelle encapsulation has allowed us to probe the detailed structure of small (~1 nm), supported, Pt NPs with extended X-ray absorption fine structure spectroscopy (EXAFS). Furthermore, we were able to explore experimentally, for the first time, the vibrational density of states (VDOS) of supported, isolated, monodispersed, mono and bimetallic NP systems via nuclear resonant inelastic X-ray scattering (NRIX). These synchrotron-based techniques (EXAFS, NRIXS) rely heavily on the monodispersity of the NP ensemble for reliable information.

This work is dedicated to my parents, who selflessly spent the greater part of their lives ensuring that we (their children) would be happy, healthy, and loved, with every need met to achieve our dreams. If only a greater man than I were afforded such opportunities what wonderful things may have come to pass? My only hope is that my efforts and results, in my life and in my work, have been pleasing to them.

– Jason

# ACKNOWLEDGMENTS

To my wife Lindsey, who has supported me in my efforts and without whom this work would not have been accomplished, I thank you for your inexhaustible patience and understanding. To Haley and Isaac, who have given me something to smile about everyday of their lives. They have been a great source of joy in my life. And to my brother Johnny, not too many people are lucky enough to have a brother for a best friend. Thanks to Curt and Robbie Ervin who have supported me and accepted me with love and generosity as they would their own son.

I also want to thank my mentor, Dr. Beatriz Roldan Cuenya for the opportunities she has given me, her guidance, hard work, and patience in this endeavor. She has set a great example as a dedicated teacher and successful scientist and is an inspiration for young women in her field. During my education our relationship has evolved from student-teacher to friends and collaborators. It is a friendship that has included my wife and children, and one which will continue throughout my personal and professional life. I consider myself a better person to have known her and lucky to be among the first members of the Roldan group at UCF.

I want to say thank you to my collaborators, lab mates, and friends Simon Mostafa, Luis Ono, Ahmed Naitabdi, and Farzad Behafarid for endless discussions and help pertaining to my work. Thanks to Prof. Werner Keune and Prof. A. I. Frenkel for being teachers, friends, and wonderful examples of the kind of scientist I would like to become. Thanks also to David W. Bradford for sharing his wide array of technical knowledge with me so generously.

Thanks also to my committee members Prof. Abdelkader Kara, Prof. Sergey Stolbov, and Prof. Yongho Sohn for taking time from their busy lives to evaluate my work.

– Thanks at last to all those who know their included when I say “friends”.

## TABLE OF CONTENTS

# LIST OF FIGURES

# LIST OF TABLES

# ABBREVIATIONS

| | |
|---|---|
| AFM | ATOMIC FORCE MICROSCOPY |
| BE | BINDING ENERGY |
| EXAFS | EXTENDED X-RAY ABSORPTION FINE STRUCTURE |
| HAADF | HIGH-ANGLE ANNULAR DARK FIELD |
| HR-TEM | HIGH RESOLUTION TRANSMISSION ELECTRON MICROSCOPY |
| IC | IONIZATION CHAMBER |
| LEED | LOW ENERGY ELECTRON DIFFRACTION |
| MFC | MASS FLOW CONTROLLER |
| MeOH | METHANOL |
| NP(s) | NP(s) |
| NRIXS | NUCLEAR RESONANT INELASTIC X-RAY SCATTERING |
| VDOS | VIBRATIONAL DENSITY OF STATES (PHONONS) |
| PID | PROPORTIONAL-INTEGRAL-DIFFERENTIAL |
| QMS | QUADRUPOLE MASS SPECTROMETER |
| RT | ROOM TEMPERATURE |
| SMSI | STRONG METAL-SUPPORT-INTERACTIONS |
| STM | SCANNING TUNNELING MICROSCOPY |
| STEM | SCANNING TRANSMISSION ELECTRON MICROSCOPY |
| TPD | TEMPERATURE PROGRAMMED DESORPTION |
| UHV | ULTRA HIGH VACUUM |
| XAS | X-RAY ABSORPTION SPECTROSCOPY |
| XANES | X-RAY ABSORPTION NEAR EDGE STRUCTURE |
| XPS | X-RAY PHOTOELECTRON SPECTROSCOPY |

# PREFACE

Abu Musa Jābir ibn Hayyān al azdi (Geber), the eighth century natural philosopher, is often given credit for transforming the mysterious art of alchemy into a practical, experimental science. His uniquely scientific approach enabled him to discover, and or invent, a great number of chemical substances, instruments, and processes. His work impacted many areas of practical and economic importance including the manufacture and treatment of steel, leather, cloth, and glass. It was Geber's work that ultimately led alchemists to fervently search for the elusive *lapis philosophorum* (philosopher's stone), a pursuit which would occupy some of the world's greatest minds for many years including Sir Isaac Newton himself. Although my goal is not an historical development of chemistry or catalysis, nor do I deem it necessary for the present purpose, the above, eighth century account strikes an interesting chord of similarity with the state of modern catalysis. Only recently has the "science" of catalysis lost its artistic connotations and entered full force into the theoretical realm of calculation and microscopic scrutiny. This is due in no small part to the experimental discovery that catalysts, on the nanoscale, exhibit unusual properties compared to their bulk counterparts. In addition, progress in computation and experimental instrumentation has made it possible to study nanoscale systems in greater detail than ever before. Likewise, and perhaps more so than in Geber's time, small advances in catalysis have enormous potential in many areas of practical and economic importance. Therefore, it has come to pass that the alchemists of today are fervently searching for their own *philosopher's stone* hidden somewhere in the depths of the nanoworld; a quest which has proven to be nonetheless mysterious and more elusive than the original.

# PART I – ELECTRONIC, STRUCTURAL, AND CATALYTIC PROPERTIES OF METAL NANOPARTICLES

# CHAPTER 1: INTRODUCTION

*Catalysis – "Science of enhancing chemical reaction rates and selectivities based on the use of materials (catalysts) that are not consumed during the course of the reaction."*

*– Gabor A. Somorjai*

## 1.1 Motivation

Specific reference to platinum (Pt) appears in European history as early as 1557 and the first scientific account of this metal was given to the Royal Society in 1750 [1]. Pt has been known as an active catalyst for many years and industrially employed as such since the early 1900's for the production of fertilizers [2] . Since that time the wide variety of catalytic processes, both practical and profitable, which have found a use for Pt make it one of the most important and studied metals to date. For example, Pt can be found in one capacity or another in processes involving fertilizers [3], explosives detectors [4], catalytic converters for automobiles [5], refining of petroleum [6], cancer drugs [7], and much more [8]. Thus, the significant economic status of Pt cannot be understated. This being the case, the demand for Pt is great, and since Pt is a precious metal it is desirable and necessary to reduce the amount of Pt used in various processes while at the same time maximizing efficiency. Efficiency in the catalytic sense encompasses four major factors which include activity, selectivity, stability (lifetime), and cost. Selectivity is also of particular importance to environmentally-friendly or "green" chemistry, which has become the focus of modern catalysis [9]. One of the areas which would greatly benefit from improvements in any of these "efficiency-factors" is chemical catalysis; especially energy-related processes. The most publicized example is the use of Pt in fuel cell electrodes [10]. Pt is known as one of the most active metals for this application, however, a major disadvantage is the great expense associated with its use. To make Pt-based fuel cells economically viable the amount of Pt used in their construction must be minimized while maintaining sufficient performance. In addition, Pt is extensively used in the refining of petroleum to gasoline, the current use of which is ~140 billion gallons per year in the United States alone [11]. Therefore, even small improvements in the four efficiency factors could have significant economic and environmental impacts.

A promising avenue of research in catalysis is nanocatalysis. Nanocatalysis is catalysis in the normal, chemical sense of the word but with the principle catalytic materials themselves having dimensions on the nanoscale. This field was pushed to the forefront of investigation by the discovery that Au, when on the nanoscale, is highly active for many chemical reactions such as the partial oxidation of hydrocarbons [12], the water-gas shift (WGS) reaction [13], and low temperature CO oxidation [14]; whereas bulk Au has been historically known as an inert substance [15]. To date the study of nanocatalysts has evolved to include all of the catalytically-employed metallic elements (of which there are 12 from the 3d, 4d, and 5d metals) [16]. However, many questions of fundamental importance still remain. For example, under what conditions are the oxides of metal nanoparticles (NPs) stable and what influence do they exert in different reactions; how can NPs be synthesized with reliable size-distributions; what supports will promote the desired activity and selectivity as well as stability; how do synthesis and reaction conditions affect the dynamics of NP-structure and stability? These are but a few of the many questions that nanocatalysis must answer in order to implement the rational design of modern catalysts.

This thesis is an investigation into the major influences governing the catalytic performance of NPs, in particular supported Pt and Pt-Metal (Pt-M) NPs. The next section will briefly introduce these considerations one by one, however, nanocatalysts are complex systems and no parameter, internal or external, should be taken individually when describing catalytic behavior as a whole. Nanocatalysts are only recently beginning to be understood as dynamic systems [17-20]. As such, the factors discussed below are not fully understood, individually or synergistically.

## 1.2 Considerations at the Nanoscale

It is now common knowledge that many catalytic metals having dimensions less than 10 nm possess size-dependent physical and chemical properties. Perhaps some of the most famous reports have come from Haruta et al. [21-23] concerning supported Au NPs. Haruta's group reported that not only is the activity of Au NPs size-dependent, but so also is the selectivity [21]. In addition, the structure of the $TiO_2$ support used (rutile vs. anatase) as well as the synthesis conditions played a vital role in the final state and structure of the NPs. These observations, among others [24], sparked great interest in supported NPs and researchers have proposed several models to explain such phenomenon. The models include quantum size-effects (electron confinement), increased density of low-coordinated atoms with decreasing particle size, and perhaps the most complicated of all, NP-support interactions [25], which include the possibility of charge transfer to and from the supported particles, active sites on the support itself and at the particle-support interface. Roldan Cuenya has recently given an extensive review outlining the novel properties and complexities of nanoscale catalysts [26]. The following sections will briefly introduce some of the reported observations related to the models listed above.

### 1.2.1 Size and Shape Effects

Goodman's group first reported the appearance of a band gap in Au NPs having dimensions less than ~3 nm marking a metal to insulator transition [27]. The onset of these quantum size-effects was correlated to the onset of activity for low temperature CO oxidation over Au NPs evaporated on $TiO_2$(110). The authors also found that NPs consisting of two layers of Au were the most active, implying that structure and not size might be the most important consideration. This observation of structure-sensitive reactivity complicates matters in that NP shape depends on various factors such as size, support, preparation method, impurities, and adsorbates [28]. As an example, it was found that Pt deposited on $\alpha$-$Al_2O_3$ can form flat particles which are stable through direct Pt-O-Al bonding [29]. Reifsnyder et al. [30] have also reported that chemisorbed $H_2$ can increase Pt-Pt distances in small Pt clusters supported on silica. Furthermore, different crystallographic facets that accompany different NP shapes [28] can in fact display differences in catalytic performance. Xu et al. [31] have studied the oxidation of styrene over cubic, truncated triangular nanoplates, and near-spherical Ag NPs. The authors reported that the (100) facets of nanocubes are highly reactive, whereas the rate over the (111) facets of nanoplates was fourteen times less. Komanicky et al. [32] have also recently shown a cooperative effect in the oxygen reduction reaction (ORR) between the (111) and the (100) facets of Pt NPs.

On a different note, it is generally believed that an increase in surface area and number of under-coordinated sites, such as kinks and steps, play a vital role in catalytic reactions that occur at surfaces [33]. Because the fraction of under-coordinated atoms increases with decreasing particle size [34], NP activity has been related to the high density of low-coordinated atoms in small NPs [34-36]. These under-coordinated sites are known to display distinct electronic properties [37]. In Ref. [34] the authors have done calculations of the adsorption of O, CO, and $O_2$ and find two effects which lead to enhanced activity of Au. The first is that adsorbates bind more strongly to the under-coordinated sites. The second is that lattice strain, which may be induced by interactions with the support, can affect the reactivity of surface Au atoms in a positive way. Similarly, Mehmood et al. [38, 39] have also calculated increasing binding energies with decreasing coordination for CO on Cu  and Au surfaces.

Another interesting observation for NPs is the shift in binding energies (BEs) reported in XPS (see Chapter 2). These shifts are attributed to both initial and final state effects. Initial state effects arise from the modified electronic properties of small particles whereas final state effects arise from loss of electrons due to the photoemission process [40, 41]. These shifts may also be influenced by particle-support interactions [42]

### 1.2.2 Role of the Support

The term "strong metal-support interaction" (SMSI) was first used in connection with the chemisorption properties of noble metals supported on titanium oxide [43]. Such oxide-metal catalytic systems are complex and their properties depend on both structural and chemical characteristics. These properties originate from the supported particles, the support itself, and the particle support interface. As previously mentioned, the geometry and size of the supported particles can influence the catalytic character of the system, not only because of size effects, but also because of strong interactions with the support [44]. Properties originating from the support encompass both weak and strong interactions. Weak interactions include processes such as diffusion of reactant adsorbates, which can take place in systems with weakly chemisorbed states on the support. For instance, in Ref. [45] the authors concluded that on Pd/$Al_2O_3$ most of the $O_2$ and CO (incident from a molecular beam) adsorbed on Pd particles were initially trapped on the support and reached the particles by way of surface diffusion. Strong interactions can occur when the support is directly involved in the reaction process. This can happen, for example, in oxide storage compounds [46] that accumulate oxygen or nitrogen oxide, as is well known for NO removal in automotive exhaust catalysts [47]. It should also be noted when talking about support effects the tendency of particles to nucleate at defect sites such as kinks, steps [48], and oxygen vacancies [49, 50]. Therefore, the stoichiometry of the support is also an important consideration in supported metal catalysts. As an example, on reduced $TiO_2$, charge redistribution and accumulation around oxygen vacancies has been predicted and the possibility of charge transfer to small, supported Au NPs suggested [51]. The subsequent anionic Au species interact more strongly with electronegative adsorbates and the system favors reactions like CO oxidation. Rodriguez et al. [52] have also observed polarization of Au atoms at the Au/TiC perimeter and interface, making this system highly active for the oxidation of CO. Furthermore, Kang et al. [53] and Sanchez et al. [54] have reported a negative thermal expansion for sub-nanometer Pt on $\gamma$-$Al_2O_3$. The authors believe, based on X-ray absorption near edge structure (XANES) data, that this is a support specific effect due to the transfer of charge to Pt clusters because of their tendency to occupy vacancy sites of the alumina support. On the other hand, non-reducible supports have also been reported to show SMSI and enhanced activity, as in Pd/$ZrO_2$ for MeOH decomposition [55]. In addition, it has been shown that the acidity of the support plays a major role in the electronic state of the supported NPs and thus influences catalytic performance [56]. Support-metal interactions are also responsible for varying degrees of encapsulation of the supported NPs in a variety of oxide systems including Pt/$TiO_2$ [57-60]. Supports are also of key interest when considering coarsening and particle stability and the affects are non-trivial [61-63]. For example, SMSI exist between Pt/$TiO_2$ [64] and Pt/$CeO_2$ [65, 66], however Pt NPs coarsen on these supports under WGS reaction conditions at 300°C [67]. On the other hand, in systems with weaker NP-support interactions such as Pt/$Al_2O_3$, Pt NPs have been observed to be stable for reactions such as methane combustion at 600°C [68]. These studies reveal the importance of not only the particle-support interactions, but also the preparation conditions and reaction environments when considering sintering processes.

The interface of the metal-support system plays a significant role as well. For example, hydrogen layers situated between the supported particles and the surface of the support create large distances between the supported particles and surface oxygen. Subsequent removal of the hydrogen (annealing) can bring the particles into contact with surface oxygen, and changes in their shape from hemispherical to "raft-like" are observed [69]. The support can also introduce strain, affecting the reactivity of surface atoms [34]. The particle-support interface has also been recognized as the active site for several reactions including CO oxidation, methanol synthesis, and the steam reforming of methanol [23, 70, 71].

### 1.2.3 Oxidation and its Effects

In addition to the parameters discussed above, the oxidation of nanocatalysts, and catalysts in general, is one of the most complex and dynamic processes in all of surface science. As such, we give specific emphasis to this topic throughout this work, as its effects have wide and far-reaching implications.

The oxidation of Pt is of significant importance both practically and scientifically. On one level, a fundamental knowledge of the stages of, and structures formed by, oxidation of metal surfaces is still lacking. This knowledge in turn is of basic importance for catalytic processes including CO oxidation, $NO_x$ storage/reduction, and combustion of volatile organic compounds (VOCs) [72]. All of these reactions are critical to environmental applications, especially in the abatement of automobile exhaust gases. In fact the highest demand for Pt comes from its use in automotive applications [73]. It has been suggested that these reactions proceed via a Mars-van Krevelen process. This means that reactants are oxidized by oxygen atoms that are initially part of the Pt surface and subsequent reaction with gas-phase oxygen re-oxidizes Pt, completing the cycle. Therefore, characterizing the oxide phases that develop on Pt surfaces is crucial for the development and tailoring of catalysts for these reactions.

The Pt(111) surface and its interaction with oxygen has been studied in detail by numerous researchers. The technique of TPD (see Chapter 2) is a fundamental tool in these studies and we will use it in our investigations of Pt-oxides in Chapter 9. We will give here a brief account of the major findings so far [74-80] (and Refs. therein). Gland [77] has shown that oxygen adsorbs molecularly on Pt(111) below ~150 K. At higher temperatures oxygen dissociates resulting in a maximum atomic oxygen coverage of ~one oxygen atom for every ~4 platinum atoms. This "saturation" coverage is used as the standard for calibrating coverages in TPD spectra on single crystal surfaces. For example, the surface atom density of Pt(111) is $1.51 \times 10^{15}$ atoms/cm$^2$, therefore, the saturation of atomic oxygen by molecular dissociation is defined as 0.25 monolayers (ML) of oxygen, where a monolayer represents a 1:1 ratio of oxygen to platinum atoms. Hence, by molecular dissociation of $O_2$ (or $NO_2$ [79]), one can achieve a known coverage ($\Theta$) of 0.25 ML of atomic oxygen on Pt(111). The area under the TPD trace of this coverage becomes the calibration for all other spectra. On Pt(111), $0 < \Theta < 0.25$ ML results in oxygen atoms occupying fcc hollow sites arranged in p(2 x 2) domains [74, 81, 82]. In this range desorption is second-order and binding energy decreases with increasing coverage due to lateral, repulsive forces between oxygen atoms [76, 80]. The desorption of this low-coverage state (called $\beta_3$) results in a peak at ~735 K for $\Theta =$ 0.25 ML. A coverage $\Theta > 0.25$ ML cannot be achieved through molecular adsorption and dissociation and higher coverages must be obtained by the use of atomic oxygen, ozone ($O_3$), or dissociation of $NO_2$, or other aggressive treatments [76, 79, 82]. At coverages of $0.25 < \Theta$ $<0.5$ ML a second state ($\beta_2$) appears at ~630 K. Devarajan et al. [81] have shown by STM and TPD that in this range of $\Theta$, oxygen atoms form p(2 x 1) domains and desorption of these domains is responsible for the $\beta_2$ state in TPD spectra. For $\Theta > 0.5$ ML the surface starts to lose its order, as evidenced by low energy electron diffraction (LEED) experiments [74], and the formation of Pt-oxide chains is observed by STM. These chains have been identified as the precursor to bulk-like $PtO_2$ on the Pt(111) surface at coverages exceeding 0.75 ML [81]. At these high coverages, Pt atoms are drawn out of the surface and new Pt-O bonds are formed at the expense of Pt-Pt bonds between the first and second layers of Pt. Therefore, oxides can form without oxygen atoms having to first diffuse into the subsurface layers as has been reported [83]. This is especially interesting for fuel cell anodes where dissolution of Pt has been associated with the initial stages of surface oxide formation [84].

Interestingly, once an oxide forms, further oxidation may proceed rapidly through an autocatalytic process. For example, oxidation generally requires the dissociation of $O_2$ as a first step and, as discussed above for Pt, this process becomes kinetically limited even at relatively low coverages. However, it has been shown for both Pb and Ru that once oxide formation starts, $O_2$ dissociation readily happens over PbO and $RuO_2$ respectively, increasing rapidly the supply of atomic oxygen. Therefore, the process is said to be "self-accelerating" [85, 86].

The oxidation of NPs presents further, unique challenges in that their surfaces are not so well defined as bulk samples. For example, size, coordination of surface atoms, substrate effects, and different surface terminations must be taken into consideration. In general, Pt NPs present a combination of the two lowest energy, (111) and (100) surfaces [87, 88]. Therefore, any properties observed are likely a convolution of the properties of these two surfaces. Seriani et al. [87] have calculated the Wulff's shape of metallic and $Pt_3O_4$ NPs having diameters of ~5 nm. For Pt they find a truncated octahedron terminated by (111) and (100) facets; the (100) being only ~14 % of the total. For $Pt_3O_4$ NPs the shape is a cube with (100) surfaces. However, Mittendorfer et al. [89] have predicted, theoretically, drastic changes in the morphology and equilibrium shape of Pd and Rh nanocrystals upon $O_2$ adsorption, with closed-packed (111) facets dominating under low $O_2$ pressures, and nanocrystal rounding occurring at elevated $O_2$ pressures due to its higher adsorption energy on the initially less stable (110) open surfaces. Grazing incidence X-ray diffraction and TEM experiments by Nolte et al. [90] on Rh NPs supported on MgO(001) indicated an increase in the total area of (100) facets at the expense of (111) surfaces upon oxidation. Such shape changes were found to be reversible upon subsequent NP reduction during CO oxidation. High resolution TEM images, obtained by Giorgio et al. [91, 92] under $H_2$ and $O_2$ atmospheres, using an environmental TEM, demonstrated the faceting of $TiO_2$-supported, Au NPs under $H_2$ (truncated octahedron shape), and their rounding and de-wetting under

$O_2$. In analogy to the previous observation of Rh clusters, the latter shape changes also appeared to be reversible. These studies demonstrate that chemisorption-induced morphological changes in NPs need to be considered when models to explain oxidation and catalytic reactivity are proposed, since certain reaction environments might lead to a decrease/increase in the relative area of the most catalytically active surface facets/sites.

Another complication when dealing with NPs is the control over size distributions. As mentioned in Chapter 2, most techniques used for NP characterization measure ensemble averages. As such, if the size distribution is broad, meaningful results cannot be obtained. For example, Wang et al. [93] have observed that the type of oxide that preferentially forms on Pt NPs changes as a function of NP size, therefore, broad size distributions become somewhat ambiguous when interpreting experimental results. In addition, Balbuena's group [94] has shown, using density functional theory calculations, that the activation energy for dissociation of adsorbed oxygen on small Pt clusters decreases with decreasing particle size. Seriani et al. [87, 95] have also calculated that the transition temperature of $\alpha$-$PtO_2$ to $Pt_3O_4$ to Pt is highly dependent on particle size. The authors point out that if the NP distribution is broad there will exist large concentrations of $\alpha$-$PtO_2$ at temperatures where $Pt_3O_4$ is stable. This is also interesting in that under these conditions $Pt_3O_4$ was calculated as being active for the oxidation of CO and $CH_4$ dissociation, whereas $\alpha$-$PtO_2$ was inactive in the absence of defects. Olsson et al. [96] have also shown that the rate of $NO_2$ dissociation over $Pt/Al_2O_3$ decreased as oxides were formed on the supported Pt NPs. They also report that the rate decreased with decreasing particle size and speculated that small particles are more easily oxidized and so become less active for $NO_2$ dissociation. In connection with the autocatalytic growth of oxides on bulk surfaces discussed above, Bi et al. [97] have reported interesting calculations for the oxidation of Ag NPs to $Ag_2O$. They find that oxidation of Ag NPs begins with the formation of an oxide shell surrounding a metallic core. As the thickness of the shell increases the change in the Gibb's energy, $\Delta G$, decreases, making further oxidation of the NPs more facile. Furthermore, there is a critical radius for the NPs, below which, complete oxidation of the particle is possible and, above which, oxidation will cease at some point leaving an oxide shell surrounding a metallic core. Chernavskii et al. [98] have also given details of a model describing oxidation of NPs starting from the surface layer and growing inward creating core/shell (metal/oxide) NPs.

These examples reiterate the difficulty with characterizing the oxidation of NPs and the necessity for strict control of NP size distributions if meaningful results are to be obtained. Furthermore, progressive oxidation, accompanied by local restructuring of the surface, seems likely under "real world" catalytic conditions, revealing the dynamic nature and complexity of the problem.

Recently, much attention has been directed towards the oxidation state of active metal NP-catalysts and whether or not oxidized metals may be beneficial with respect to their reduced counterparts. As such, the interaction of various chemicals with oxidized surfaces has been investigated and some interesting results obtained [99-105]. For example, the adsorption of MeOH on Cu is found to be greatly enhanced by oxygen [106], either in the feed gas or as part of the catalyst due to an incomplete reduction process [107]. Over et al. [108] showed that the $RuO_2(110)$ surface is highly active for CO oxidation and oxidized Ru is also preferred over its metallic state in bimetallic Pt-Ru anode catalysts for fuel cell applications [109]. $PtO_2$ surfaces have also been reported to be more active for CO oxidation than metallic Pt [110]. Theoretical work by Gong et al. [111] shows that $RuO_2(110)$,

$RhO_2(110)$, $PdO_2(110)$, $OsO_2(110)$, $IrO_2(110)$ and $PtO_2(110)$ are indeed more reactive than the corresponding metal surfaces for CO oxidation. Recent work by Friend's group on O-covered Au(111) also demonstrates the enhanced reactivity of the pre-oxidized gold surface [112, 113]. Therefore the view of oxidation as a process leading to reduced catalytic performance must be re-examined [85]. However, in the case of Pt there seems to be a debate regarding the benefits of Pt oxides. For example, the temporal decay in the performance of Pt-based fuel cell electrodes has been attributed to the formation of PtO and Pt dissolution [114]. On the other hand, there also exist a number of reports suggesting that the presence of Pt-oxides could have a positive effect on catalytic performance. Dam et al. [115] have shown that Pt dissolution reaches a saturation level due to the presence of a protective platinum oxide layer. Further, a study by Hull et al. [116] shows enhanced activity for Pt-carbon nanotubes catalysts, where the Pt particles are covered by a thin Pt-oxide shell. It is thus necessary to understand the oxidation of NPs as well as their behavior under specific reaction conditions.

Furthermore, with the ever increasing industrial use of nanomaterials, their impact on the environment has become an issue of great importance. Specifically, thermally or mechanically induced emissions of particulate Pt from automobile catalytic converters is a source of toxicological concern [117-120]. Therefore, not only are the activity, selectivity, and stability of the working catalysts important, but so also is the state in which they might be emitted into the environment upon reaction (oxidized, chlorinated, etc.). Although catalysts are prepared in a certain state (i.e. $Pt^0$), the oxidation state of the working catalyst might be different, and how this state evolves and reacts under environmental conditions is of interest.

### 1.2.4 Secondary Metals

Pt-Metal (Pt-M) bimetallic catalysts are important in a variety of applications ranging from fuel cells [121] to thermal coatings [122]. In addition, recent years have witnessed a surge in the interest of methanol (MeOH), especially as a potential storage fuel for hydrogen, ultimately used for the production of electricity in on-board applications such as the direct methanol fuel cell (DMFC), portable electronics, or stationary power generation. These applications potentially involve electro-oxidation, steam reforming, and the direct decomposition of MeOH, each encompassing unique reaction conditions [123].

In order to take advantage of Pt-M systems in the design of new catalysts for any of these applications, the structural, chemical, and electronic modifications, brought about by the addition of secondary metals [103, 124-130], need to be fully understood. In particular, the surface compositions of such catalysts are influenced by a number of factors. Besides such familiar properties as surface energy, atomic volume, and heats of sublimation, nanoscale systems require additional considerations. For instance, it has been shown theoretically that Pt atoms may preferentially segregate to sites of low (edges, vertices, etc.) or high (facets) coordination depending on the structure of the particles as well as the metal M [131]. In addition, the presence of oxygen has been shown to heavily influence atomic segregation in NPs, and the presence of metal M on the NP surface can affect the stability of oxide species on active nanocatalysts [132, 133]. In addition, reactivity may be enhanced or hindered by a change in the electronic properties of metals due to alloying. This is know as the "ligand effect" and can heavily influence metal-adsorbate interactions, especially in transition metals [134]. For example, changes in the electronic properties of these metals may be caused by compressive or tensile strain brought about by lattice mismatch.

Compressive strain causes an increase in the amount that the d-orbitals overlap, shifting the d-band center (average energy) to lower energy, away from the Fermi level [135, 136]. This shift makes them less likely to interact with adsorbates, thereby decreasing the activity. The opposite occurs for the case of tensile strain which increases metal-adsorbate interactions. In reference to fuel cells, alloying Pt with metals such as Fe, Ru, Ni, Co, as well as others, has been reported to enhance the oxygen reduction reaction (ORR) [125, 126], increase activity [137], and improve resistance to CO poisoning [138]. In connection with the latter, Pt-Ru catalysts are known to be efficient and some detailed theoretical studies already exist concerning this catalyst's role in CO oxidation [139]. For example, Stolbov et al. [140] have calculated that CO on small Pt islands will spillover to the Ru substrate where OH preferentially adsorbs. Further, when CO and OH meet at the Pt-Ru-edges of these Pt islands, CO oxidation proceeds with an enhanced rate as compared to the Pt(111) surface, relieving the effects of CO poisoning. One of the most recent developments for an ORR electrocatalyst is reported by Zhang et al. [130]. In this report the authors describe a non-noble metal core surrounded by a protective, noble metal shell, which is in turn covered by a monolayer of Pt. The non-noble core reduces the amount of Pt needed, while the noble shell serves to protect the core from the acidic electrolyte as well as improve the catalytic properties of the Pt monolayer through their interaction. However, as stated earlier, these systems hold importance in a broader sense than power generation alone [113, 141-154] and a large number of works have been dedicated to understanding their synthesis, characterization, and catalytic properties [155-166].

### 1.2.5 Importance of Methanol

Presently, with the world's demand for energy projected to double by the year 2050 [167], the development of enabling technologies for alternative energy sources is no longer a question of debate but rather one of necessity. Hydrogen is seen as one of the most promising alternatives and can be produced in a myriad of ways [168]. The quest for a hydrogen economy has attracted much attention to the reforming of liquid hydrocarbons, and in particular to the reforming of MeOH. Because of its adaptability to the existing infrastructure, and high hydrogen density, methanol is seen as one of the most viable options for widespread use in fuel cell vehicles [169]. Direct methanol fuel cells (DMFC) are also being put to use as power supplies for the next generation of personal electronics. MeOH has an associated energy efficiency 40 to 60 times that of Li-ion batteries, and early fuel cells are anticipated to have a 5 to 1 or greater advantage over traditional batteries [170].

The decomposition of methanol for the production of synthesis gas ($CO/CO_2/H_2$) is also industrially relevant in the production of high-purity hydrogen for metallurgical processes and the generation of electricity, thus it has been the subject of intensive study [171, 172]. There are several decomposition processes currently in use and under investigation including direct decomposition, steam reforming, and oxidation [172]. These processes require the use of metallic NP catalysts such as Cu, Pt, and Pd supported on various metal oxides [173]. In the reverse direction, the synthesis of methanol is a process that is better understood in that there is now a preferred catalyst in widespread industrial use ($Cu/ZnO/Al_2O_3$) [174]. However, the reaction site and pathway mechanisms of this catalyst are still under investigation [174-176].

In addition, MeOH can be produced from a number of renewable resources such as black liquor, animal waste, and dedicated energy crops, giving it environmental as well as economic appeal. As such, MeOH as a chemical commodity has become a staple of the modern world. In the U.S. alone it is a multi-billion dollar/year industry [177]. Its versatility and importance is demonstrated by its use in an enormous and varied range of applications. For instance, MeOH can be found at work in artificial sweeteners, paints, plastics, construction materials, and even the annual running of the Indianapolis 500. In Shanxi, China, sales of methanol as a transportation fuel, both neat (M-100) and blended (M-15, M-85), have reached 160,000 tons per year (2006), four new engines have been developed for use with MeOH, and two fleets of intercity buses now operate on neat methanol [177].

In the coming chapters we will use MeOH decomposition and oxidation reactions to probe the catalytic properties of micelle-synthesized Pt and Pt-M NPs (M = Au, Fe, Pd, Ru).

# CHAPTER 2: METHODS OF EXPERIMENT AND INSTRUMENTATION

## 2.1 Laboratory Techniques and Instrumentation

This chapter describes the various techniques used to characterize the properties of our NP samples. These techniques include laboratory instrumentation as well as beamlines at two synchrotron facilities; the Advanced Photon Source (APS) at Argonne National Laboratory (USA), and the National Synchrotron Light Source (NSLS) at Brookhaven National Laboratory (USA).

### 2.1.1 Atomic Force Microscopy (AFM)

Atomic force microscopy (AFM) is based on the forces of attraction and repulsion (i.e. van der Waals, electrostatic, magnetic) between a sharp tip and the atoms that make up the sample surface. The major advantage of AFM is that it can accommodate any sample type; conducting and non-conducting [178], or even soft, biological materials [179]. Thus, in addition to morphology, one can conduct electric force microscopy (EFM), magnetic force microscopy (MFM), or lateral force microscopy (LFM) to probe the electric, magnetic, and frictional properties of materials, respectively. AFM can operate in several topographical regimes; i) contact mode, in which a static tip is very close (~angstroms) to the sample surface, and ii) tapping mode, where a vibrating tip comes into intermittent contact with the sample only at its maximum deflection towards the surface. In this work we utilize tapping mode AFM exclusively.

A common tapping mode AFM measurement is shown schematically in Figure 1 . In general, the tip is mounted on a flexible cantilever and the whole assembly is made to vibrate at its resonant frequency given by equation (1) [180]:

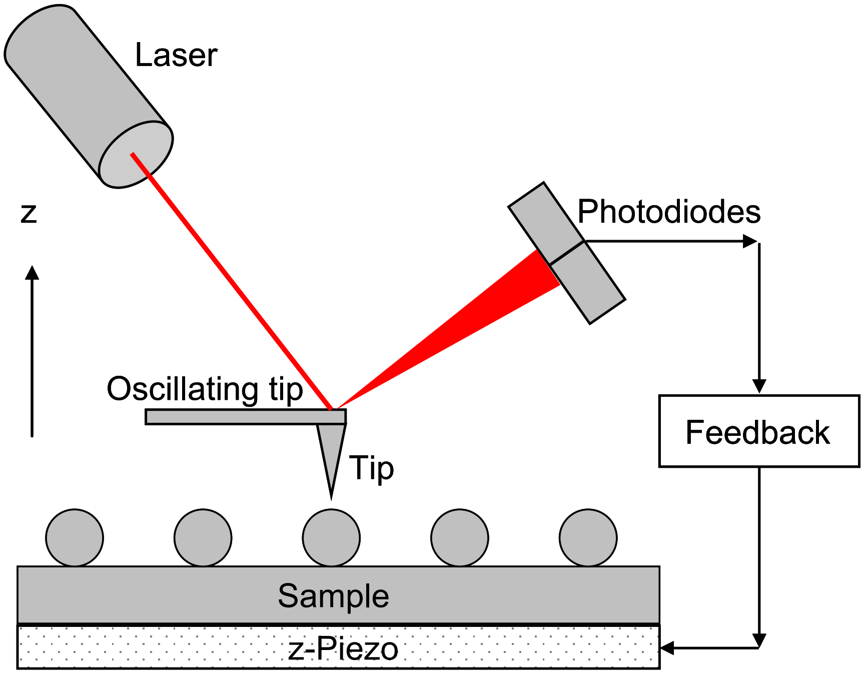

Figure 1 – Schematic showing the components of a typical AFM instrument.

$$f_0 = 0.162 \frac{t}{L^2} \sqrt{\frac{Y}{\rho}} \qquad (1)$$

Where t is the thickness of the cantilever, L is its length, $\rho$ is the mass density, and Y is Young's modulus. A laser is focused on the top edge of the vibrating cantilever and reflected evenly onto a split photodiode detector. While the tip is scanned over the sample its amplitude of vibration changes due to tip-sample interactions. This causes the signals received by the different sides of the split photodiode to differ by an amount proportional to the tip deflection. This signal is then rectified and converted to RMS amplitude. A feedback loop then adjusts the sample z-position in order to maintain the RMS amplitude at a constant, user-defined set-point. The variation in z is used to construct morphological images of the sample [181]. It should be kept in mind, however, that AFM images are a convolution of the sample and the tip [182]. Therefore, features that are similar in size or smaller than the tip will be over-represented in the re-created image. A typical tapping mode tip is etched from silicon and has a radius on the order of ~10 nm or more [183, 184]; measured as the radius of curvature of the apex of the tip. As such, when dealing with small NP samples AFM gives us reliable information about NP height only and not diameter. In addition, it is useful for calculating the distribution and distance between centers of NPs, giving information on interparticle distance. The instrument used for all AFM images in this work was a Nanoscope Multimode$^{\text{TM}}$ III (Digital Instruments) operating in tapping mode. More detailed information on the theory of tip-sample interactions and AFM measurement and instrumentation can be found in recent reviews by Giessibl and Gan [180, 185].

### 2.1.2 Transmission Electron Microscopy (TEM)

Transmission electron microscopy (TEM) was first developed in the 1930's [186] in an effort to surpass the resolution of ordinary optical microscopes. The technique is now highly evolved and widely used in materials science for its ability to image subnanometer details [187-190]. In optical microscopy the resolution, $D$, is ultimately limited by the wavelengths of light employed (~500 nm) as given by equation (2) [191]:

$$D = \frac{0.61\lambda}{\mu \sin\alpha} \tag{2}$$

Where $D$ is the distance between two separable (resolvable) features, $\lambda$ is the wavelength of the light, $\alpha$ is the angle between the incident and deflected ray of light, and $\mu$ is the refractive index of the medium between object and lens. The deflected ray must then pass through an aperture where it can be focused, thus $\alpha$ is known as the aperture angle. The term $\mu \sin\alpha$ has a maximum of about 1.7 [191]. Therefore, according to equation (2) the limit of $D$ is ~200 nm for visible light. If, however, an electron beam is used in place of ordinary light, the wavelengths obtainable are much smaller. For example, electrons accelerated through a potential of 200 keV have a wavelength $\lambda$ given by de Broglie:

$$\lambda = \frac{h}{\sqrt{2mVe}} \tag{3}$$

Where $h$ is the Planck constant, $m$ is the mass of the electron, $V$ is the potential, and $e$ is the charge of an electron. Substitution of numerical values gives a wavelength of 0.00251 nm; five orders of magnitude smaller than visible light. To create the beam, electrons are generated from a cathode and accelerated towards an anode, after which a set of electromagnetic lenses focuses the beam on the sample. Once the beam passes through the sample another set of lenses, as well as the aperture opening, combine to define and magnify an image of the sample. If the beam passes through a crystalline material the electrons can be treated as waves which will interfere constructively or destructively according to the Bragg equation:

$$n\lambda = 2d\sin\theta \tag{4}$$

Where $n\lambda$ represents an integer multiple of the wavelength, $d$ is the lattice spacing of the material, and $\theta$ is the angle between incident and scattered beam. From the pattern formed by these focused Bragg spots, one can obtain information about the crystalline lattice [186, 191].

In addition to scattering, electron-sample interactions also produce secondary electrons, as well as characteristic photons, which allow the possibility of probing the elemental and chemical make-up of the sample [191]. Contrast images produced by high-angle scattering of electrons from elements with differing atomic numbers (Z) can also give element specific information using high-angle annular dark-field (HAADF) detectors (Z-contrast images) [192]. Furthermore, *in-situ* electron microscopy is now available which allows one to study the dynamics of systems (i.e. restructuring of NP surfaces) under high temperatures and elevated pressures, as in catalytic reactions [18, 193, 194]. A more detailed discussion of TEM and its use can be found in Refs. [186, 191, 195].

### 2.1.3 X-ray Photoelectron Spectroscopy (XPS)

XPS is a commonly used technique to obtain electronic and chemical (i.e. oxidation state) information about sample materials and several works exist on its application in catalysis [196-199]. Briefly, an X-ray source is used to irradiate the sample and photoelectrons are generated with a broad distribution of kinetic energies. An electromagnetic lens system in combination with a hemispherical analyzer is used as an energy-filter to select a particular range of energies for which photoelectrons will be measured. When scanning this range of energies, the lens system configures itself accordingly such that incoming electrons having the desired kinetic energies will be focused onto the entrance slits of the analyzer. In addition, the electrons will be accelerated (or retarded) to match a user defined "pass energy". The pass energy is set by applying a potential difference across the inner and outer radii of the hemispherical analyzer. Electrons retarded to this energy will then safely pass along the curved path of the analyzer and be counted by the detector. The detector is an electron multiplier (i.e. channeltron) which amplifies the signal to acceptable levels to be collected by the computer. Figure 2 shows a schematic of the components used in an XPS system.

Kinetic energies collected by the analyzer are usually converted to binding energy (BE). This is accomplished through the application of equation (5):

$$E_K = h\nu - E_B - \varphi \qquad (5)$$

Where $E_K$ is the kinetic energy of the photoelectron, $h\nu$ is the energy of the incident photon, $E_B$ the binding energy of the photoelectron, and $\varphi$ is the work function of the spectrometer. We use as an X-ray source an Al anode, yielding $h\nu = AlK_\alpha = 1486.6$ eV,

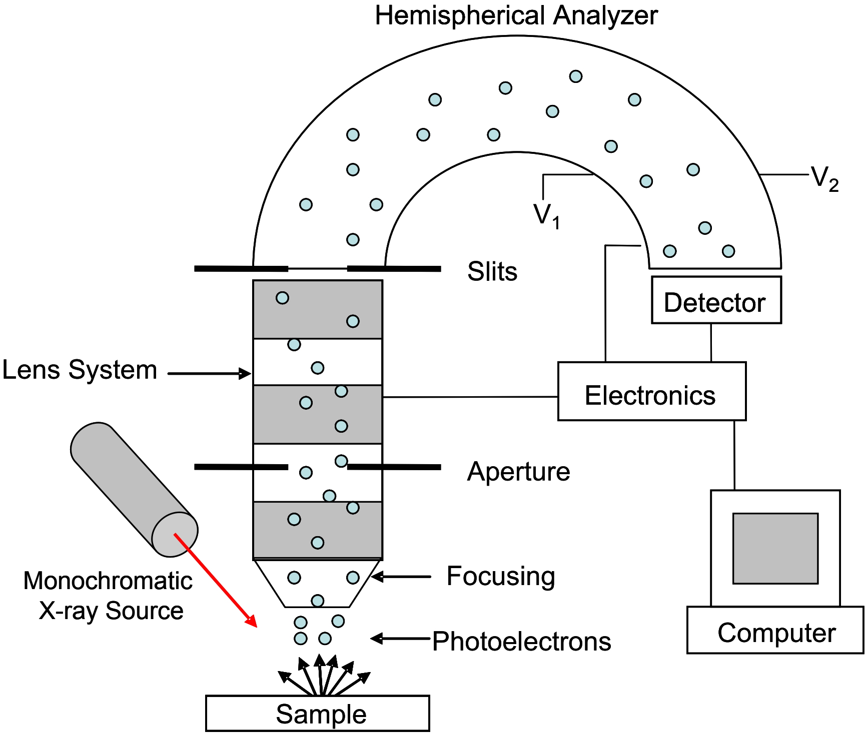

Figure 2 – Schematic showing the components of an XPS system.

and our spectrometer's work function is 4.3 eV. Following equation (5) we can then derive the BE of the photoelectron and thus its origin, for example, the element and orbital from which it was generated. Table 1 shows the spectroscopic notation for photoelectrons generated from different atomic orbitals. This notation is based on n, *ℓ*, and j, which are the principal quantum number, orbital momentum, and total momentum (*ℓ* + *s*), respectively, and *s* is the electron spin with values of ± ½. From Table 1 we see that any orbital with orbital momentum *ℓ* greater than zero will have two photoelectron peaks associated with it.

Table 1 – Spectroscopic notation for XPS photoelectron peaks.

| n | l | j | X-ray Level | $nl_j$ |
|---|---|---|---|---|
| 1 | 0 | 1/2 | K | 1s |
| 2 | 0 | 1/2 | $L_1$ | 2s |
| 2 | 1 | 1/2 | $L_2$ | $2p_{1/2}$ |
| 2 | 1 | 3/2 | $L_3$ | $2p_{3/2}$ |
| 3 | 0 | 1/2 | $M_1$ | 3s |
| 3 | 1 | 1/2 | $M_2$ | $3p_{1/2}$ |
| . | . | . | . | . |
| . | . | . | . | . |
| . | . | . | . | . |
| 4 | 3 | 5/2 | $N_6$ | $4f_{5/2}$ |
| 4 | 3 | 7/2 | $N_7$ | $4f_{7/2}$ |

These peaks are called spin-orbit doublets and the ratio of their intensities can be calculated from the degeneracy of the level given by 2j+1. In our work we will see the Pt-4f doublets quite often, so we use them as an illustration. The Pt-4f orbital has quantum numbers n=4, $\ell$ = 3, and s = ± ½ (the quantum number $\ell$ is also represented as s, p, d, and f for $\ell$ = 0, 1, 2, and 3 respectively, as seen in the last column of Table 1). As such, the two peaks we observe in XPS are denoted as $4f_{7/2}$ (j=3 + ½) and $4f_{5/2}$ (j=3 - ½). The degeneracy of 2j+1 gives an intensity ratio of $4f_{5/2}$:$4f_{7/2}$ = 0.75 and the spin orbit splitting for this pair is 3.3 eV [200]. These numbers are important parameters for correctly interpreting and fitting the Pt-XPS spectra. In addition to the nominal peak positions, chemical information can be obtained from peaks that are shifted from their expected BE values. For example, oxidation of Pt can occur through its interaction with oxygen or substances such as chlorine. When Pt becomes oxidized it essentially loses some of its electrons; $PtO_2$ loses 4 ($Pt^{4+}$), PtO and $PtCl_2$ lose only 2 ($Pt^{2+}$) and Pt metal is neutral ($Pt^0$). The remaining electrons in these oxides now see an increased potential due to the loss of electrons and a decrease in the "shielding" of the positive nuclear charge. This increases the BE observed for the remaining electrons in the peaks of the XPS spectrum. In addition, BE shifts are common when dealing with NPs due to so-called initial and final state effects [201]. Small particles with reduced coordination have different electronic properties than their bulk counterparts (initial state). When these NPs lose electrons due to the photoelectric effect of XPS, there remain relatively few electrons to screen the potential of the nucleus compared to the bulk metal. Therefore, the emitted photoelectron feels a greater potential than it would in a bulk material (final state effect), and its BE appears shifted to higher energies, similar to oxidation. Figure 3 shows an example of these effects in the Pt-4f doublets of a Cl-containing Pt NP sample before and after the Cl has been removed (i.e. the sample has been reduced) by an *in-situ* $O_2$-plasma and annealing treatment. Note that the dashed grey line marks the BE position of the bulk metallic Pt-$4f_{7/2}$ peak at 71.1 eV [202]. The bottom curve (a) shows the 4f peaks highly shifted, with the $4f_{7/2}$ at ~75.2 eV corresponding to $Pt^{4+}$ in $PtCl_4$ [202]. After the reduction treatment the top curve (b) shows that the $4f_{7/2}$ peak has shifted to lower energy and is now at ~71.4 eV corresponding to metallic $Pt^0$. This is 0.3 eV higher than the expected 71.1 eV for metallic Pt and is a consequence of initial and final state effects due to the small particle size (~3.5 nm).

In addition to the effects discussed above care must be taken to properly compensate for sample charging during XPS data acquisition. For non-conducting samples escaping photoelectrons cannot be replenished through the substrate and a surface charge builds up. This is usually accounted for by the use of a low-energy (0-10 eV) electron flood gun. The electron gun is adjusted to flood the surface with enough charge to compensate for

BE shifts and peak irregularities caused by sample charging. A suitable, "bulk-like" reference peak within the sample is then used to shift the entire spectrum to the correct position.

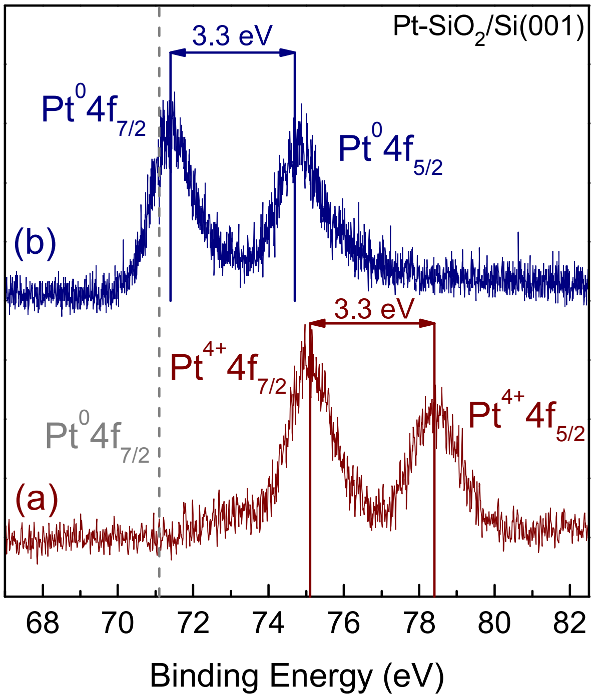

Figure 3 – Raw XPS spectra of the Pt-4f region of ~3.5 nm (AFM height) Pt NPs deposited on $SiO_2$/Si(001). The bottom curve (a) shows Pt in an oxidized state due to its interaction with Cl remaining from the synthesis process. The top curve (b) shows the same sample after an in-situ $O_2$-plasma treatment followed by annealing at 910°C. The solid lines in each curve show the positions of the $4f_{7/2}$ and $4f_{5/2}$ peaks and the dashed grey line shows the BE position of the $4f_{7/2}$ peak of bulk metallic Pt.

### 2.1.4 Temperature Programmed Desorption (TPD)

TPD is an *in-situ* technique used to extract kinetic information on the adsorption of gases on surfaces. This is done by monitoring desorption as a function of temperature and coverage. From the data one can extract rates of desorption, coverage of the adsorbing gas, activation energies, reaction order, and more [199]. The experimental set-up consists of a sample stage equipped with heating/cooling capabilities (i.e. electron beam heating/liquid $N_2$ cooling) coupled to an external, programmable proportional-integral-differential (PID) temperature controller. The temperature is recorded by a thermocouple spot-welded to the sample holder so that it makes contact with the underside of the sample. A differentially – pumped quadrupole mass spectrometer (QMS) can be brought close (~2 mm) to the sample stage to monitor the partial pressures of desorbing gases. In practice, the temperature of the sample is brought to some initial level and it is then dosed with the gas/gases of interest. In many cases the sample is cooled to liquid $N_2$ temperature to increase the sticking coefficient of the reactants of interest. The sample is then heated in a linear fashion over some temperature range while the QMS records partial pressures of the desorbing gases as a function of temperature. TPD spectra can be described by an Arrhenius expression known as the Polanyi-Wigner equation (PW) [203]:

$$r(\theta) = -\frac{d\theta}{dt} = \nu(\theta)\theta^n \exp\left[\frac{-E(\theta)}{RT}\right] \tag{6}$$

Where $r$ is the rate of desorption, $\theta$ is the coverage in monolayers, $t$ is time, $\nu$ is the pre-exponential factor, $n$ is the order of desorption, $E$ is the activation energy, $R$ is the gas constant, and $T$ is the temperature. Figure 4 shows example TPD spectra of $O_2$-desorption from a Pt(111) single crystal surface. At least ten different methods have been suggested for the analysis and interpretation of such data [204]. These methods have been evaluated by de Jong and Niemantsverdriet [204] and only the so-called leading-edge and complete analysis methods were found to give reliable information over the range of coverages studied. We can see from the PW equation that the quantities to be calculated are the desorption order $n$, the pre-exponential factor $\nu$, and the activation energy $E$. However, unless a single desorption feature (state) can be isolated, and multilayer desorption avoided, it is a difficult

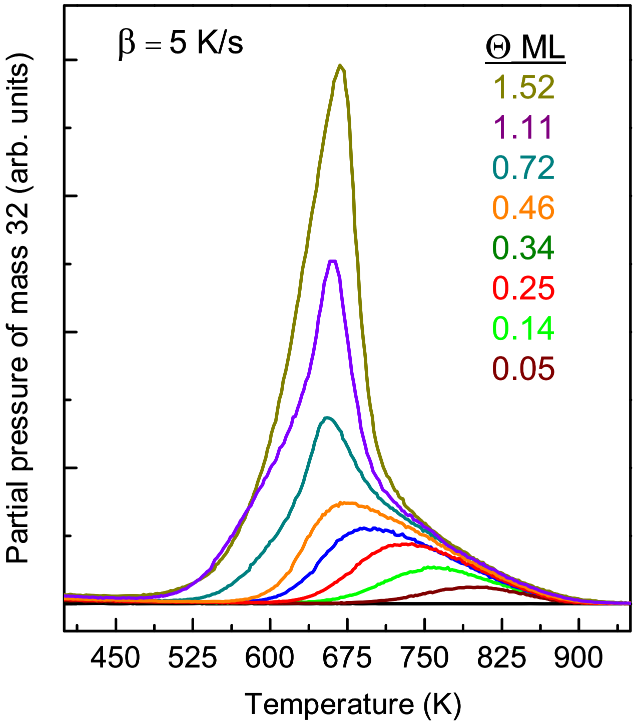

Figure 4 – TPD spectra of $O_2$ desorption from Pt(111). A linear heating ramp of $\beta = 5$ K/s was used for all coverages (Θ) given in monolayers (ML). For Pt(111), 0.25 ML is defined as the saturation coverage of atomic oxygen, equal to 25 % of the Pt(111) surface atom density of $1.51 \times 10^{15}$ atoms/cm$^2$.

task to extract reliable information from such analysis. Furthermore, $n$ and $\nu$ might also depend on the adsorbate coverage. The leading edge analysis has been used to estimate $E$ and $n$ for desorption of high coverages of oxygen on Pt(111) [79]. This method relies on assuming a constant temperature and coverage by only analyzing a small portion of the spectrum on its leading edge [199], however for supported NP samples this method is challenging. First, because of the low signals obtained from NP samples, the leading edge region is too noisy to be reliable. In addition, subtraction of background peaks (from substrate desorption) may introduce large errors [205]. Similarly, the complete analysis method also requires non-overlapping states of adsorption [199, 205]. Furthermore, this method is most accurate when $E$ and $\nu$ are coverage-independent. For example, Nieskens et al. [206] have shown that the complete analysis works well for attractive interactions among adsorbates, but errors are introduced when repulsive interactions exist. As we will see for $O_2$-desorption from bulk Pt(111), the type of interactions that exist between surface oxygen change from attractive to repulsive depending on the coverage. In addition isolation of single desorption states from supported NPs will prove to be a major challenge for TPD experiments. As a first step in understanding Pt NP TPD spectra, we will prepare model systems of monodisperse, size-selected, Pt NPs supported on $SiO_2$/Si(100) and extract qualitative information based on the comparison with coverage and desorption data from $O_2$-TPD experiments on bulk Pt(111).

Figure 5 shows the UHV chamber used in this work for the acquisition of XPS and TPD data, as well as sample preparation (i.e. $O_2$-plasma, annealing, sputtering, etc.). The XPS system has a crystal monochromater and two switchable, dual anode X-ray sources, one with Al and Mg anodes, and one with Al and Ag anodes (used with the monochromator). The QMS is mounted opposite the monochromator in the chamber in the picture. In addition, the system is equipped with a molecular beam epitaxy (MBE) chamber for sample preparation, *in-situ* heating and cooling capabilities, electron and sputtering guns, a quartz-crystal microbalance for vapor deposition, and a plasma source. Other instruments include low energy electron diffraction (LEED), scanning tunneling microscopy (STM), and ultraviolet photoelectron spectroscopy (UPS).

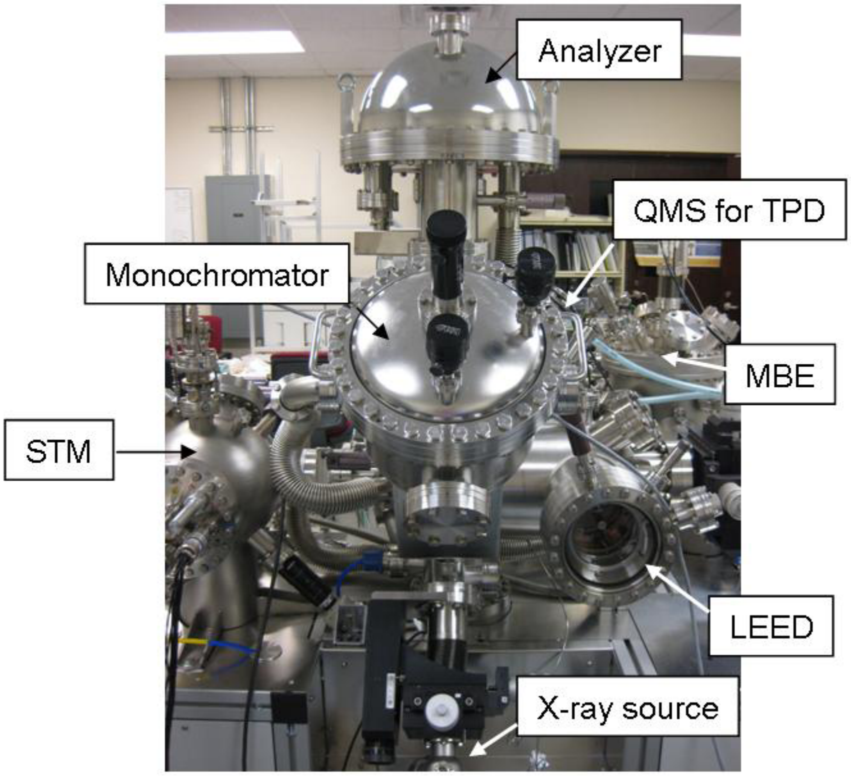

Figure 5 – Ultra high vacuum (UHV) chamber used for *in-situ* XPS and TPD characterization studies.

### 2.1.5 Packed-Bed Reactor

Figure 6 shows a schematic of the atmospheric packed-bed reactor used for reactivity experiments in our work. Mass flow controllers (MFC) are used to regulate the flow of reactant and carrier gases through the reactor stage which contains the catalyst bed. The outlet of the reactor is then coupled to a QMS for monitoring the composition of the reactor effluent. A total of four MFCs are used allowing up to four different reactant gases to be mixed. A bubbler has also been installed for the option of using liquid reactants such as methanol. For this purpose, the carrier gas (i.e. helium) is passed through the bubbler containing the liquid reactant and carries away a vapor concentration as given by equation (7):

$$F_v = F_C \times \frac{P_v(T)}{P_H - P_v(T)} \tag{7}$$

Where $F_v$ is the flow of the vapor, $F_C$ is the flow of the carrier through the bubbler, $P_v(T)$ is the vapor pressure of the liquid in the bubbler at temperature $T$, and $P_H$ is the pressure in the head space of the bubbler (i.e. between the top of the liquid and the top of the bubbler vessel) [207]. From equation (7) we see that we can control the concentration of vapor by increasing the temperature of the bubbler, which increases the vapor pressure $P_v(T)$, or by increasing the flow of the carrier, $F_C$. In addition, Figure 6 shows that a second MFC can be used to dilute the outlet of the bubbler with the carrier gas. These three factors allow for precise control of the concentration of vapor through the reactor stage. The reactor itself is a quartz glass tube; chosen for its inertness and resistance to high temperatures. Typically, the catalysts used are metallic NPs supported on nanocrystalline powders. These powders are held in place by quartz wool plugs inside the reactor tube and the assembly is inserted into an insulated tubular furnace. A K-type thermocouple is placed outside of the reactor at the position of the sample and a programmable PID temperature controller is used to control the temperature of the reactor throughout the experiments.

The exhaust of the reactor is coupled to the QMS (HPR-20, Hiden Analytical) for monitoring partial pressures of product and reactant gases. The QMS is equipped with a heated silica capillary (inside diameter 0.3 mm) from which the sample gases exit at low pressure and high velocity, and subsequently impinge on a platinum orifice (0.02 mm). The orifice provides a second stage of pressure reduction from which sample gases enter directly into the mass spectrometer ion source. These stages of pressure reduction allow us to directly sample gases at atmospheric pressure. The inlet of the capillary has a maximum consumption of 16 ml/min and the setup can be operated in a pressure range of 10 mbar to 2 bar. Figure 7 shows the packed-bed mass flow reactor used in this work.

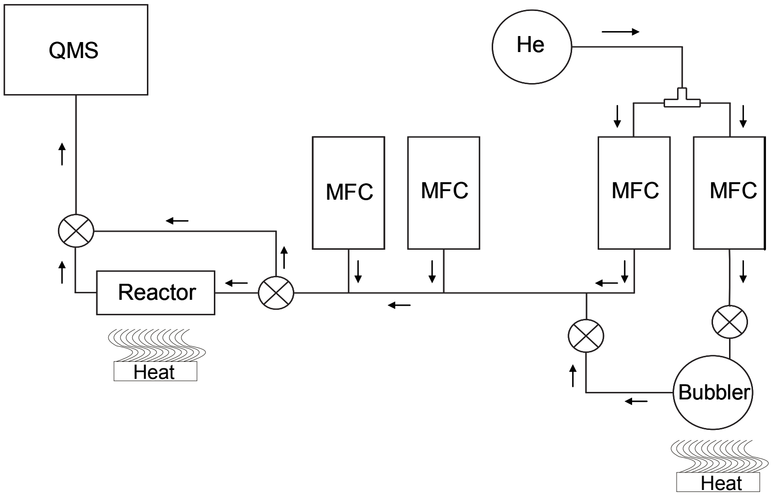

Figure 6 – Schematic of the packed-bed reactor (reactor I in Figure 7) used in this work. Mass flow controllers (MFC) are used to control the flow of reactant and carrier gases through the reactor stage and into the inlet of the QMS. An optional bubbler for carrying liquid vapors to the feed gas has been installed.

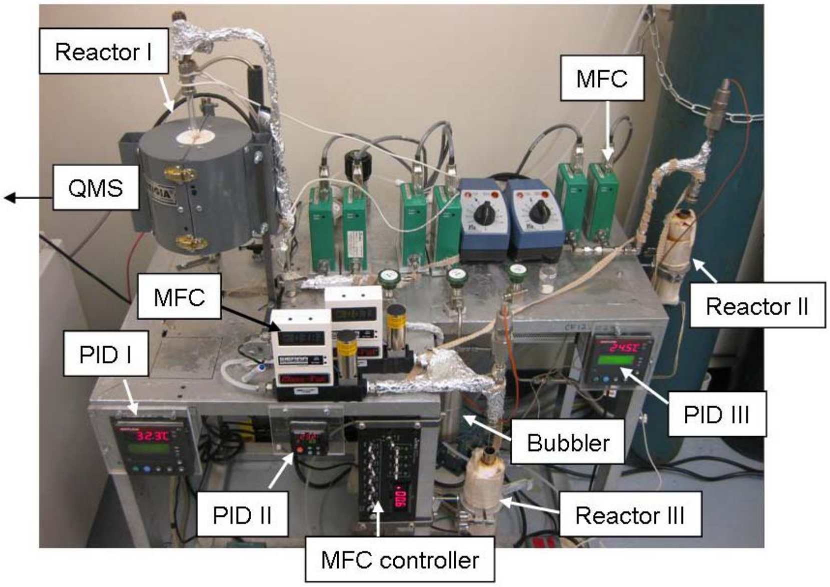

Figure 7 – Packed-bed reactor used for reactivity and annealing experiments in this work. The system has three separate reactors each equipped with a furnace, MFCs, and PID controllers. In addition, reactors I and II each have a Hiden HPR-20 QMS connected to their outlets.

## 2.2 Synchrotron-based Techniques

### 2.2.1 Nuclear Inelastic X-ray Scattering (NRIXS)

**Introduction**

Nuclear Inelastic X-ray Scattering (NRIXS) is a synchrotron-based technique which relies on the resonant absorption of incident photons by nuclei within a sample material. The products of de-excitation (i.e. fluorescence, conversion electrons) can be measured as a function of incident photon energy and information regarding the sample properties can be extracted. Of particular convenience is the fact that the phonon (vibrational) density of states (VDOS) can be directly obtained from the experimental data, from which follows a thermodynamic description of the material. Another advantage of this technique is its isotope selectivity, as it is sensitive only to vibrations of the isotopically enriched resonant nuclei. Therefore, local vibrations can be measured in materials having resonant nuclei at specific locations, as in layered thin films. In such cases it is the partial density of states that is obtained from the data, where *partial* refers to the fact that only vibrations associated with the resonant nuclei are being probed. The main reasons for the emergence of NRIXS are the advent of modern synchrotron facilities and advances in X-ray optics and detector technology [208, 209]. However, even in light of its success and advantages, there are restrictions on which elements may be gainfully employed in NRIXS. Atoms which participate in NRIXS must display an observable Mössbauer Effect (from its discoverer, Rudolf L. Mössbauer), as described in the next section.

## Phonons and the Lamb-Mössbauer factor

A γ-ray of energy $E_\gamma$ may be absorbed by an atom if the atom contains a nucleus having an excited state transition energy $E_0 = E_\gamma$. Decay of the nucleus back to the ground state may be accompanied by the re-emission of a photon with the same energy $E_\gamma$ (fluorescence via nuclear de-excitation). The excitation probability $S(E)$ for fixed nuclei is shown in Figure 8(a) and consists of a single, elastic peak (Mössbauer peak) centered on the nuclear transition energy $E_0$, with a width determined by the nuclear level mean lifetime τ. In the lattice of a real solid, atoms are tightly bound but still vibrate about some equilibrium position and their motion can be described by the harmonic oscillator. Each normal mode of vibration is treated as a quasi-particle called a phonon with quantized energy levels, $E_n = \left(n + \frac{1}{2}\right)\hbar\omega$ (n = 1, 2, 3 …). Phonons carry no net momentum and thus are referred to as quasi-particles. Taking Einstein's model as a base, all atoms vibrate with the same frequency $\omega$. The effect of vibrational modes on $S(E)$ is to reduce the Mössbauer peak at $E_0$ and to add low intensity peaks at energies equal to $E_0 \pm E_n$, Figure 8(b). These sidebands in $S(E)$ correspond to resonant events triggered by incoming photons with energies other than the resonant energy $E_0$. This is made possible by an exchange of energy between the incoming photon and the lattice vibrations of the solid in processes called phonon annihilation ($E_\gamma < E_0$) and creation ($E_\gamma > E_0$). If the incoming photon's energy is below $E_0$ it may take energy from the lattice and still cause resonant excitation to occur by phonon annihilation. Likewise, if a photon's energy is greater than $E_0$ it may still cause resonant excitation of nuclei by giving its excess energy to the lattice via phonon creation. In reality, the atoms of a solid vibrate with many frequencies and $S(E)$ becomes nearly continuous. The fraction of events which do not alter lattice vibrational modes (i.e. recoilless) compared to all events is known as the f-factor and is given by (8) [210]:

$$f_{LM} = \exp\left(-\frac{k^2\langle u^2\rangle}{3}\right) \tag{8}$$

Where $\langle u^2\rangle$ is the average square displacement of an atom in the lattice and $k$ is the wave number of the emitted or absorbed photon. The subscript LM stands for Lamb-Mössbauer and refers to two pioneers in the field.

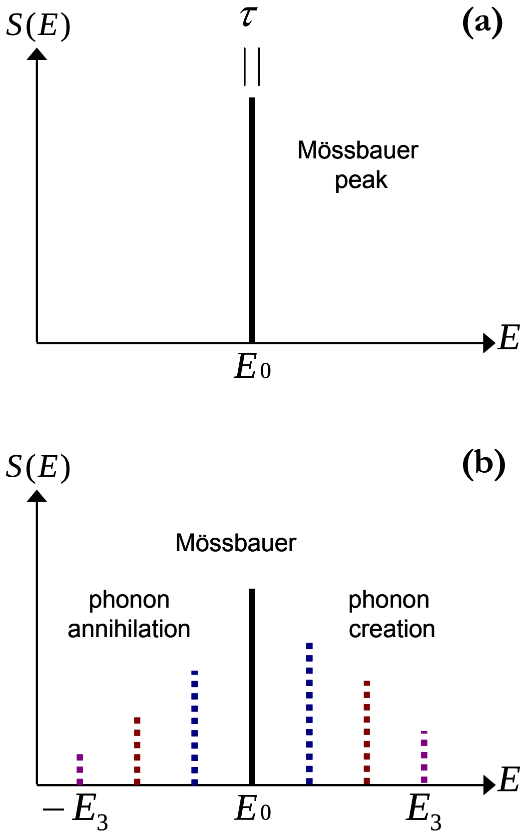

Figure 8 – Probability of nuclear excitation for (a) fixed nuclei and (b) the Einstein Model where all atoms are allowed to vibrate with the same frequency.

## Density of States and Derivable Quantities

The VDOS and other quantities are derived directly from the experimental data and the process has been reviewed in detail [211-213]. Considering the f-factor, the absorption probability $S(E)$ can be broken into elastic and inelastic contributions given by:

$$S(E) = f_{LM}\delta(E) + \sum_{n=1}^{\infty} S_n{}'(E) \tag{9}$$

Here, the term $\delta(E)$ represents the fact that the width of the resonant, elastic peak is orders of magnitude smaller than typical phonon energies and may be approximated by the Dirac $\delta$-function. $S_n{}'(E)$ represents the inelastic contribution and is the probability of exciting $n$ phonons. The first three moments of the function $S(E)$ are known as Lipkin's sum rules and have been shown to be:

$$\int E\,S(E)\,dE = E_R \tag{10}$$

$$\int (E - E_R)^2 S(E)\,dE = 4E_R E_K \tag{11}$$

$$\int (E - E_R)^3 S(E)\,dE = \frac{\hbar^2}{m} E_R K \tag{12}$$

Where $E_R$ is the recoil energy of the free atom, $E_K$ is the average kinetic energy of the resonant nuclei, and $K$ is the mean force constant of the bound nuclei.

In practice, one counts the number of resonant photons at each energy in a range of energies centered about $E_0$. The intensity (number of counts) is given by:

$$I(E) = a\,S'(E) + b\,f_{LM}\,\delta(E) \tag{13}$$

where $a$ and $b$ are normalization constants. If we subtract the elastic contribution we are left with the inelastic intensity $I^{'}(E) = a\,S^{'}(E)$, and since $\int S^{'}(E)\,dE = 1 - f_{LM}$, we obtain directly from the measured spectrum:

$$f_{LM} = 1 - \frac{1}{a}\int I^{'}(E)\,dE \tag{14}$$

with the constant $a$ determined from the first moment of the acquired spectrum [Lipkin's sum rule equation (10-12)].

$$a = \frac{1}{E_R}\int I(E)EdE \tag{15}$$

From here the normalized multiphonon contributions $S_n(E)$ can be extracted from the measured data and the one-phonon term gives directly the phonon density of states $g(E)$ by the relation:

$$S_1(E) = \frac{E_R g(E)}{E(1-e^{-\beta E})} \tag{16}$$

Where $\beta = k_B T^{-1}$ and $k_B$ is the Boltzmann constant. The Lamb-Mössbauer factor (f-factor) is also related to the multiphonon terms by:

$$\int S_n(E)\,dE = \frac{(-\ln f_{LM})^n}{n!} \tag{17}$$

Therefore, when the Lamb-Mössbauer factor is close to one, higher order phonon terms will not contribute significantly. On the other hand, if the Lamb-Mössbauer factor is too low, higher order terms may dominate and the distinction of one-phonon processes becomes difficult. In such cases the determination of $g(E)$, via the extraction of $S_1(E)$ may not be possible. Equation (17) now gives some meaning to our earlier statement that useful nuclei for NRIXS must have an *observable* Mössbauer Effect. In general, the transition energy of the nucleus in question should not be too large and/or the atoms of the solid must not be too lightly bound. Both cases may result in a recoil energy, $E_R$, that is large compared to the phonon energies, thus increasing the probability of multi-phonon scattering.

From a complete analysis more than ten different quantities of interest can be derived from the VDOS [214]. The important thing to note is that these quantities are all obtained directly from the experimentally measured spectrum, $I(E)$. In the next section we will see exactly how this spectrum is acquired using third generation synchrotron technology.

## Experimental Set-up

There are several factors to consider when collecting data using the technique of NRIXS as discussed above. This section will describe the experimental set-up and data acquisition at beam-line 3-ID of the APS at Argonne National Laboratory, USA.

A typical schematic of the APS set-up, from storage ring to sample detectors, is shown in Figure 9. The process starts with electrons accelerated to ~4.5 MeV in the linear accelerator (LINAC), they then enter the booster/injector synchrotron ring where they are accelerated to 7 GeV and injected into the larger, outer ring called the storage ring. The electrons are kept in orbit about the storage ring by a system of bending magnets. Devices called undulators, consisting of a linear section of permanent magnets with alternating polarities, are placed in the path of the orbiting electrons. The alternating magnetic field in the undulator section causes the electrons to undulate as they pass through, which produces an intense beam of X-ray radiation. This beam has a wide bandwidth (6 to 100 keV) and is called the white beam. Since the electrons are relativistic (7 GeV) the beam is highly collimated in the forward direction along the beam-line, at the end of which, awaits the experimental station. After the undulator the beam passes through two monochromators. The first consists of two diamond crystals and is called the high-heat-load mono (HHM), or pre-mono. The HHM serves to reduce the power of the beam and to narrow the bandwidth to about ~1 eV. The next stage is the high resolution mono (HRM) with a four-crystal nested geometry. The HRM further reduces the bandwidth down to energies typical for phonons (~1 meV) and is used to tune the energy of the beam about $E_0$ during data acquisition; centered in the present case on the nuclear resonance of $^{57}$Fe equal to 14.413 keV. The HRM defines the maximum possible energy resolution of the experiment. The beam also passes through ionization chambers (IC-1 and IC-2), placed after each monochromator, in order to monitor and adjust photon flux to the sample stage. After IC-2 the beam is incident on a set of focusing mirrors (FM) which reduce the size of the beam to ~10 μm. The beam is then incident on the sample and two avalanche photodiode detectors (APD) count the scattered photons. APD-1 is located close to the sample and monitors the spatially incoherent, inelastic scattering processes while IC-2 is located far from the sample and counts coherent, forward scattering events; which measures the actual resolution function of the HRM used for subtraction of the elastic peak as mentioned above.

## APS Time Structure and Data Acquisition

The spectrum $I(E)$ is obtained by tuning the HRM through a wide range of energies (relative to the phonon energies of interest, ~± 90 meV) across $E_0$ while collecting counts with the APD detectors at each energy. However, a timing trick is needed to separate

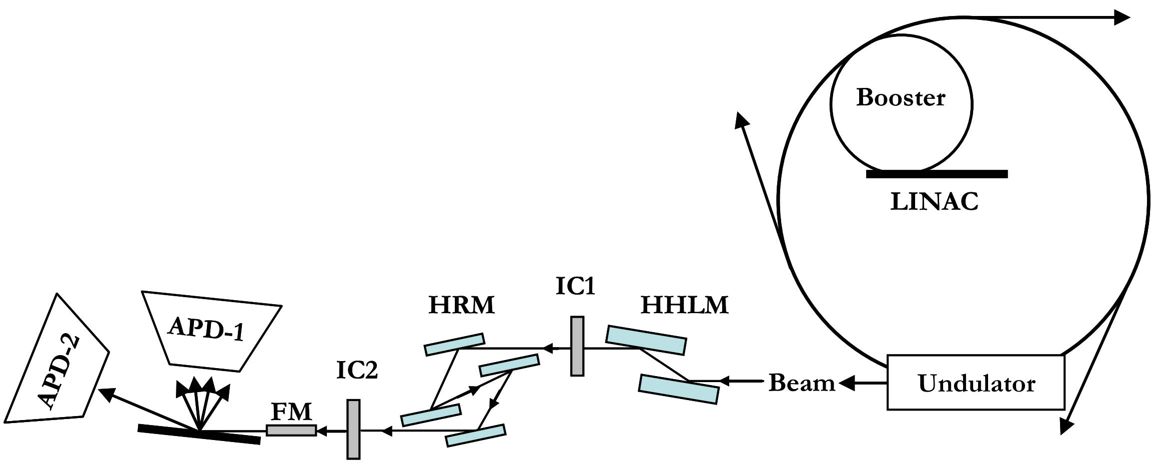

Figure 9 – Intense, highly collimated X-ray radiation is produced in a synchrotron when orbiting, relativistic electrons pass through the spatially alternating magnetic field of the undulator. The beam is then passed through two monochromators before reaching the sample where avalanche photodiode detectors monitor nuclear fluorescence. The HHLM consist of two diamond crystals and is used to reduce as well as center the bandwidth of the incoming beam. The HRM has a four-crystal nested geometry and is used to scan the energy of the beam across resonance while the detectors count photons at each energy increment. IC1 and IC2 monitor the flux of photons after each monochromator.

the intense electronic scattering (i.e., Compton scattering) from the less intense resonant response from nuclear scattering. This is accomplished by the time structure of the synchrotron itself. Electrons may only occupy certain stable orbits in the storage ring called buckets. The APS ring has a circumference of 1108 m and 1296 possible buckets. When 24 of these buckets are filled with electrons the time between each bunch of electrons traveling through the undulator is 154 ns. This means that a pulse reaches the sample every 154 ns. Since the intense electronic scattering from the sample takes place instantaneously ($10^{-15}$ s) compared to the delayed nuclear events (for example the excited state lifetime of $^{57}$Fe is 141 ns), we can use a time-delayed acquisition method to filter out electronic scattering and record only the delayed photons from nuclear resonant scattering. This is possible because we know the fill pattern of the ring which tells us the timing of pulses reaching the sample and, therefore, the timing of electronic and resonant events. The APD detectors are well suited for this because of their ability to quite down quickly after the first, prompt response, and begin taking counts again only after a specified delay. This greatly increases the signal to noise ratio of the experiment since we measure only those photons related to nuclear resonant events.

## 2.2.2 X-ray Absorption Fine Structure Spectroscopy (XAFS)

### Introduction

X-ray absorption spectroscopy (XAS) is a synchrotron-based technique that is able to probe the chemical, compositional, and local atomic structure of materials. It is an element-specific probe and applies to both amorphous and crystalline materials. In general, XAS is a measurement of the absorption coefficient $\mu$ as a function of incident photon energy. The energies of interest lie close to and above core-level transitions (absorption edges) of the absorbing atoms. XAS is divided into two main energy regions; X-ray absorption near edge spectroscopy (XANES), which is within ~30 eV of a main absorption edge, and extended X-ray absorption fine structure spectroscopy (EXAFS), where the energy region of interest is well above the absorption edge (~30-200 eV). XANES is most sensitive to the chemical state of the atoms such as the oxidation state, while EXAFS can be used to determine the distances, coordination, and species of neighboring atoms. XAFS experiments are carried out much the same way as in NRIXS with the exception of a few details given below.

## EXAFS Theory

Like NRIXS, the history of EXAFS follows closely the development of synchrotron technology and a full theoretical description was not realized until the 1990's. For full details of EXAFS interpretation the interested reader should see Refs. [215-218]. What follows is a brief description of the main points of EXAFS theory.

The probability that an X-ray will be absorbed by an atom is given by Beer's Law:

$$I = I_0 e^{-\mu t} \tag{18}$$

Where the absorption coefficient $\mu$ is dependent on the photon energy $E$, the density of the absorbing material $\rho$, the atomic number $Z$, the atomic mass $A$, and the thickness of the material $t$, by the relation:

$$\mu \approx \frac{\rho Z^4}{AE^3} \tag{19}$$

Because $\mu$ describes the probability of a transition between two states it is given by Fermi's Golden Rule:

$$\mu(E) \propto \left| \langle i \mid H \mid f \rangle \right|^2 \tag{20}$$

Where $\langle i|$ is the initial state (X-ray plus core-electron), $| f \rangle$ is the final state (core-hole plus photoelectron), and $H$ is the perturbing Hamiltonian. When a photoelectron is generated by the absorption process it travels outward from the absorbing atom as a spherical wave. This "electron wave" can then scatter from neighboring atoms and reflect back to the original, absorbing atom. The amplitude and phase of the scattered electron's wave function, at the position of the absorbing atom, will add constructively or destructively to the outgoing photoelectron wave. This will affect the absorption coefficient $\mu$ by its modulation of $| f \rangle$ in equation (20). This alteration in $\mu$ due to the scattered photoelectron is the origin of EXAFS and appears as oscillations in the spectrum. Thus, the EXAFS region has been defined as the normalized, oscillatory part of the absorption spectrum, above a given absorption edge, by the equation:

$$\chi(E) = \frac{\mu(E) - \mu_0(E)}{\Delta\mu_0(E)} \tag{21}$$

Here, $\mu(E)$ is the measured absorption coefficient, $\mu_0(E)$ is a background function that represents the absorption of an isolated atom, and $\Delta\mu_0(E)$ is a normalization factor given by the rise (or "jump") in absorption at the edge energy $E_0$. Equation (21) is known as the EXAFS fine-structure function. Due to the wave-nature of EXAFS it is customary to convert energy to $k$, the wave number of the photoelectron, given by:

$$k = \sqrt{\frac{2m(E - E_0)}{\hbar^2}} \tag{22}$$

Where $E_0$ is the absorption edge energy and $m$ is the mass of the electron. $k$ is given in inverse wavelength as $\frac{1}{\lambda}$ where $\lambda$ is the de Broglie wavelength. As an illustration, consider a photoelectron that scatters from the nearest-neighbor atoms (first shell). This photoelectron will acquire a phase difference of $\sim 2kR$, where $R$ is the distance to the neighboring atoms. With increasing energy, $\lambda$ will decrease (changing the acquired phase) and thus destructive and constructive interference will occur as the energy of the incoming photons is changed. This interference is also dependent on the strength of the scattering from neighboring atoms as well as the number of scatterers.

In addition, multiple scattering paths, differing species of neighboring atoms, inelastic scattering, and the core-hole lifetime, can have an influence on the measured spectrum. Sayers et al. [215] have developed a quantitative expression for $\chi(E)$ in terms of $k$ taking all of the above mentioned factors into consideration. This expression is the basis for data analysis and is known as the EXAFS equation given by:

$$\chi(k) = \sum_{R} S_0^2 N_R \frac{|f(k)|}{kR^2} \times \sin(2kR + 2\delta_c + \Phi) e^{-2R/\lambda(k)} e^{-2\sigma^2 k^2} \qquad (23)$$

Here $S_0^2$ is a constant damping factor due to inelastic losses, $R$ is the average distance from the absorbing (central) atom to each surrounding shell, $N_R$ is the number of equivalent scatterers at $R$ (coordination number), $\sigma$ is the quadratic mean temperature-dependent fluctuation in bond length relative to the absorbing atom, $|f(k)|$ and $\Phi$ represent the back-scattering amplitude and phase factor introduced by the scattering atom, respectively, $\delta_c$ is the central atom partial-wave phase shift induced by the absorbing atom, $k = 2\pi/\lambda$ is the photoelectron wave number, and $\lambda(k)$ is the photoelectron mean free path. The last term of the EXAFS equation (23), $e^{-2\sigma^2 k^2}$, is due to structural disorder as well as the thermal motion of atoms and gives the Debye-Waller factor. In addition, Sayers et al. [215] also showed that a Fourier transform of the EXAFS equation with respect to $k$, gives a distribution of distances, $R$, with peaks corresponding to the first few nearest-neighbor distances. Therefore, a combination of $N_R$ and $R$ has the potential for giving detailed structural information about the sample.

**Experiment**

In practice one measures the intensity $I$ of the X-ray beam as a function of energy. As with NRIXS, the energy is tuned using a monochromator placed in the path of the beam and $\mu$ is given as:

$$\mu(E) = \ln\left(\frac{I_0}{I}\right) \tag{24}$$

where $I_0$ is the intensity of the incoming beam and $I$ is the intensity of photons transmitted through the sample. Equation (24) is valid for measurements made in transmission mode only as shown in Figure 10 (top). Measurements can also be done by monitoring fluorescence from the sample as in Figure 10 (bottom), in which case:

$$\mu(E) \propto \left(\frac{I_f}{I_0}\right) \tag{25}$$

Where $I_f$ is the intensity of a fluorescence peak.

Figure 11 shows XAS data taken of a Pt-foil in transmission mode. The intense peak at 11562 eV marks the Pt-$L_3$ absorption edge which begins at ~11550 eV. This peak occupies the XANES portion of the spectrum, as discussed above, and is called the white line. The intensity of the white line is proportional to the number of unoccupied 5d-states in 5d metals like Pt [219]. Therefore, if Pt is oxidized (i.e. loss of 5d electrons) then transitions from the $2p_{3/2}$ to the 5d orbitals are more likely and the intensity of the absorption peak goes up. This makes XANES especially sensitive to the oxidation state of the sample. In addition, the white line intensity is also sensitive to the size and shape of small particles. [220]. The blue line in Figure 11 is the measured absorption data and the red line is the single-atom background function used to extract the EXAFS data. The oscillations in the blue line are the data of interest for EXAFS. Bulk-foil data such as those shown in Figure 11 are acquired at the same time as the sample data (Figure 10) and are used for energy calibration.

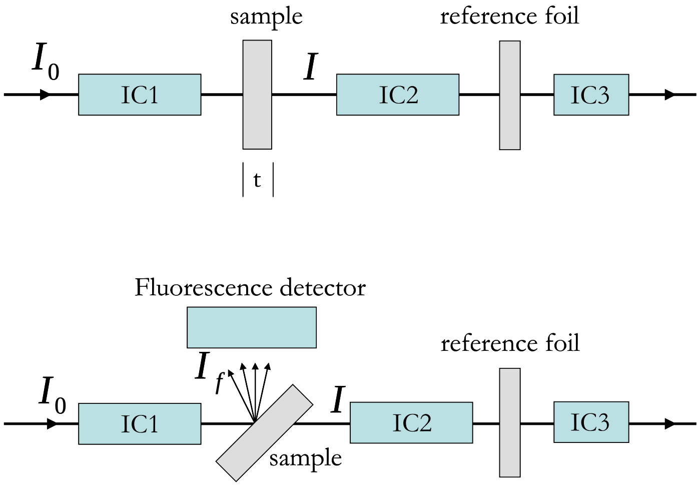

Figure 10 – Experimental setups for XAS measurements. Transmission mode (top) or fluorescence mode (bottom). In fluorescence mode the sample is tilted 45° with respect to the beam and both transmission and fluorescence data can be obtained simultaneously. IC1 monitors the intensity of the incident beam ($I_0$), IC2 the flux transmitted through the sample ($I$) and IC3 monitors the flux of the beam through the reference foil. The foil is used as a reference for energy calibration.

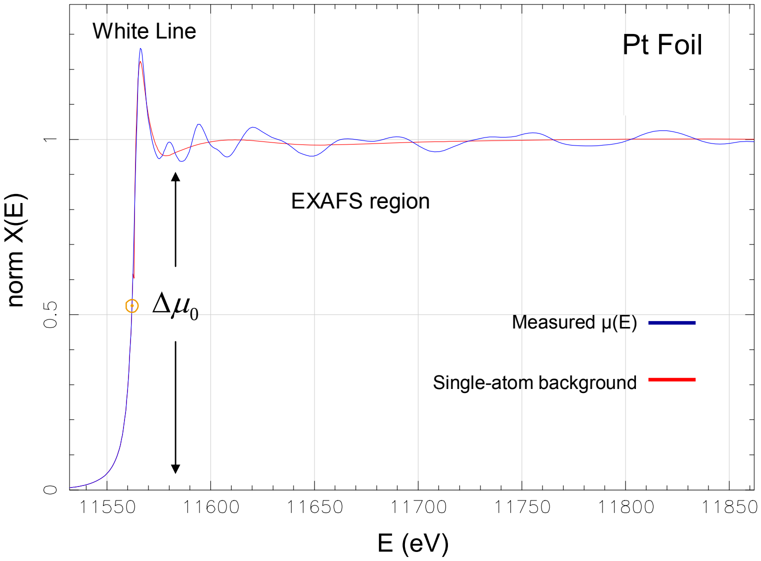

Figure 11 – XAS data from a Pt foil (blue) and the single-atom background function used to extract the EXAFS data (red). $\Delta\mu_0$ is the rise in the absorption at the edge (edge jump) and is used for normalization as given in equation (21). The spectrum shown has already been normalized so that the edge jump is equal to 1.

# CHAPTER 3: NANOPARTICLE SYNTHESIS

## Introduction

As we have seen NPs present unique physical and chemical properties. However, one of the major challenges in working with such materials as catalysts is the difficulty in producing highly dispersed NPs with controllable size and spatial distributions. Narrow size distributions are a necessity when characterizing the chemical, structural, and electronic properties of NPs. This is clear from Chapter 2, as all techniques described there measure ensemble averages over the entire sample. Well-defined distributions are also important because NP size can influence catalytic activity [27, 35, 221] and selectivity [35] as well as the stability of some metal-oxide species [102, 222, 223]; which might themselves present enhanced chemical reactivities [108]. In addition, thermally-induced sintering must be minimized during catalysts preparation and subsequent exposure to chemical reactants [62]. In some cases this can be facilitated by the use of zeolites as supports [224]. Zeolites are aluminosilicates with well-defined pore sizes into which metal complexes can be introduced and then converted into metal clusters [225]. The clusters are then too large to diffuse through the pores, leaving them trapped and stable against sintering. An additional concern is the cleanliness of the catalytically active component (e.g. precious metal) which is dictated by the preparation method and may vary from one technique to the next [226, 227]. Although many advances have been made and a number of NP synthesis routes are available [226-232], not many adequately meet the criteria with respect to the goal of reliably controlling all parameters (i.e. size, spatial distribution, thermal and chemical stability, oxidation state, and the absence of undesired residues).

The technique we will use to create well-defined NPs for the investigations to be described is that of micelle encapsulation. This technique is based on the concept of self-assembly [233] and utilizes diblock copolymers to produce micelles [234, 235]. These micelles then serve as sites for NP formation via the introduction of a metal precursor in the form of an acid (i.e. $H_2PtCl_6$) [236, 237].

## 3.1 Micelle Encapsulation

The micelle encapsulation process begins with the dissolution of amphiphilic diblock copolymers [PS(x)-b-P2VP(y)] in a non-polar solution such as toluene. Here, x and y are the molecular weights of the PS and P2VP groups respectively. The polar P2VP groups form small cages with surrounding non-polar PS tails. These cages are known as inverse micelles. Introduction of an acid into the micellar solution and subsequent stirring, results in dissolving of the acid and protonation of pyridine in the P2VP [236], which forms the core of the micelles. Once the solution has been made the micelle-encapsulated NPs can be deposited on planar substrates [i.e. $SiO_2$/Si(111), $TiO_2$/(Si(111)…] by dip-coating the substrate at a speed $s \approx 10\,\mathrm{mm/min}$. The polar P2VP is strongly bound to the surface while the PS has only a weak attraction [238], however, along with the dip-coating speed $s$, the length of the PS tail helps to control the interparticle distance on flat substrates. A schematic of these processes is shown in Figure 12. In addition, the micellar solutions can be used to impregnate nanocrystalline, powdered substrates (i.e. $ZrO_2$, $Al_2O_3$, $CeO_2$ …). In this case the desired powder is mixed with the solution and dried in air while stirring at low temperature (~60°C). This leaves the micelle-encapsulated NPs uniformly dispersed throughout the

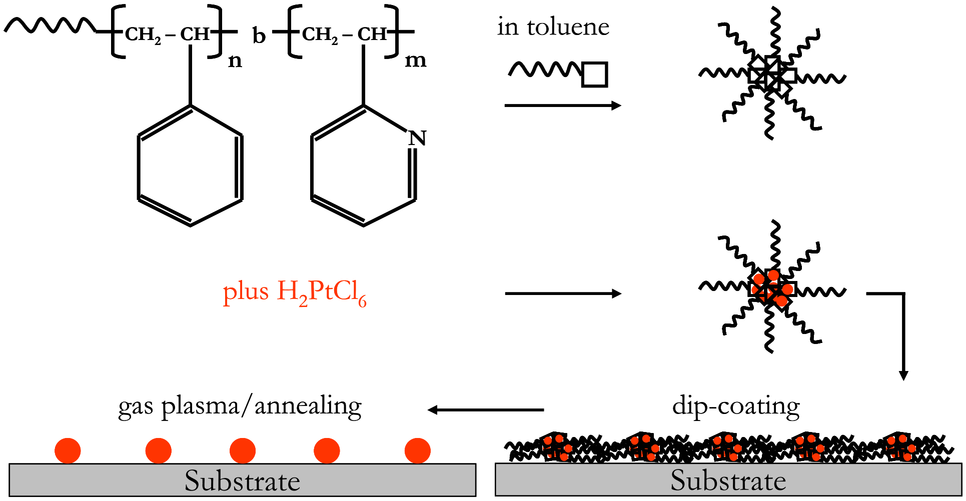

Figure 12 – Schematic showing the process of micelle encapsulation and subsequent deposition of NPs on a planar substrate.

powdered nanocrystalline support. Subsequent annealing at high temperature (~300-500°C) removes the polymeric shell.

The main advantages of the micelle encapsulation method lie in the ability to produce small NPs with narrow size and spatial distributions [237, 239-242]. The size distribution can be tuned by varying the molecular weight of the P2VP polymer-head, and/or the molar ratio, $r$, of metal-salt to polymer-head. For example, $r = 0.5$ implies one metal atom for every 2 P2VP units ($H_2PtCl_6$/P2VP = 0.5). Common values for $r$ used in our group range from 0.05 to 0.6. The interparticle distance, when dealing with planar substrates, can be tuned by varying the molecular weight of the PS block. Typical distances seen in our work are ~20-80 nm depending on the polymers used [221, 240]. Furthermore, this technique is easily adaptable to various metals and bimetallic compositions [241, 243].

The major concern with micellar NPs is how to completely remove the encapsulating polymer, along with precursor elements such as Cl, without broadening too much the initially narrow size distribution. For example, chlorine is known to be a poison for Pt in oxidation reactions [230] and its removal is also dependent on the choice of support [244]. Therefore, NP-support combinations which not only facilitate reactions but also promote stability against agglomeration are necessary. With planar substrates, thermal effects (i.e. sintering) may be overcome by use of low-temperature polymer removal treatments such as gas plasmas ($O_2$ and $H_2$) [102, 245]. Figure 13 shows examples of micelle-synthesized NPs deposited on different substrates. Figure 13(a) shows a 3 x 3 $\mu m^2$, AFM image of Pt NPs dip-coated on $SiO_2$/Si(100), where the encapsulating polymer has not yet been removed. Figure 13(b) shows the same sample after an *in-situ* $O_2$-plasma treatment has removed the polymer. We can see that the particles remain separated and the plasma treatment does not induce coarsening. In addition, images (a) and (b) demonstrate a uniform coverage of the particles over a large area. Figure 13(c) shows a HAADF (Z-contrast) image of Pt NPs deposited on $\gamma$-$Al_2O_3$ taken after annealing at 500°C (for polymer removal) for 8 hours in a flow of 50 % $O_2$ balanced with helium. The particles are ~1 nm in diameter and a uniform deposition of NPs throughout the powder has been obtained. Figure 13(d) shows a high resolution TEM image of a faceted, bimetallic, $Pt_{0.8}Au_{0.2}$ NP deposited on nanocrystalline $ZrO_2$.

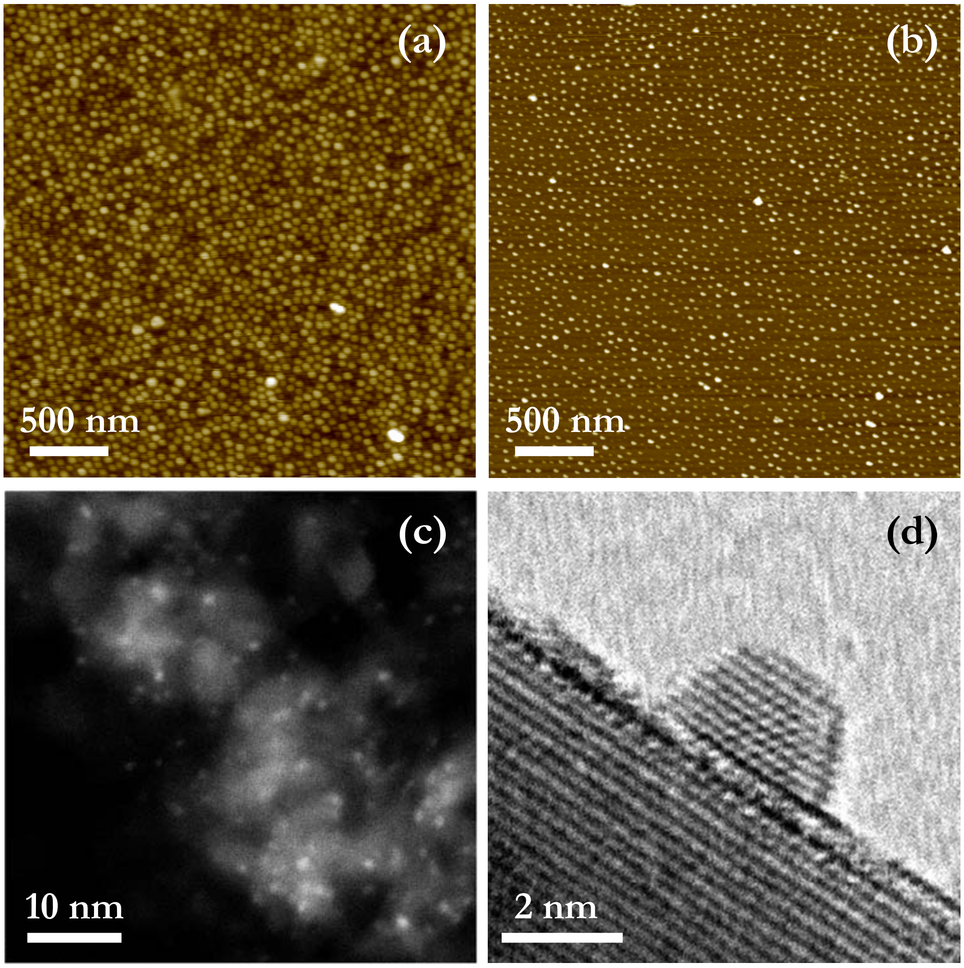

Figure 13 – (a) AFM image of Pt NPs synthesized from PS(81000)-b-P2VP(14200), with $r = 0.6$, (a) before the removal of the encapsulating polymer and (b) after an *in-situ* $O_2$-plasma treatment to remove the polymer. (c) HAADF (Z-contrast) TEM image showing Pt NPs dispersed on a $\gamma$-$Al_2O_3$ powder after annealing in 50 % $O_2$ (balanced with helium) for 8 hours at 500°C for polymer removal. (d) High resolution TEM image of a bimetallic $Pt_{0.8}Au_{0.2}$ NP supported on a $ZrO_2$ substrate. TEM images acquired by L. Li, (Prof. J. Yang's group, University of Pittsburgh).

# CHAPTER 4: STRUCTURE AND OXIDATION STATE OF Pt NPs SYNTHESIZED BY MICELLE ENCAPSULATION

B. Roldan Cuenya, J. R. Croy, S. Mostafa, F. Behafarid, L. Li, Z. Zhang, J. C. Yang, Q. Wang, and A. I. Frenkel, Submitted.

## 4.1 Experimental

In order to study the structure of supported Pt NPs, prepared by micelle encapsulation, NPs were synthesized as described in Chapter 3 using a PS(16000)-P2VP(3500) polymer. $H_2PtCl_6 \cdot H_2O$ was added to obtain metal-salt/P2VP ratios (r) of 0.05 and 0.1, and 0.4 for sample #1 (S1), sample #2 (S2), and sample #3 (S3), respectively. Therefore, we have different amounts of Pt metal in the same size micellar nanocages. The NP solutions were then loaded on nanocrystalline $\gamma$-$Al_2O_3$ powder (~40 nm) and stir-dried in air at ~60°C for 24 hours. The dried powders were then annealed for 24 hours in a packed-bed reactor in 50 % $O_2$ at 375°C for S1 and S3, and 70 % $O_2$ at 425°C for S2. All flows were 50 ml/min balanced with helium. Details of the synthesis process are shown in Table 2.

Nanoparticle solutions were dip-coated onto $SiO_2$/Si(100) substrates for morphological characterization by *ex-situ* AFM. The images were taken after polymer removal in UHV by an $O_2$-plasma treatment (4 x $10^{-5}$ mbar, 120 min). NP samples for TEM were prepared by making an ethanol suspension of the Pt/$\gamma$-$Al_2O_3$ powders and placing a few drops of this liquid onto an ultra thin C grid and allowing the sample to air dry. HAADF images of the Pt/$\gamma$-$Al_2O_3$ samples were acquired under scanning mode within a JEM 2100F TEM, operated at 200 kV. The probe size of the STEM is about 0.2 nm. The Pt diameter

Table 2 - Description of synthesis parameters and size information of our micellar Pt NPs supported on nanocrystalline γ-$Al_2O_3$ (TEM) and $SiO_2$/Si(100) (AFM). The AFM value for S3 corresponds to the NP height measured at RT after polymer removal by an $O_2$-plasma treatment at RT. The TEM values correspond to NP diameters. The volume-weighted TEM diameters are also shown. TEM images acquired by L. Li (Prof. J. Yang's group, University of Pittsburgh).

| | **Synthesis details** | | | **Particle size analysis** | | |
|---|---|---|---|---|---|---|
| **Sample name** | **Polymer** | **r** | **Annealing T (°C) [( % $O_2$)]** | **AFM height (nm)** | **TEM diameter (nm)** | **TEM weighted diameter (nm)** |
| **S1** | PS(16000)-P2VP(3500) | 0.05 | 375 [50] | | 1.0 (0.2) | 1.1 (0.2) |
| **S2** | PS(16000)-P2VP(3500) | 0.1 | 425 [70] | | 1.0 (0.2) | 1.2 (0.3) |
| **S3** | PS(16000)-P2VP(3500) | 0.4 | 375 [50] | 1.2 (0.5) | 1.7 (1.5) | 5.7 (2.2) |

was determined by measuring the full width at half maximum of the HAADF intensity profile across the individual Pt NPs.

XPS measurements were carried out on each powder sample before the XAFS measurements to monitor the removal of the encapsulating polymer (C-1s signal) as well as any possible Cl residues (Cl-2p) from the NP synthesis. No contaminants were detected on these samples after the calcination treatments in $O_2$ described above. All XPS spectra were referenced to the Al-2s peak in $Al_2O_3$ at 119.2 eV.

XAFS measurements were carried out at beamline X18B at the National Synchrotron Light Source (NSLS) at Brookhaven National Laboratory (BNL, NY). The data were collected in transmission mode using the Pt $L_3$ edge. The XAFS samples were prepared by pressing the Pt/γ-$Al_2O_3$ powders into thin pellets which were mounted in a sample cell that permitted sample heating via an external PID controller, liquid nitrogen cooling, controlled flow of gases throughout data acquisition, and on-line mass spectrometer analysis [246]. A bulk Pt foil was measured in transmission mode simultaneously with all samples for energy calibration purposes. The EXAFS data were collected at RT before (as-prepared) and after annealing at 375°C in 50 % $H_2$ balanced with He for a total flow rate of 50 ml/min. Multiple scans were collected at each temperature of interest and averaged in order to improve signal-to-noise ratios.

## 4.2 Results and Discussion

### 4.2.1 Morphological and Structural Characterization

For this study, the small polymer and metal-salt loadings (r) that were used result initially in very small (< 1 nm) micelle-encapsulated NPs. In this size range, AFM imaging is challenging. For example, Figure 14(a) shows a 1 x 1 $\mu m^2$ AFM image of Pt NPs supported on $SiO_2$/Si(100) taken after removal of the encapsulating polymer. The NPs shown were synthesized with a PS(27700)-P2VP(4300) polymer with r = 0.1. Analysis of this image gives an average height of 0.4 ± 0.2 nm as shown in the histogram of Figure 14(c). However, these results are not very precise or reliable in that the surface roughness of the $SiO_2$ substrate is ~0.2 nm. Either way a comparison of the larger P2VP micelle-core of this polymer (y = 4300) with that of the smaller polymer-core used for our current S1 and S2 (y = 3500), which results in smaller NPS, and the low loading ratios (r) of 0.05 (S1) and 0.1 (S2) shows why AFM images of these two samples (S1, S2) were unobtainable. Figure 14(b) shows an AFM image of Pt NPs analogous to S3 with a P2VP(3500) micelle-core and r = 0.4. We can see with these parameters that the NPs are large enough to image via AFM. Figure 14(d) shows the corresponding AFM height histogram for this sample, giving an average height of 1.2 ± 0.5 nm. In addition, we can see that the coverage of NPs on the substrate is quite high and our AFM analysis gives a NP density of ~1000 NP/$\mu m^2$.

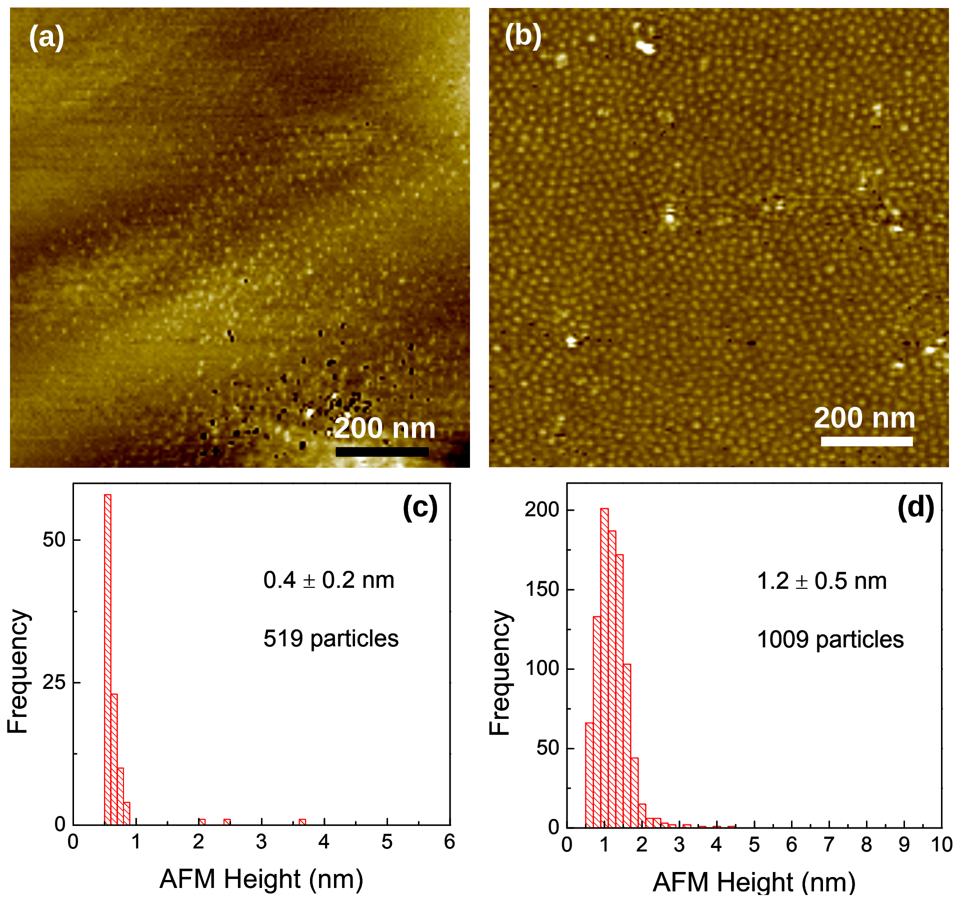

Figure 14 – AFM image of (a) ~0.4 nm Pt NPs, showing the difficulty of AFM-imaging in this size range. (b) 1.2 nm Pt NPs analogous to S3 supported on $SiO_2$/Si(100). The corresponding AFM height distributions for each image (a) and (b) are shown directly below each sample [(c) and (d), respectively]. Images were acquired after polymer removal.

Figure 15 displays examples of HAADF-STEM images (acquired by L. Li, University of Pittsburgh) and diameter distributions obtained for micellar Pt NPs supported on nanocrystalline $\gamma$-$Al_2O_3$. The HAADF images correspond to S2 (a) and S3 (c) and were acquired after polymer removal by a prolonged annealing in $O_2$ (see Table 2) and subsequent *in-situ* XAFS characterization after reduction in $H_2$. Histograms of the Pt NP diameters as measured from the HAADF images are included in Figure 15(b) (602 NP-count) and (d) (367 NP-count), respectively. Size histograms extracted from HAADF measurements of S1 were identical to S2, giving an average TEM diameter of 1.0 ± 0.2. We can see that S3

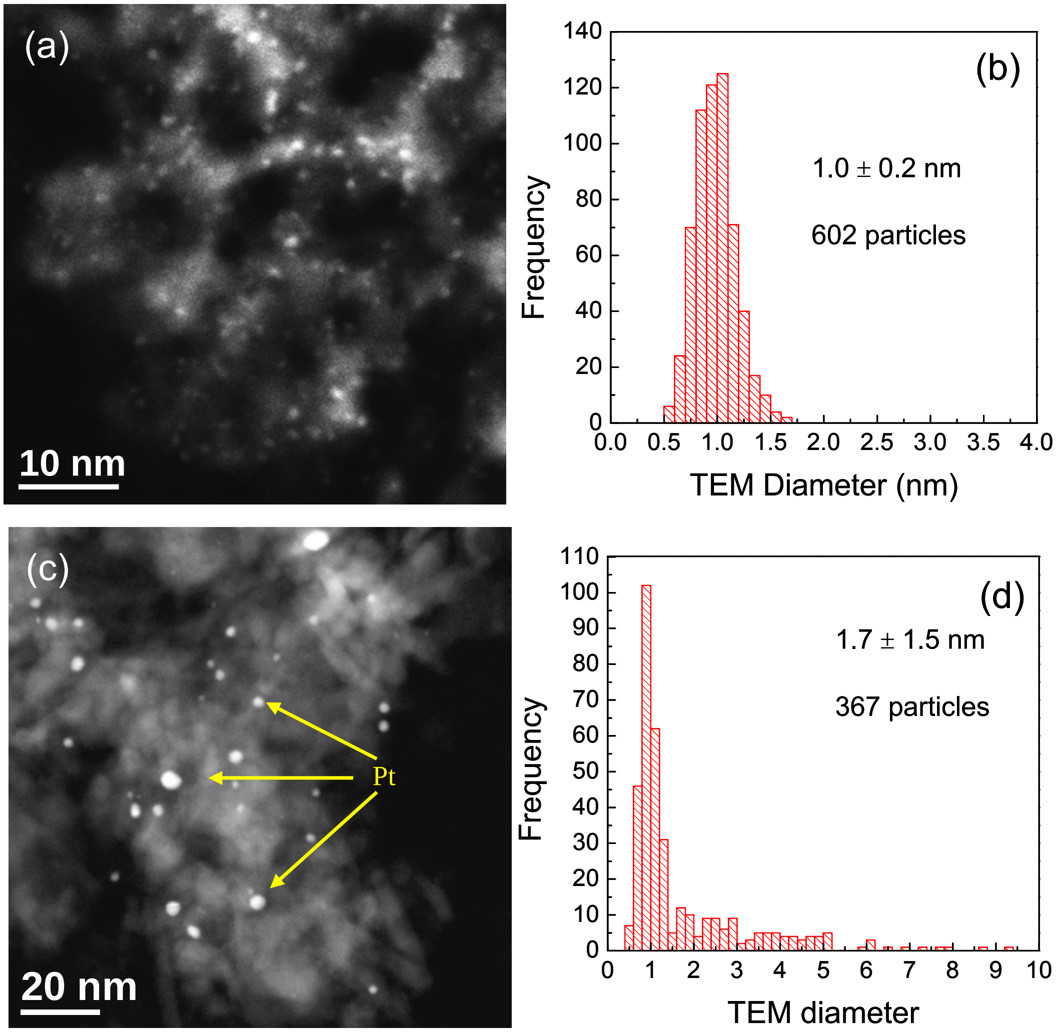

Figure 15 – Images and histograms of the diameter distributions obtained by HAADF-STEM on micellar Pt NPs supported on $\gamma$-$Al_2O_3$ after polymer removal by annealing as given in Table 2. The data correspond to (a)(b) S2 and (c)(d) S3. Images acquired by L. Li (University of Pittsburgh).

underwent some coarsening during the polymer removal pre-treatment leading to a certain population of large NPs, whereas S1 and S2 are narrowly distributed with identical TEM diameters (1 ± 0.2 nm).

### 4.2.2 Structural, Electronic, and Chemical Characterization

Figure 16 shows X-ray absorption near-edge structure (XANES) spectra of the Pt $L_3$ edge of the micellar Pt NPs supported on $\gamma$-$Al_2O_3$ acquired (a) before and (b) after *in-situ* reduction in $H_2$ at 375ºC. Reference data obtained from a Pt foil are also displayed. The resonance peak at the absorption edge is known as the white line (WL) and it arises from $2p_{3/2}$ to $5d_{5/2}$, $5d_{3/2}$ transitions. The intensity of the WL increases with decreasing d-band occupancy, and it is very strong for transition metals with a partially filled d-band (e.g. Pt-$5d_{5/2}$ orbital). The area under the WL can be used to extract information on d-charge redistributions [218]. The spectra in Figure 16(a) reveal the strongly oxidized character of the as-prepared Pt NPs samples. The WL intensities of the oxidized samples are significantly higher than those of the reduced samples, Figure 16(b), due to the electron-withdrawing nature of oxygen. This result is in agreement with EXAFS data acquired for these same samples which will be discussed in greater detail below. Furthermore, a size-dependence in the WL intensity is observed, with the lowest value measured for the largest NPs (S3, 1.7 ± 1.5 nm), followed by the 1.0 ± 0.2 nm NPs (S1, S2). Surprisingly, the similarly sized NPs of S1 and S2 (1.0 ± 0.2 nm) showed clear differences in WL intensity, with S1 being higher. The more facile oxidation of small metal NPs can explain the differences between samples S3 (~2 nm) and S2 (~1 nm), but not the higher WL intensity of S1 (~1 nm). We will elaborate on this point in the discussion section.

After NP reduction in $H_2$, the WL intensity of all NP samples is significantly decreased, reaching the value of bulk-Pt. In agreement with previous reports [247-254], we

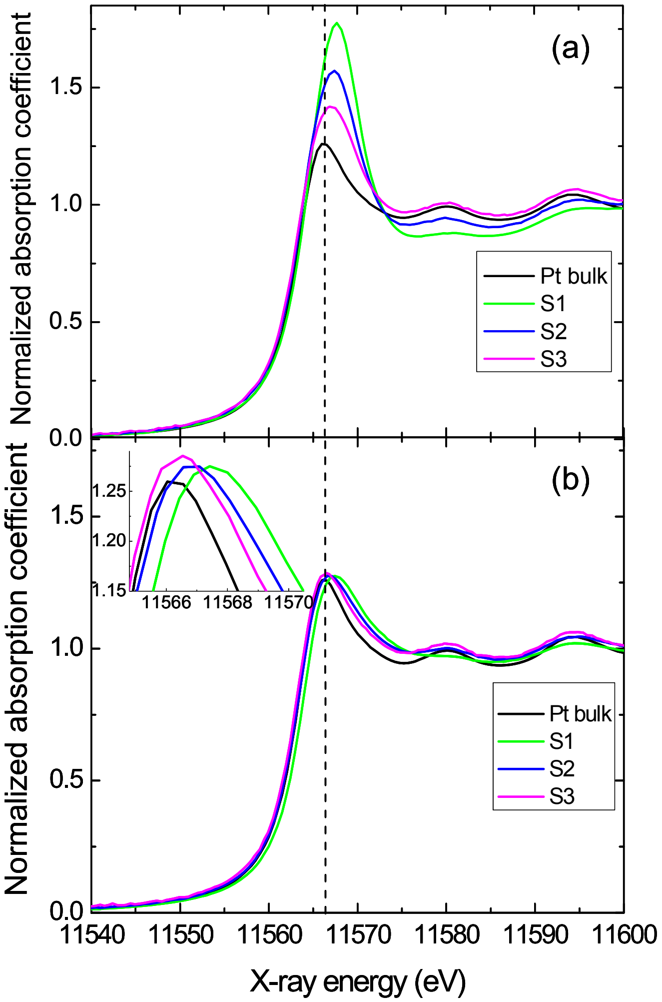

Figure 16 – XANES region [μ(E) versus E] of (a) oxidized “as-prepared” micellar Pt/γ-$Al_2O_3$ samples at RT in He, and (b) reduced samples at RT in $H_2$ measured after annealing in $H_2$ at 375ºC. Similar data from a Pt foil are also displayed. The inset in (b) shows a positive shift in the energy of the Pt $L_3$ edge of Pt NPs as compared to the bulk Pt reference.

also observe a shift of the peak position to higher energies (relative to the bulk), and an overall peak broadening for all NP samples. The origins of these effects are subjects of intense debate in the literature [249, 250, 252, 255-261]. The blue shift of the WL observed for the NP samples relative to the Pt foil [inset in Figure 16(b)] is most noticeable for S1 (+ 1.2 eV) but is also present for the other samples.

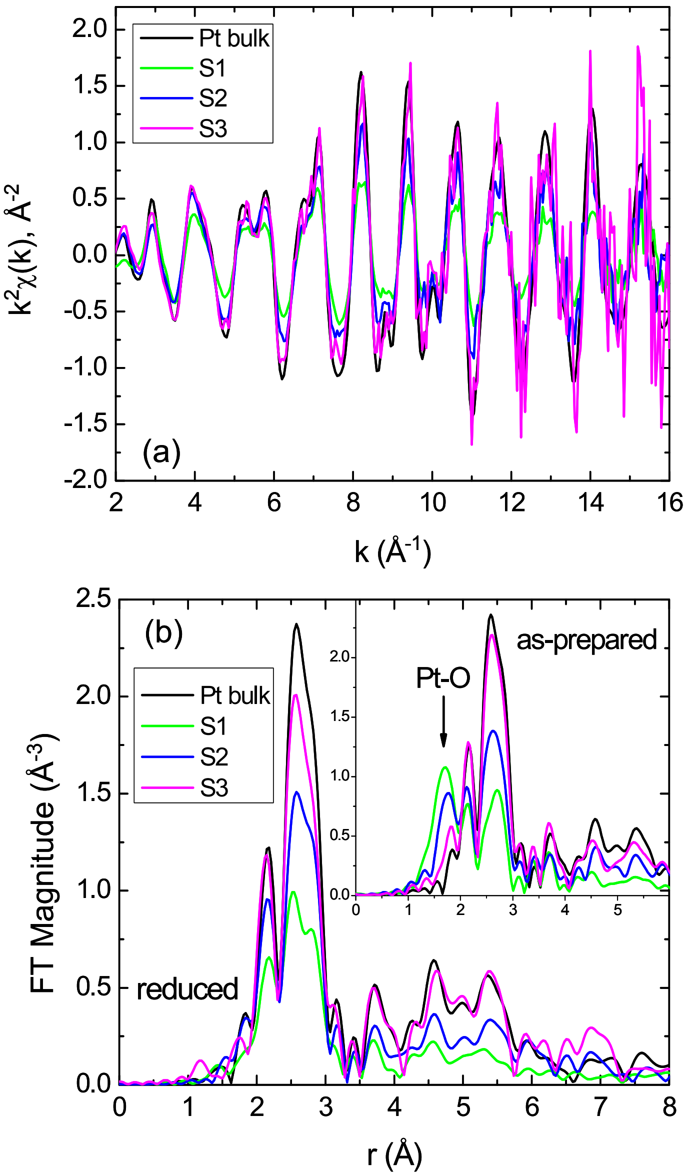

Figure 17 – $k^2$–weighted EXAFS data in k-space (a) and r-space (b) for all reduced samples in $H_2$ at room temperature. The inset in (b) shows data from the as-prepared samples measured in helium at RT. Fourier transform parameters are as follows: the k-range is from 2 to 16 Å$^{-1}$, the Hanning window sills are $\Delta k$ = 2 Å$^{-1}$.

Figure 17 displays $k^2$-weighted EXAFS data in k-space (a) and r-space (b) acquired at RT in $H_2$ for all reduced samples. A comparison with the data obtained for the oxidized (as-prepared) samples at RT in He is shown in the inset of Figure 17(b). For NPs of identical shape, the amplitudes of the EXAFS oscillations in Figure 17(a) are related to the values of average NP size and bond length disorder, with small (< 5 nm), disordered NPs showing significantly damped signals. For our samples, S3 appears to contain large NPs (similar signal to the bulk Pt foil), while the EXAFS data from sample S1 indicate the smallest and/or most atomically disordered NPs among all samples. The same trend is observed in the r-space data of Figure 17(b). We point out here, as discussed previously, that the coordination numbers of the 1NNs do not provide conclusive information on the NP size, since many clusters of different shapes and sizes may have the same 1NN coordination number [262]. Furthermore, visual examination of the data does not allow easy discrimination among the individual effects of size, shape, and atomic disorder. In this work, we use multiple-scattering fitting analysis to extract 1st through 4th coordination numbers for the quantitative analysis of NP shapes. Details in this respect will be given in the next section. The inset in Figure 17(b) reveals a strong Pt-O peak in the as-prepared samples measured in helium. Interestingly, S2 and S3 display a well-ordered fcc structure, while the highest Pt-O signal and highest atomic disorder were observed for sample S1.

## 4.3 Discussion

As was mentioned in the previous section, the unusually high WL intensity of S1 as compared to S2 [Figure 16(a), as-prepared samples] cannot be understood simply based on the stronger degree of oxidation of smaller NPs, since both samples were found to contain relatively monodispersed ~1 nm (diameter) NPs according to TEM. Instead, we attribute the enhanced density of unoccupied 5d states in S1 to a distinct shape of the NPs in this sample, namely, a flatter geometry with the same apparent TEM diameter, but an enhanced NP/support contact area. Indeed, such a model is consistent with the enhanced WL intensity, since XANES data contain ensemble-averaged information about the density of unoccupied Pt-5d states. Thus, the greater the fraction of Pt atoms with a large 5d-hole density (i.e. those which are oxidized, for example via support interaction), the larger the WL intensity. One possible explanation for the WL enhancement in the Pt atoms at the NP-substrate interface is the large charge transfer from Pt to defects in $Al_2O_3$ [263]. The inset in Figure 17(b), displaying r-space EXAFS data from the as-prepared oxidized samples also reveals the highest Pt-O signal for sample S1, consistent with the XANES observation.

A comparison of the r-space plots shown in Figure 17(b) for the reduced micellar Pt NPs to that of a bulk Pt foil revealed that despite their small size, all of our NPs have good crystalline fcc structure, in contrast with previous literature reports on similarly-sized NPs prepared by deposition-precipitation methods [54]. This difference could be attributed to several factors: (i) the inverse micelle encapsulation method leads to more ordered structures, (ii) the prolonged annealing times (24 h) used during the pre-treatment of the micellar NP samples (before XAFS characterization) lead to an enhanced long-range order, and (iii) the shape of two of our NP samples (S2, and S3) is 3D, instead of raft-like (2D for S1) as has been commonly reported for $Pt/\gamma\text{-}Al_2O_3$ [54]. In the latter case, strain from the larger NP/support contact area is expected to lead to more disordered structures. In addition, it should be noted that our XAFS measurements were carried out in a $H_2$ atmosphere, and that $H_2$ has been reported to induce faceting on NPs [91, 92]. Sanchez et al. [54] also suggested, by comparing EXAFS results from Pt/C and $Pt/\gamma\text{-}Al_2O_3$ measured under He and $H_2$ flows, that $H_2$ relieves surface-induced strain. Wang and Johnson [264] have interpreted those results theoretically by attributing the increased order in the clusters to removal of the inherent {100}-to-{111} shear instability, stabilizing the truncated cuboctahedral shape when the particles are passivated by hydrogen. Interestingly, S1 shows the least resemblance to the Pt foil, and since the diameter of the NPs in this sample is nearly identical to that in sample S2, qualitatively, a more anisotropic, 2D shape might be inferred for S1.

The EXAFS data from Figure 17 (RT measurements) as well as low-temperature (-85ºC to -100ºC) data (not shown) have been fit by multiple scattering analysis. From these fits, coordination numbers have been extracted for the 1st through the 4th nearest neighbor shells for all samples, Table 3, and used to gain information on the NP shape by comparison with model fcc cluster shapes as calculated by PhD student Farzad Behafarid (Roldan Group, UCF). Frenkel et al. [246] have previously used the sequence of nearest neighbor atomic distances and coordination numbers extracted from EXAFS measurements to correlate different models for cluster shapes with average cluster diameters obtained independently. In the present study, the synergistic combination of the EXAFS multiple scattering analysis, NP size information obtained by TEM, and calculations of model clusters shapes, have revealed a 3D cluster shape for the NPs in S2 and S3, and a 2D, raft-like NP shape for S1.

For S3, a significant number of large (coarsened) NPs were detected by TEM (see Figure 15), leading to a broad volume-weighted NP size distribution and large coordination numbers in EXAFS. Therefore, for this sample a large number of shapes were found to fit the EXAFS data, and no conclusive shape determination could be made. For S1 and S2, the discrimination between different model shapes was much more conclusive, and the modeling gives a cuboctahedron shape for S2, and a flat (2-layers high) truncated octahedron

Table 3 – Coordination numbers (N1-N4) obtained from the multiple scattering analysis of EXAFS data acquired on micellar Pt NPs supported on γ-$Al_2O_3$. The fits were carried out on EXAFS spectra measured at low temperature (-85° to -108°C) for all samples. The experimental diameters obtained from TEM measurements correspond to values obtained after volume-weighting the particle diameter histograms. Uncertainties are shown in parentheses.

| **Sample** | **N1** | **N2** | **N3** | **N4** | **TEM vol-weighted Diameter (nm)** |
|---|---|---|---|---|---|
| **S1** | 7.3 (0.5) | 1.3 (0.7) | 5.1 (1.8) | 4.4 (1.1) | 1.1 (0.2) |
| **S2** | 8.7 (0.6) | 3.4 (1.7) | 6.9 (2.3) | 5.6 (1.4) | 1.2 (0.3) |
| **S3** | 10.9 (1.0) | 3.9 (5.6) | 14.1 (4.5) | 8.5 (2.7) | 5.7 (2.2) |
| **Pt bulk** | 12.0 (0.4) | 5.0 (1.2) | 24.0 (4.0) | 10.8 (1.6) | Thin foil |

for S1 [265-267]. The most common NP shapes, observed by our group via STM for annealed micellar NPs supported on $TiO_2$(110), were used as reference to discard unstable cluster shapes consisting of non-energetically favorable facets. Our data analysis indicates the possibility of creating NPs with distinct shapes after annealing (~400°C) using the inverse micelle encapsulation method by changing the size of the micellar core (different molecular weight of the P2VP block), as well as by tuning the metal-salt to P2VP ratio (r). In particular, our only 2D shape (S1) was obtained for the lowest loading of the micellar nanocage (r = 0.05). More importantly, our results demonstrate that the micelle encapsulation synthesis method allows one to overcome strong NP/support interactions that would normally prevent the stabilization of high-surface area, 3D cluster shapes. For NPs in the present size range (~1 nm), such 3D cluster shapes might display distinct catalytic activity and selectivity as compared to raft-like 2D Pt/γ-$Al_2O_3$ NPs prepared by deposition-precipitation methods, due to the larger number of facets in 3D clusters.

## 4.4 Conclusions

The structure (size and shape) of small (< 2 nm) size-selected micellar Pt NPs synthesized by inverse micelle encapsulation has been resolved by a combination of microscopic (TEM, AFM), and spectroscopic (XANES and EXAFS) tools, all integrated within a self-consistent geometric modeling method.

Our work demonstrates that the NP preparation method plays a key role in the final shape of the synthesized NPs. Following our synthetic approach, NP-support interactions that commonly lead to the stabilization of 2D-raft-like cluster shapes in systems such as Pt/$\gamma$-$Al_2O_3$ can be overcome, resulting in faceted 3D NPs that might be good candidates for catalysis applications. Furthermore, our EXAFS data evidence the high degree of atomic ordering that can be achieved in very small NPs (~1 nm) using micelle encapsulation synthetic routes as compared to traditional deposition-precipitation methods. This effect might be due in part to the annealing pre-treatment that our micellar samples underwent, but also to their interaction with $H_2$ during the EXAFS measurements. $H_2$ is known to induce NP faceting, and due to their enhanced surface area, our 3D NPs should be more prone to restructuring under $H_2$ as compared to traditional 2D Pt/$\gamma Al_2O_3$ clusters.

The present study highlights the importance of integrated analysis methodology involving multiple complementary techniques [268], and also the uniqueness of EXAFS, combined with cluster shape modeling, for the extraction of information on cluster shapes in size-selected NP samples. Such insight is crucial for the understanding of structure-reactivity relationships in real-world (3D) nanocatalysts in the ~1 nm size range which constitutes a serious challenge for state-of-the-art high-resolution TEM microscopes.

# CHAPTER 5: SIZE DEPENDENT STUDY OF METHANOL DECOMPOSITION OVER Pt NPs ON $TiO_2$

Jason R. Croy, S. Mostafa, J. Liu, Yong-ho Sohn, B. Roldan Cuenya

Catalysis Letters 118 (2007) 1

## 5.1 Experimental

Pt NP solutions were made as described in Chapter 3 and deposited on a nanocrystalline, anatase $TiO_2$ support (nominal size ~32 nm). Our TEM data give an average $TiO_2$ particle diameter of ~42 nm after annealing at 500°C for 2.5 hours. Each Pt/$TiO_2$ catalyst sample had a total weight of 150 mg and contained 2 % by weight Pt. The amount of Pt salt used in each sample is derived from the Pt-salt/P2VP ratio (r) as reported in Table 4. In these experiments three polymers [PS(x)-b-P2VP(y)], having head groups with different molecular weights, were used in order to create three distinct particle sizes. Further sample preparation details can be found in Table 4.

Powder samples were deposited on carbon conductive tabs and transferred to an ultra high vacuum (UHV) system for surface analysis by XPS. XPS data were collected using a monochromatic X-ray source (Al-Kα, 1486.6 eV) operating at 400 W. The binding energies of all samples were referenced to the Ti $2p_{3/2}$ peak in $TiO_2$ at 458.6 eV [269].

To study the effect of calcination on the activity of the catalyst, as well as to remove the encapsulating PS-P2VP polymers, the samples were annealed before the reaction at two different temperatures. One set of samples was annealed at 315 °C for 3 hours and another set at 500 °C for 2.5 hours. Activity tests were then conducted on each of the sample sets.

Catalytic decomposition of methanol in the vapor phase was carried out in a packed-bed mass flow reactor. A vertical quartz tube (inside diameter 4 mm) served as the reactor vessel and the 150 mg powder catalysts were supported between glass wool plugs, giving a bed height of ~3.5 cm. A thermocouple (K-type) in contact with the reactor at the location of the catalyst was used to monitor temperature and the entire assembly was insulated to minimize heat losses. Immediately prior to the reaction all catalysts were heated for one hour at ~ 200 °C (below the initial calcination temperatures used for polymer removal) in a flow of helium at 10 ml/min. Activities were measured at atmospheric pressure in the range of 100-330°C. The temperature was increased stepwise and kept constant at the recorded values. Regions of stable activity were obtained and averaged over ~3-5 min intervals. Helium was used as the carrier gas during methanol decomposition. The helium flow was regulated by a mass flow controller at 10 ml/min. The composition of the feed was 2 % MeOH, relative to the flow of helium as determined by the partial pressures of helium and the main fragment ion of MeOH (mass 31). The product stream of the reactor was monitored by a quadrupole mass spectrometer. Several tests involving the flow of the carrier

Table 4 - Synthesis parameters and average height (AFM) and diameter (TEM) distributions of Pt NPs synthesized by inverse micelle encapsulation. Here the symbol * represents size distributions of the samples measured after annealing but before exposure to methanol, and ** represents distributions done after annealing and subsequent exposure to methanol. MW is the molecular weight of x and y.

| Sample | Polymer x/y MW (g/mol) | salt/P2VP ratio | Annealing (°C) | AFM Height (nm) | TEM diameter (nm) |
|---|---|---|---|---|---|
| #1 | 27700/4300 | 0.6 | 500 | 3.7 ± 0.6 | 8.6 ± 1.2 *<br>8.2 ± 1.7 ** |
| #2 | 27700/4300 | 0.6 | 315 | --- | --- |
| #3 | 53400/8800 | 0.3 | 500 | 6.3 ± 1.1 | 20.8 ± 2.7* |
| #4 | 53400/8800 | 0.3 | 315 | --- | --- |
| #5 | 81000/14200 | 0.6 | 500 | 8.1 ± 1.4 | 11.4 ± 1.6* |
| #6 | 81000/14200 | 0.6 | 315 | --- | --- |

gas were carried out until an optimum flow of 10 ml/min was selected for our experiments. Partial pressures of all gases were monitored using the system's Faraday cup detector.

The polymer-salt solutions were also dip-coated on $SiO_2$/Si(001) substrates in order to obtain particle size information (height) via AFM. In addition, TEM was carried out on all of the powder samples.

## 5.2 Results and Discussion

### 5.2.1 Morphological and Structural Characterization

Figure 18 displays AFM images of the three different polymer-salt solutions dip-coated on $SiO_2$/Si(001) before (left) and after (right) UHV annealing for 30 min at 500°C. At this temperature removal of the encapsulating polymer is observed by monitoring the C-1s XPS signal. As seen in Figure 18, the size distribution in each sample is narrow, demonstrating that the method of micelle encapsulation can consistently synthesize size-selected Pt NPs. Analysis of the images taken after annealing gives an average particle height of (b) 3.7 ± 0.6 nm, (d) 6.3 ± 1.1 nm, and (f) 8.1 ± 1.4 nm. Since the NP diameters measured are significantly enhanced due to tip-convolution effects, the AFM heights will be used as the representative size of the NPs throughout the text.

Figure 19 shows typical bright-field TEM images of Pt NPs prepared by micelle encapsulation, which are supported on anatase $TiO_2$ powder. Contrasts from these images were also employed to measure the size of the Pt NPs as reported in Table 4.

### 5.2.2 Electronic and Chemical Characterization

Figure 20 shows XPS spectra of the Pt-4f region for three samples annealed at 315°C (samples #2, #4, #6) and three samples annealed at 500 °C (samples #1, #3, #5) before

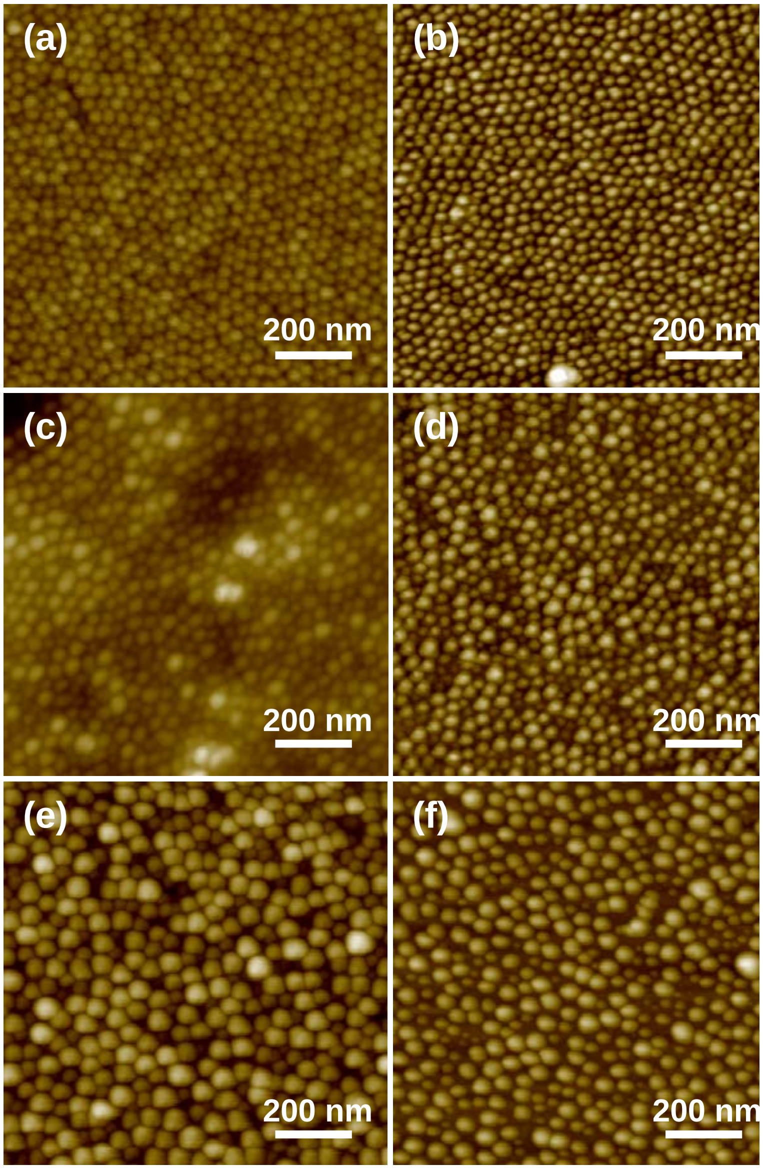

Figure 18 – Tapping mode AFM images of size-selected Pt NPs dip-coated on $SiO_2$/Si(001). The left column shows (a) samples #1, (c) #3, and (e) #5 before annealing. The right column shows (b) samples #1, (d) #3, and (f) #5 after annealing in UHV at 500 °C for 30 min. The z scale is 0-12 nm for (b), 0-25 nm for (f), and 0-20 nm for all others.

reaction with methanol. The solid lines (blue) indicate the positions of the main core-level peaks of metallic Pt at 70.4 eV ($4f_{7/2}$) and 73.7 eV ($4f_{5/2}$) [270], the dashed lines (red) to $Pt^{2+}$ in PtO (72.4 and 75.7 eV) [271], and a the second set of dashed lines (green) to $Pt^{4+}$ in $PtO_2$ (74.6 and 77.9 eV) [272]. All samples annealed at 315°C display a convolution of mainly $Pt^0$

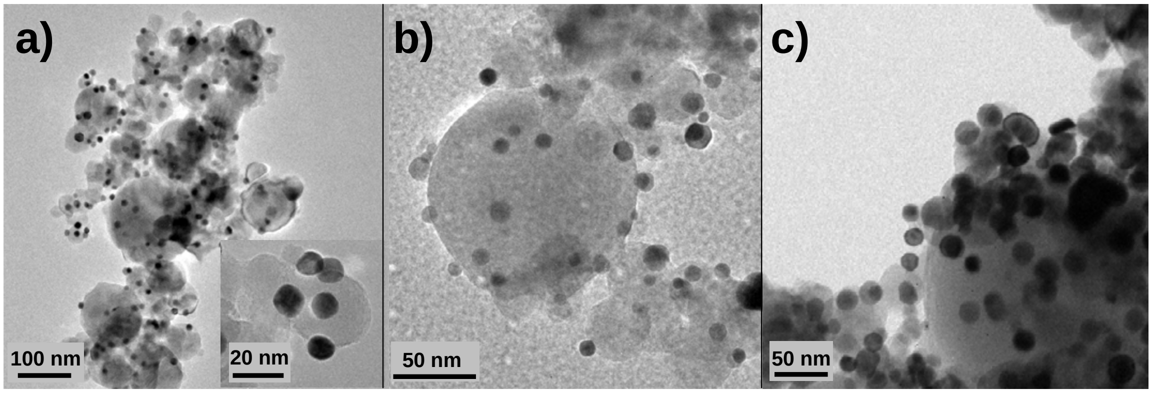

Figure 19 – Bright-field TEM images showing Pt NPs prepared by micelle encapsulation supported on anatase $TiO_2$ powder: (a) sample #1 before reaction with methanol and (b) sample #1 after methanol exposure, (c) sample #3 before reaction with methanol. All samples shown were calcined at 500 °C. Images acquired by J. Liu and Prof. Y.H. Sohn (UCF).

and $Pt^{2+}$. Since a residual Cl signal was measured after this low temperature thermal treatment (315 °C) for samples #2, #4, and #6 (Figure 21 shows Cl-2p XPS data from sample #2), we conclude that the $Pt^{2+}$ found in these samples must be mainly present in chlorinated compounds. This is in agreement with the binding energies measured by Zhao et al. [273] on dendrimer-encapsulated Pt NPs before the removal of the encapsulating ligands (72.8 eV and 75.7 eV). Furthermore, in these samples the $Pt^{2+}/Pt^{0}$ ratio was found to increase with increasing particle size. In particular, the XPS spectrum from the sample containing the largest NPs (sample #6) shows mainly $Pt^{2+}$-4f peaks at ~72.4 and 75.7 eV. The difference in the Cl content of NP samples with different sizes (higher Cl content for larger clusters) can be tentatively attributed to the different number of low-coordinated Pt atoms in these systems, as well as to the distinct melting temperature of clusters with different sizes. Small clusters have a larger number of atoms at the surface and a reduced melting temperature. It is therefore plausible that chlorinated compounds in such systems, available mainly at the NP surface, are easier to decompose upon thermal treatment. For

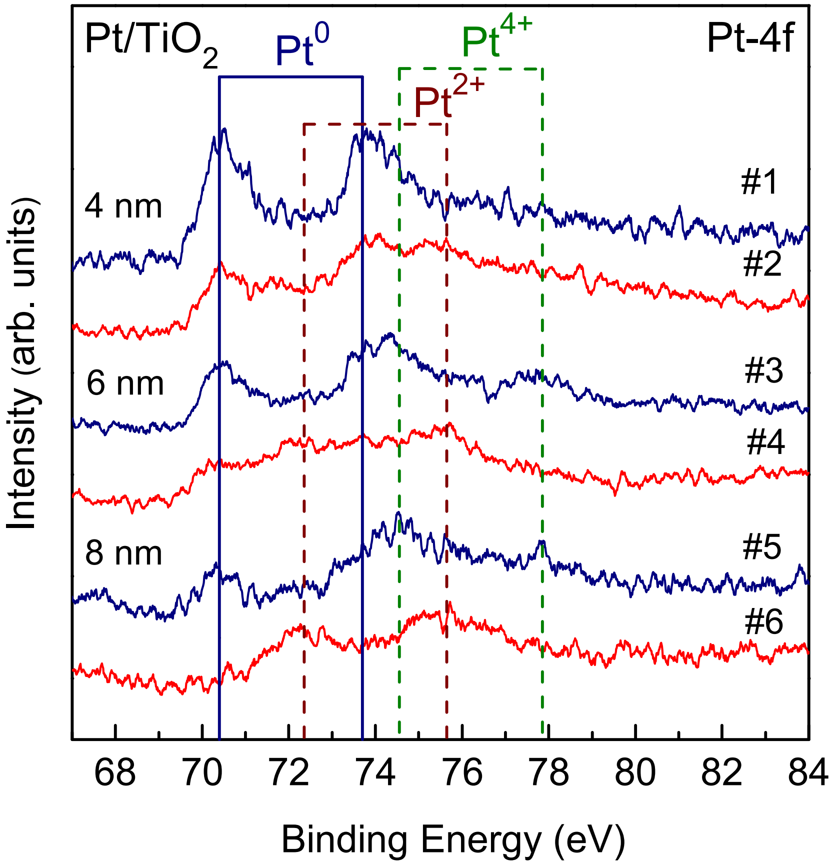

Figure 20 – XPS spectra of Pt NPs supported on anatase $TiO_2$ measured at room temperature. The reference lines show the positions of the 4f peaks of: metallic Pt (solid lines), $Pt^{2+}$ (dashed lines) and $Pt^{4+}$ (dashed lines at high energy). The spectra number at the right corresponds to the sample from which the data were obtained and is described Table 4.

larger clusters, the complete Cl removal from the bulk requires higher annealing temperatures as well as longer annealing times. Upon annealing to 500 °C (samples #1, #3, #5), no residual Cl signal was observed (Figure 21, sample #1) and the binding energies measured were attributed to $Pt^0$, PtO, and $PtO_2$. After identical thermal treatments, it was found that the oxidation state of the NPs depends on the NP size. The smallest NPs (sample #1) were fully reduced at 500 °C, while samples #3 and #5 still contained $Pt^{2+}$ and $Pt^{4+}$ compounds. It is interesting to note that the main Pt peak ($4f_{7/2}$) of all samples appears at

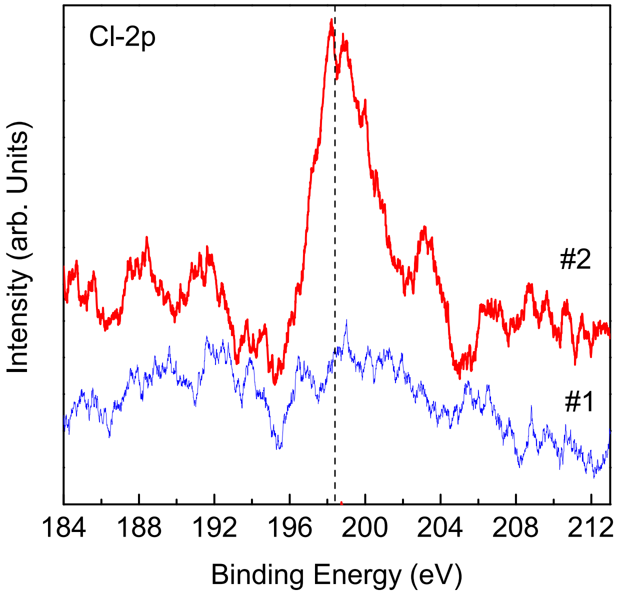

Figure 21 – XPS data showing the Cl-2p core-level at ~198.4 eV. All samples show residual Cl after calcination at 315 °C (sample #2 is shown here). After calcination at 500 °C the Cl is removed and all samples show spectra similar to that of sample # 1 shown here.

~70.4 eV. This value is close to those reported by Silvestre-Albero et al. [274] for similar $TiO_2$-supported Pt NPs, and corresponds to a negative shift of ~0.7 eV when compared to the most common value measured for bulk $Pt^0$ at 71.1 eV [275]. Such negative shifts can be explained by SMSI. Charge transfer from the support to the particle, especially in systems with metallic particles on reducible metal oxides, can alter the electronic properties of the NP [51]. Small particles also have a large number of surface atoms with reduced coordination numbers. This feature is known to induce negative BE shifts relative to the value measured for the bulk metal [276].

### 5.2.3 Catalytic Activity

Figure 22 displays the activity as calculated from data acquired by the quadrupole mass spectrometer. Activity is defined in terms of partial pressures measured by the QMS and given by the equation $(PH_2\text{-}PH_0)/P_{m31}$. Here $PH_2$ is the pressure of $H_2$ at a given temperature, $PH_0$ is the initial background pressure of $H_2$, and $P_{m31}$ is the pressure of the main fragment ion of methanol. A clear size dependence of the catalytic activity of Pt NPs supported on $TiO_2$ is observed. For the sample set annealed at 315 °C (open symbols in Figure 22) we can see a well-defined trend where an increase in activity is associated with a decrease in particle size. A similar trend was observed for the set of samples annealed at 500 °C (closed symbols in Figure 22), although samples #3 and #5 displayed almost identical activities. This effect can be attributed to NP coarsening, since our TEM measurements indicate that significant agglomeration occurred in sample #3 after annealing at 500 °C (Figure 19), rendering an average size distribution comparable to sample #5. Furthermore,

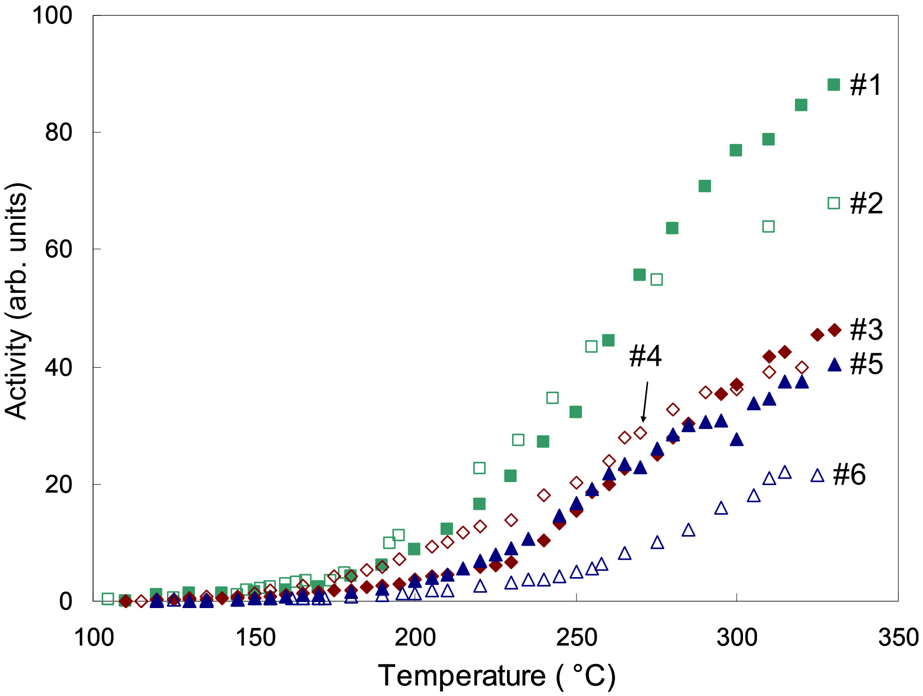

Figure 22 – Activity of size-selected Pt NPs, supported on anatase $TiO_2$ powder, for methanol decomposition. Activity is defined as described in the text.

the most dramatic improvement in activity was observed for the largest NPs (sample #5) after the high temperature pre-treatment. This may be related to the fact that the analogous sample, annealed at 315 °C (sample #6), showed the largest $Pt^{2+}/Pt^{0}$ ratio, and that subsequent annealing to 500 °C served to remove residual Cl, increasing the amount of metallic Pt species. The other two sizes annealed at 500 °C also displayed enhanced activities as the temperature in the reactor approached 260 °C for sample #1 and 300 °C for sample #3. This suggests that after low temperature annealing (315 °C) there is residual Cl in the samples which is detrimental to the reaction, and that the higher annealing temperature is of greater advantage as long as the sintering is minimized. Our mass spectroscopy data from samples #3 and #4 indicate that any benefits gained from the removal of the chlorine can be offset by a corresponding increase in particle size. This size effect also reveals itself in the low temperature region of Figure 22, where we see a clear decrease in activity for sample #3 as compared to its counterpart (sample #4) calcined at lower temperature (315 °C).

We also note that all samples show $H_2$ production well below 200 °C with the smallest particles (sample #1) becoming active when the reactor temperature is about 145 °C. This is especially important for the development of heat recovery systems [277] and compares favorably with values reported elsewhere [278-282]. During the course of all reactions no significant amounts of byproducts such as methane ($CH_4$), carbon dioxide ($CO_2$), or dimethyl ether ($CH_3OCH_3$) were observed. Therefore, the main process involved is the direct decomposition of MeOH and competing $H_2$ reactions (i.e. methanation) are not a factor. The water-gas-shift (WGS) reaction [see equation (30)] is also not prevalent, as we are not directly introducing water into the feed.

Figure 22 shows that the smallest NPs, which were also more easily reduced from $Pt^{\delta+}$ to $Pt^0$, displayed the highest activities. This effect is further illustrated in Figure 23 where the activity, measured at four different reaction temperatures for samples calcined at 500 °C (samples #1, #3 and #5), is plotted versus the NP height as measured by AFM. Here again we can see the effects of increased NP size in sample #3, which shows a slightly lower activity than sample #5 at 250 °C (squares), and is comparable to sample #5 even at 300 °C (diamonds). Thus, the removal of the Cl from this sample has been negated by an increase in particle size. We conclude that NP coarsening in sample #3 is not due to temperatures in the reactor since all experiments were conducted in the range of 100-330 °C, which is well below the pretreatment temperature of samples #1, #3, and #5 at 500 °C. In addition, TEM analysis reveals that the most active particles (sample #1) did not coarsen during reaction with methanol, having an average size of 8.6 ± 1.2 nm before reaction, and 8.2 ± 1.7 after reaction (Table 4). We may note also that each experiment lasted for about 6 hours, and no deactivation was observed during that period of time for any sample.

On similarly synthesized gold NPs supported on TiC, our group has also demonstrated a dependence of the particle size on the catalytic activity of this system for low temperature CO oxidation [283]. However, we must mention that smaller particles do not always perform better, and reducing particle size may only be advantageous to a point. For example, It is known that a minimum number of atoms per cluster is required to observe high reactivities, in particular the enhanced activities displayed by small clusters for CO oxidation decrease below a particle size of about 2-3 nm [27, 284].

Although the present study focuses on the influence of the NP size on chemical reactivity, it should be stated that the nature of the metal oxide support also plays a crucial

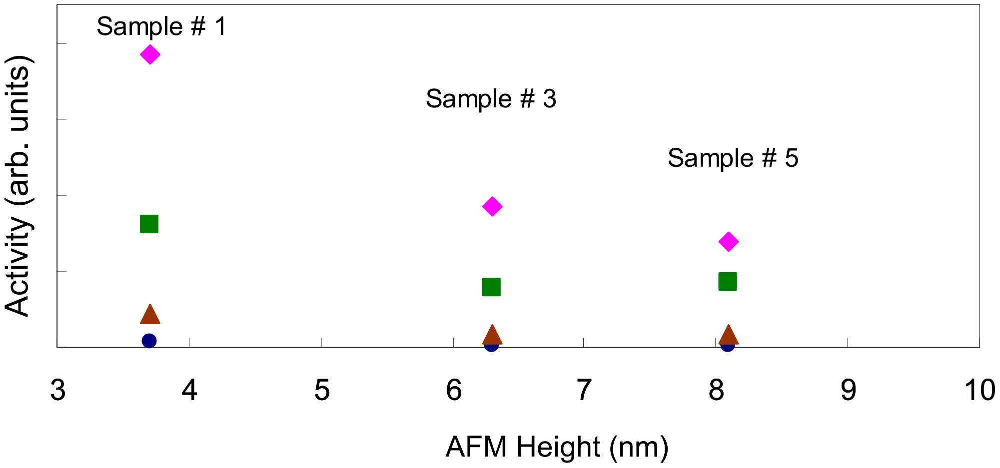

Figure 23 – Activity plotted as a function of particle height (AFM) at four different reaction temperatures for samples previously calcined at 500 °C (samples #1, #3 and #5). Circles represent a reactor temperature of 150 °C, triangles 200 °C, squares 250 °C, and diamonds 300 °C. Columns are denoted by the sample number as given in Table 4.

role in catalytic processes mediated by supported NPs. For example, the use of ZnO, $TiO_2$, $SiO_2$, $CeO_2$, and $Al_2O_3$ as supports can effect particle sintering, catalytic activity, and selectivity in reactions such as MeOH decomposition [285], steam reforming of MeOH [70], CO oxidation, and propylene hydrogenation [286]. It is believed that the oxygen vacancies that easily appear in some of these materials upon annealing may play a crucial role [287, 288]. We will take up the subject of support effects in the next chapter.

## 5.3 Conclusion

Micelle encapsulation has been used to create size-selected Pt NPs highly dispersed on polycrystalline anatase-$TiO_2$ supports. These nanocatalysts were found to be active for the decomposition of MeOH and subsequent production of $H_2$ at temperatures as low as 145 °C. Mass spectrometry data show that on these Pt NPs $H_2$ production proceeds mainly through the direct decomposition of MeOH and that the activity increases with decreasing particle size. Furthermore, the influence of the oxidation state of the Pt NPs and chemical residues from NP synthesis (Cl) on their activity and selectivity was investigated. Our mass spectrometry data reveal that the samples annealed at higher temperature, where a larger percentage of metallic Pt species was detected by XPS, are the most active. However, this is not the case when the high temperature treatment leads to NP coarsening and significant increase in particle size. In addition, the residual Cl present in our catalysts after low temperature annealing (315 °C) was found to hinder the reaction. However, the size of the particles turned out to be the dominant factor in determining the relative activity of these samples, and the smallest Pt NPs (~4 nm) were found to be the most active.

# CHAPTER 6: SUPPORT DEPENDENCE OF METHANOL DECOMPOSITION OVER SIZE-SELECTED Pt NPs

Jason R. Croy, S. Mostafa, J. Liu, Yong-ho Sohn, H. Heinrich, and B. Roldan Cuenya

Catalysis Letters 119 (2007) 209

## 6.1 Experimental

In order to study the support dependence of Pt NPs in the decomposition of MeOH Pt NP solutions were synthesized using a PS(27700)-b-P2VP(4300) polymer. The solutions were then mixed with a series of oxides [$TiO_2$ (anatase), $CeO_2$, $ZrO_2$, $\alpha$-$Al_2O_3$, and $SiO_2$] in the form of a powder (excepting $SiO_2$) having nominal grain sizes of ~32 nm, 40 nm, 45 nm, and 37 nm, respectively. The $SiO_2$ was in the form of small pellets (1/8") which were ground to a fine powder before the addition of Pt. All samples were placed in a tubular furnace open to the air for calcination at 500°C for 2.5 hours. Each catalyst sample had a total weight of 100 mg and contained 2 % by weight Pt. A Pt-salt/P2VP concentration ratio (r) of 0.6 was used for all samples to create supported Pt NPs having narrow size distributions. The one exception was a second Pt/$CeO_2$ sample prepared with the same polymer, but with a smaller ratio, r = 0.2. This resulted in a solution of Pt NPs with a smaller size distribution. This sample will be referred to in the text as Pt/$CeO_2$(#2). A solution containing smaller Pt NPs was desirable in the case of $CeO_2$-supported NPs since significant NP sintering was observed in this support upon our thermal treatment.

As previously described, powder samples were deposited on carbon-coated stickers and transferred to an UHV system for surface analysis by XPS. XPS data were collected using Al-$K_\alpha$ radiation at 300 W and a flood gun (~3 eV) was used to correct for surface charging during measurement. The respective BEs of the powder samples were referenced to the Ti-$2p_{3/2}$ [$TiO_2$] peak at 458.6 eV [269], Ce-$3d_{5/2}$ [$CeO_2$] at 882.2 eV [289], Al-$2p_{3/2}$ [$Al_2O_3$] at 74.5 eV [290], Si-$2p_{3/2}$ [$SiO_2$] at 103.8 eV [291], and Zr-$3d_{3/2}$ [$ZrO_2$] at 183.0 eV [292]. Using carbon as a BE reference is difficult in our case because the carbon coated stickers used in the measurements have a peak at ~286.0 eV, the intensity of which is strongly reduced when the powder samples are placed on top. In addition, the amount of powder used for these measurements is small, resulting in a weak signal attributed to adventitious carbon (285 eV). The convolution of these two C-1s peaks makes such a reference unreliable. Using the Ce-3d peaks in $CeO_2$ as reference may be troublesome because they have been shown to shift in the presence of Pt due to strong metal-oxide interactions [66]. However, the amount of Pt in our samples is small compared to the amount of $CeO_2$. Furthermore, in using the Ce-$3d_{5/2}$ [$CeO_2$] as a reference, binding energies of ~285.0 eV and 529.2 eV were obtained for our C-1s and O-1s peaks respectively. These values are in good agreement with literature values [293, 294] and we can conclude that the Ce-$3d_{5/2}$ is a reliable reference for this system.

Catalytic decomposition of methanol in the vapor phase was carried out in a packed-bed mass flow reactor, as previously described. In order to promote flow through the reactor, the powder catalysts (100 mg, 2 % wt Pt) were mixed with 200 mg of inert quartz sand and divided into six, 50 mg segments. These segments were separated and supported in the reactor by glass wool plugs. A thermocouple (K-type) in contact with the reactor was used to monitor temperature, and the entire assembly was insulated to minimize heat losses. Immediately prior to the reaction all catalysts were heated for one hour at ~200°C in a flow of helium at 10 ml/min. Activities were measured at atmospheric pressure in the range of 100 to 300 °C. The temperature was increased stepwise and held constant at the recorded values. Regions of stable activity were obtained and averaged over ~6-10 min intervals. Helium was used as the carrier gas during all reactions and regulated at 10 ml/min by a mass flow controller. The product stream of the reactor was monitored by a QMS. Partial pressures of the product gases were monitored using the system's Faraday cup and SEM detectors. The composition of the feed was 0.01 % MeOH relative to the flow of helium, as determined by the partial pressures of helium and the main fragment ion of MeOH (m/q = 31).

The polymer-salt solutions were also dip-coated on $SiO_2$/Si(001) substrates in order to obtain particle size information (height) via AFM. In addition, TEM was carried out on the powder samples.

## 6.2 Results and Discussion

### 6.2.1 Morphological and Structural Characterization

Figure 24 displays AFM images of the NP polymeric solutions dip-coated on $SiO_2$/Si(001) after UHV annealing for 30 min at 500 °C. Figure 24(a) shows the particle solution used in all samples except the Pt/$CeO_2$(#2) which is shown in Figure 24(b). At this temperature removal of the encapsulating polymer is observed by monitoring the C-1s XPS signal. As seen in Figure 24, the size distribution in each sample is narrow. Analysis of the images taken after annealing gives average particle height distributions of 5.1 ± 0.6 nm for (a), and 2.7 ± 0.5 for (b).

Figure 25(a-d) and Figure 26(a-d) show typical TEM images of Pt NPs supported on selected oxide powders. All samples underwent the same thermal treatments as described above and were prepared using the same NP polymeric solution analogous to Figure 24(a)

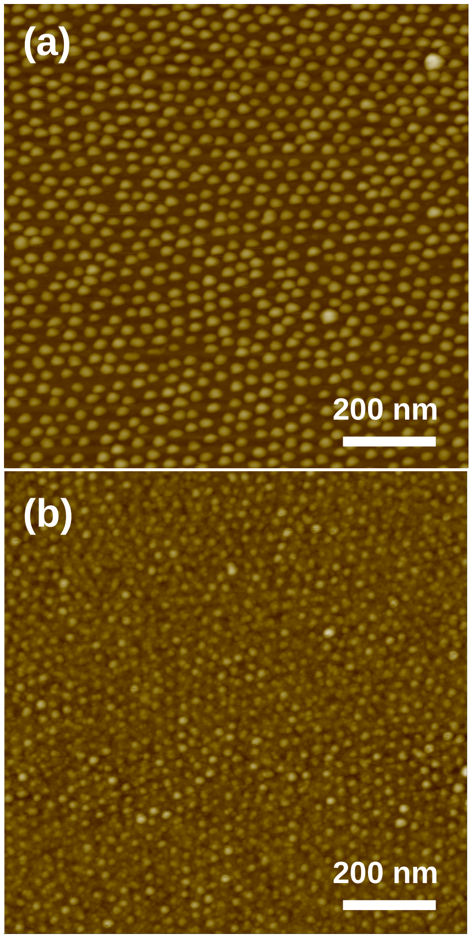

Figure 24 – Tapping mode AFM images of size-selected Pt NPs dip-coated on $SiO_2$/Si(001) and annealed in UHV at 500ºC for 30 min. Samples were prepared using Pt-salt/P2VP concentrations of (a) 0.6 and (b) 0.2. The z scale for (a) is 0-20nm and 0-10nm for (b).

[except Pt/$CeO_2$(#2), analogous to Figure 24(b)]. Low magnification images were employed to obtain the average diameter of the Pt NPs supported on the oxide powders.

Figure 25(a) displays a HAADF-STEM image of the Pt/$CeO_2$(#1) sample. The light-colored areas in this image correspond to Pt-rich regions (high-Z element). Figure 25(b) shows a bright field image of the same region, and (c) shows a high resolution image of the Pt particle (~14 nm) marked by the two circles in (a) and (b). From Figure 25(c) a lattice parameter of 3.95 ± 0.04 Å was obtained, in good agreement with literature values of 3.92 Å

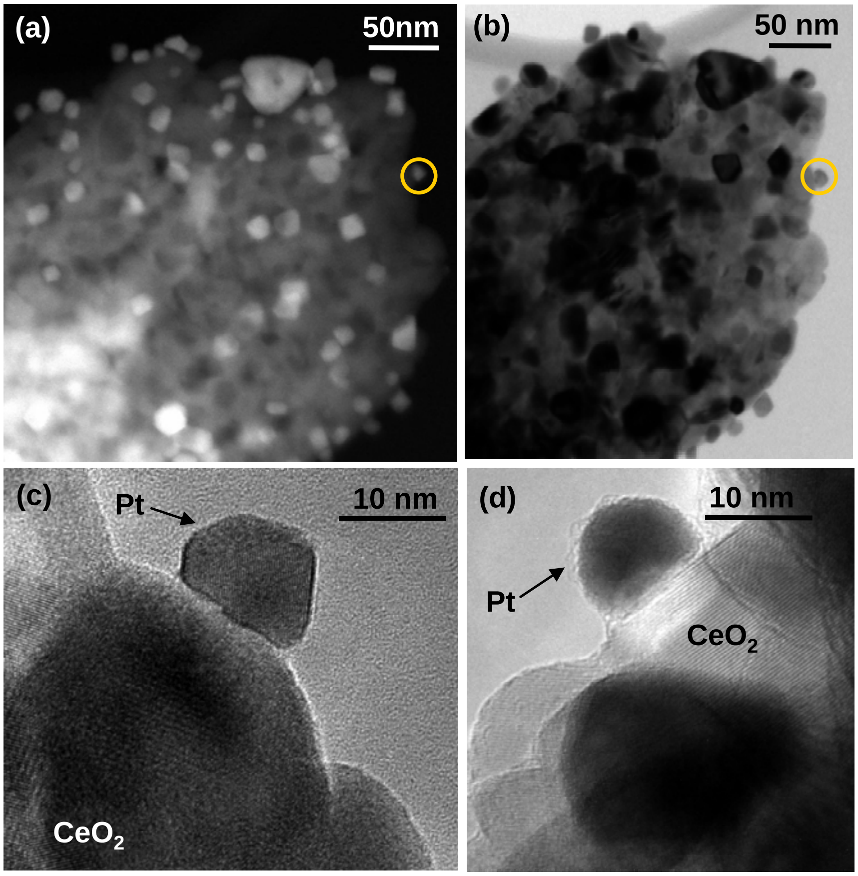

Figure 25 – Pt NPs prepared by micelle encapsulation supported on $CeO_2$: (a) HAADF-STEM image of Pt/$CeO_2$ (#1). (b) Bright field image of same region as in (a). (c) High magnification image of the Pt NP indicated by circles in (a) and (b). (d) Pt NP on $CeO_2$ from Pt/$CeO_2$(#2) prepared initially with a solution of smaller Pt NPs [Figure 24(b)]. Both samples were annealed at 500°C. TEM images acquired by J. Liu, Prof. Y.H. Sohn, and Prof. H. Heinrich (UCF).

for fcc-Pt [295, 296]. In Figure 25(c) the NP appears faceted and Pt(111) spacing is observed. For this sample, the support itself ($CeO_2$) displays significant agglomeration after annealing in air. In addition, the average Pt particle size in this sample was 14.6 ± 2.7 nm, indicating that strong NP coarsening had occurred. One explanation for sintering could be, as given by Perrichon et al. [297], the destabilization of Pt particles on ceria. This effect stems from surface reorganization induced by $O^{2-}$ mobility at temperatures near 300°C, which is below our calcination temperature (500°C). The authors also show an encapsulation/decoration effect which increases with increasing annealing temperatures with smaller particles being more susceptible to this phenomenon. This will be discussed in connection with the activity of our two Pt/$CeO_2$ samples. Figure 25(d) shows a Pt particle (~12 nm) in our sample labeled Pt/$CeO_2$(#2). This sample was made from a particle solution having a size distribution roughly half the size of the Pt/$CeO_2$(#1) sample. Analysis of the HRTEM image of a small Pt particle in this sample indicated a slightly higher lattice parameter (4.0 ± 0.04 Å). Penner et al. [298] have observed the formation of Pt-ceria alloys starting at ~450°C with a lattice parameter of 4.16 Å. Because this sample underwent the same thermal treatment as the Pt/$CeO_2$(#1) sample, and both samples show similar activities and size distributions, we might conclude that Pt particles, supported on $CeO_2$, are not stable at annealing temperatures of 500°C or more, and Pt ceria alloys can be formed. In particular, smaller Pt particles seem to be more susceptible to the interaction with $CeO_2$, in agreement with Perrichon et al. [297]. On Ce thin films deposited on Pt foils, Tang et al. [66] found evidence of strong Ce-Pt interactions and interdiffusion (rather than encapsulation) at and above room temperature. Similarly, using EXAFS as a probe, our group has observed related behavior in small (~1 nm) Pt NPs deposited on $CeO_2$. In that case, no fcc-Pt structure could be revealed in the Fourier-transformed r-space data of the acquired EXAFS. Revealing the possibility of single Pt atoms dispersed throughout the $CeO_2$ matrix. The presence of Pt-oxides at the NP's surface could not be detected by TEM, but will be discussed in the next section based on our XPS data.

For the Pt/$SiO_2$ sample, Figure 26(a), a similar sintering behavior was observed. However, in this sample the distribution of particle sizes was very broad and averaged 15 ±

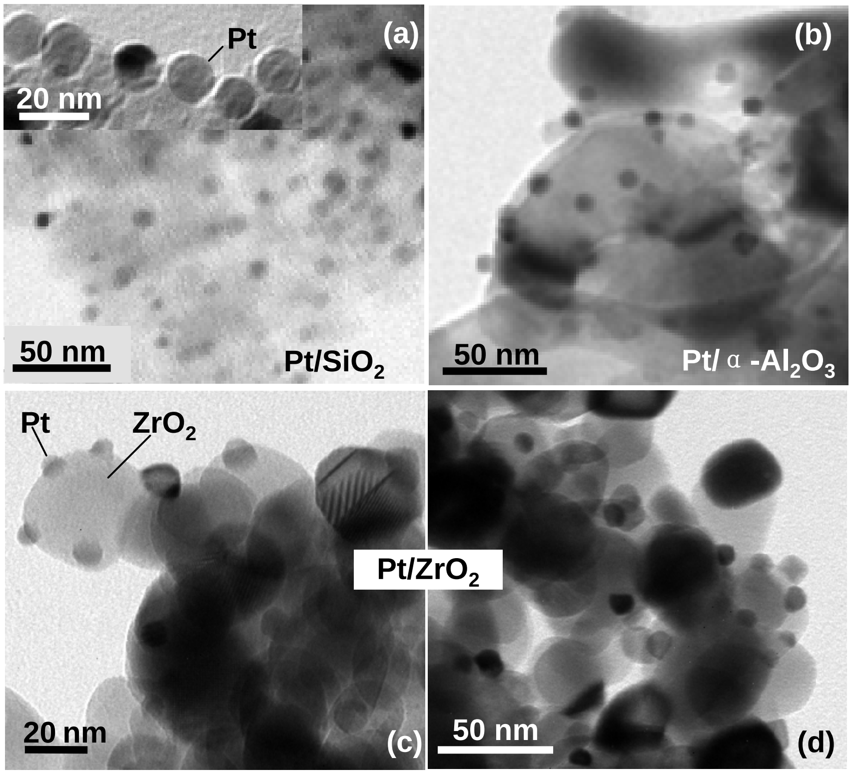

Figure 26 – Pt NPs prepared by micelle encapsulation supported on selected oxide powders: (a) Pt/$SiO_2$, (b) Pt/α-$Al_2O_3$, (c)-(d) Pt/$ZrO_2$. All samples were annealed at 500°C. Images acquired by J. Liu, Prof. Y.H. Sohn, and Prof. H. Heinrich (UCF).

10 nm. This might be related to the fact that the support itself was not of nanometer scale, but rather started out as large (1/8”) pellets and was ground by hand into a fine powder. This may present to the supported particles a more widely distributed set of surface sites available for nucleation as compared to the already nanometer-sized ceria support. However, sintering of Pt on $SiO_2$ is not a new phenomenon and can be more prominent when heating takes place in air as compared to an inert atmosphere [299]. Figure 26(a) (inset) displays a uniform region within the Pt/$SiO_2$ sample.

The Pt/α-$Al_2O_3$, Figure 26(b), and Pt/$ZrO_2$, Figure 26(c),(d), each show similar size distributions with diameters of 8.7 ± 2.1 nm and 8.3 ± 1.6 nm, respectively. These values are also in close proximity to the distribution of the Pt/$TiO_2$ sample having an average particle diameter of 8.6 ± 1.2 nm, details and images of which can be found in the Chapter 5 and in Ref. [300].

### 6.2.2 Electronic and Chemical Characterization

Figure 27 shows XPS spectra of Pt deposited on the different oxide powder supports measured after annealing at 500°C. From our previous studies [300] we know that the annealing temperature employed here is sufficient to completely reduce $Pt^{\delta+}$ species originating from chlorinated compounds, therefore, the observed high BE peaks have been assigned to their respective $PtO_x$ species. For the $Pt/TiO_2$ sample, we see that it is predominantly metallic with the Pt-$4f_{7/2}$ peak appearing at ~70.5 eV. This corresponds to a negative BE shift of ~0.6 eV with respect to the bulk value of 71.1 eV. This is in agreement with our previous results [300] and is close to values reported elsewhere for similar $TiO_2$-supported Pt NPs [274]. The $Pt/ZrO_2$ and $Pt/SiO_2$ show a convolution of $Pt^{2+}$ and $Pt^{4+}$, with the former being mainly $Pt^{2+}$ and the latter slightly favoring contributions from $Pt^{4+}$. The $Pt/CeO_2$(#1) sample appears highly oxidized (mainly $Pt^{4+}$) and the BEs indicate a strong interaction between the $CeO_2$ support and the Pt NPs. As was mentioned before, the possible formation of Pt-Ce alloys might explain the anomalously large BEs observed in the XPS data of these samples. For the $Pt/CeO_2$(#2) sample, a similar spectrum was obtained as that shown for the $Pt/CeO_2$(#1) sample. Tang et al. [66] have shown shifts to higher BEs (+0.2 eV with respect to bulk Pt) for ultra thin Ce films deposited on a metallic Pt foil. In this work, the authors highlight the formation of Ce/Pt mixed layers due to enhanced interdiffusion at and above RT. In the case of our supported Pt NPs, the large BE shifts observed for the Pt-4f core levels can be attributed to $Pt^{\delta+}$ species alloyed with cerium atoms

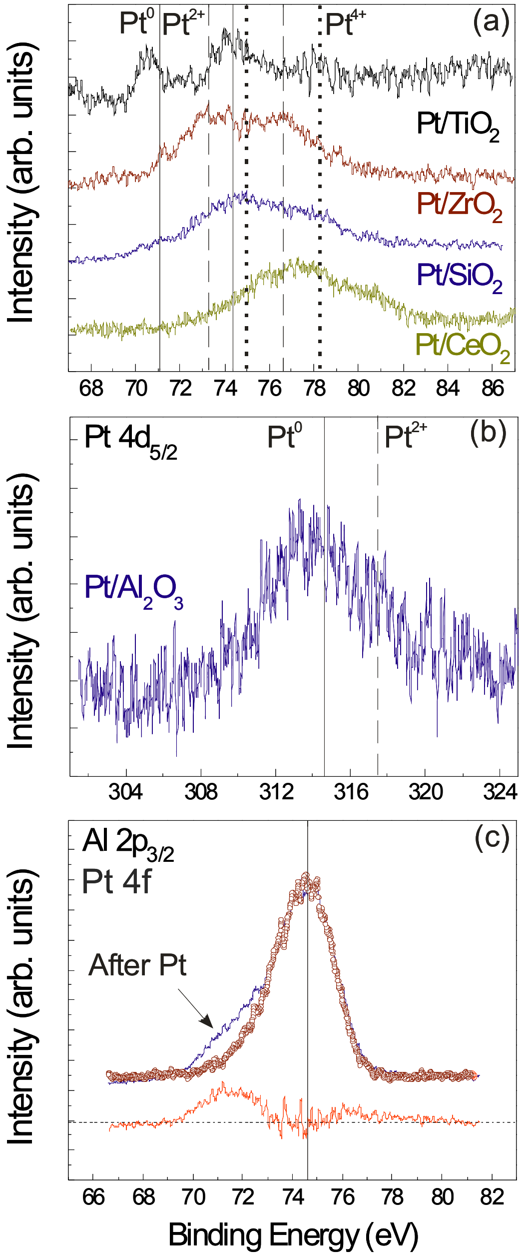

Figure 27 – (a) Pt-4f core level XPS spectra of Pt NPs supported on: (from top to bottom) $TiO_2$, $ZrO_2$, $SiO_2$, $CeO_2$(#1). (b) Pt-$4d_{5/2}$ from Pt/α-$Al_2O_3$. (c) Al-$2p_{3/2}$/Pt-4f region before and after the addition of Pt. The bottom curve in (c) shows the difference of the top two curves before and after the addition of Pt. All spectra were measured after removal of the encapsulating polymer by annealing in air at 500°C. The solid lines indicate the positions of the main core-level peaks of metallic Pt at 71.1 eV ($4f_{7/2}$) and 74.3 eV ($4f_{5/2}$), the dashed lines $Pt^{2+}$ in PtO (73.3 and 76.6 eV), and the dotted lines $Pt^{4+}$ in $PtO_2$ (75.0 and 78.8 eV).

upon annealing at 500°C. Simply based on our XPS data (averaged from the sampling depth, where a Ce concentration gradient exists) we cannot conclude whether Ce atoms are at the surface of the Pt clusters (encapsulation effects) or they are surrounded by Pt atoms intermetallic compounds. A previous work by Fu et al. [65] also discusses the possibility of Pt ion diffusion into subsurface $CeO_2$ layers. Interestingly, and in agreement with our results, their XPS spectra obtained on 2.5 nm Pt NPs, supported on 6 nm-$CeO_2$ after calcination at 500°C, indicate the presence of Pt-oxide species, mainly $Pt^{4+}$.

Figure 27(b) shows the Pt-$4d_{5/2}$ peak in the Pt/α-$Al_2O_3$ sample appearing at ~314.0 eV for $Pt^0$ (solid line) and ~317.5 eV for $Pt^{2+}$ (dashed line). Here again, as in the case of Pt/$TiO_2$, this sample is mainly $Pt^0$ and shows a negative binding energy shift of ~0.6 eV as compared to the bulk value of metallic Pt at 314.6 eV. Figure 27(c) shows the Pt-4f/Al-2p region for the Pt/α-$Al_2O_3$ sample. Here the Al-$2p_{3/2}$ peak at 74.5 eV falls in the middle of the range where we expect to see the Pt-4f peaks. Shown is a superposition of two spectra taken before and after the addition of Pt to our α-$Al_2O_3$ support. The shoulder, due to Pt, is emphasized with an arrow and the difference between the two curves (Pt contribution) is plotted at the bottom of the graph.

### 6.2.3 Catalytic Activity and Selectivity

Figure 28 displays the activity and selectivity for the decomposition of MeOH of the different oxide powders prior to the addition of Pt. Activity is defined in terms of MeOH conversion and is given by the equation:

$$\frac{P_i - P_T}{P_i} \times 100 \tag{26}$$

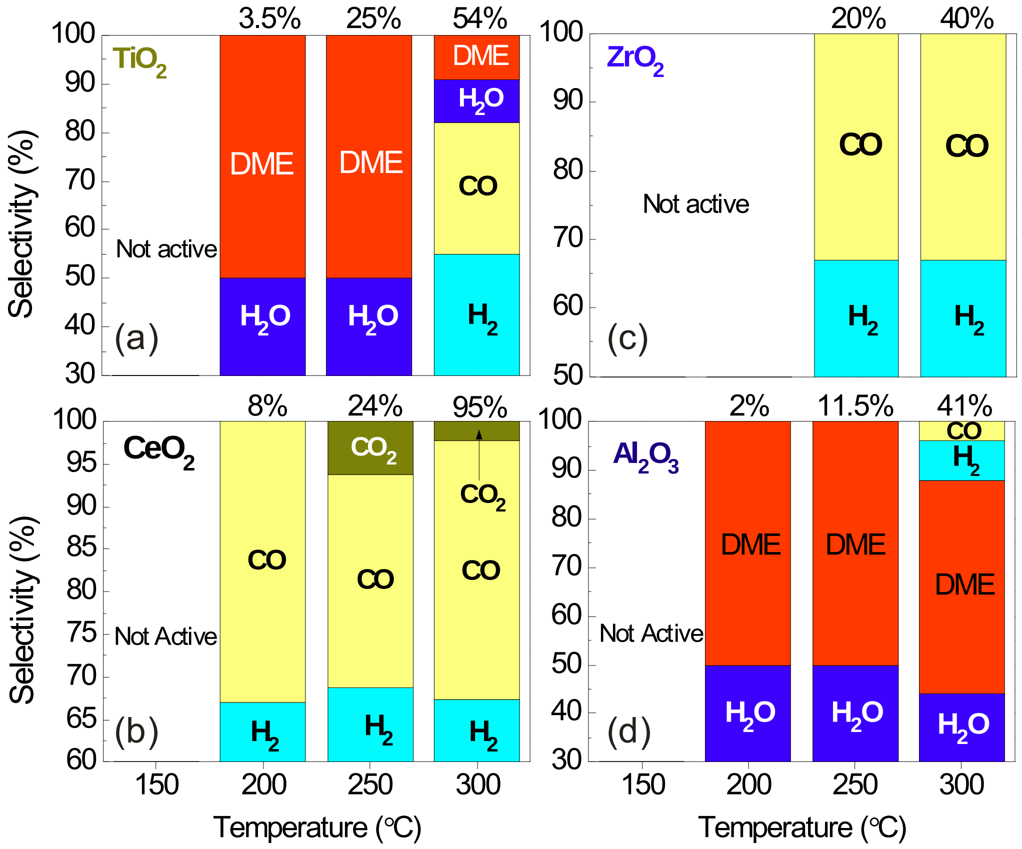

Figure 28 – Catalytic activity (conversion) and selectivity of Pt-free commercial nanocrystalline oxide powders for MeOH decomposition with average grain sizes of (a) ~32 nm for $TiO_2$, (b) ~40 nm for $CeO_2$, (c) ~45 nm for $ZrO_2$, and (d) ~35 nm for α-$Al_2O_3$. The number across the top of each chart gives the MeOH conversion (%) at each temperature. $SiO_2$ (not shown) is almost completely inert, showing only ~3 % MeOH conversion at 300°C. All powders have been calcined at 500°C for 2.5 hours before the reaction.

where $P_i$ is the initial partial pressure of the main fragment ion of methanol $(m/q = 31)$ and $P_T$ is the partial pressure at a given temperature throughout the experiment. The percentages along the top of each graph represent the MeOH conversion at a particular temperature as given by equation (26). Selectivity for each product gas is derived from the QMS data, along with stoichiometric considerations [equations (28)-(31)], and is defined as the percent of the total product that each particular partial gas pressure represents, given by:

$$selectivity\,(\%) = \frac{A_n}{\sum A_n} \times 100 \tag{27}$$

Where $A_n$ represents the output of the $n^{\text{th}}$ product gas. In our experiments $CO_2$, and Dimethyl ether (DME) were obtained as by-products. $CO_2$ originates from CO produced in the decomposition of MeOH, reaction (28), and possible mechanisms involved in the production of $CO_2$ are the Boudouard and water gas shift reactions, (29) and (30) respectively:

$$CH_3OH = CO + 2H_2 \tag{28}$$

$$2CO = CO_2 + C \tag{29}$$

$$CO + H_2O = CO_2 + H_2 \tag{30}$$

Although no water was directly introduced into the feed, some residual water is always present in the lines and available for the WGS reaction (30).

DME may be formed according to equation (31).

$$2CH_3OH = CH_3OCH_3 + H_2O \tag{31}$$

We note that during the catalyst's time on-line (~7 hours) we do not observe any deactivation or visible change in the catalyst and we might then rule out reaction (29) as giving a significant contribution, since C-poisoning would have resulted in catalyst deactivation. However, long-term deactivation studies were not performed in this study.

The $SiO_2$ support is absent in Figure 28 because it was found to be inert over the range of temperatures used in the experiment (100°C to 300°C). The $TiO_2$, Figure 28(a), and the α-$Al_2O_3$ supports, Figure 28(d), each show similar selectivity with a tendency towards the formation of DME. However, the selectivity of DME for the α-$Al_2O_3$ support remains high even at 300°C, whereas the $TiO_2$ shows a marked switch towards $H_2$ at that temperature.

The $ZrO_2$ sample, Figure 28(c), remains inactive at temperatures below 200°C and no byproducts are detected up to 300°C. For the $CeO_2$ sample, Figure 28(b), which becomes active at temperatures above 150°C, we see a high selectivity for $H_2$ and ~6 % for $CO_2$ at 250°C decreasing to ~2 % by 300°C. The formation of $CO_2$ could favor catalyst lifetime since CO poisoning will be reduced. From the QMS data, equations (28) and (30) [neglecting (29)], it was estimated that ~20 % of the CO from MeOH decomposition goes to $CO_2$ through the shift reaction at 250°C. This sample also shows excellent activity relative to the other supports with almost 100 % conversion at 300°C. $TiO_2$ being the second most active with only 54 % conversion at 300°C. None of the supports tested were active for MeOH decomposition at or below 150°C.

Figure 29 shows the same type of data as Figure 28 for the nanocrystalline oxide supports after the addition of Pt NPs. Here we show a plot of MeOH conversion (%) as a function of reactor temperature with the dotted line denoting 50 % conversion. In all of the Pt containing samples no byproducts were observed in the range of temperatures tested. Therefore, the reaction proceeds by way of direct decomposition, equation (28). Again, as in Figure 28, we see similarities between the $Pt/TiO_2$ and $Pt/\alpha\text{-}Al_2O_3$ samples. $Pt/TiO_2$ and $Pt/\alpha\text{-}Al_2O_3$ have similar average particle size distributions of ~8.6 - 8.7 nm, and show similar activity with the reaction proceeding via the direct decomposition of MeOH. The $Pt/\alpha\text{-}Al_2O_3$ slightly outperforms the $Pt/TiO_2$ sample reaching a higher conversion at 250°C. For the $Pt/ZrO_2$ sample (Pt diameter ~8.3 ± 1.6 nm) we see that it is by far the most active at low temperatures, reaching 73 % conversion at 200°C. The $Pt/SiO_2$ (Pt diameter ~15.0 ±

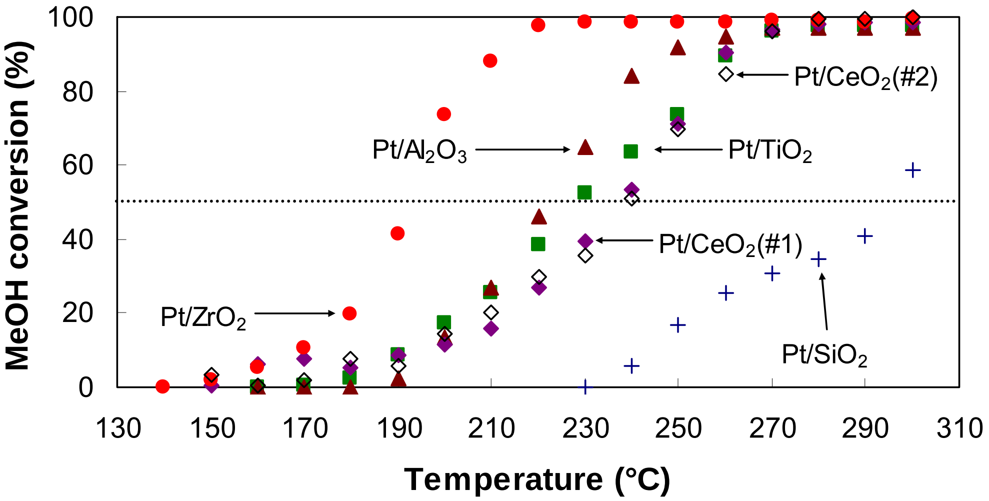

Figure 29 – MeOH decomposition over Pt NPs supported on nanocrystalline oxide powders: Pt/$ZrO_2$ (full circles), Pt/α-$Al_2O_3$ (full triangles), Pt/$TiO_2$ (full squares), Pt/$CeO_2$(#1) (full diamonds), Pt/$CeO_2$(#2) (open diamonds), Pt/$SiO_2$ (crosses). All samples have been calcined at 500°C for 2.5 hours before the reaction.

10.4 nm) now becomes active above 150°C with excellent selectivity for $H_2$ and ~60 % conversion at 300°C. Because the $SiO_2$ support was completely inactive we may attribute this activity to the addition of Pt. Although the average Pt particle size in the Pt/$CeO_2$(#1) sample is much larger than that on the other substrates (~14.6 ± 2.7 nm) its activity is only slightly lower than that of Pt/$TiO_2$ and Pt/α-$Al_2O_3$. This effect may be attributed to the relatively high MeOH conversion observed on our Pt-free nanocrystalline $CeO_2$ powders and the addition of even large Pt particles further enhanced the activity. Because this support performed relatively well before the addition of Pt, and our TEM images show agglomeration on this sample [Figure 25(a),(b)], an additional sample was prepared with the goal of minimizing particle growth. This was done by preparing an alternate micelle solution with an average Pt NP size distribution roughly half the size of the initial sample, as seen in the AFM images of Figure 24. From here the same thermal treatment was done as on the initial sample and TEM images were taken. Unfortunately the new sample, denoted as

$Pt/CeO_2$ (#2), produced analogous reactivity results, also shown in Figure 25. The TEM images obtained from this sample, after annealing in air at 500°C and before the reaction, were very similar to those of the first $Pt/CeO_2$ (#1) sample (Figure 25) revealing considerable particle sintering. It is clear from the behavior displayed by this sample that Pt NPs in this size range are highly unstable and prone to coarsening on $CeO_2$ supports upon air annealing.

The general order for reaching the 50 % conversion mark may be listed as follows: $Pt/ZrO_2$, $Pt/\alpha\text{-}Al_2O_3$, $Pt/TiO_2$, $Pt/CeO_2$, and $Pt/SiO_2$. Surprisingly, this trend does not seem to correlate with the enhanced catalytic activity expected for NPs supported on highly reducible oxides ($CeO_2$ and $TiO_2$). However, it is in agreement with Ref. [55] and results obtained by Usami et. al [278] who have shown that $Pd/ZrO_2$ is more active for MeOH decomposition than $Pd/CeO_2$, $Pd/TiO_2$, as well as $Pd/SiO_2$. In addition, the authors determined that cationic Pd was advantageous for this reaction, in agreement with the XPS data (Figure 27) of our $Pt/ZrO_2$ sample.

An important point to note is that the least active samples ($Pt/CeO_2$ and $Pt/SiO_2$) both show particle coarsening with a significant increase in particle size. There are arguments which suggest that the support may be of minimal importance as long as the particles themselves have certain qualities, in particular, a high concentration of low coordinated surface sites [301]. The density of these sites increases with decreasing particle size, and therefore, we do not expect the density of such sites in the $Pt/SiO_2$ and $Pt/CeO_2$ samples to be high as compared to the other samples. With the addition of Pt, the previously inert $SiO_2$ displays a dramatic increase in catalytic activity. In addition, the $CeO_2$ support alone (without Pt) outperforms the $Pt/SiO_2$ sample (Figure 28, Figure 29) and the addition of Pt to the

$CeO_2$ support is expected to enhance its performance even further. Although this was indeed observed, the increase in activity was not as significant as in some of the other catalysts investigated, such as Pt/$ZrO_2$. It has been reported that the Pt in Pt/$CeO_2$ is the main catalytic species for the decomposition of MeOH [302]. This suggests that the relatively small improvement observed in this sample can be attributed to the large size of the Pt particles considered, a partial encapsulation of the Pt particles by $CeO_2$, or perhaps interdiffusion of Pt into the $CeO_2$ matrix. As previously discussed, the possibility of alloy formation in the Pt/$CeO_2$ samples might also give rise to detrimental effects in the reactivity of this system. Due to the large NP sizes available in the Pt/$CeO_2$ and Pt/$SiO_2$ samples, we will exclude these samples from the comparative discussion of the support effects.

The remaining samples (Pt/$ZrO_2$, Pt/$\alpha$-$Al_2O_3$, and Pt/$TiO_2$) all have similar size distributions of ~8-9 nm. For these three samples the Pt/$ZrO_2$ is clearly the most active for the decomposition of MeOH (Figure 29) and a support-dependence for this reaction might be inferred. It is interesting to note that the Pt/$ZrO_2$ and Pt/$\alpha$-$Al_2O_3$ are more active than the Pt/$TiO_2$ suggesting that irreducible supports may be of advantage for this reaction. In a study done by Ivanov and Kustov [56] on the electronic state of Pt supported on different oxides, using diffuse reflectance IR spectroscopy and CO as a probe molecule, it was found that Pt/$ZrO_2$ revealed absorption bands characteristic of CO complexes with Lewis acid sites on the surface of $ZrO_2$. In the same study no such features were observed for Pt/$TiO_2$, Pt/$\gamma$-$Al_2O_3$, or Pt/$SiO_2$. However, the $Al_2O_3$ in their study was $\gamma$-$Al_2O_3$. It has also been found, in a study of MeOH adsorption and dissociation over $SnO_2$, that the dissociation of MeOH to methoxide occurs preferentially at $Sn^{2+}$ cationic sites. Therefore, acidic sites on the surface of the Pt/$ZrO_2$ sample may account for its superior performance relative to the other samples.

## 6.3 Conclusion

We have investigated the decomposition of MeOH over Pt deposited on various oxide supports. The samples obtained may be roughly grouped into categories consisting of large (~15-18 nm) and small (~8-9 nm) Pt NPs deposited on *reducible* ($CeO_2$, $TiO_2$) and *non-reducible* ($SiO_2$, $ZrO_2$, $\alpha$-$Al_2O_3$) supports. For all Pt/oxide samples tested the reaction proceeds mainly through the direct decomposition of MeOH. For the large particles deposited on highly reducible $CeO_2$, as well as non-reducible $SiO_2$, the Pt/$CeO_2$ is clearly more active. For these two samples, the superior performance of the Pt/$CeO_2$ sample can be related to the relative performances of the Pt-free supports themselves. However, for the smaller particles, deposited on $TiO_2$, $ZrO_2$, and $\alpha$-$Al_2O_3$, the Pt/$ZrO_2$ is the most active, much more so than the Pt/$TiO_2$ which reaches 50 % conversion at ~230°C as compared to ~195°C for the Pt/$ZrO_2$. The Pt/$ZrO_2$ is also cationic as opposed to the mainly metallic Pt on $TiO_2$ and $\alpha$-$Al_2O_3$. Further, our XPS data indicate that for similarly sized NPs the final state of oxidation of Pt depends on the support. Because all samples underwent identical thermal treatments, we may conclude that the stability of $Pt^{\delta+}$ species can be affected by the choice of support. These data suggest that for MeOH decomposition, or perhaps in general, for reactions not involving the dissociation of $O_2$, the reducibility of the support plays a secondary role to the more important parameter of particle size and oxidation state of Pt. The role of the support is that of a stabilizer, a provider of preferential/additional sites of interaction, and a mediator among the different oxides of Pt.

# CHAPTER 7: EFFECT OF SECONDARY METALS ON THE OXIDATION STATE, ACTIVITY, AND SELECTIVITY OF Pt NPs IN MeOH DECOMPOSITION

Jason R. Croy, S. Mostafa, L. Hickman, H. Heinrich, and B. Roldan Cuenya

Applied Catalysis A: General 350 (2008) 207

## 7.1 Experimental

In the last two chapters we have explored the size and support dependence of Pt NPs in MeOH decomposition reactions. The current study moves on to deal with the influence of secondary metal dopants in Pt-M catalysts with M = Au, Pd, Ru, and Fe. To this end, we have use a PS(27700)-P2VP(4300) and a metal-salt/P2VP ratio (r) of 0.2 for all samples. The salts used were $H_2PtCl_6 \cdot 6H_2O$, $HAuCl_4 \cdot 3H_2O$, $RuCl_3$, $PdCl_2$, $FeCl_3$. The metal content of all bimetallic samples by weight (wt) was 80 % Pt and 20 % secondary metal. The solution was then mixed with nanocrystalline $ZrO_2$ (~45 nm) in the form of a powder. All samples were dried in air at ~100°C for 24 hours then placed in a tubular furnace, open to the air, for calcination at 500°C for 2.5 hours. Each catalyst sample had a total weight of 50 mg and contained 1 % by weight metal.

XPS data were collected using a monochromatic X-ray source (Al-Kα, 1486.6 eV) operating at 350 W and a flood gun was used to correct for sample charging during measurement. All spectra were referenced to the Zr-$3d_{5/2}$ [$ZrO_2$] peak at 182.6 eV [303].

Catalytic decomposition of methanol in the vapor phase was carried out in a packed-bed mass flow reactor. Immediately prior to the reaction all catalysts were heated for one hour at ~200°C (below the initial calcination temperatures of 500°C used to remove the polymeric NP shell) in a flow of helium at 10 ml/min. Activities were measured at atmospheric pressure in the range of 100 to 220°C. The composition of the feed was 0.05 % MeOH relative to the flow of He, as determined by the partial pressures of helium and the main fragment ion of MeOH (m/q = 31).

The polymer-salt solutions were also dip-coated on $SiO_2$/Si(001) substrates in order to obtain particle size information (height) via AFM. In addition, TEM was carried out on the powder samples.

## 7.2 Results and Discussion

### 7.2.1 Morphological and Structural Characterization

Figure 30 displays representative images of the NP polymeric solutions dip-coated on $SiO_2$/Si(001). Here the three images show bimetallic samples [(a) Pt-Au, (b) Pt-Pd, and (c) Pt-Fe] before the removal of the polymeric shell. The images demonstrate the validity of our preparation method for the synthesis of bimetallic catalysts with narrow size distributions. Analysis of the images taken after the removal of the polymer (not shown), by heating in ultrahigh vacuum (UHV) for 30 min at 500°C, gives an average particle height of ~3 nm.

Figure 31 shows elemental distribution maps of (a) Pt (M-edge) and (b) Fe (L-edge) obtained by TEM in the same region of the Pt-Fe sample. We can see a uniform distribution of the metals with Pt and Fe appearing in the same regions within a NP. Figure 31(c) shows a faceted particle from the Pt-Au sample with a measured lattice parameter of 3.96 ± 0.02 Å. A pure Pt particle in a monometallic Pt sample, with a lattice parameter of 3.74 ± 0.04 Å, is displayed in Figure 31(d). The lattice parameters for bulk Pt, bulk Au, and a $Pt_{0.8}Au_{0.2}$ alloy are 3.92 Å, 4.07 Å, and 3.94 Å respectively [304, 305]. Thus, our value of 3.96 Å for the Pt-

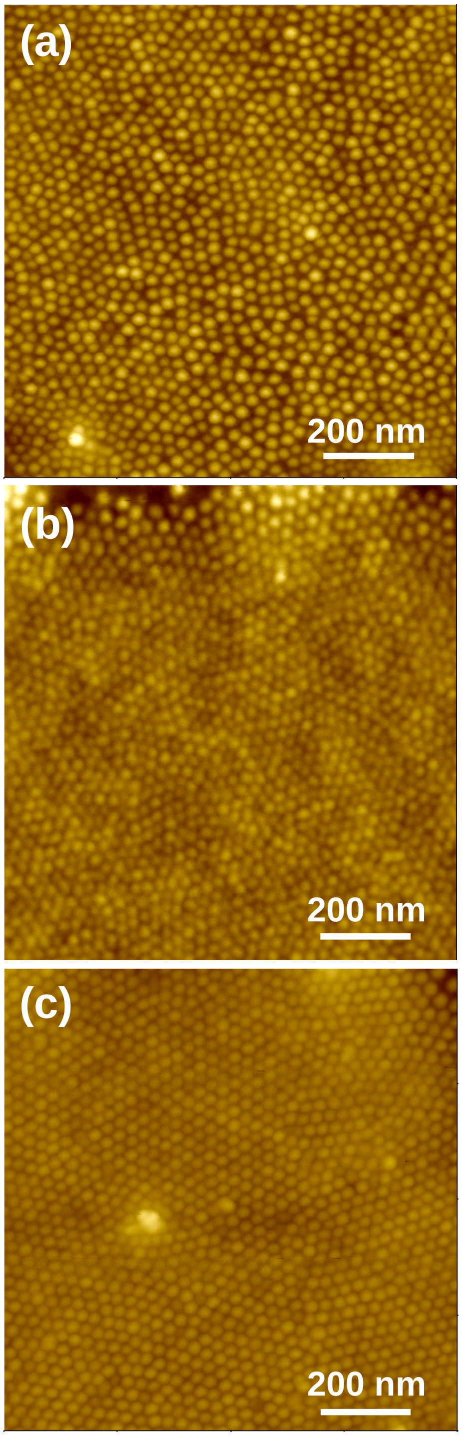

Figure 30 – AFM images of (a) Pt-Au, (b) Pt-Pd, and (c) Pt-Fe NPs (20 % wt M) supported on $SiO_2$/ Si(001). The images were taken before polymer removal.

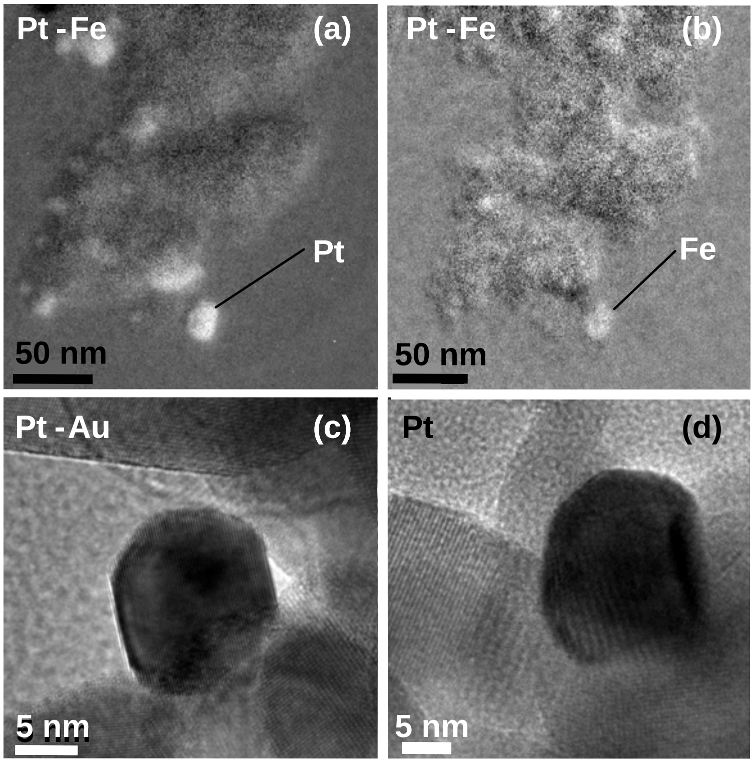

Figure 31 – Elemental distribution map (using energy-filtered TEM) of the Pt-Fe NPs supported on $ZrO_2$ showing homogeneous distribution of Pt (a) and Fe (b) in individual clusters. (c) High resolution image of a particle in the Pt-Au sample, (d) a particle in the pure Pt sample. Images acquired by Prof. H. Heinrich (UCF).

Au particle is in agreement with the formation of a Pt-rich, Pt-Au alloy. The TEM images of Figure 31 reveal our particles to be ~10 nm in diameter.

### 7.2.2 Electronic and Chemical Characterization

Figure 32 and Figure 33 show XPS spectra and Figure 34 exhibits related compositional information for the monometallic Pt and Pt-M NP samples deposited on $ZrO_2$ powder. The fits were done after linear background subtraction using a product of Gaussian and Lorentzian functions, as defined in the software CASA XPS, with the maximum width (FWHM) of each component held constant [$Pt^0$ (1.8 eV) , PtO (2.4 eV), $PtO_2$ (2.8 eV)] from spectrum to spectrum. The distinction of PtO and $PtO_2$ species, especially on small NPs, is difficult. An initial attempt to fit the Pt-4f region of our samples with only two doublets (one corresponding to metallic $Pt^0$, the other to $PtO_x$) was made, but such a fit resulted in an unreasonably large FWHW (> 3). Figure 32 displays data from the Pt-4f core level region. These reference values for PtO and $PtO_2$, as well as the energy difference between $Pt^0$ and $PtO_2$ (~3.6 eV), are consistent with several reports of supported Pt and Pt-M systems [306, 307], as well as with preliminary data obtained by our group on similarly synthesized Pt NPs supported on thin film oxide surfaces after exposure to atomic oxygen in UHV and subsequent annealing. The $Pt^0$-$4f_{7/2}$ peak in our monometallic Pt NPs is shifted 0.6 eV higher than the value of bulk Pt [308]. This positive shift may be attributed to final state effects in our small clusters and/or an interaction with the support itself [201]. One possible interaction is the formation of interfacial Pt-Zr or Pt-O-Zr compounds. Alloying of Pt and Zr has been observed at 500°C (our annealing temperature) [309] and the observed shift to higher BE of the $Pt^0$-$4f_{7/2}$ peak is in agreement with Ref. [310]. What effect these possible interfacial compounds have on the chemical properties of our systems will be investigated in more detail in the future. The relative content of the different Pt species and XPS BEs obtained from the analysis of the data in Figure 32 are summarized in Table 5. The estimated error in the fit of the area of the peaks is ± 3 %. An interesting trend appears in the concentration of Pt-oxides for these samples as shown in Figure 34. The Pt-Au is the least metallic in composition being 22 % $Pt^0$. As we go from Pt-Au to Pt-Pd we see a substantial increase in the amount of metallic $Pt^0$. This increase continues as we go across Figure 34 to Pt-Fe with a metallic Pt content of 60%.

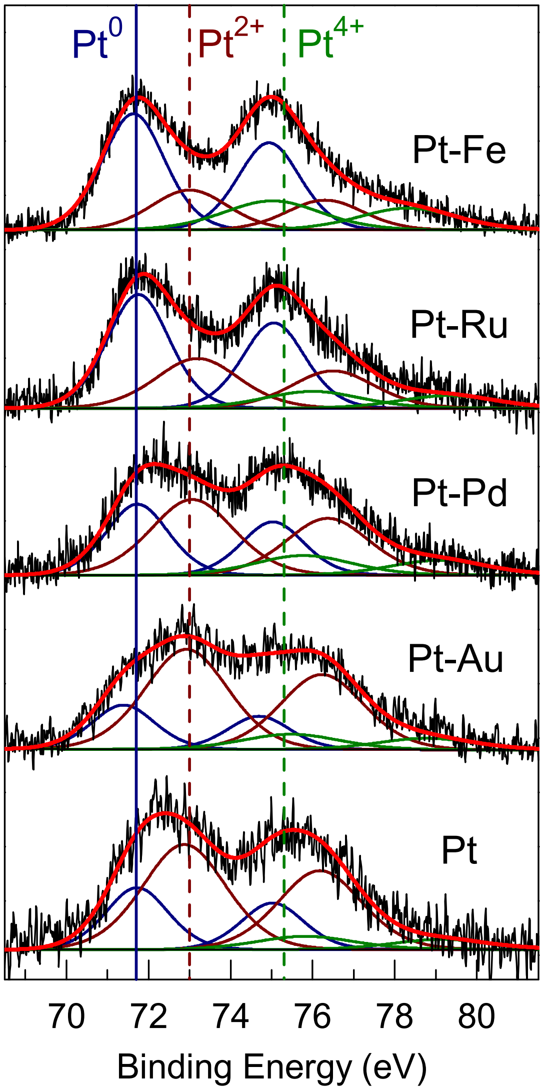

Figure 32 – XPS spectra of the Pt-4f region comparing monometallic Pt with bimetallic (Pt-M) NPs deposited on $ZrO_2$. From bottom to top, the Pt-M spectra reveal a trend of decreasing oxidation. The solid and dashed lines represent the Pt-4$f_{7/2}$ peaks of $Pt^0$, PtO, and $PtO_2$, respectively.

Figure 33 shows XPS spectra of the most intense photoelectron peaks associated with the secondary metals before and after the addition of Pt. The following core-level regions are shown in Figure 33: (a) Au-4f, (b) Fe-2p, (c) Pd-3d (and $ZrO_2$-3p), and (d) Ru-3d. In Figure 33(c) we can see that the Pd-3d region overlaps with the $ZrO_2$-3p substrate peaks

Table 5 – Relative phase content of the different Pt and Pt-oxide species as well as the BE of metallic Pt obtained from the Pt-4f XPS spectra shown in Fig. 32. Also shown are the corresponding values of the Pt-Au sample after reaction with MeOH (spectrum in Fig. 38).

| Sample | $Pt^0$ B.E (eV) | $Pt^0$ (%) | PtO (%) | $PtO_2$ (%) |
|---|---|---|---|---|
| Pt | 71.7 | 28 | 63 | 9 |
| Pt-Au | 71.4 | 22 | 66 | 12 |
| Pt-Au/MeOH | 71.5 | 34 | 53 | 13 |
| Pt-Pd | 71.7 | 35 | 50 | 15 |
| Pt-Ru | 71.8 | 55 | 32 | 13 |
| Pt-Fe | 71.6 | 60 | 25 | 15 |

and we have superimposed the Pd sample's spectrum on that of the Pt-free $ZrO_2$ substrate's (bottom). The Pt-Pd sample is shown on top. Similarly for Ru, shown in Figure 33(d), the Ru-3d region coincides with C-1s and a deconvolution has been done to identify the constituent components of the monometallic Ru (bottom) and the Pt-Ru (top) samples. The C present in these samples is adventitious C from the sample transfer in air to the UHV chamber were XPS measurements were carried out.

In order to better understand the segregation phenomena occurring in our bimetallic NPs during the post-synthesis annealing treatment in air at 500°C, several fundamental properties of the monometallic metals should be kept in mind. For example, the order of decreasing size for the atomic radii (metallic and Wigner-Seitz) of our metals is Au > Pt > Pd > Ru > Fe [311, 312]. The order of the heats of sublimation from high to low is Ru > Pt > Fe ~ Pd > Au [313, 314]. The surface energies from high to low go as Ru > Pt > Fe >Pd > Au [315] (experimental values). And finally, since our bimetallic NPs were annealed in the presence of oxygen (air), a parameter that should be taken into account is the heat of

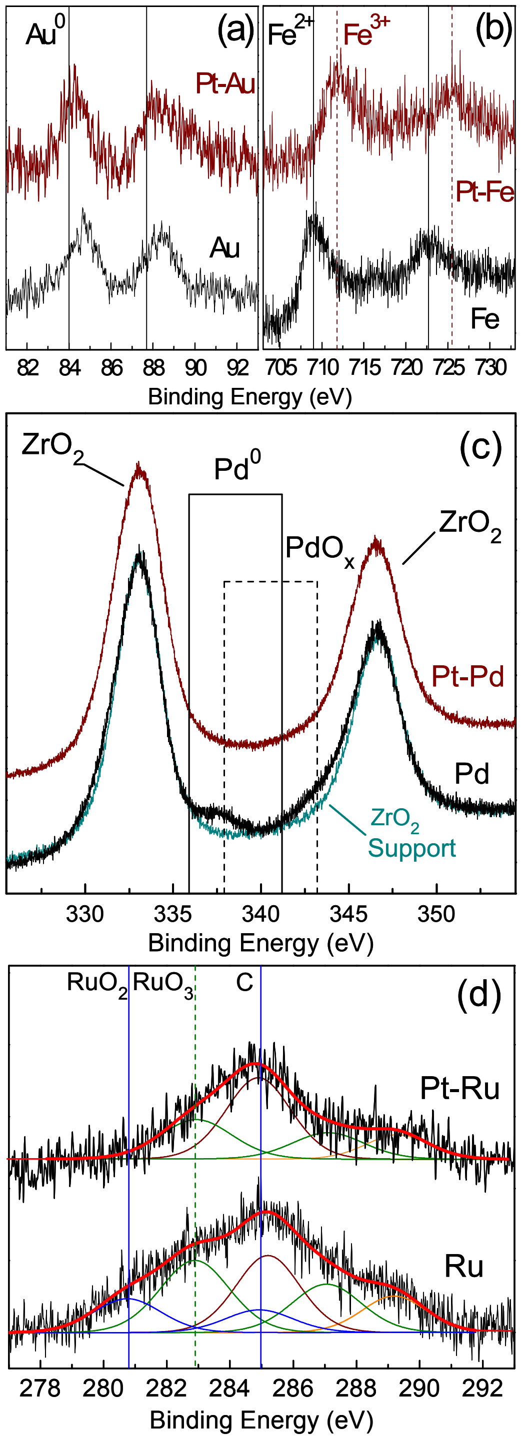

Figure 33 – XPS spectra of (a) Au-4f region of pure Au (bottom) and bimetallic Pt-Au NPs (top). (b) Fe-2p binding energy region of pure Fe (bottom) and bimetallic Pt-Fe NPs (top). (c) Pd-3d region of the monometallic Pd sample superimposed on the Zr-3p region of the substrate (bottom). The top spectrum shows the Pt-Pd sample. Two shoulders in the lower spectra reveal the presence of $PdO_x$ . (d) Ru-3d core level region of the pure Ru (bottom) and bimetallic Pt-Ru (top) NP samples.

formation of the different oxides. Starting with the most stable oxide, the trend goes as Ru > Fe > Pd > Pt > Au [311].

Although all of the above trends refer to bulk systems, due to the relatively large size of our NPs (~ 10 nm in diameter) they are expected to be a reasonable referent for our studies. Theoretically it has been shown (for Cu-Ni systems) that clusters containing less than 1000 atoms are dominated by geometric effects, while those above this size are driven by thermodynamic effects reported for the macroscopic systems [316]. Using data from Ref. [131], a cubo-octahedral fcc Pt NP of 5 nm in diameter consists of at least 4000 atoms. Therefore, thermodynamic arguments of segregation given above should be valid. However, from the above parameters, the different affinities for oxygen of the distinct secondary metals are believed to play a key role. Alloys are notably affected by adsorbates from the surrounding gaseous environment and the metal having the highest affinity for these adsorbates will preferentially segregate to the surface [317, 318]. This segregation effect has been observed, for example, in Pt-Rh catalysts [317]. There, the performance of the catalysts varied between pure Pt and pure Rh depending on the surface concentrations of each metal, with Rh preferentially occupying the surface under oxidizing conditions, and Pt under reducing conditions. We might note that many of the studies mentioned in Ref. [317] are on single crystals under controlled vacuum environments whereas our samples consist of multi-faceted, metal-oxide-supported, metallic NPs. Because all of our samples have been prepared under identical conditions, have similar size distributions, are on the same support ($ZrO_2$), and were calcined in air at the same temperature, the varying concentrations of the different Pt and $PtO_x$ species (Table 5) must be related to the tendency of the secondary metals to segregate to the surface where oxygen is present during annealing. Therefore, larger amounts

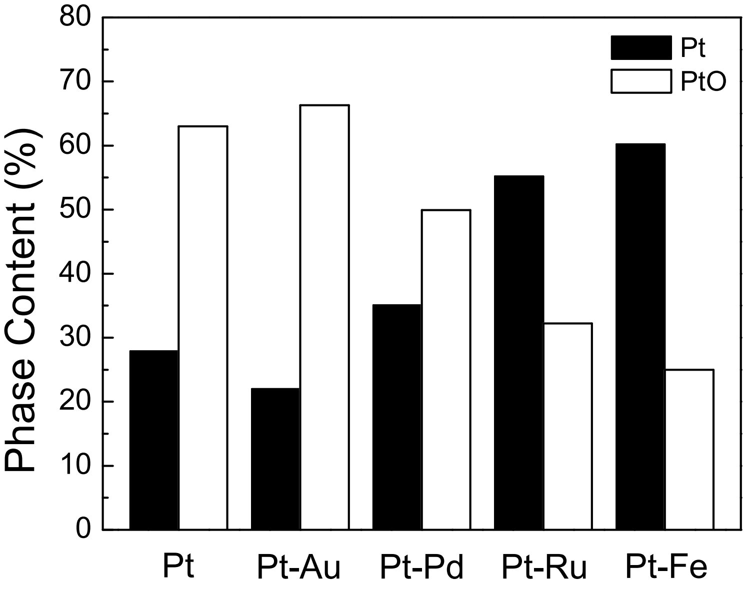

Figure 34 – Relative phase content (%) of metallic Pt PtO in $Pt_{0.8}M_{0.2}$ NPs supported on $ZrO_2$ obtained from the XPS data in Figure 32.

of $PtO_x$ in our samples could be related to the presence of a larger number of superficial Pt atoms, while lower $PtO_x/Pt^0$ ratios would indicate that the secondary metal has segregated to the NP surface, minimizing Pt oxidation.

From the Pt-Au spectrum in Figure 32 and Table 5, we see that the addition of Au seems to have had little effect on the oxidation state of Pt in this system as compared to the similarly prepared pure Pt NPs. The atomic radius of Au is larger than that of Pt so we would expect lattice strain to contribute to the segregation of Au to the NP surface. In addition, the surface energy and heat of sublimation of Au are each lower than the corresponding values for Pt, again promoting surface segregation of Au. It has also been shown theoretically that Au will segregate in a $Pt_{0.75}Au_{0.25}$ system [319], which is close to our $Pt_{0.8}Au_{0.2}$. However, Au does not have a high affinity for oxygen, and our annealing in air should not further favor the segregation of Au to the surface. The metallic state of Au in our pure Au and Pt-Au catalysts is confirmed in the Au-4f XPS spectra of Figure 33(a). In Figure

33(a), the Au-4$f_{7/2}$ peak appears at 84.7 eV in the pure Au (bottom) NP sample, which is 0.7 eV higher than the value for bulk Au at 84.0 eV [320], and the same peak appears at 84.2 eV in the Pt-Au (top) sample (-0.5 eV shifted with respect to the pure Au NPs). For the latter sample we also see a negative shift in the binding energy of $Pt^0$ of 0.4 eV with respect to the pure Pt sample (Table 5). Bastl et al. [321] have also reported negative binding energy shifts for both Pt and Au in Pt-Au alloys formed by vapor deposition of Au on polycrystalline Pt foils. Based on our XPS and TEM data (average representation of the particle structure) we conclude that the Pt-Au sample is a homogeneous nano-alloy with a slightly Au rich surface. It is interesting to note that Zhang et al. [322] have reported that Au can stabilize Pt against dissolution in fuel cells by raising the oxidation potential of Pt, whereas in our Pt-Au system we do not find Pt to be reduced compared to the pure Pt sample. The authors point out that Au will interact differently when deposited on a metallic versus oxide substrate and that Au deposited on Pt is unlikely to intermix with Pt. In our system we have evidence [TEM image shown in Figure 31(c)] of the formation of a Pt-Au alloy, most likely due to our chemical synthesis method versus deposition of Au on a Pt (111) single crystal surface by Zhang et al. [322]. In addition our cluster diameters are roughly three times larger than their ~3 nm particles.

Since the surface energies of Pd and Fe are lower than that of Pt, and the heats of oxide formation of the former metals are higher, the segregation of Pd and Fe to the NP surface is expected. Anti-segregation has been predicted for Fe and a somewhat neutral behavior for Pd when these metals are alloyed with Pt in the absence of oxygen [319, 323]. This emphasizes the importance of taking into account the affinity of the different metals for oxygen in understanding segregation phenomena in "real-world" nanocatalysts. In our samples, the segregation of Fe to the NP surface results in a Pt rich core and a decrease in the amount of surface Pt oxide compounds formed upon air annealing, as is seen in Table 5, Figure 32, and Figure 34. From Figure 33(b) we see the pure Fe NP sample (bottom) showing $Fe^{2+}$ in FeO (after air annealing, 500°C) at ~709 eV and the corresponding Pt-Fe (top) reveals Fe in the 3+ state ($Fe_2O_3$) at ~711.8 eV. The higher oxidation state of iron in the bimetallic sample suggests the possibility of Fe promoting the reduction of the Pt oxide compounds that are formed in these NPs. The results for the Pt-Fe sample are in qualitative agreement with a study by Niemantsverdriet et al. [324] who found Pt to be zero valent in an Fe-Pt alloy with the formation of Fe ions at the surface of the alloy particles.

The main XPS peaks of Pd-3d overlap with those of Zr-3p and could not be resolved in the Pt-Pd sample. However, the presence of $PdO_x$ in the monometallic Pd sample can be inferred from the two shoulders visible in the Pd-3d region of Figure 33(c). Here we see the spectrum of the monometallic Pd sample superimposed on the Zr-3p region of the substrate (bottom), and that of the Pt-Pd sample (top), with the solid and dashed vertical lines indicating the binding energies of the $Pd^0$ (335.9 eV, 341.2 eV) and $Pd^{2+}$ (337.9 eV, 343.2 eV) 3d doublets, respectively. The peaks at ~333.1 eV and 346.6 eV correspond to the $ZrO_2$-3p substrate. In a study done by Graham et al. [325] on alumina-supported Pt-Pd catalysts, it was suggested that Pd on the surface of Pt-Pd alloys inhibited the formation of $PtO_x$. This might certainly be the case here in light of Pd's greater affinity for oxygen and the large amount of $Pt^0$ that was detected in this sample. Balbuena et al. [132] have also shown theoretically that the incorporation of Pd, as well as Ru, into Pt decreases the stability of subsurface oxygen, especially in the case of Ru. These calculations agree with our observation that Pt-Ru contains less PtO than Pt-Pd, and both samples are more reduced in comparison to the monometallic Pt sample.

As seen in Figure 33(d), the Ru-3d region overlaps with the C-1s region. However, upon deconvolution of the monometallic Ru spectrum (bottom) we uncover two states of oxidation, $Ru^{6+}$ ($RuO_3$) at ~283 eV and $Ru^{4+}$ ($RuO_2$) at ~281 eV The peak at ~289 eV is a peak visible in the NP-free substrate ($ZrO_2$) spectrum and is attributed to a carboxylic species [326]. Analysis of the Pt-Ru sample (top) reveals the disappearance of the $RuO_2$ component (present in the monometallic Ru sample) at ~281 eV, and only the $RuO_3$ (~ 283 eV) remains. According to the literature [311] $RuO_2$ should be the most stable oxide. However, analogous to the above discussion concerning Pt-Fe, the combination of Pt-Ru/$ZrO_2$ seems to favor the higher state of oxidation for Ru and possibly promotes the reduction of Pt.

From Ref. [131] we expect the surface atoms to be ~15 % of the total number of atoms. Although it is possible for our $Pt_{0.8}M_{0.2}$ systems to form core-shell structures, the presence of $PtO_x$ in all our samples leads us to conclude that we do not form such clusters.

### 7.2.3 Catalyst Activity

Figure 35 shows the rate of MeOH conversion (in units of μmol of MeOH/min/g·cat) for each bimetallic Pt-M sample in the range of 150-220°C. We mention here that no Pt-M catalysts achieved the same rate as the pure Pt sample which had a rate of ~4.5 μmol of MeOH/min/g·cat at 200°C (not shown). However, the pure Pd sample was comparable to pure Pt with an overall average rate of about 80 % that of Pt, and the monometallic Ru sample was comparable to the Pt-Pd sample shown in Figure 35. The

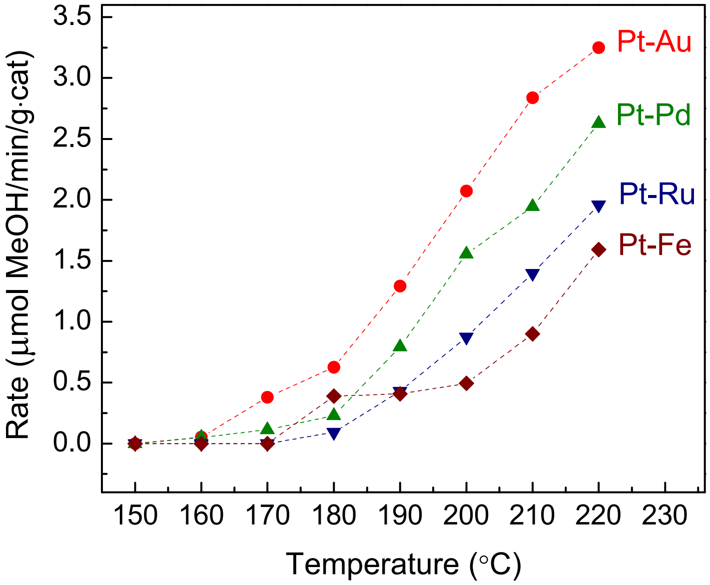

Figure 35 – Rate of MeOH decomposition given in µmol of MeOH/min/g·cat for all bimetallic Pt-M samples in the temperature range of 190-220°C. The monometallic Pt rate was 4.5 µmol of MeOH/min/g·cat at 200°C.

monometallic Fe sample achieved a maximum activity of 31 % that of Pt (220°C) and the monometallic Au sample was not active in this temperature range.

Unexpected results were obtained while monitoring the reactivity of Pt-Ru and Pt-Pd samples. Pt-Ru alloys are generally accepted as being better catalysts than Pt alone, especially for use in fuel cells [323]. It is interesting that our Pt-Ru sample is relatively poor in comparison to our Pt-Au and Pt-Pd bimetallic samples, as shown in Figure 35. This could be due to several factors. First of all, our tests were not done in an electrochemical environment where we might expect reactions to proceed differently than in our gas-phase packed-bed reactor. Waszczuk et al. [327] have also shown that MeOH behaves quite differently in UHV as compared to an electrochemical environment. Similarly, the rate of CO oxidation on Ru is much greater at higher oxygen coverages than under UHV conditions [328] and the selectivity for MeOH oxidation over a Ru catalyst is observed to be significantly different at low and high pressures [329]. Second, the concentration of the secondary metal is important and for Pt-Ru catalysts Pt:Ru concentrations of 3:1 and 1:1 are common [330]. Our Pt-Ru samples are 4:1 (Pt:Ru) and this low concentration of Ru might not be enough for the Pt to benefit from the presence of Ru.

The other point we would like to make note of concerns the Pt-Pd sample. Although both the monometallic Pt and Pd samples show high activity, the bimetallic Pt-Pd sample shows a decrease in activity with respect to both monometallic counterparts. In a recent paper by Zhang et al. [130] it was demonstrated that particles consisting of a monolayer of Pt covering a Pd/Co core showed high activity for $O_2$ reduction. The enhanced activity was partly attributed to lattice mismatch and a change in the d-band properties of Pt caused by interaction with Pd (ligand effect, Chapter 1). In our case we imagine the reverse situation to be the prevailing one, in which Pd is enriched on the surface compared to Pt. It is feasible that the interaction of Pd with the underlying Pt is not as favorable as the geometry of Ref. [130], and that this interaction decreases the Pd activity towards MeOH decomposition. Further studies on this system should be carried out to answer this question.

Figure 36 displays an Arrhenius plot [ln (Reaction Rate) vs. 1/T] for the Pt-M samples in the range of 190-220°C. From this plot, activation energies ($E_a$) for MeOH decomposition can be obtained. The calculated activation energy for the monometallic Pt sample is 28 kJ/mol. The bimetallic $E_a$ values are 59, 73, 96, and 89 kJ/mol for the Pt-Au, Pt-Pd, Pt-Ru, and Pt-Fe respectively.

Figure 37 correlates these data with the phase content (%) of $Pt^0$ (bottom axis) and PtO (top axis) in each Pt-M sample. The elemental labels denote the M in each of the Pt-M nanocatalysts. For the y-axis we have calculated the percent difference of the rate for each

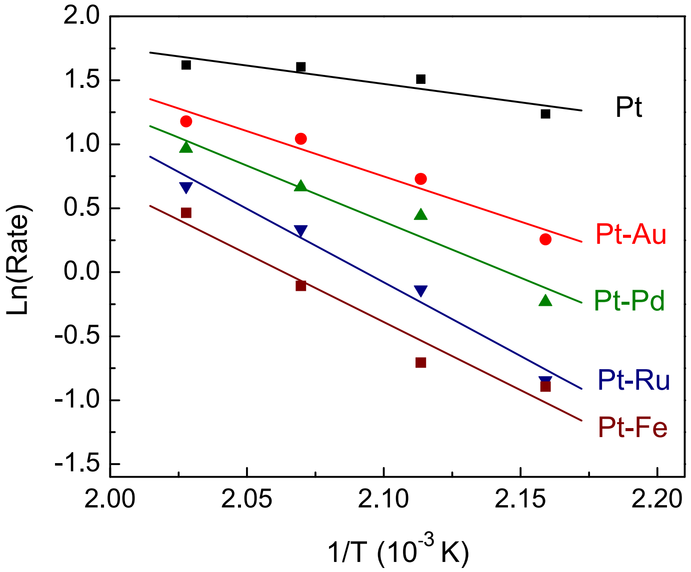

Figure 36 – Arrhenius plot of the methanol decomposition rate [ln(R) versus 1/T] over Pt-M NPs supported on $ZrO_2$.

sample, with respect to the monometallic Pt, at T = 190, 200, 210, and 220°C, and plotted the average as:

$$\Delta R_{Pt}(\%) = \langle \frac{R_{Pt}(T) - R_{Pt-M}(T)}{R_{Pt}(T)} \times 100 \rangle \tag{2}$$

For example, the higher the average percent difference, the lower is the rate of MeOH conversion for a particular sample compared to the monometallic Pt. A clear trend emerges relating increasing amounts of metallic Pt with decreasing catalytic activity, and increasing amounts of PtO with increasing activity. The fits of the Pt-4f spectra in Figure 32 show that only a small amount ($\leq$ 15 %) of $PtO_2$ is present in our samples. Two factors may be discussed in connection with this trend: (i) the concentration of $Pt^0$ and PtO are related to the amount of surface segregation of M, as discussed in the XPS section; and (ii) PtO may play some role in the decomposition of MeOH. We will give only brief comments regarding

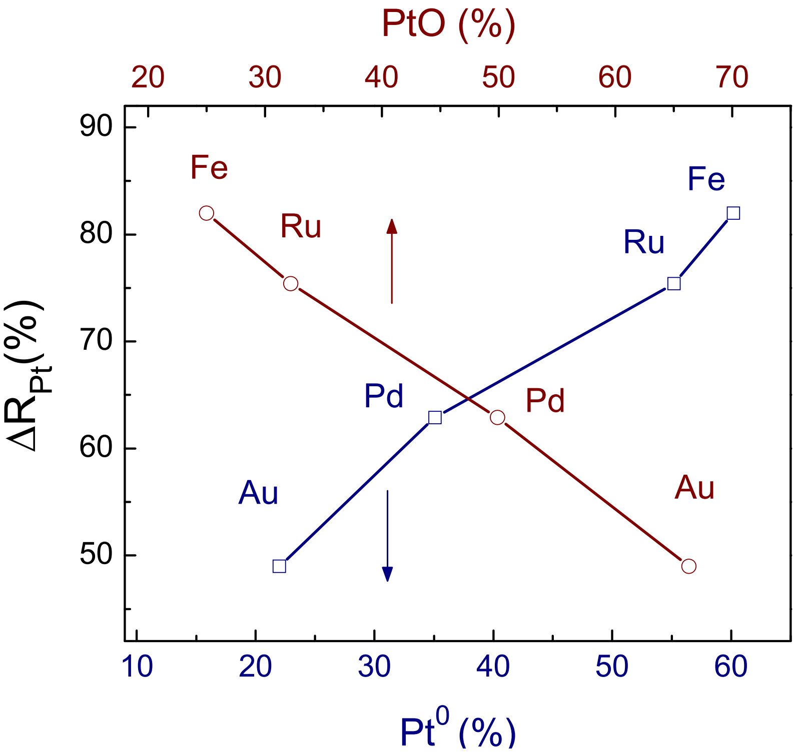

Figure 37 – Relative decrease in activity for Pt-M samples with respect to the monometallic Pt sample. The y-axis gives the average percent difference in the rate of MeOH decomposition in the range of 190-220°C as explained in the text. The bottom and top x-axes relate this decrease to the concentration of $Pt^0$ and PtO respectively. The elemental labels denote the M in Pt-M.

(ii) as a detailed study on the stability of PtO under reaction conditions, and its catalytic reactivity for MeOH decomposition and oxidation reactions, will be presented in Chapter 8 [331].

### 7.2.4 Catalyst Selectivity

Selectivity for each product gas is derived from the mass spectrometer data, along with stoichiometric considerations of the decomposition, water gas shift, and methanation reactions (equations 34-36), and is defined as the percentage of the total product that each particular partial gas pressure represents:

$$Selectivity\,(\%) = \frac{A_n}{\sum A_n} \times 100 \qquad (33)$$

Where $A_n$ represents the output of the $n^{\text{th}}$ product gas.

$$CH_3OH = CO + 2H_2 \tag{34}$$

$$CO + H_2O = CO_2 + H_2 \tag{35}$$

$$CO + 3H_2 = CH_4 + H_2O \tag{36}$$

In the course of our experiments, only $CO_2$ and $CH_4$ were obtained as byproducts and only in small amounts at high temperatures. We can conclude from this that the reaction proceeds mainly through the direct decomposition of MeOH shown in equation (34). It is interesting to note that the Pt reference sample produced $CO_2$ at low temperatures (~2.5 % at 150°C). The amount of water in the experiment was ~0.2 % as compared to the flow of the carrier gas helium, which helps to facilitate reaction (35). This is in accord with the results of Iida et al. [332] who reported high activity for the low temperature water gas shift reaction (WGS) on $Pt/ZrO_2$ catalysts. The authors were using a feed containing an $H_2O$ to CO molar ratio of 5. The amount of water in our experiments is low compared to CO (~27 %) since we are not directly introducing it into the feed, this will limit the occurrence of the WGS reaction in our experiments. None of the other samples showed this behavior for the WGS reaction at low temperatures. Bera et al. [333] have also reported $Pt/CeO_2$ active for the low temperature WGS reaction, with Pt being found mostly in the 2+ state (PtO). One interesting exception is the Ru sample which shows ~1 % selectivity for $CO_2$ close to 300°C. The corresponding Pt-Ru sample shows a switch to small amounts of $CH_4$ at the same temperature.

## 7.3 Further Discussion

### 7.3.1 Stability and Reactivity of PtO

The monometallic Pt sample (Figure 32, Table 5) is composed mainly of PtO ($Pt^{2+}$, 63 %) as well as a fairly large (28 %) contribution from the metallic component ($Pt^0$), with $PtO_2$ ($Pt^{4+}$) being considerably smaller (9 %). The heats of oxide formation of PtO and $PtO_2$ [311] and theoretical calculations [95], indicate that $PtO_2$ should be the more stable oxide. However, possibly due to strong metal-support interactions, previously confirmed for this system [334], PtO is the most prevalent species under our preparation conditions. Interestingly, the most common terminations of Pt NPs are the (111) and (100) planes [335], for which it has been calculated that $\alpha$-$PtO_2$ and PtO, respectively, are the most stable oxide phases [95]. However, new data from Seriani et al. [336] have also shown that $PtO_2$ can be stable on the Pt(100) surface and that $Pt_3O_4$ is also highly stable. Abe et al. [337] have also experimentally observed these phases to be stable up to 500°C and the presence of large amounts of PtO might be related to the structure of our NPs. It has been reported for Pt single crystals that oxides can form at sites of low coordination (i.e. steps) where they are more stable than what is normally expected for bulk oxides [338]. Weaver et al. [82] have also observed enhanced thermal stability of oxides on Pt(111) due to the formation of three dimensional oxide particles accompanied by significant surface restructuring.

It is still not clear, even for bulk systems, which oxide species is the most stable, and NPs complicate the situation further because of their inherent complexity (i.e. high density of low coordinated sites, surface facets with different orientations, etc.) For example, Wang et al. [93] have observed experimentally that the surface oxide species that forms on Pt particles with diameters < 1.3 nm is $PtO_2$, while above 2 nm, as in the case of our particles, PtO is observed. Oxide stability is observed in our bimetallic Pt-M systems with PtO being the most stable $PtO_x$ species.

In Figure 38 we show the Pt-4f core level region of the Pt-Au sample before (bottom) and after (top) reaction with MeOH. The temperature ranged from 100-300°C during the reaction with MeOH, and the total time on-stream was ~8 hours. As we can see from Table 5, this sample is only moderately reduced under our reaction conditions and PtO is highly stable. More extreme $H_2$ reductions were also carried out in our reactor with the same result that the $PtO_x$ compounds could not be fully reduced. These samples were taken from the reactor and transferred in air to the UHV system where we still observed them to be reduced. Thus, complete re-oxidation does not occur during its exposure to air. However, this exposure during transfer is short (< 10 min) and the initial air oxidation occurs at 500°C. In addition to these experiments, preliminary data from *in-situ* XANES measurements (not shown), acquired before and during long exposures (up to 10 hours) of the pure Pt and Pt-Au catalysts to CO at various temperatures (up to 200°C) at BNL, reveal that the initial $PtO_x$ compounds in these samples cannot be fully reduced [339], in agreement with our *ex-situ* measurements of Figure 38. Furthermore, *in-situ* EXAFS data by our group, of similar $Pt/ZrO_2$ NP samples reduced in $H_2$ resulted in similar findings. Several interesting works have been published revealing the importance of oxides in catalytic systems [99-101, 106, 107, 340] which lead to the question of whether or not PtO may play some role in the decomposition of MeOH. For example, in a recent paper by Li et al. [340], DFT calculations show that three-phase boundaries are particularly active sites for chemical reactivity. These boundaries involve the contact of the gas-phase reactants and products with the metallic and oxidized phases of the catalyst. Another example is the adsorption of MeOH on Cu which is greatly enhanced by the availability of oxygen [106], either from the feed gas or from the catalyst due to an incomplete reduction process [107]. Our XPS and reactor data associate increasing activity with increasing concentrations of PtO and the presence and stability of PtO in our catalysts reveal a novel aspect of these systems. However, one should keep in mind that the enhanced reactivity of the bimetallic NPs containing PtO may also be simply due to the higher content of Pt atoms (versus atoms from the less active secondary metal, M) at the NP surface in these samples. Finally, we would like to highlight that the choice of oxide support is crucial in the stability of surface and subsurface oxides on supported metal NPs. For example, our group has observed faster and lower temperature $PtO_x$ and $Au_2O_3$

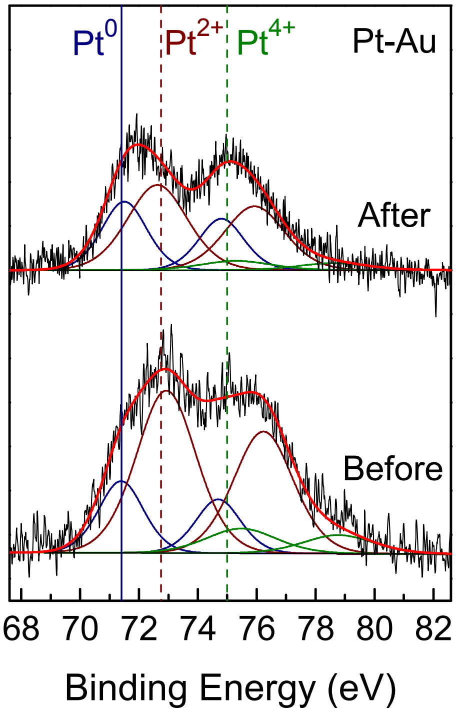

Figure 38 – Pt-4f core level region of the Pt-Au sample before (bottom) and after (top) reaction with MeOH. Temperature during the reaction ranged from 100–300°C with a total time on-stream of ~8 hours.

reductions on pre-oxidized Pt and Au clusters deposited on $TiO_2$ as compared to the higher stability observed when $ZrO_2$ and $SiO_2$ substrates were considered [102, 334].

### 7.3.2 Segregation

Reactor data (Figure 35), in conjunction with XPS (Figure 32) data, lead us to a model of segregation in our Pt-M samples, dictated largely by the affinity of metal M for oxygen. In Figure 39 we present a simplified scheme of this model showing truncated, faceted NPs in contact with the $ZrO_2$ support. The light circles represent Pt atoms and the dark circles represent the atoms of the secondary metal M. The Pt-Au sample, Figure 39(a), appears to be the most homogeneous alloy of all our samples. This is due to a combination of Au's favorable surface segregation (thermodynamic) properties attenuated by Pt's higher affinity for oxygen. The remaining samples have a segregation trend that follows the same line of reasoning, where the expected segregation due to lower surface energy, higher atomic volume, heats of sublimation, etc. are overcome by metal M's favorable interaction with oxygen during the process of sample annealing in air. Figure 39(b) shows the Pt-Pd and Pt-Ru to have a Pt-rich core and Figure 39(c) includes most of the Fe in the Pt-Fe at the NP surface. In addition to this scheme, as previously discussed, there may exist regions or patches of different species ($Pt^0$, $PtO_x$, $M^0$, $MO_x$) in contact with each other at the NP surface. These boundaries may enhance interactions with the gas phase reactants and/or products. Future research on the reactivity of Pt-Oxides in reactions that involve oxygen (e.g. CO oxidation) should provide further insight into some of the challenging, open questions described above.

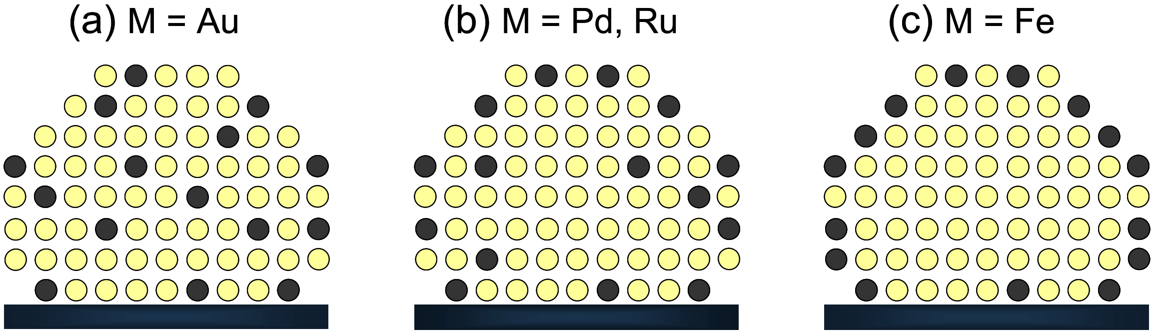

Figure 39 – Simplified cross sectional schematic of surface segregation phenomena in Pt-M alloys where the oxygen affinity of metal M dominates its distribution within the segregation profile. Image (a) represents the homogeneous Pt-Au alloy, (b) Pt-Pd and Pt-Ru, and (c) Pt-Fe. Light circles represent Pt atoms and dark circles represent the metal M.

## 7.4 Conclusions

We have tested a series of monometallic (M) and bimetallic (Pt-M) nanocatalysts for the decomposition of MeOH. All catalysts had the same initial particle size distribution, support, and preparation conditions. We therefore attribute any differences in the properties of these catalysts to the addition of the secondary metals. XPS analysis reveals the most stable component of these systems to be PtO, which proves to be highly stable under our reaction conditions. XPS, in conjunction with reaction data, shows a trend relating the concentration of $Pt^0$ and PtO to the segregation of metal M and subsequent catalytic activity as follows. Because all samples were calcined in air, the metals with the highest affinity for oxygen tended to surface segregate in the Pt-M NPs. This directly affected the NP's catalytic activity by way of metal M's occupation of surface sites available for reaction with MeOH and possibly through its influence on the oxidation state of Pt.

We hope this study will stimulate further theoretical investigations on the effect of the chemical environment on segregation phenomena at the nanoscale, as well as on the activity and stability of Pt-oxides as a function of metal dopants in bimetallic systems.

# CHAPTER 8: EFFECT OF PRETREATMENT AND OXIDATION STATE IN MeOH DECOMPOSITION AND OXIDATION REACTIONS

Jason R. Croy, S. Mostafa, H. Heinrich, and B. Roldan Cuenya

Catalysis Letters 131 (2009) 21

## 8.1 Introduction

In this study we address the open question of Chapter 7; do Pt-oxides play some significant role with respect to catalytic activity in their interaction with MeOH? Micelle-synthesized, monometallic Pt NPs supported on $ZrO_2$ powder were used as catalysts. Specific emphasis has been placed on the pretreatment conditions in order to obtain samples of high purity with narrow size distributions and distinct degrees of oxidation. The effect of the pretreatment conditions on the oxidation state and activity of our micellar Pt NPs has been tested for MeOH decomposition and oxidation reactions. The first part of our discussion will focus on sample preparation/characterization and subsequently on the performance of these samples for MeOH decomposition and oxidation. We are particularly interested in addressing the following specific questions: i) what are the best pre-treatment conditions for optimizing the catalytic performance of micelle-synthesized NPs, ii) to what degree, and under which conditions, are the different oxides of Pt in our systems stable, and (iii) how does the presence of Pt-oxide species affect the reactivity of our $Pt/ZrO_2$ nanocatalysts?

## 8.2 Experimental

Pt NP solutions were synthesized using a PS(27700)-P2VP(4300) polymer loaded with a Pt-salt ($H_2PtCl_6 \cdot 6H_2O$) and a salt/P2VP ratio (r) of 0.3 was used for all samples. The solution was then mixed with nanocrystalline $ZrO_2$ (~45 nm grain size) in the form of a powder resulting in a loading of 1 % wt Pt. The sample was stir-dried in air at ~100°C for 48 hours, after which four different calcination experiments under different gaseous atmospheres were carried out, each utilizing a fresh 110 mg sample of the dried Pt-salt/$ZrO_2$ powder. The four pretreatments were each carried out at 500°C on four analogously prepared fresh samples and included calcination in: i) a flow of $O_2$ for 8 hours, ii) a flow of helium for 8 hours, iii) a flow of $H_2$ for 8 hours, and iv) a flow of $O_2$ for 4 hours followed by a flow of $H_2$ for 2 hours. All flows were 50 ml/min total with the $O_2$ and $H_2$ treatments containing 50 % $O_2$ or $H_2$ respectively, balanced with helium. All gas-flow treatments were done in a packed-bed reactor.

The powder samples were transferred to UHV for analysis by XPS immediately after the different ex-situ pretreatments as well as after exposure to MeOH. XPS data were collected using a monochromatic X-ray source (Al-Kα, 1486.6 eV) operating at 350 W, and a flood gun was used to correct for sample charging during measurements. All spectra were referenced to the Zr-$3d_{5/2}$ [$ZrO_2$] peak at 182.6 eV [303]. The fits of the Pt-4f spectra were done after Shirley background subtraction using asymmetric Gaussian-Lorentzian line-shapes (Casa XPS software). An asymmetry index of 0.2 was obtained for the $Pt^0$-$4f_{7/2}$ in all fits, in agreement with the 0.19 value reported in the literature for bulk Pt-4f [341]. For each spectrum the ratio of the two XPS lines in the Pt-4f spin-orbit coupling doublet (Pt-$4f_{7/2}$ and

$4f_{5/2}$) and their difference in energy were held constant at the theoretical values of 0.75 and 3.3 eV respectively. The spectra were fitted with three doublets corresponding to metallic Pt ($4f_{7/2}$ ~71.7 eV), PtO ($4f_{7/2}$ ~73.1 eV) and $PtO_2$ ($4f_{7/2}$ ~75.3 eV) [202]. The maximum width (FWHM) of each component was held constant [$Pt^0$ (1.6 eV), PtO (1.8 eV), $PtO_2$ (1.9 eV)] from spectrum to spectrum. A tolerance of ± 0.2 eV was allowed in order to account for broadening associated with changing concentrations, for example, after significant reduction of $Pt^{\delta+}$ species. For comparison, the FWHM of our Zr-3d $_{5/2}$ reference peak is ~1.4 eV. This makes the FWHM assignments given above for Pt species reasonable as Pt makes up only 1 % of the total sample weight compared to the $ZrO_2$ support material.

Catalytic decomposition/oxidation of methanol in the vapor phase was carried out in a packed-bed mass flow reactor with a vertical stainless steel tube (inner diameter = 7.4 mm) serving as the reactor vessel. Immediately following the above pretreatments the reactor was flushed with helium and activities for MeOH decomposition and oxidation reactions were measured at atmospheric pressure at a temperature of 260°C (decomposition) and at 260°C and 50°C (oxidation), each for a period of 4 hours. Mass flow controllers were used to flow helium through a stainless steel bubbler (containing MeOH) as well as a bubbler-bypass line which was used to control the concentration of MeOH. The total flow was 50 ml/min resulting in a MeOH flow of 38 μmol/min for decomposition and oxidation reactions. MeOH oxidation was carried out in an excess of $O_2$ with an $O_2$/MeOH ratio of ~2. Reactions were monitored by a QMS. Sixteen different masses were monitored to identify and distinguish reactant and product gases. In order to ensure the reproducibility of the acquired data, each experiment was conducted twice with fresh samples and the average values reported. The experimental error bars displayed correspond to the difference of the reactivity values obtained from the two measurements. For reference purposes, the reactivity of the stainless steel reactor (loaded with the inert quartz wool) was tested within the temperature range of our experiments (≤ 260°C). Under these conditions, a maximum of approximately 3 % MeOH conversion was obtained at 260°C and 50°C for MeOH decomposition and oxidation reactions, respectively.

TEM measurements were carried out on the powder samples with a Tecnai F30 TEM operating at an accelerating voltage of 300 kV. In parallel to TEM studies, the polymer-salt solutions were also dip-coated on $SiO_2$/Si(001) substrates in order to obtain particle size information (height) via AFM.

## 8.3. Results and Discussion:

### 8.3.1 Morphological and Structural Characterization

The morphology of our micellar Pt NPs was studied by AFM. Figure 40(a) displays an AFM image of the NP polymeric solution dip-coated on $SiO_2$/Si(001). Figure 40(b) shows particles after the removal of the encapsulating polymer by and *in-situ* (UHV) $O_2$-plasma treatment. It is clear from these images that our synthesis technique allows for a high level of control and results in Pt NPs having a narrow size distribution. Analysis of the image in Figure 40 (b) gives an average height of 2.1 ± 0.4 nm.

Figure 41 displays high resolution TEM images of our NP samples after annealing for 8 hours in $O_2$ (a-c), helium (d-f), and $H_2$ (g-i). The images in Figure 41(a-f) reveal the presence of crystalline NPs. The average NP diameters obtained by TEM are: 4.2 ± 0.7 (8 hours $O_2$), 4.4 ± 0.7 nm (8 hours He), and 3.3 ± 0.8 nm (8 hours $H_2$). These average particles diameters are about twice the value of those measured by AFM after polymer removal, Figure 40(b). This is evidence that the micelle encapsulated particles form a strong

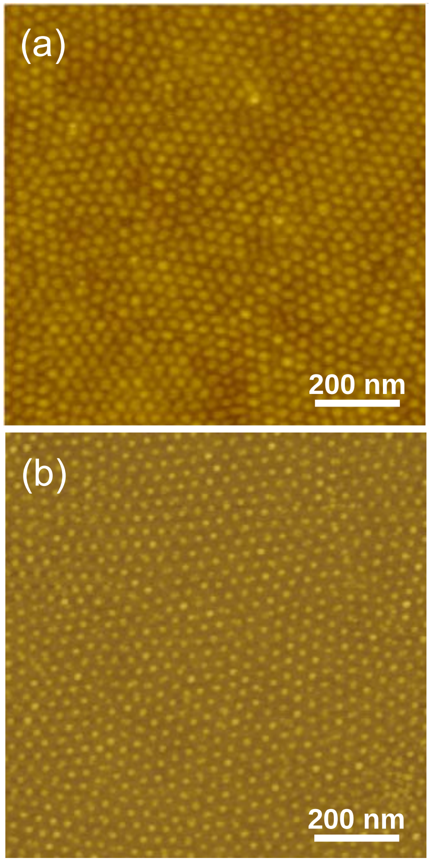

Figure 40 – AFM images of micellar Pt NPs deposited on $SiO_2$/Si(001) taken (a) before and (b) after polymer removal via an in-situ (UHV) $O_2$-plasma treatment.

contact with the $ZrO_2$ support [see region marked by an arrow in Figure 41(e)]. The analysis of high-resolution TEM images of NPs in Figure 41 gives a lattice parameter of ~3.91 ± 0.04 Å for NPs annealed in $O_2$ [Figure 41(b)], and an average value of 3.94 ± 0.04 Å after annealing in He [Figure 41(d), (e) and (f), respectively]. This average value was obtained from two sets of {111} planes and one set of {200} planes. All samples appear to be polymer-free with the exception of the sample $H_2$-treated sample, Figure 41(g-i), where a thin amorphous

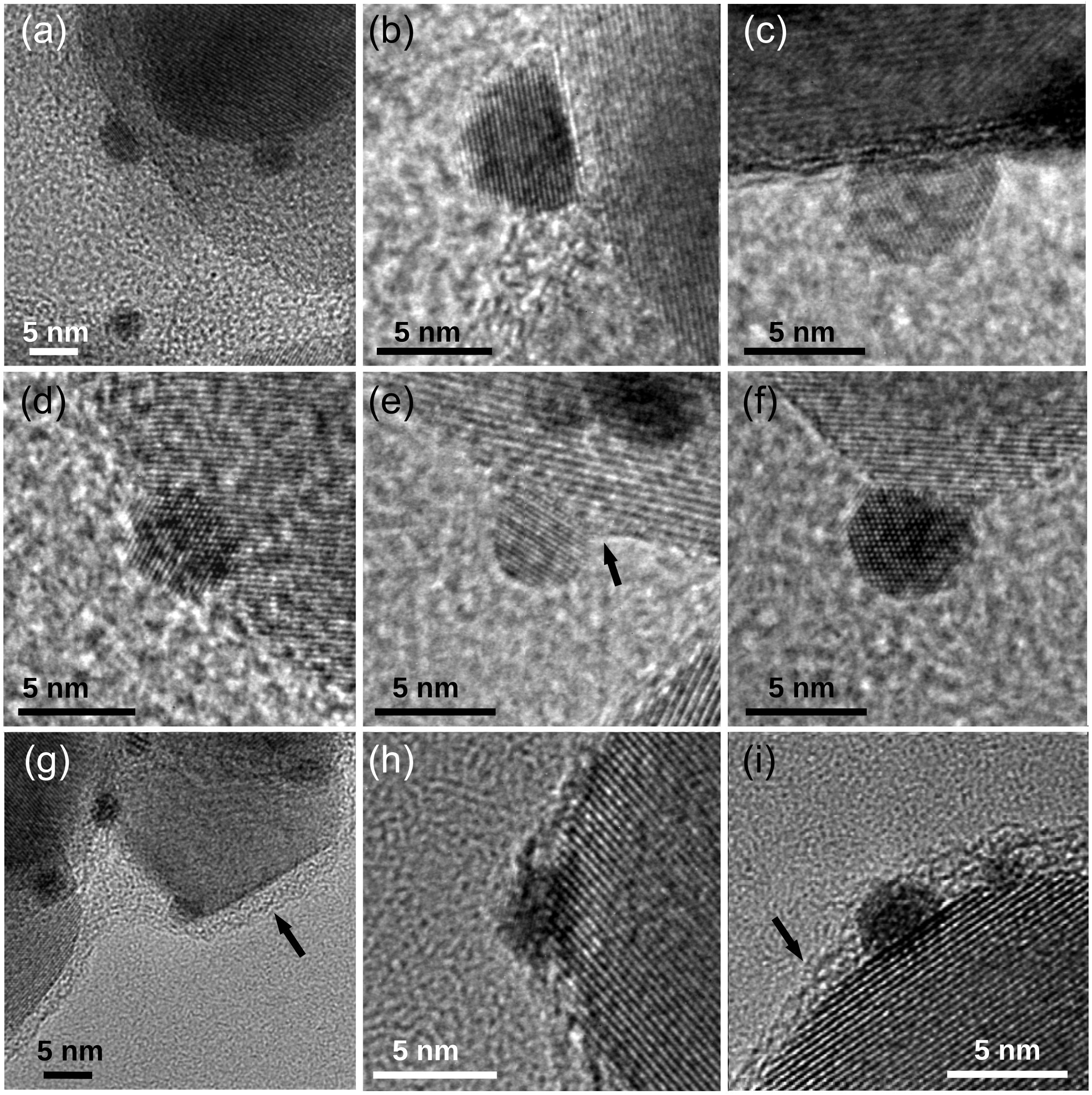

Figure 41 – TEM images of Pt NPs deposited on nanocrystalline $ZrO_2$ powder. (a)-(c) show particles from the sample annealed in a flow of $O_2$ for 8 hours, (d-f) in a flow of He for 8 hours, and (g-i) in a flow of $H_2$ for 8 hours. Images acquired by Prof. H. Heinrich (UCF).

shell enveloping the NPs as well as the $ZrO_2$ support is observed [highlighted by arrows in Figure 41(g,i)]. This observation is attributed to the presence of a residual polymeric shell (C-coating) on this sample. Due to this surface coating, no lattice parameter could be extracted from these images. As will be discussed later, this TEM observation is in agreement with a significant residual C signal in the XPS spectrum of this sample.

## 8.3.2 Electronic and Compositional Characterization

### A) Effect of Sample Pre-treatment

Figure 42 shows XPS spectra from the Pt-4f core level region of the Pt NPs deposited on nanocrystalline $ZrO_2$ powder directly after the different pretreatments but before exposure to methanol. The relative content of the different Pt species obtained from the analysis of the data in Figure 42 are summarized in Table 6. The metallic Pt-4$f_{7/2}$ peak in our Pt NPs is shifted ~0.7 eV higher than the value of bulk Pt [308]. This positive shift may be attributed to final state effects in our small clusters and/or an interaction with the support itself [201]. One possible interaction is the formation of interfacial Pt-Zr compounds. Jung et al. [342] have studied the interfacial properties of $ZrO_2$-supported precious metals using DFT calculations for $Pt_4$, $Pd_4$, and $Rh_4$ clusters on the surface of $ZrO_2$(111). They found the adsorption of Pt to be associated with the largest surface rearrangement and strong Pt-Zr interaction as well as Pt-O bond formation. The same authors also report that oxidation of their clusters increased the metal-support interaction [342]. In addition, their calculations revealed a charge transfer from metal atoms in the clusters to the support and a polarization of the deposited clusters, consistent with our observed positive BE shifts. We also see from the TEM images evidence of this strong particle-support interaction. For example, the He treated sample of Figure 41(e) shows the substrate drawn up and around the perimeter of the NP-support interface (region highlighted by an arrow). In addition, even though our initial encapsulating micelles were spherical, most particles imaged show some degree of flattening and faceting at the support interface after annealing at 500°C as in Figure 41(e), highlighting strong particle-support interactions. However, since the lattice parameter of a

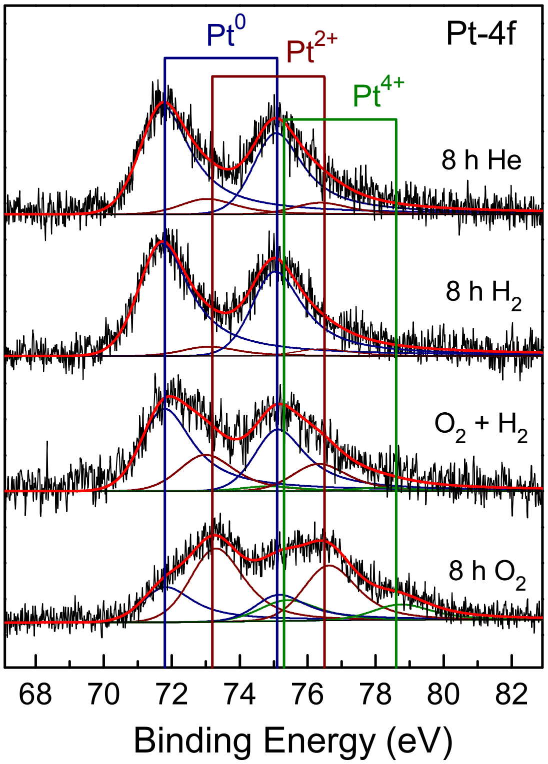

Figure 42 – XPS spectra of the Pt-4f region of Pt NPs deposited on $ZrO_2$ following the different pretreatments as listed on the right hand side of the graph. The vertical reference lines indicate the binding energies of the Pt-4f-doublets of $Pt^0$, PtO, and $PtO_2$ as labeled. Each pretreatment was conducted on a separate, fresh sample.

$Pt_3Zr$ alloy (3.99 Å [343]) is close to that of Pt (3.96 Å), distinguishing pure Pt from Pt-Zr compounds is a difficult task, especially considering our experimental TEM error ~0.04 Å . In addition, much of the alloying is expected to take place at the particle-support interface, and the TEM values that we have obtained (3.91-3.94 Å) were averaged over entire particles.

From Table 6 and Figure 42 we see that the sample treated in a flow of $O_2$ for 8 hours consists of ~25 % $Pt^0$, ~57 % PtO, and ~18 % $PtO_2$ indicating that the dominant component is PtO. We have shown in a previous study (Ref. [344], Chapter 7) that PtO in $Pt/ZrO_2$ NP systems is the preferentially formed oxide, especially in Pt NPs greater than ~2 nm, in agreement with Wang et al. [93]. Furthermore, PtO appears to be stable in this system, and as will be shown below, cannot be completely reduced even under our reaction conditions for MeOH decomposition, as shown in Figure 43.

Table 6 – Relative phase content of the different Pt and Pt-oxide species from the Pt-4f XPS spectra shown in Figs. 42, 43 and 44. This table contains data obtained after different sample pre-treatments and after MeOH decomposition and oxidation reactions.

| **Pre-treatment** | | **$Pt^0$ (%)** | **PtO%)** | **$PtO_2$ (%)** |
|---|---|---|---|---|
| 8 hours $O_2$ | Before MeOH | 25.2 | 57.2 | 17.6 |
| | After MeOH decomposition | 86.8 | 13.2 | 0 |
| 4 hours $O_2$ | Before MeOH | 24.3 | 55.6 | 20.1 |
| | After MeOH oxidation, 50°C | 25.0 | 56.3 | 18.7 |
| | After MeOH oxidation, 260°C | 32.9 | 41.9 | 25.2 |
| 4 hours $O_2$ + 2 hours $H_2$ | Before MeOH | 63.8 | 31.7 | 4.5 |
| | After MeOH decomposition | 88.7 | 11.3 | 0 |
| | After MeOH oxidation, 50°C | 65.6 | 29.0 | 5.4 |
| | After MeOH oxidation, 260°C | 62.3 | 31.7 | 6.0 |
| Reduction in MeOH | After MeOH oxidation, 50°C | 90.0 | 10.0 | 0 |
| 8 hours He | Before MeOH | 86.6 | 13.4 | 0 |
| | After MeOH decomposition | 93.9 | 6.1 | 0 |
| 8 hours $H_2$ | Before MeOH | 90.9 | 9.1 | 0 |
| | After MeOH decomposition | 94.3 | 5.7 | 0 |
| | Before MeOH, after 48 hours air | 83.6 | 12.6 | 3.8 |

The possibility of detecting $Pt^{2+}$ and $Pt^{4+}$ species by way of chlorides (residues from the $H_2PtCl_6$ salt in the NP preparation) instead of Pt oxide formation has been considered. If stable, such species would show XPS peaks at ~73.6 eV and ~75.5 eV for the $4f_{7/2}$ of $PtCl_2$ and $PtCl_4$ respectively [202] , which are similar values to the PtO and $PtO_2$ BEs. Unfortunately, the main XPS peak for Cl (2p) resides at ~200 eV, a BE where the $ZrO_2$ support also shows a feature, rendering the identification of residual Cl in the $Pt/ZrO_2$ samples difficult. However, the absence of Cl in our samples after all the different annealing treatments at 500°C can be concluded based on: (i) the lack of a Cl signal in analogous micellar Pt NPs deposited on $TiO_2$, $Al_2O_3$, $CeO_2$, and $SiO_2$ (where the support does not

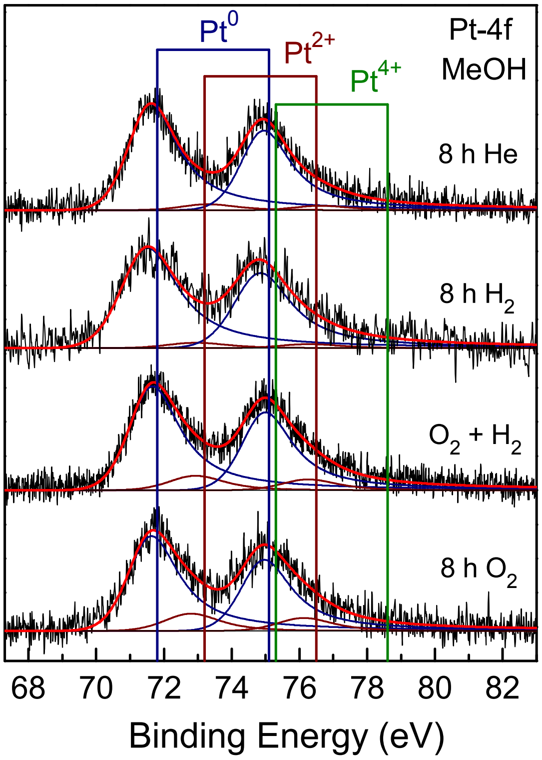

Figure 43 – XPS spectra of the Pt-4f region of Pt NPs deposited on $ZrO_2$ following the different pretreatments indicated on the right-hand side and subsequent reaction with MeOH at 260°C for 4 hours. The vertical reference lines indicate the BEs of the $4f_{7/2}$ peaks of $Pt^0$ (solid line), PtO (dashed line), and $PtO_2$ (dashed line). Each pretreatment and reaction was conducted on a separate, fresh sample.

show an XPS peak in the Cl-2p region) after annealing at 500°C [300, 334], and (ii) the fact that the high BE Pt-4f peaks are present on the samples annealed under an oxidizing environment ($O_2$).

The samples annealed in flows of $H_2$ and helium are considerably reduced and consist of mainly metallic Pt, with both samples reducing to ~90 % $Pt^0$. Furthermore, there seems to be a limit of reducibility for our samples (~90 % $Pt^0$), since complete reduction was not observed even after MeOH exposure in decomposition reactions at 260°C, Figure 43 and Table 6. The 10 % content of Pt oxides present in these samples is assigned to stable Pt-O-Zr species at the $Pt/ZrO_2$ interface. Interestingly, once our samples had been reduced ($H_2$ treatment), a subsequent air exposure for 48 hours resulted in minimal re-oxidation (from ~94 % to 84 % $Pt^0$). This experiment also corroborates that our *ex-situ* XPS data are not significantly affected by the short transfer time (~15 min) which takes place after calcination and/or reaction between the pre-treatment chamber (mass flow reactor) and the surface analysis UHV system. In addition, recent EXAFS data acquired on our $Pt/ZrO_2$ samples also verify the observation of a stable $PtO_x$ compound.

### B) Stability of Pt Oxides

We have investigated by XPS the stability of Pt oxides in our $Pt/ZrO_2$ nanocatalysts after direct MeOH decomposition (Figure 43) and MeOH oxidation (Figure 44) reactions. We can see from the analysis given in Table 6 that the $Pt^{4+}$ ($PtO_2$) component has been completely reduced in all samples after direct methanol decomposition, Figure 43. However, as seen in Figure 42 and Table 6, even reduction in a flow of $H_2$ does not completely eliminate PtO from these catalysts (~9 %). A possible explanation for the stability of this oxidized Pt species is the strong interaction between Pt atoms at the interface of the NPs and the $ZrO_2$ substrate as discussed above. Nagai et al. [345] have recently shown the importance of the Pt-O-support bond strength in the re-dispersion of agglomerated Pt-based automotive catalysts. Here, the mobility of Pt and Pt oxide species, dictated by the choice of support, leads to the possibility of catalyst regeneration and increased lifetime. $PtO_x$ species that form on large, sintered particles become mobile and can re-disperse over the surface where they are stabilized because of the strong interaction between Pt and the support [345]. Another possibility for the incomplete reduction of oxides in our NPs is the presence of subsurface as well as surface oxide species. Surface oxide species may be more easily decomposed upon gas exposure whereas subsurface components can remain stable, especially when deposited on non-reducible oxides [102]. Yazakawa et al. [346] have also noted that Pt supported on $ZrO_2$ is difficult to reduce when compared to other supports which are more acidic (i.e. $SiO_2$-$Al_2O_3$). The authors also reported that the stability of these oxides is responsible for the inferior performance of their Pt/$ZrO_2$ catalyst in the combustion of methane as compared to more easily reducible systems. In addition, it should be noted that even though our oxidized Pt species were formed upon annealing in an oxygen-rich environment at 500°C, our experimental reaction temperature of 260°C during MeOH exposure is relatively low, and significant thermal decomposition of our oxides is not expected under these circumstances. For example, TPD studies of pre-oxidized Pt(111) surfaces utilizing an atomic oxygen beam revealed $O_2$ desorption features at temperatures as high as 500°C [82].

From Table 6 we see that after MeOH decomposition reactions most samples reduce to fairly similar final states, with ~5-13 % PtO detected after MeOH exposure at 260°C. Our

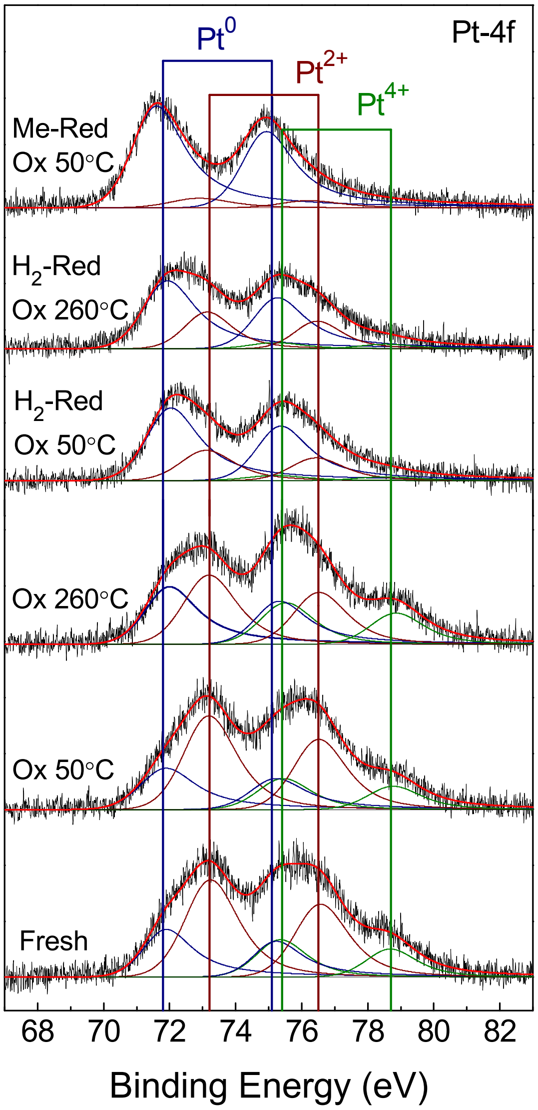

Figure 44 – XPS spectra of the Pt-4f region of Pt NPs deposited on $ZrO_2$ following the different pretreatments listed on the left hand side of the graph and subsequent MeOH oxidation. The vertical reference lines represent the Pt-4f-doublets of $Pt^0$, PtO, and $PtO_2$ as labeled. Each pretreatment and reaction was conducted on a separate, fresh sample.

MeOH decomposition experiments result in the catalysts being exposed to MeOH at 260°C for four hours followed immediately by XPS measurements. In order to further investigate the stability of Pt oxide species in our samples during direct methanol decomposition, a test was conducted in which a sample was exposed to MeOH at 260°C for only a short time interval (10 min) followed immediately by XPS measurements. For this test a new sample was prepared by pre-treating it with $O_2$ for four hours at 500°C (for polymer removal and oxidation), and then exposing it to MeOH from room temperature up to the reaction temperature of 260°C with a heating ramp of 8°C/min. Our XPS data (Figure 45) shows that this sample was also reduced to a maximum value of ~90 % $Pt^0$. This is evidence that the oxides in our samples are not chemically stable under MeOH exposure and reduce rather quickly, most likely due to the presence of CO upon MeOH decomposition. This idea is supported by the detection of $CO_2$ in all MeOH decomposition experiments as will be noted in the reactivity section. Similar observations were also made for thin films of oxidized Rh exposed to MeOH at 200-350°C [347].

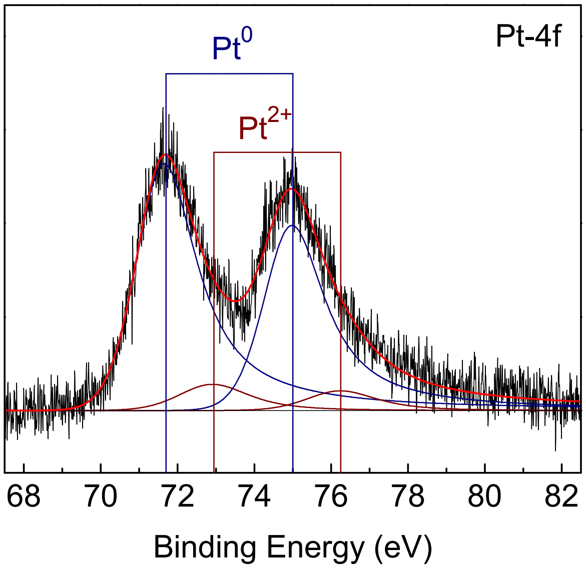

Figure 45 – XPS of the Pt-4f region of a Pt/$ZrO_2$ sample exposed to MeOH from RT up to the reaction temperature of 260°C with a heating ramp of 8°C/min. The initial state of this sample corresponds to the fresh, highly oxidized sample shown in Figure 44 (bottom).

The stability of Pt oxide species during MeOH oxidation reactions was also evaluated. Different sample pretreatments were carried out on a second batch of samples, before MeOH oxidation, in order to obtain samples with different contents of $Pt^0$ and Pt-oxides (Table 6). The treatments included: i) $O_2$ annealing for 4 hours at 500°C (polymer removal) plus $H_2$ reduction at 500°C for 2 hours, ii) $O_2$ annealing for 4 hours at 500°C plus reduction via the decomposition of MeOH at 260°C for 4 hours (as shown in Figure 43 and Table 6), and iii) $O_2$ annealing for 8 hours at 500°C. Figure 44 shows XPS of the Pt-4f core level region for these $Pt/ZrO_2$ samples before (bottom spectrum, 4 hours $O_2$ treatment only) and after MeOH oxidation reactions at 50°C and 260°C. Table 6 gives the corresponding results of the XPS analysis. The spectrum of the as-prepared sample (annealed for 4 hours in $O_2$) indicates that this sample is highly oxidized and Table 6 shows that it contains oxide concentrations analogous to the sample treated for 8 hours in oxygen shown in Figure 42. This suggests that a limit to the oxidation of these particles under our conditions has been reached after four hours. Contrary to the results displayed in Figure 43, where all samples appeared mainly reduced after MeOH decomposition reactions, Figure 44 indicates that simultaneous exposure of oxidized NPs to MeOH and $O_2$ at 50°C does not result in the reduction of $Pt^{\delta+}$ species. Nevertheless, when the MeOH oxidation temperature was increased to 260°C, a small decomposition (~14 %) of the PtO component was observed. From these data we see that both samples remain in highly oxidized states after reaction. These results are opposite for the case of MeOH decomposition reactions in which the oxides were found to be chemically unstable. In the presence of oxygen the oxides of Pt remain relatively stable at least up to 260°C during MeOH oxidation. Wang et al. [348] have also reported a slight stabilization of $AgO_x$ species under MeOH oxidation conditions.

The two samples that were reduced in $H_2$ and subjected to MeOH oxidation at 50°C and 260°C did not display changes with respect to their oxidation state after reaction, Table 6. The same applies to the sample reduced during MeOH decomposition and subsequently exposed to MeOH and $O_2$ at 50°C, Table 6. All three samples contain mainly metallic Pt, although none of our samples were found to completely reduce under any of our reaction conditions. We note here the possibility that highly active sites on the surface of our NPs may be prone to rapid re-oxidation upon air exposure, therefore, even though transfer times are less than 15 min, this process cannot be ruled out as responsible for the small Pt oxide contents detected on the $H_2$ and MeOH reduced samples. However, as we will see in Chapter 9, it is possible that XPS is not sensitive to such small concentrations of dilute oxides.

### 8.3.3 Reactivity

#### A) MeOH Decomposition: Activity and Selectivity

Figure 46 shows the rate of MeOH conversion at 260°C for differently treated $Pt/ZrO_2$ samples (left axis) as well as the Pt-free $ZrO_2$ support (right axis) given in μmol(MeOH)converted/s/g·Pt. Conversions listed are at the beginning of each reaction run, however, no significant deactivation was found for these samples. The main products observed for all $Pt/ZrO_2$ samples were CO and $H_2$ indicating the direct decomposition of MeOH given by:

$$CH_3OH \Leftrightarrow CO + 2H_2 \tag{37}$$

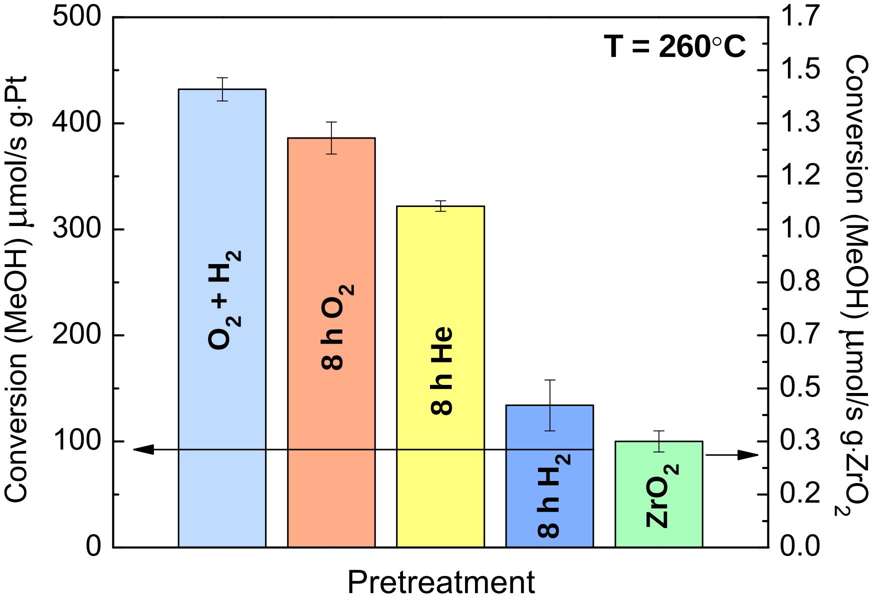

Figure 46 – Rate of MeOH decomposition at 260°C for all Pt/$ZrO_2$ samples (left axis) as well as the Pt-free $ZrO_2$ support (right axis) given in µmol(MeOH)/s/g·Pt. Pretreatments applied to each sample are listed on the graph. Each pretreatment and reaction was conducted on a separate, fresh sample.

The Pt-free $ZrO_2$ substrate, after a 4 hour pretreatment in $O_2$, was found to give ~5 % conversion at 260°C with small amounts of CO, $H_2$, $CO_2$, methyl formate ($HCOOCH_3$), and water as products. All Pt/$ZrO_2$ samples showed small amounts of $CO_2$, which might be attributed to reactions occurring at the $ZrO_2$ support, to the water-gas-shift (WGS) reaction, and/or to the reduction of Pt-oxides by CO in the case of pre-oxidized samples. The low levels of $CO_2$ detected make a deconvolution of these processes difficult.

The addition of Pt to the $ZrO_2$ support almost eliminated completely the production of methyl formate at 260°C in all samples. Instead, methyl formate was detected at low temperatures, (~100°C) prior to reaching the target temperature of 260°C, at which point only trace levels of this gas could be observed.

It can be seen from Figure 46 that the $H_2$ treatment leads to a sample having the lowest activity for MeOH decomposition. This is attributed to the insufficient removal of the encapsulating polymer, as evidenced in the TEM images of Figure 41(g-i), resulting in a contaminated catalyst surface before MeOH exposure. Figure 47 shows XPS spectra of the C-1s core level region of our NPs before (solid curves) and after (open symbols) MeOH decomposition reactions. The arrows labeled $C_p$ span a range of energies representative of carbon associated with the polymer used in the synthesis of the NPs [71]. The dashed lines represent CO bound to Pt in bridged and linear configurations at 285.6 eV and 286.3 eV respectively [349]. Before reaction (solid curves) all samples except the $H_2$-treated sample show negligible amounts of carbon, with a very broad peak (low intensity) around ~285.2 eV. This energy is typical of adventitious carbon. The $O_2 + H_2$ sample shows the lowest C signal before the reaction with MeOH, while a clear C peak was observed on the $H_2$-treated sample before reaction, Figure 47 (top solid curve). Considering the range of binding energies taken up by polymeric carbon ($C_p$), we assign the large C signal of the latter sample to an insufficient removal of the polymeric shell from our NPs. This indicates clearly that annealing in $H_2$ is not an efficient way of cleaning micelle-synthesized NPs, and that the amorphous layer covering this sample observed in the TEM images of Figure 41(g-i) is certainly of carbonaceous origin. In this case, hydrogen can react with O and N in P2VP suppressing the reactions between N and O with C, and leading to an incomplete removal of polymer-related carbonaceous species.

Figure 46 and Table 6 might suggest that an increased presence of Pt-oxides in the $O_2$ exposed samples could be responsible for improved reactivity. However, an additional test was conducted on our samples consisting of a $H_2$ pretreatment (2 hours at 500°C) after

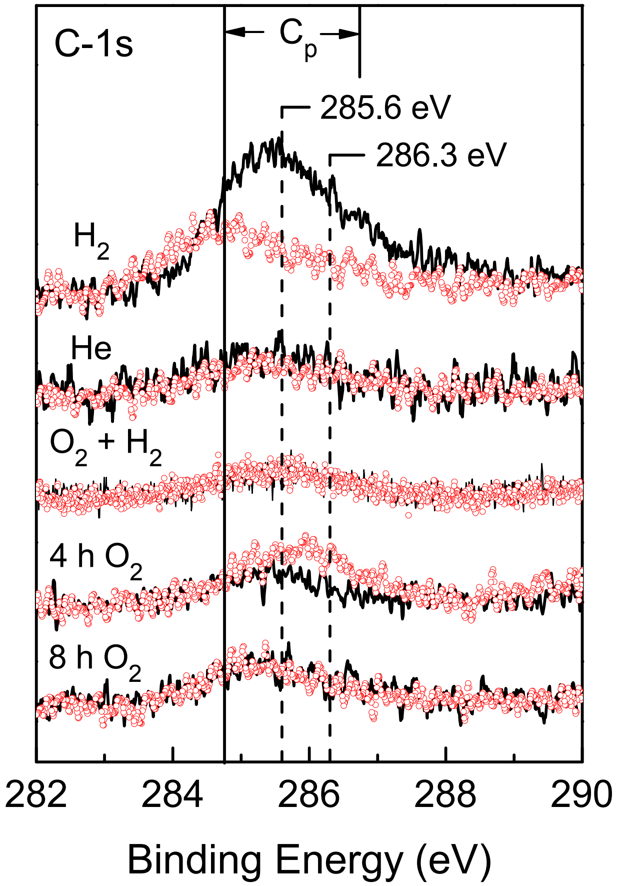

Figure 47 – XPS spectra of the C-1s region of all samples before (solid lines) and after (open symbols) reaction with MeOH. $C_P$ is a range of binding energies where C associated with polymers used in the NP synthesis may be found. The dashed lines represent CO bound to Pt in bridged and linear configurations at 285.6 eV and 286.3 eV respectively. The pretreatments applied to each sample are listed along the left hand side of the graph. Each pretreatment was conducted on a separate, fresh sample before interaction with MeOH.

the initial $O_2$ exposure (4 hours at 500°C). Even though the $H_2$ treated sample contained a lower amount of Pt oxides (32 % PtO and 5 % $PtO_2$, Table 6), it turned out to be the most active from the entire series. This result could be due to several reasons: (i) the exposure to $H_2$ induces changes in the structure and reactivity of the NPs, or (ii) once the encapsulating polymer has been completely removed by the $O_2$ treatment, the subsequent $H_2$ exposure serves to reduce the NPs and metallic Pt species are more reactive than oxidized species for the direct decomposition of methanol. The C-1s XPS data in Figure 47 indicate a very small background C signal in this sample, and the spectra acquired before and after MeOH exposure are nearly identical. However, similar results were also obtained on the sample annealed in $O_2$ for 8 hours, indicating that the presence of a lower content of residual polymeric carbon in this sample cannot explain its improved reactivity. With respect to the effect of $H_2$, it has been reported for Pd [350] that the presence of surface $H_2$ enhances the decomposition of methoxy groups, which is regarded as the rate limiting step for MeOH decomposition in several systems including Pd, Cu, and Pt [55, 302, 350-352]. This could explain the superior activity of the $O_2 + H_2$ treated sample. This enhanced activity might also be due to the improved reactivity of metallic Pt, as compared to Pt-oxides, simply due to the $H_2$ reduction process. However, our MeOH-decomposition-ramp experiment (annealing from room temperature to 260°C with a heating rate of 8°C/min) revealed that these samples are already reduced beyond the point of the $H_2$ treated sample by the time we reach the reaction temperature of 260°C. This suggests that it is not just metallic Pt that plays a role in the observed activity of this sample but that $H_2$, on or incorporated into the surface, might also have a positive influence in the decomposition of MeOH. In order to corroborate this point, we tried reducing our samples by a treatment in $O_2$ + He at 500°C, but found that they contain ~25 % less metallic Pt than the $O_2 + H_2$ samples, making a direct comparison of similar systems impossible.

From the above results we can conclude that the oxides of Pt play no significant role in the decomposition of MeOH over these catalysts, as they are chemically unstable in the presence of MeOH at 260°C.

**B) MeOH Oxidation: Activity and Selectivity**

The MeOH oxidation reactions were carried out in an excess of oxygen with an $O_2$/MeOH ratio of ~2 (see eqn. 38) while maintaining a total flow of 50 ml/min (38 μmol/min MeOH) as in the decomposition reactions. For all oxidation reactions $CO_2$ and water are the main products detected suggesting the complete oxidation of MeOH via reaction (38).

$$CH_3OH + \frac{3}{2}O_2 \Leftrightarrow CO_2 + 2H_2O \tag{38}$$

The $ZrO_2$ support (pretreated in $O_2$ for 4 hours at 500°C) shows a conversion of ~27 % with the additional products of methyl formate and dimethyl ether appearing in small amounts. This is in agreement with observations of Hu et al. [353] for $ZrO_2$ supports in their study of supported molybdenum oxide catalysts and is also an indication of zirconia's acid-base properties [354]. All Pt/$ZrO_2$ samples showed 100 % conversion of MeOH when the oxidation reaction was carried out at 260°C accompanied by the disappearance of methyl formate and dimethyl ether.

Figure 48 shows the rate of MeOH conversion in μmol(MeOH)converted/s/g·Pt at 50°C for the different sample pretreatments. We can see that there is virtually no difference in activity, under our reaction conditions, for the oxidized versus the reduced samples, each showing ~93-96 % MeOH conversion at 50°C.

It is interesting that the initial state of the catalyst is maintained for all samples after oxidation reactions, Figure 44 and Table 6. For example, the reduced samples remained reduced while the oxidized samples remained oxidized. For oxidation at 50°C the concentration of Pt species is virtually unaffected, however, for oxidation reactions at 260°C

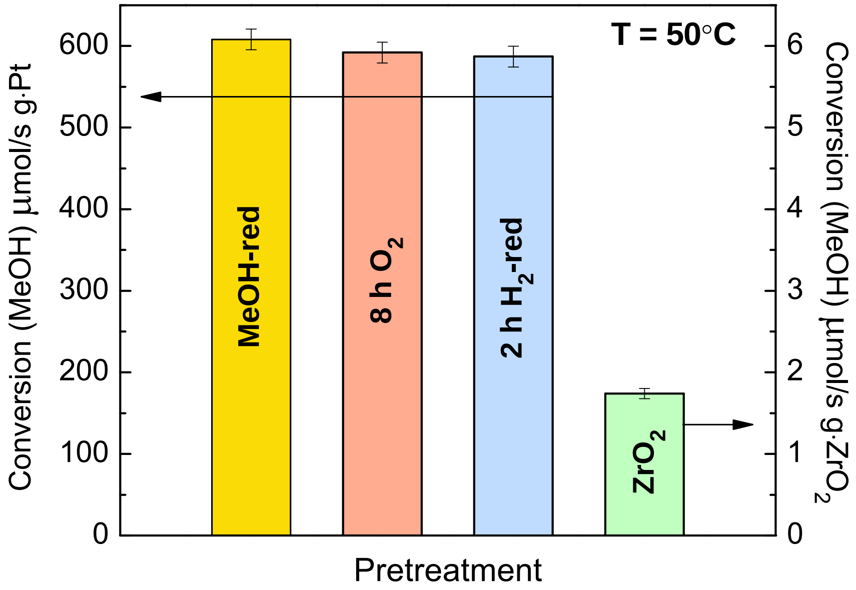

Figure 48 - Rate of MeOH conversion given in µmol(MeOH)converted/s/g·Pt during oxidation reactions at 50°C for the Pt/$ZrO_2$ NPs pretreated in oxygen, and reduced in hydrogen and MeOH. Also shown is the conversion of the Pt-free $ZrO_2$ support pretreated in $O_2$ for 4 hours. Each pretreatment and reaction was conducted on a separate, fresh sample.

we see an overall reduction of the oxides of ~9 % and even a small increase (~5 %) in the $PtO_2$ component suggesting additional oxidation beyond the initial treatment. It has been noted that pure Pb surfaces are quite resistant to oxidation, however, oxide formation can be stimulated by impurities, and once nucleated, PbO can actually catalyze the growth of additional oxides in an autocatalytic process [86]. It has also been shown that a $RuO_2$ film grows autocatalytically on the Ru(0001) surface [355]. A similar situation may exist in our Pt-oxide species dominate the particle composition they may take part in a Mars-van Krevelen-type of process whereby oxygen depleted from the catalyst surface is replenished by gas-phase $O_2$. Support for this mechanism is also evident in the ~90 % reduction of all samples after decomposition reactions with MeOH, i.e. in the absence of gas-phase $O_2$ all samples reduce (Table 6), however, even after oxidation reactions at 260°C the oxides of Pt remain.

## 8.4 Conclusions

The present study highlights the importance that the sample pretreatment has on the removal of residual contaminants from the sample preparation method, the oxidation state, and subsequent reactivity of colloidal (polymeric) Pt NPs. We have demonstrated that micelle-encapsulated Pt NPs supported on $ZrO_2$ can be calcined at 500°C under a flow of oxygen and that such a pre-treatment is highly efficient for the removal of polymeric carbon leading to highly reactive and thermally stable nanocatalysts. Pretreatments in the presence of different gases lead to differing degrees of oxidation with micelle encapsulated NPs forming strong contacts with the $ZrO_2$ support. This latter idea is reinforced by the observed, highly stable Pt-O compounds, most likely at the NP-support interface, which do not fully reduce under our reaction conditions or $H_2$ treatments. In addition, we observe that $O_2$-treated samples exposed to $H_2$ before reaction are the most active for the decomposition of MeOH, likely due to promotional effects of $H_2$ in the decomposition of methoxy species. Nevertheless, $H_2$-induced changes in the NP shape (faceting) might also need to be considered.

The complete oxidation of MeOH takes place over our catalyst in the presence of excess oxygen at 50°C with no appreciable difference in activity for oxidized versus reduced samples and 100 % conversion for all samples is obtained at 260°C regardless of pre-treatment. This is evidence that the oxidized surfaces of our Pt NPs are active for the oxidation of MeOH and reduction pre-treatments commonly reported in the literature may not be necessary. Furthermore, the oxidized surface appears to take part in a Mars-van Krevelen-type of process, exchanging oxygen from the particle's Pt oxide shell with gas-phase $O_2$, allowing it to remain oxidized during/after MeOH oxidation reactions.

# CHAPTER 9: EVOLUTION AND STABILITY OF Pt OXIDES IN SIZE-SELECTED Pt NPs AND BULK Pt(111)

Jason R. Croy, L. K. Ono, and B. Roldan Cuenya

## 9.1 Experimental

Size-selected Pt NPs were obtained by micelle encapsulation using PS(27700)-b-P2VP(4300) for samples #1, #4, and #5, PS(81000)-b-P2VP(14200) for sample #2, and PS(48500)-b-P2VP(70000) for sample #3. The micelles were then loaded with $H_2PtCl_6 \cdot 6H_2O$ having metal-salt/P2VP ratios of 0.3, 0.6, 0.2, 0.6, and 0.3, respectively. The Pt NPs thus obtained were deposited on $SiO_2$/Si(100) by dip-coating the silicon wafers. Morphological characterization was carried out via AFM. The NP's Polymeric shell, due to the synthesis process, was removed by an *in-situ* $O_2$-plasma treatment. Synthesis parameters and AFM heights are listed in Table 7 – Synthesis parameters AFM heights for XPS samples 1-3 and TPD samples 4 and 5.

. In addition to the NP samples, a Pt(111) single crystal was used in the experiments as a bulk Pt reference. Cleaning the crystal consisted of sputtering, annealing in the presence of oxygen (800 K), and annealing without oxygen (1000 K). The process was repeated until no contaminants could be detected by way of XPS.

Temperature-dependent decomposition experiments of Pt-oxide species were carried out by first exposing the samples [NPs and Pt(111)] to an *in-situ* oxygen plasma in order to obtain oxidized Pt species. Second, XPS was carried out for compositional analysis (i.e. $Pt^{\delta+}$ concentrations), and the samples were subsequently heated stepwise from RT to 1000 K. The samples were held at each temperature for 10 min and then cooled quickly under liquid nitrogen flow, after which, XPS data were immediately acquired. Sample heating was done

Table 7 – Synthesis parameters AFM heights for XPS samples 1-3 and TPD samples 4 and 5.

| Sample | PS(x)-b-P2VP(y) | Metal-salt/P2VP ratio (r) | AFM Height (nm) |
|---|---|---|---|
| 1 | x=27700, y=4300 | 0.3 | 1.8 ± 0.4 |
| 2 | x=81000, y=14200 | 0.6 | 3.6 ± 0.8 |
| 3 | x=48500, y=70000 | 0.3 | 6.6 ± 1.3 |
| 4 | x=27700, y=4300 | 0.6 | 3.6 ± 1.0 |
| 5 | x=27700, y=4300 | 0.2 | 1.1 ±0.4 |

using an electron beam heating system, in conjunction with a PID temperature controller, and a linear heating ramp of $\beta$ = 3 K/s. XPS data were collected using a monochromatic X-ray source (Al-K$\alpha$, 1486.6 eV) operating at 350 W. All NP spectra were referenced to the substrate $Si^0$-$2p_{3/2}$ peak at 99.3 eV. The fits of the Pt-4f spectra were done using a Shirley background subtraction and an asymmetric line-shape-function built into the software CASA XPS. The spectra were fitted with three doublets corresponding to metallic Pt ($4f_{7/2}$ ~71.1 eV), PtO ($4f_{7/2}$ ~72.2 eV) and $PtO_2$ ($4f_{7/2}$ ~73.8 eV) [202]. The maximum width (FWHM) of each component was held constant (± 0.2 eV) [$Pt^0$ (1.2 eV), PtO (1.7 eV), $PtO_2$ (1.9 eV)] from spectrum to spectrum for the NP samples. For the Pt(111), the higher intensity of the XPS signal allowed peak widths of ~ 1.0 ($Pt^0$), ~1.3 ($Pt^{2+}$), and ~1.5 ($Pt^{4+}$).

For TPD experiments the samples [NPs and Pt(111)] underwent $O_2$-plasma treatments at RT to generate the initial atomic oxygen coverages for the TPD ramps. To obtain the TPD spectra the samples were placed ~3 mm away from the opening of the QMS and heated at a rate of $\beta$ = 5 K/s (up to the temperatures indicated in the text) while recording the partial pressure of molecular oxygen (m/q = 32). For the Pt(111) single crystal, an atomic oxygen coverage of 0.25 ML appears at ~735 K [76]. This peak was used as the calibration for all calculated coverages ($\Theta$) given as discussed in Chapter 1. In addition, the Langmuir (L) will be used as the unit of exposure. One L is defined as exposure to a gas pressure of 1 x $10^{-6}$ Torr for a duration of 1 second.

## 9.2 Results and Discussion

### 9.2.1 Morphological Characterization

Figure 49 shows AFM images of the three NP solutions [dip-coated on $SiO_2$/Si(100)] used in the XPS experiments after polymer removal by the *in-situ* $O_2$-plasma treatment. We can see from the figure that we have obtained samples with uniform dispersion in both size and surface coverage. Figure 49(a) shows sample #1, the smallest NP solution, with an average AFM height of 1.8 ± 0.4 nm, (b) shows sample #2 with a height of 3.6 ± 0.8 nm, and (c) shows sample #3 with a height of 6.6 ± 1.3 nm.

Figure 50(a)(b) shows AFM images of sample #4 (a) and sample #5 (b) used in the TPD experiments. The images shown were also taken after polymer removal. Figure 50(c)(d) show the corresponding AFM height histograms calculated for samples #4 and #5, respectively. The average NP heights were 3.6 ± 1.0 nm (sample #4) and 1.1 ± 0.4 nm. The images were analyzed with a MATLAB code written by Farzad Behafarid (UCF).

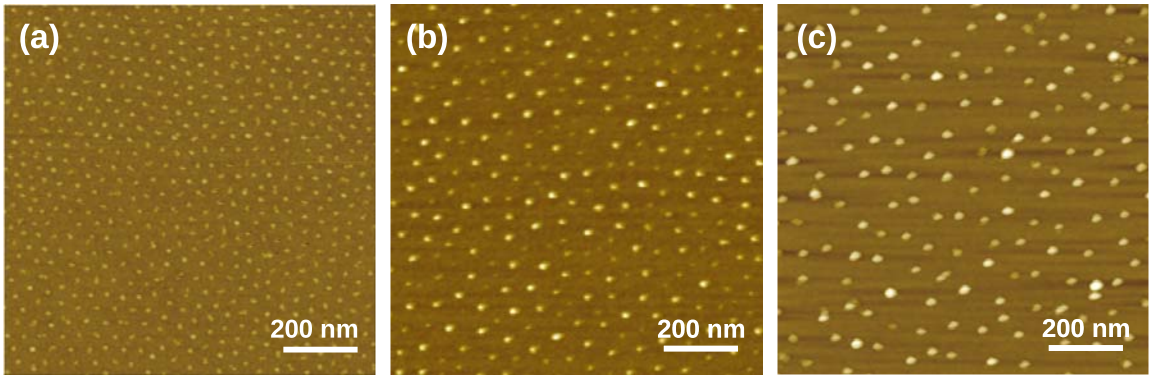

Figure 49 – AFM images of Pt/$SiO_2$/Si(100) after removal of the encapsulating polymers. (a) sample #1 (1.8 nm), (b) sample #2 (3.6 nm), and (c) sample #3 (6.6 nm).

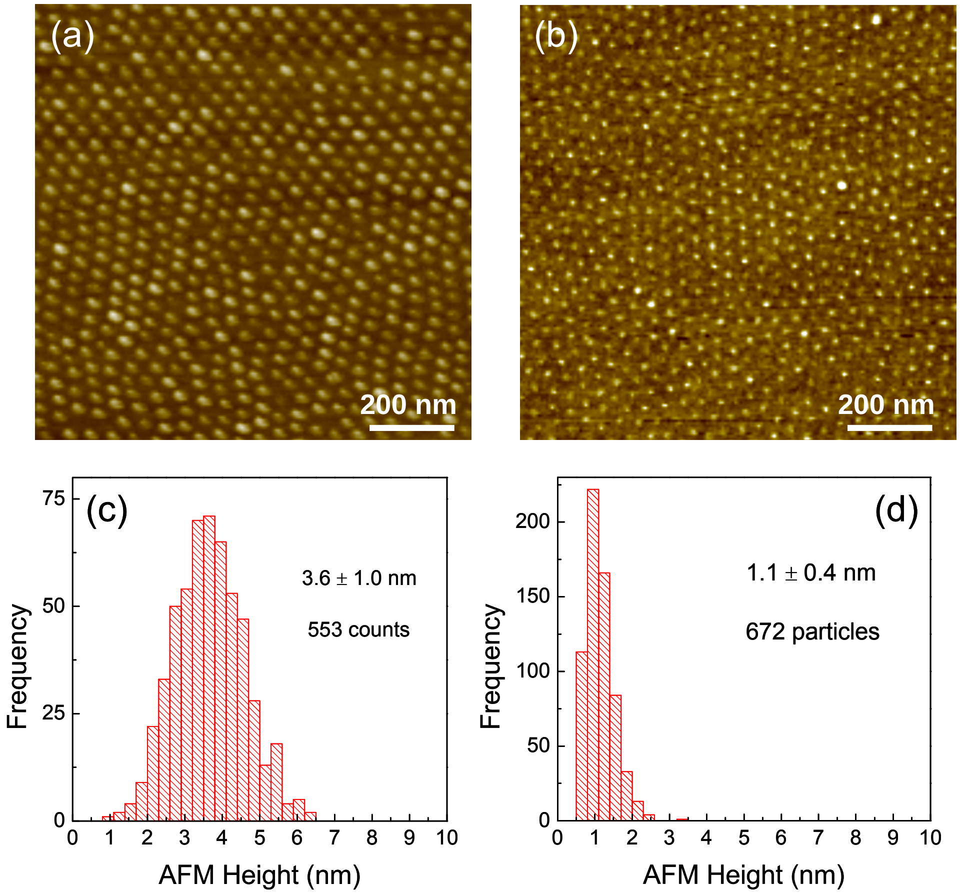

Figure 50 – AFM images of samples #4 (a) and #5 (b) after polymer removal. (c) AFM height distribution for sample # 4 shown in (a). (d) AFM histograms for these samples are shown in (c) sample #4 and (d) sample #5.

### 9.2.2 Stability of $PtO_x$ in Bulk Pt(111) and Pt NPs

#### A. Pt(111)

Figure 51(a) displays XPS data of the Pt-4f core level region obtained from a Pt(111) single crystal after exposure to a RT $O_2$-plasma treatment (4.3 x $10^{-5}$ mbar, 120 min). The identification of PtOx species based on XPS is a challenging task. For example, $Pt_3O_4$ has been reported as a stable Pt-oxide structure [95]. However, the oxidation state of Pt in $Pt_3O_4$

(8/3 +) is higher than in PtO (2+) and lower than in $PtO_2$ (4+). Identifying such intermediates compounds is difficult, especially with the ~1 eV resolution of laboratory XPS such as the one employed in the current study. Considering that $\alpha$-$PtO_2$ should be thermodynamically favored over $Pt_3O_4$ [82, 311], and noting the wide range of BE's reported for Pt-oxides [202], we have assigned the commonly reported PtO and $PtO_2$ species to the oxides in our samples, while remaining aware of other possibilities (i.e. $Pt_3O_4$, $Pt_2O_3$, etc.)[356].

Figure 51(b) shows the corresponding content (%) of each Pt species at every temperature studied. We can see that after $O_2$-plasma exposure at RT we have the formation of $Pt^{2+}$(PtO) and $Pt^{4+}$($PtO_2$) compounds, however, ~50 % of the signal originates from $Pt^0$ [Figure 51(b)]. As the probing depth of XPS is ~10 nm we have some idea as to the extent, or limit, to which the surface has been oxidized under our conditions. Upon heating the sample we see that there is no real, discernable decomposition of the oxides until ~450-500 K. From 500 K to 600 K we see a steady decrease of the $Pt^{4+}$ component accompanied by an increase in the $Pt^{2+}$ and $Pt^0$ components. This suggests that the $Pt^{4+}$ is the least stable compound and decays into $Pt^{2+}$ and subsequently to $Pt^0$. This sequence of stabilities has also

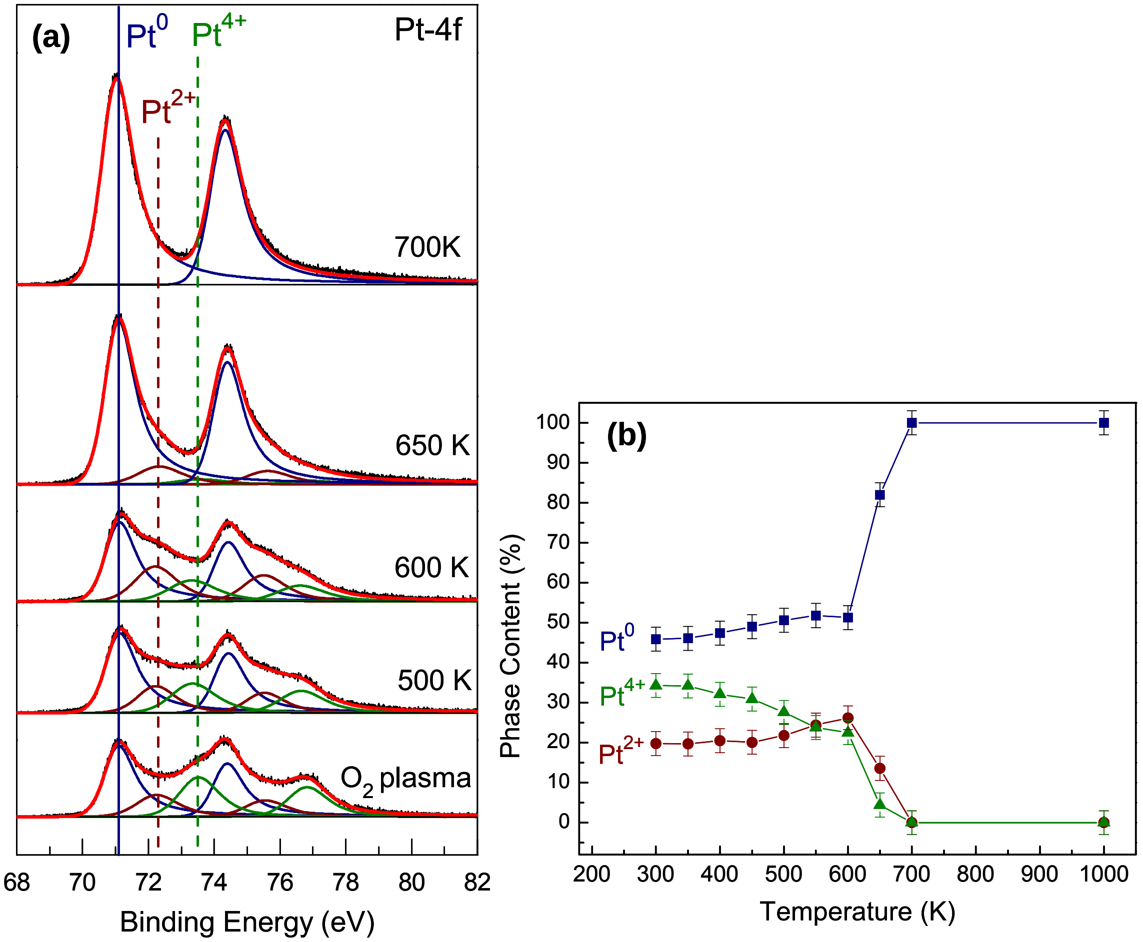

Figure 51 – (a) XPS spectra of the Pt-4f region of a Pt(111) single crystal after atomic oxygen exposure (bottom) and subsequent annealing at the given temperatures. (b) Phase content (%) of each oxide species at every annealing temperature calculated from the data in shown in (a). The vertical lines in (a) mark the positions of the $4f_{7/2}$ peak of metallic Pt (solid line), $Pt^{2+}$ in PtO (dashed line), and $Pt^{4+}$ in $PtO_2$ (dashed line) at the energies given in the experimental section.

been predicted theoretically with $\alpha$-$PtO_2$ → $Pt_3O_4$ (or PtO in our case) → $Pt^0$, and also follows reported heats of formation of bulk Pt-oxides [95, 357] (and Refs. therein). At temperatures above 600 K we see an abrupt decomposition of Pt-oxide species and a complete reduction by 700 K. This abrupt change is consistent with reports by Weaver et al. [82] and Saliba et al. [76], suggesting the decomposition of small Pt-oxide particles formed on Pt(111) surfaces pre-exposed to high oxygen coverages desorbing above ~700 K.

More information may be obtained by looking at the XPS data of Figure 52(a) corresponding to the O-1s BE region of the Pt(111) sample after exposure to the oxygen plasma (bottom curve) and after several subsequent annealing steps. After exposure to atomic oxygen (bottom) it was necessary to include three peaks to fit the spectrum. We have labeled these peaks as species I, II, and III. Qualitatively, charge transfer from Pt to oxygen (i.e. oxidation of Pt) should decrease the BE of O-1s, giving some idea of the relative

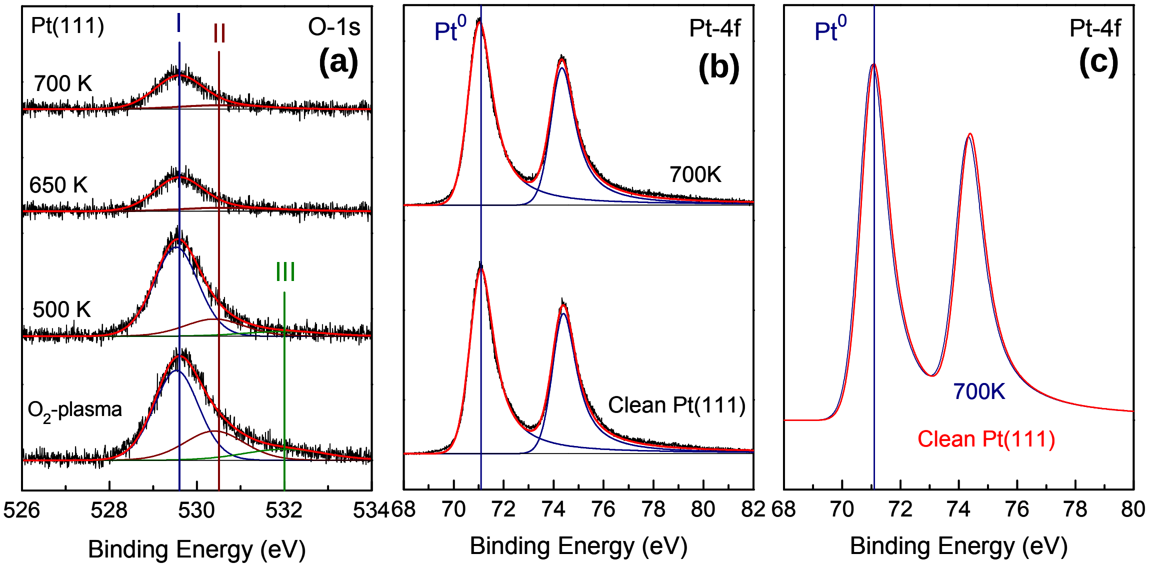

Figure 52 – (a) XPS data from the O-1s region of the Pt(111) single crystal after exposure to an oxygen plasma (bottom) and subsequent annealing at the temperatures indicated. The three solid lines mark the positions of distinct oxygen species as described in the text. (b) XPS spectra from the Pt-4f region of the clean Pt(111) single crystal before exposure to the oxygen plasma (bottom), and after several stepwise annealing treatments up to 700 K (top). (c) The superimposed envelopes of the fitted Pt-4f regions shown in (b).

strength of binding of species I, II, and III. Species I appears at ~529.5 eV and is consistent with atomic oxygen in an O-(2 x 2) chemisorbed overlayer on the Pt(111) surface [74, 358], as will be discussed in the TPD section. Note that this species (I) persists even after the high temperature annealing at 700 K. Evidently this species has no effect on the fit of the Pt-4f region, at least within our error (~± 3 %), as can be seen in Figure 52(b)(c). In (b) we see a comparison of the Pt(111) after several cycles of cleaning and before $O_2$-plasma exposure (bottom) and after RT $O_2$-plasma exposure and subsequent annealing to 700 K (top). In both spectra, the same fitting parameters were used to achieve satisfactory fits. This is shown in (c) where we have overlaid the envelopes of the two spectra. The only distinction is a ~0.1 eV shift of the $Pt^0$-$4f_{7/2}$ peak to lower BE after annealing at 700 K. This shift is also in agreement with reports of an O-(2 x 2) layer on the Pt(111) surface [74], although our estimated error for BE assignments ~0.1 eV. Species II appears at ~530.5 eV and shows the same dramatic decrease in concentration above 600 K as do the PtO and $PtO_2$ species of the Pt-4f region, Figure 51(b). This species (II) persists up to the 700 K annealing temperature, although in small amounts within the ± 3 % error. This BE (530.5 eV) is again consistent with reports of the O-(2 x 2) overlayer, but also PtO and $PtO_2$ species. Component II has been identified as one of two chemisorbed molecular phases of oxygen on Pt(111) [358], the BE of the other molecular phase appears within 0.2 eV of the atomic phase and is therefore nearly indistinguishable from it in Figure 52(a). It is likely that species II in the O-1s region is a convolution of PtO and $PtO_2$, as seen in the Pt-4f region, and a chemisorbed phase of oxygen which is seen in the O-1s region. These three species appear within ~1 eV of each other and cannot be separated in the O1-s region. Species III appears at ~532.0 eV and is absent above 500 K. This BE has been reported as O in $PtO_2$ [202]. However, the binding energy of this component is much higher than the other phases and should represent O atoms having less interaction with the Pt surface (i.e. less charge transfer). Puglia et al. [358] have identified physisorbed states of molecular oxygen on Pt(111) appearing as high as ~539 eV. We therefore assign this component as a weakly interacting form of molecular oxygen, possibly in multilayers, as discussed below in connection with our TPD data.

The above XPS data are evidence that the exposure of Pt(111) to our oxygen plasma has created at least three distinct oxide phases: I) an atomic, chemisorbed overlayer which persists even after high temperature annealing, II) a species with intermediate BE in the Pt-4f region and intermediate thermal stability in both the O-1s and Pt-4f regions; likely a combination of $PtO_x$, and chemisorbed molecular oxygen, and III) a component with high BE in both the Pt-4f and O-1s regions showing the lowest thermal stability, possibly associated with physisorbed molecular oxygen in multilayers.

### B. Pt NPs

Figure 53(a)-(c) shows the XPS data for the 1.8 nm [sample #1, (a)], 3.6 nm [sample #2 (b)], and 6.6 nm [sample #3, (c)] Pt NPs after $O_2$-plasma treatment (bottom) and subsequent heating in UHV. We can see that the data for sample #2 corresponds closely to that of sample #3. Figure 54(a)-(d) shows the corresponding phase content (%) of Pt species at every temperature studied for all samples, including again the Pt(111) for comparison. We can see from Figure 53 that all NP samples start out completely oxidized after the initial $O_2$-plasma exposure (~70%/30% $PtO_2$/PtO). As the XPS probing depth of ~10 nm is larger than the size of our NPs, the lack of a $Pt^0$ component in the Pt-4f region proves that the particles are oxidized throughout their volume. In addition, the BEs of the three species labeled in Figure 53 match very closely those of the same species found on the bulk Pt(111) [$Pt^0$, PtO, and $PtO_2$]. This is evidence that Pt does not interact strongly with the $SiO_2$, inducing BE shifts as is the case with other support materials [300, 331, 334, 344]. At 450 K we see two dramatic changes in the NP samples, Figure 54. First, the metallic $Pt^0$

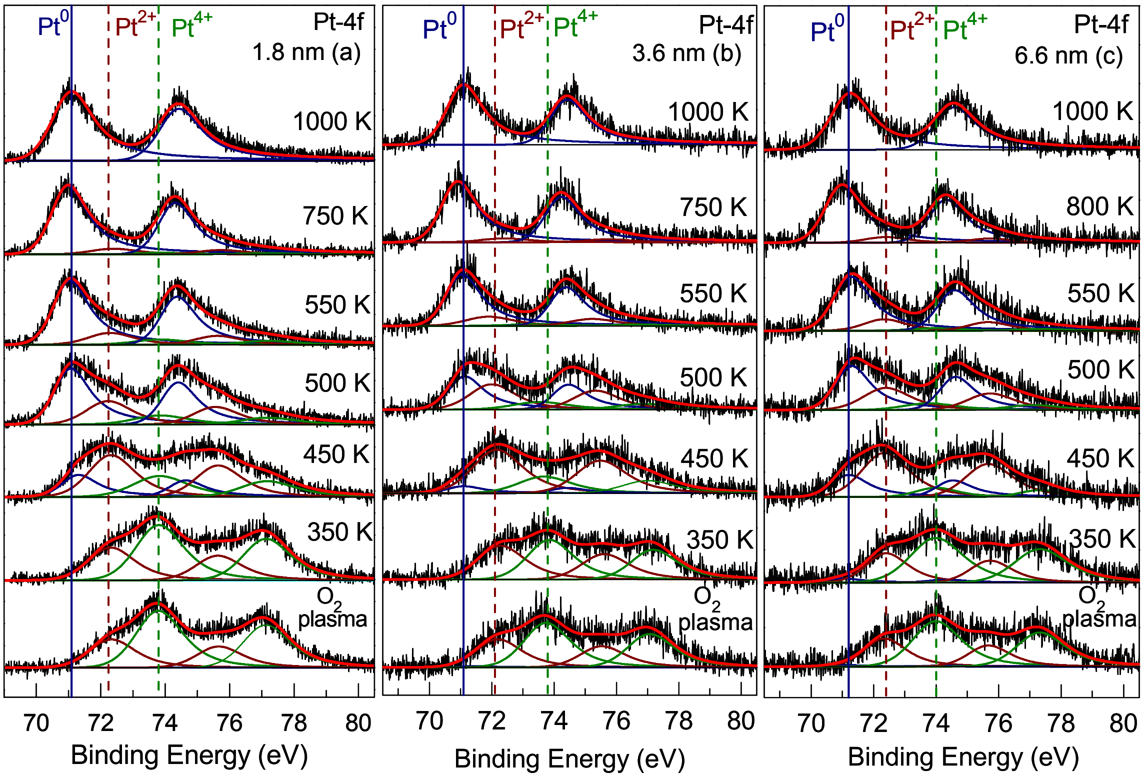

Figure 53 – XPS data of the Pt-4f region of (a) 1.8 nm, (b) 3.6 nm, and (c) 6.6 nm Pt NPs supported on $SiO_2$/Si(100) after exposure to an $O_2$-plasma treatment (4 x $10^{-5}$ mbar for 120 min, bottom curves) and subsequent annealing temperatures as indicated.

component appears in all three NP samples (Figure 53), indicating the reduction of oxide species. Second, there is a difference in the stability of the $PtO_2$ component when comparing NPs of different sizes. Sample #1 (1.8 nm) and #2 (3.6 nm) show a similar $PtO_2$ content of ~30 % and ~25 % at 450 K, respectively. However, for sample #3 (6.6 nm) the $PtO_2$ content at 450 is only 10 %. These data suggest a size-dependent stability of the $PtO_2$ component in the range of ~400-500 K. In each case of oxide decomposition [Figure 54(a)-(d)], the deficit of $PtO_2$ is accompanied by an increase in the PtO component. From RT up to 450 K, The PtO increases while $PtO_2$ decreases, and the metallic $Pt^0$ remains fairly constant. This indicates that PtO is stable up to 450 K on all samples and thereafter the

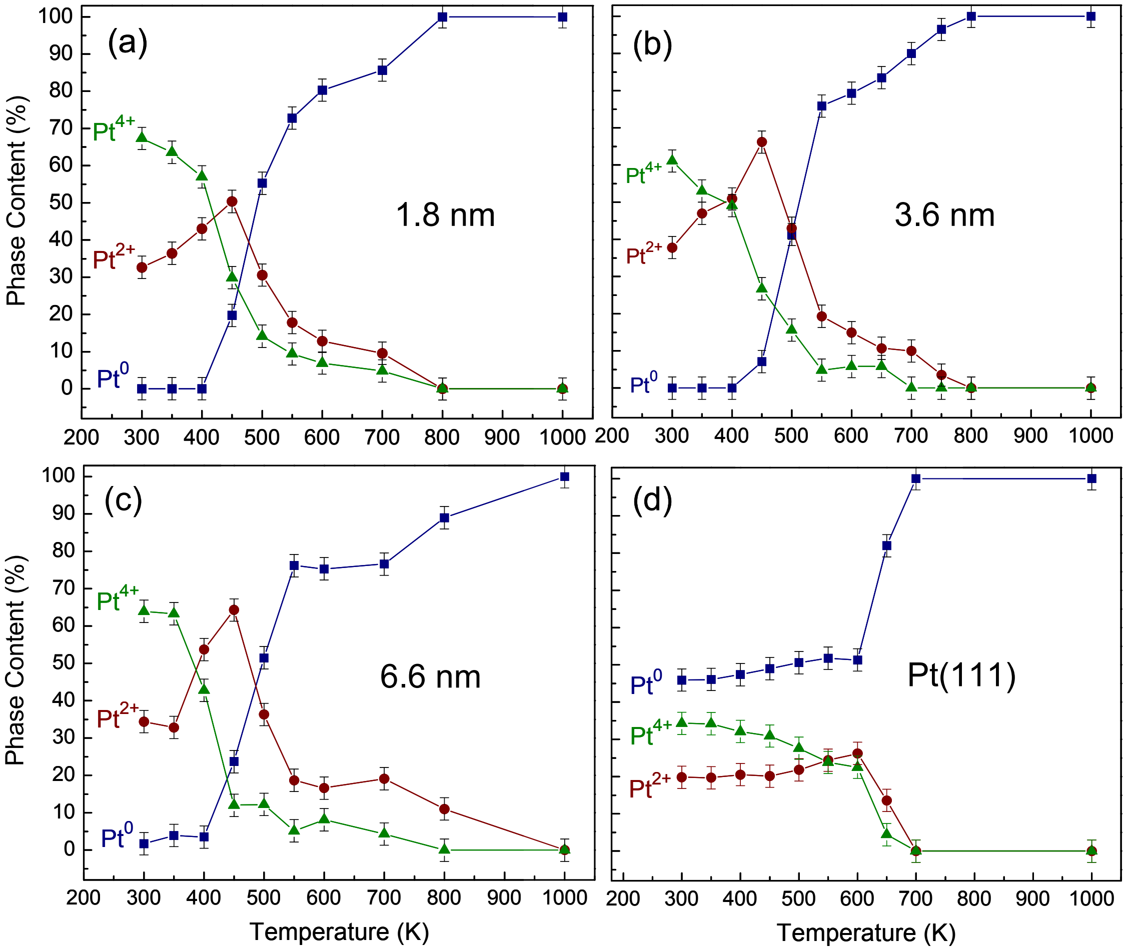

Figure 54 – Phase content (%) of oxide species after each annealing treatment in Pt NP samples #1 (a), #2 (b), #3 (c), bulk Pt(111) reference (d). Phase contents (%) were calculated from the fits in Figure 53.

decrease in its signal is accompanied by an increasing $Pt^0$ content. As with the bulk Pt(111), the sequence of oxide decomposition on the NPs goes as $PtO_2 \rightarrow PtO \rightarrow Pt^0$. Interestingly, at ~750-800 K we observe the same negative shift in BE of the $Pt^0$-$4f_{7/2}$ peak of the NPs; similar to the Pt(111), caused in that case by the O-(2 x 2) overlayer. The peak shifts positively, back to its original position, upon annealing the NPs to 1000 K (Figure 53). We rule out the formation of PtSi based since such a species is expected to appear at high BE (~73.0 eV) [359], which is not observed here. In addition, at the temperatures employed we

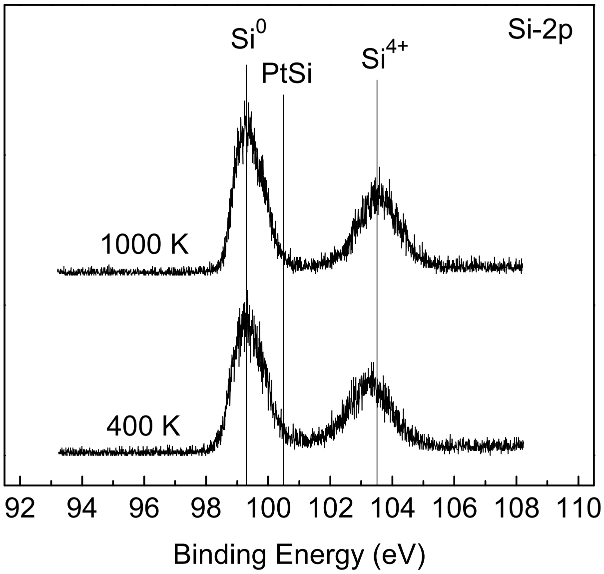

Figure 55 – $SiO_2$/Si(100) substrate of sample #2 (3.6 nm Pt NPs) after $O_2$-plasma exposure and annealing treatment to 1000 K as shown in figure 4. We can see that the $SiO_2$ is present even up to 1000 K and we are not reducing the substrate surface. The three solid lines mark the position of Si in $Si^0$, PtSi, and $Si^{4+}$ in $SiO_2$ as indicated. No component for PtSi (~100.5 eV) is visible.

do not reduce the $SiO_2$ substrate as shown in Figure 55, where a large $Si^{4+}$ peak can still be seen even after annealing to 1000 K. Also marked in Figure 55 is the BE of PtSi in the Si-2p region at ~100.5 eV [202] and we can see that no component appears in this region up to 1000 K. However, we do see a small shift (0.2 eV) to higher BE for the $Si^{4+}$ component when comparing XPS spectra acquired after annealing at 400 K and 1000 K. This might be attributed to changes in the structure of the $SiO_2$ film. The $Si^{4+}$ reference line in Figure 55 marks the most commonly reported value of ~103.5 eV [202], which matches our peak after annealing to 1000 K. Above ~700 K the Pt-4f region is completely void of all detectable oxide species in the bulk Pt(111), whereas the NPs retain some oxides until ~800 K, highlighting the enhanced stability of Pt-oxides on NPs supported on an irreducible substrate.

## 9.2.3 $O_2$ Desorption from Pt NPs and Pt(111)

### A. Pt(111)

Figure 56 shows $O_2$-desorption spectra obtained from the Pt(111) single crystal for the range of oxygen coverages, $0.07 < \Theta < 0.98$ ML. The crystal was oxidized *in-situ* by exposure to an $O_2$-plasma at RT. These data are in good agreement with studies reported in the literature, as discussed in Chapter 1, for $O_2$-desorption from Pt(111) and were repeated

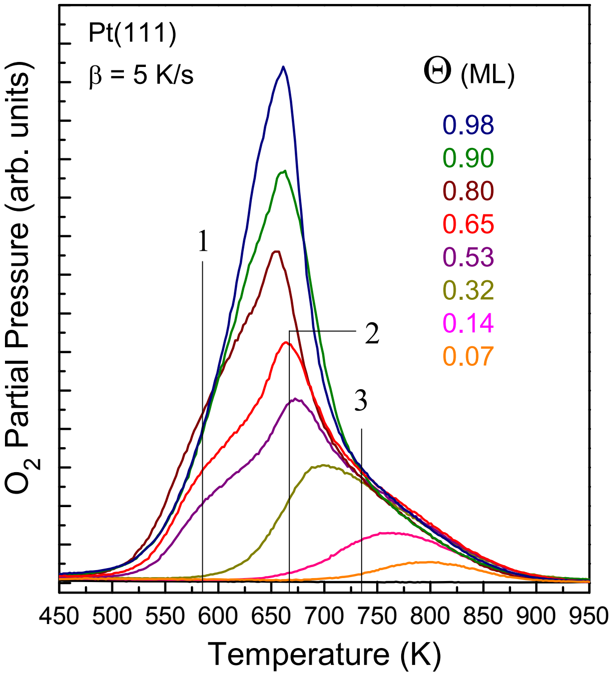

Figure 56 – TPD spectra of $O_2$-desorption from the Pt(111) single crystal after oxygen plasma exposures at RT to generate the listed coverages, Θ.

here as a proof of technique, a bulk reference to our NPs, and calibration purposes. For the Pt(111), a maximum temperature of 1183 K was used for the TPD cycles with a linear ramp β = 5 K/s. Briefly, as discussed above, oxygen sequentially populates 3 distinct states on our Pt(111) surface (see Figure 56). State 3 ($\beta_3$) corresponds to an O-(2 x 2) overlayer and reaches a maximum at ~735 K at which point state 2 ($\beta_2$) begins to appear. Weaver's group [81] has assigned state 2 ($\beta_2$) to the formation of O-(2 x 1) domains. At coverages of ~0.4

ML and above the state 1 ($\beta_1$) begins to appear at low temperatures (~600 K and below) and signifies the formation of Pt-oxide chains and bulk-like $PtO_2$ [81]. In connection with our XPS data in the last section we see that above 700 K only state 3 persists. This reiterates the possibility that the O 1-s BE at ~529.5 eV in our XPS data (Figure 52) corresponds to the O-(2 x 2) overlayer. In addition, the XPS data of Figure 51 reveals that the component assigned as $PtO_2$ is decomposed at temperatures of ~650 K and above. This is consistent with the $\beta_1$ state corresponding to $PtO_2$ as identified by Devarajan et al. [81]. Likewise, the PtO component of Figure 51 is also stable up to temperatures below ~700 K, after which, it is decomposed, in correspondence to the state 2. However, there is no definitive connection between $\beta_2$ and PtO other than its identification as a precursor to the formation of $PtO_2$, and its temperature dependent behavior, which is similar in both XPS and TPD (Figure 51, Figure 56).

### B. Pt NPs/$SiO_2$/Si(100)

TPD experiments of Pt NPs were carried out with a temperature ramp of $\beta = 5$ K/s in analogy to the Pt(111) single crystal. However, it was found that using the same maximum TPD temperature of 1183 K resulted in irreproducible data. Many tests were conducted and some interesting results were obtained. It was found that the maximum ramp temperature ($T_R$) used for the TPD cycles, as well as the number of successive cycles, played an important role in the stability of the experiment (i.e. reproducibility). Figure 57 shows the AFM results of a series of tests in which both $T_R$ and the number of TPD cycles were varied. A fresh sample analogous to sample #4 (~3.6 nm) was used for each test. The y-axis shows the calculated AFM NP height after various numbers of TPD cycles denoted on the x-axis. The label on each bar in the graph is the $T_R$ used for each experiment. We see that using the same

$T_R$ as in the Pt(111) experiments (1183 K) results in a decrease of NP height of over 1 nm at the end of 42 cycles. Similarly, even after only 15 cycles at just 913 K the NP height has decreased, however, only by ~0.3 nm. Similar AFM measurements conducted on sample #5 (~1 nm) revealed no change in NP height after 13 TPD cycles to 913 K. A temperature of

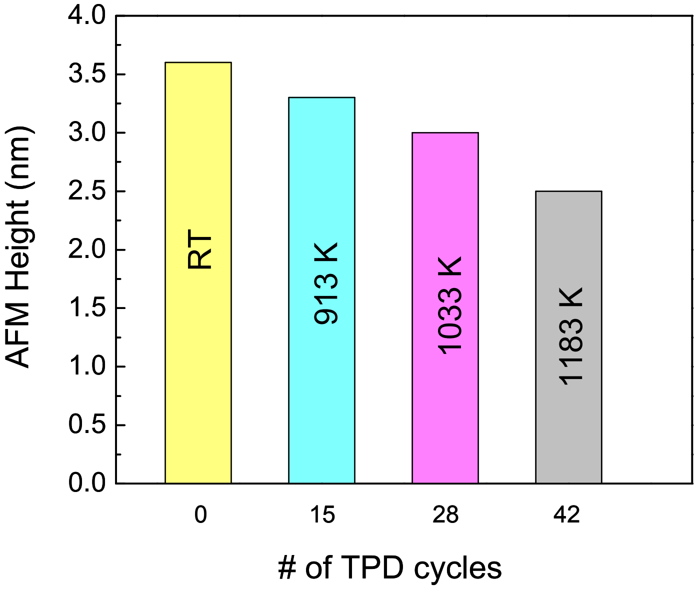

Figure 57 - A series of TPD experiments with differing $T_R$ as indicated on each bar, and differing number of cycles (x-axis) reveals a continuous decrease in calculated AFM height (y-axis) for sample #5 (3.6 nm). Each experiment utilized a fresh sample.

913 K is the lower limit to which we can go with $T_R$ and still obtain useful TPD spectra from our NP samples. As will be seen, 913 K is the cut-off temperature for obtaining the complete curve corresponding to low-coverage $O_2$-desorption from our Pt NPs. TPD cycles numbering over ~25 resulted again in irreproducible data. This could be due to a continued change in NP size, or to a more subtle effect caused by repeated cycles of $O_2$-exposure and annealing as discussed below. The decrease in NP size itself could have several origins.

The first possibility is the fact that NPs have a lower melting temperature than their bulk counterparts. For example, bulk Pt has a melting temperature of ~ 2040 K, while

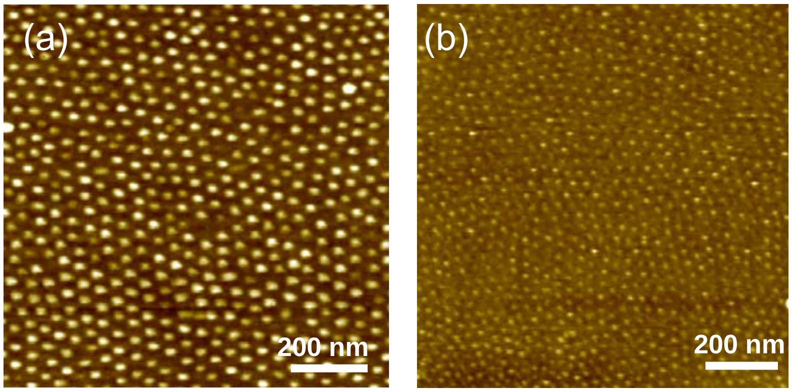

Figure 58 – AFM images of (a) 3.6 nm Pt NPs on $SiO_2$/Si(100) after 42 TPD cycles to 1183 K, and (b) 1.1 nm Pt NPs after 13 TPD cycles to 913 K.

Morrow and Striolo [360] calculate that the melting temperature of 1.2 nm and 2.5 nm Pt NPs, supported on carbon, is ~700-800 K and 1100-1200 K, respectively. The authors have also determined that surface restructuring takes place due to surface melting and Pt-atom mobility at temperatures ~200-300 K below the calculated melting temperatures of the NPs. In addition, Wen et al. [361] have calculated the melting temperature of ~4.5 nm Pt NPs to be 1720 K. According to these studies, the melting temperature of our 3.6 nm particles should be in the range of ~1200-1700 K. This range is above $T_R$ used in all of our TPD experiments. Furthermore, thermal stability of micelle-synthesized Pt NPs supported on $TiO_2$(110) has been observed by our group up to temperatures of 1333 K [64]. In this study the NP size (3.4 nm) was similar to our current samples #2 and #4 (3.6 nm). Only upon annealing at 1333 K for 20 min did the NP height change due to desorption of Pt atoms. Although in Ref. [64] the NP-support was $TiO_2$, this is not expected to significantly affect desorption of atoms from the surface of large particles, especially if they are 3D in nature as we have seen from EXAFS data (Chapter 4). However, it may play a significant role in stabilizing the particles against mobility at such high temperatures. This appears to be the case for our $SiO_2$-supported Pt NPs as well. As shown in Figure 58(a), even after 42 TPD cycles to 1183 K, our NPs in sample #4 (3.6 nm) still retain their original arrangement, although the AFM height has decreased by ~1 nm (Figure 57). For the 1.1 nm NPs of sample #5, even the lowest $T_R$ at 913 K is above the calculated melting temperature reported in Ref. [360]. However, from Figure 58(b) we can see that the NPs of sample #5 have retained their original arrangement, and the calculated AFM height distribution has also remained constant at $1.1 \pm 0.5$ nm. These data point to an unusual stability of our supported Pt NPs.

The second possibility for the decrease in NP size is the formation of volatile Pt-oxide species. It has been shown that the decay in electrode performance for fuel cell applications results from the formation of Pt-oxides and their subsequent dissolution. Wang and Yeh [93] have reported restructuring of Pt crystallites (1-2 nm) to accommodate oxygen accompanied by desorption of $PtO_2$ and loss of Pt above 750 K. Pt sintering that occurs in oxidizing atmospheres has also been shown to be caused by the formation of $PtO_x$ compounds which are mobile on the support. Furthermore, the regeneration of Pt catalysts in automotive applications occurs through oxidation and mobility of Pt particles and the process is highly support dependent as shown by Nagai et al. [345]. There, large Pt clusters adsorb oxygen to form Pt-oxides which are mobile. Depending on the strength of interaction between $PtO_x$ and the support, small clusters may again be stabilized. The stabilization was weak for irreducible supports such as $Al_2O_3$ but strong for supports containing highly reducible $CeO_2$. In addition, the process was reversible and dependent on $O_2$ concentration, temperature, and particle size. Pt-oxides are definitely formed on our NPs as evidenced by XPS, if they become mobile at elevated temperatures it is not expected that they should be stabilized on the irreducible $SiO_2$ support, and therefore are likely to desorb.

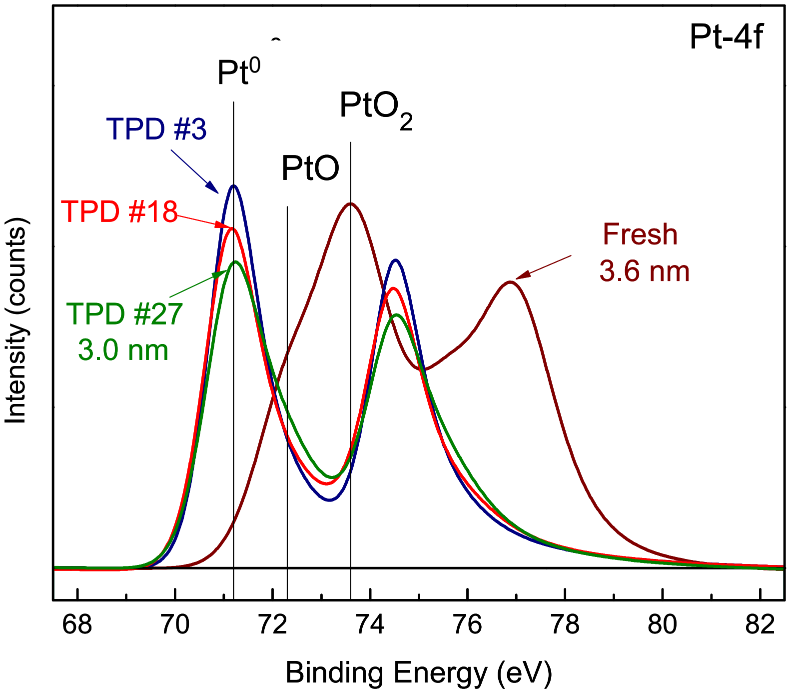

Figure 59 – XPS of the Pt-4f region of 3.6 nm Pt NPs (sample #4) after 3, 18, and 27 TPD cycles to 1033 K. Also shown is the spectrum of the initial, completely oxidized NPs after polymer removal by an $O_2$-plasma treatment at RT (labeled Fresh).

Figure 59 shows XPS spectra of the 3.6 nm Pt NPs (sample #4) after 3, 18, and 27 cycles of 3000 L exposures and TPD ramps to 1033 K. Also shown is the spectrum of the initial, completely oxidized NPs after the *in-situ* $O_2$-plasma treatment has removed the encapsulating polymer. For clarity, only the envelope of the fitted Pt spectra are shown. We can see that the intensity of the Pt-4f region decreases as the number of cycles increases. Analysis of the peaks also reveals that the oxide content remaining after cycle 3 was only ~3 %, however, after the 27th cycle the oxide content was 20 %. This shows that there are oxides which remain stable on the NPs up to 1033 K under our TPD conditions. The increase in oxide species could be the result of accumulation with TPD cycles or changes in the NP's oxidation behavior as a result of their changing size. As the NP size in this sample decreased by ~0.6 nm, our discussion of volatile Pt-oxide species is certainly plausible.

Following these results another series of TPD experiments was conducted to gain insight into the apparent instability of our NP samples. Figure 60 shows a sequence of $O_2$-TPD spectra from sample #5 (1.1 nm) taken with $T_R$ = 913 K. Once the 5 K/s ramp reached 913 K, the sample was held at this temperature for 2 min before cooling to RT under a flow of liquid $N_2$. The order of the cycles as well as their exposures (in units of L) are shown to the right of the graph. The black line labeled "blank" corresponds to a TPD cycle ran without oxygen exposure. Figure 60 reveals a large, broad peak centered at ~430 K which is consistent with $O_2$-desorption from our $SiO_2$ substrate [205]. The lowest two

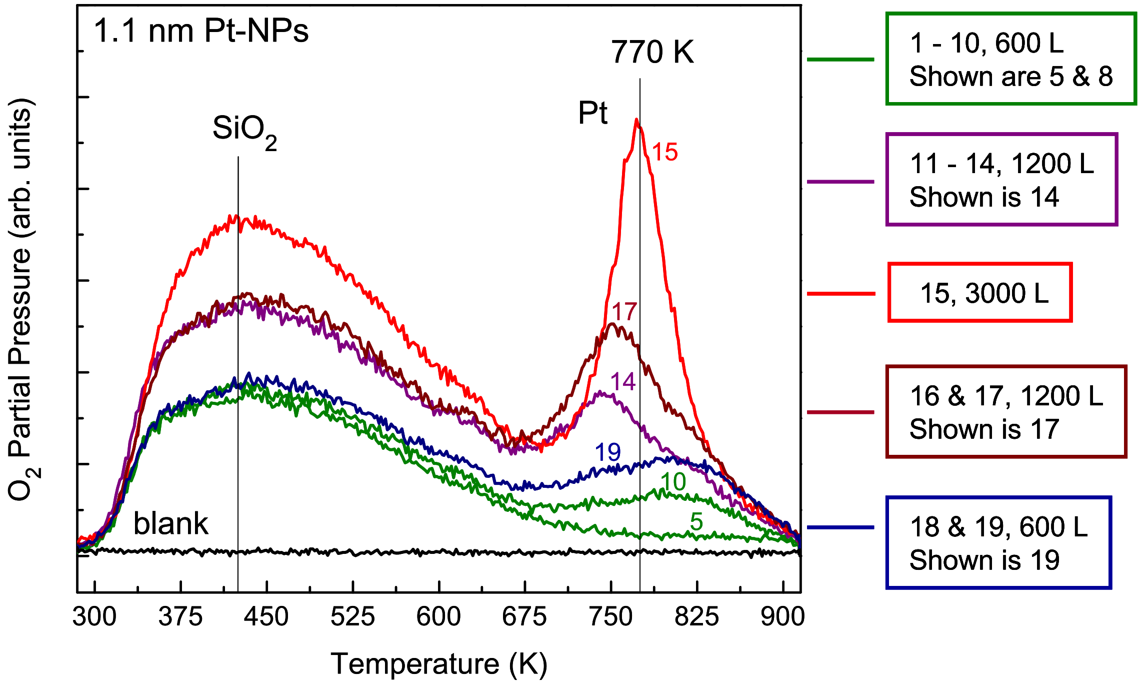

Figure 60 – Ordered sequence of 19 $O_2$-TPD spectra taken from ~1 nm Pt NPs supported on $SiO_2$/Si(100). The numbers in the boxes refer to the TPD cycle number and the corresponding exposures are given in Langmuir (L).

curves (green) are TPD cycles 5 and 10 from a series of ten consecutive, 600 L exposures to oxygen and TPD ramps. We can see that even after 5 cycles of dosing and heating, no $O_2$-

desorption is detected from the Pt region (> 450 for bulk Pt). Only after 8 cycles do we see a very broad feature arise at ~810 K (not shown), which increases slightly after the 10th 600 L dosing cycle. The next four cycles (11-14) were doses of 1200 L each and the desorption trace stabilized after cycle 14 as shown in the figure. The peak from this level of exposure is narrower than the 600 L cycles and shifted to lower temperature, centered at ~745 K. It is clear by now that increasing exposure to oxygen is causing an increase in the oxygen uptake of our Pt NPs, even though the exposures (L) remain constant. This can be seen in the reproducibility of the $SiO_2$ peak at ~430 K. Even as the intensity of the high temperature peak in the Pt region increases after consecutive, identical doses, the $SiO_2$ peak is reproduced over and over again. As a test of the hypothesis, the next cycle of the series (15) was an exposure of 3000 L. From the TPD trace we see a large peak shifted to higher temperature centered at ~780 K with a corresponding increase in the $SiO_2$ peak, which remains at ~430 K. At this point the exposure was decreased back to 1200 L and TPD traces 16 and 17 were obtained (shown is 17). These curves reproduced each other nicely but the mean desorption peak has shifted to higher temperature and is now at ~755 K, and the intensity has increased significantly with respect to the first cycle of 1200 L doses (curve 14). Finally, the exposure was returned to its original value of 600 L and curves 18 and 19 were obtained (shown is 19). Once again the cycles were reproducible. Furthermore, as in the case of the second set of 1200 L exposures (16 and 17), cycles 18 and 19 show an increase in oxygen uptake with respect to the first 10 exposures of 600 L (curves 5 and 10). In addition to these observations, we point out the high temperature region of Figure 60. Starting above ~825 K we see that all traces taken after the 3000 L dosing cycle have an increased area under their respective curves in this region. For example, the area of the final cycle of 600 L has increased significantly compared to the first 10 cycles at this exposure. It is possible that at the beginning of our TPD cycles we generate only weakly, chemisorbed layers of $O_2$ which overlap with the desorption peak of the $SiO_2$ substrate at low temperature. Once the NPs have been "conditioned" the growth of more stable oxides might then proceed.

Figure 61 and Figure 62 show $O_2$-TPD spectra from samples #4 (~3.6 nm) and #5, (~1 nm), respectively, taken with $\beta$ = 5 K/s at $T_R$ = 913 K. These spectra were acquired after several activation/pretreatment TPD cycles, using doses of 3000 L and a $T_R$ of 913 K, in order to "condition" the NPs as discussed above. After these initial cycles, oxygen exposures remained below 3000 L. The peak originating from the $SiO_2$ substrate again appears at ~430 K for both samples and its intensity increases with increasing exposures while keeping the same position. Both NP samples exhibit similar features as the bulk Pt(111) single crystal (Figure 56). However, as with the single crystal, separation and distinction between the different phases of oxygen which might exist on our NP samples is difficult. We have seen that XPS has limited sensitivity in this regime (even with the bulk sample) and techniques such as LEED yield no information about the structure of Pt-oxide overlayers on our multifaceted NPs, especially with coverages of Pt as low as the ones present here (~2 %). Likewise, traditional TPD analysis methods, such as the complete analysis or Redhead give unreliable information when individual states might overlap and cannot be isolated from multilayer desorption. In our case, we also need to consider a certain degree of overlap with $O_2$-desorption from the $SiO_2$ substrate. We therefore discuss the results obtained here in a qualitative fashion only.

In general, after low exposure, $O_2$-desorption appears as a small peak at high temperature (> 800 K) and gradually increases while shifting to lower temperature with

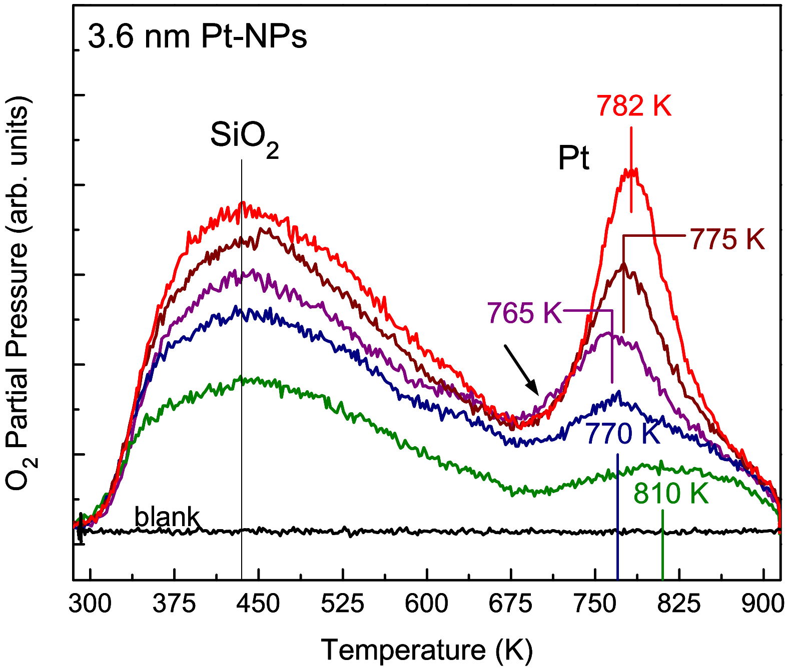

Figure 61 – $O_2$-TPD spectra from sample #4 (3.6 nm). The dosings from top to bottom are: 3000 L, 2250 L, 1500 L, 1050 L, 600 L, and 0 L (blank). The arrow marks the appearance of undercutting.

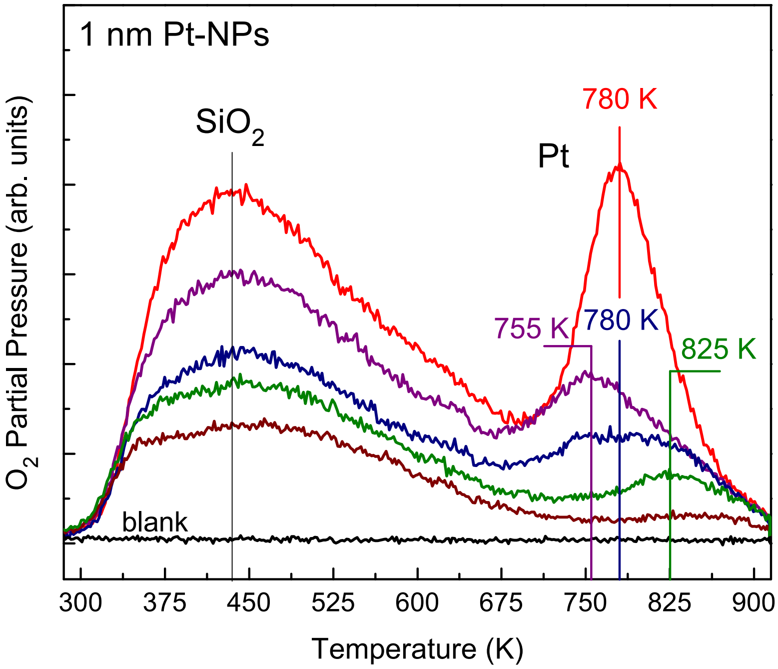

Figure 62 – $O_2$-TPD spectra from sample #5 (1.1 nm). The dosings from top to bottom are: 3000 L, 1200 L, 600 L, 450 L, 300 L, and 0 L (blank).

increasing coverage. Finally, the desorption peaks begin to shift again back to high temperatures as the coverage continues to increase. For Pt(111), this shift to higher temperature happens for coverages greater than ~1.2 ML [79]. For the Pt(111), it has been shown experimentally [76] that oxygen coverages below ~0.3 ML give a reaction order of n = 2, for $0.3 < \Theta < 1$ ML, n is closer to 1. However, for $\Theta > 1$ ML n is not linear for $0 < n < 2$ over any temperature range. This implies that the pre-exponential factor and/or the desorption energy are dependent on coverage. In addition, the leading edges of high coverage desorption curves are observed to "undercut" the leading edges of lower coverage curves. This behavior is seen in the TPD of our Pt(111) sample where the leading edges of the 0.98 and 0.9 ML curves (Figure 56) undercut the leading edge of the 0.8 ML curve. We can also see this happening in the 3000 L exposure of our NP sample #4 (Figure 61). Here the leading edge of the 3000 L exposure matches the leading edge of the preceding 2250 L exposure and undercuts the leading edge of the 1500 L exposure (marked by an arrow). This feature has been observed before on bulk surfaces of Pd and Pt and explained as the formation of small oxide clusters on the surface with increased stability, but which rapidly decompose above a certain temperature. Interestingly, Saliba et al [76] have even estimated the size of these clusters to be ~3.5 nm, which is the same size as our sample #4 (3.6 nm). The main difference between our NP samples and the bulk Pt(111) is the temperature of the maximum desorption peaks for a given coverage, with seemingly higher temperatures for the NP samples.

To try and quantify these data more, an estimate of coverage (ML) relative to the Pt(111) bulk reference was done for the NP samples. We assume that the AFM height is close to the NP diameter, and AFM also gives the density of our NPs on the substrate. From

Ref. [131], and the AFM height, we can estimate the number of atoms in our NPs as well as the percentage of atoms that occupy the surface. In addition we make an assumption that ~10 % of the atoms in the NPs are in contact with the substrate. This gives ~50 surface-atoms/NP for the 1 nm sample, and ~450 surface-atoms/NP for the 3.6 nm sample. Multiplying by the density of NPs on the substrate and dividing by the surface-atom density of Pt(111), we obtain a surface-atom density of ~0.2 % and 2 % for the 1.1 nm and 3.6 nm NPs, respectively, compared to 1.51 x $10^{15}$ atoms/$cm^2$ for bulk Pt(111). Next we consider that the area under the $O_2$-TPD desorption curve of a 1 ML coverage on the NPs should correspond to 0.2 % and 2 % of the area of the same coverage-curve for the Pt(111). All other spectra are calibrated using these numbers. Recall from Chapter 1 that 1 ML corresponds to 1 oxygen atom per Pt atom. After subtraction of the $SiO_2$ peak from the data shown in Figure 61 and Figure 62, the resulting $O_2$-desorption curves are shown in Figure 63(a)(b).

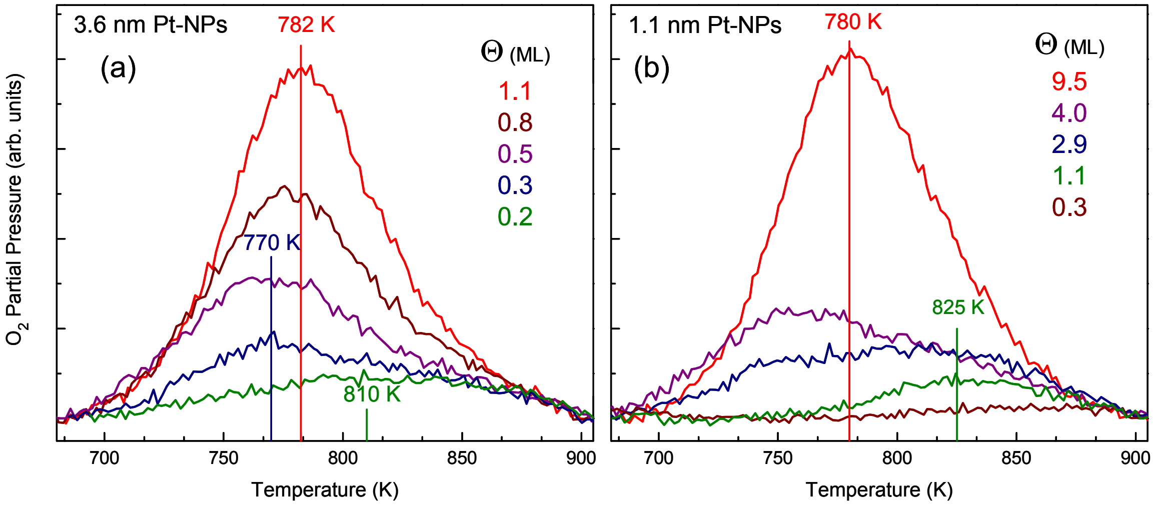

Figure 63 – Coverage (ML) calculations for sample #4 (a) and sample #5 (b) after the subtraction of the $SiO_2$ substrate peak.

For the large particles of sample #4 (3.6 nm) [Figure 63(a)], the above calculations seem to give reasonable coverage estimates with a maximum coverage of 1.1 ML, in good agreement with our maximum coverage of 0.98 ML obtained for the Pt(111) single crystal. The 1 ML coverage has a peak at ~780 K which is ~100 K higher the same peak for Pt(111). The 0.3 ML peak is also ~70 K higher than the 0.3 ML peak of the Pt(111). The 0.2 ML peak appears at ~810 K for the 3.6 nm NPs and should correspond roughly to the 0.25 ML peak of Pt(111), which appears at ~735 K [76]. In general, the coverage calculations show that the trend seen for sample #4 (3.6 nm) is the same as that seen for Pt(111) but shifted by ~70-100 K to higher temperatures. We note that the "undercutting" mentioned above happens for the 3.6 nm NPs at ~1 ML, as in the case of Pt(111).

For the small NP sample [Figure 63(b)], the calculations give very high oxygen coverages (10 ML). As the trend in the peaks is in general agreement with sample #4 (3.6 nm), this indicates that there is a problem with the assumptions made in calculating the coverages for these small particles. For example, we assume that no oxygen from the substrate finds it way to the NPs before desorption, which may not be the case. Further, ~85 % of the atoms in these NPs occupy the surface and we cannot assume that they will behave in the same way when exposed to high concentrations of oxygen as bulk-like samples, or our large NPs (~3.6 nm). As discussed below, it is likely that significant restructuring of these particles takes place during $O_2$-TPD cycles, introducing further complications. In addition, we are bringing oxygen species to the surface of the NPs which have been generated by a plasma source. This oxygen may adsorb on sites different from oxygen generated by $O_2$-dissociation, from which calibration curves are calculated.

It could be that the features we observe in our NPs are in general too broad and convoluted to distinguish any differences. In a TPD study of $O_2$-desorption from Au NPs [205], differences of ~30 K in peak temperatures for similar coverages were observed for ~1.5 and ~5 nm NPs. However, only one $O_2$-desorption state from Au NPs was identified in that study. Furthermore, Au does not easily form oxides and the most stable is $Au_2O_3$, while for Pt several oxides, with higher stabilities, can be formed (PtO, $PtO_2$, $Pt_3O_4$). Furthermore, Ref. [205] employed exposures approaching ~16,000 L to generate Au-oxide species for TPD experiments. Another possibility is that the structure of our NPs could play a role. Weaver's group [75] has shown that oxygen on Pt(100) is less stable and desorbs at lower temperature than on Pt(111). Figure 64 shows XPS spectra of sample #4 (a) and sample #5 (b) after several exposures (given in L) to the $O_2$-plasma, before TPD ramps. We see that the larger particles (a) have a tendency to form high concentrations of the $PtO_2$ component even after low doses (600 L), while the smaller particles form predominantly PtO, even after high doses (3000 L). This is in disagreement with Wang and Yeh's observation [93] that $PtO_2$ should be the favored oxide with particles sizes less than 1.3 nm and PtO with sizes greater than 2.0 nm. We have also observed unusual stability of PtO in Pt NPs >2.0 nm [331] (Chapter 8). However, Wang and Yeh's results, as well as our previous data, correspond to Pt NPs supported on oxide powders such as $\gamma$-$Al_2O_3$ and $ZrO_2$. Both of these substrates have been observed to have unique interactions with Pt, which can have an influence on Pt oxidation, especially oxidation of nm-sized particles. In addition, the interaction of Pt NPs with oxygen, outside of UHV, might be different than the current case of Pt NPs on $SiO_2$/Si(100) interacting with an oxygen plasma under UHV conditions. As mentioned above, Seriani et al. [87] have calculated that $Pt_3O_4$ should be the stable oxide,

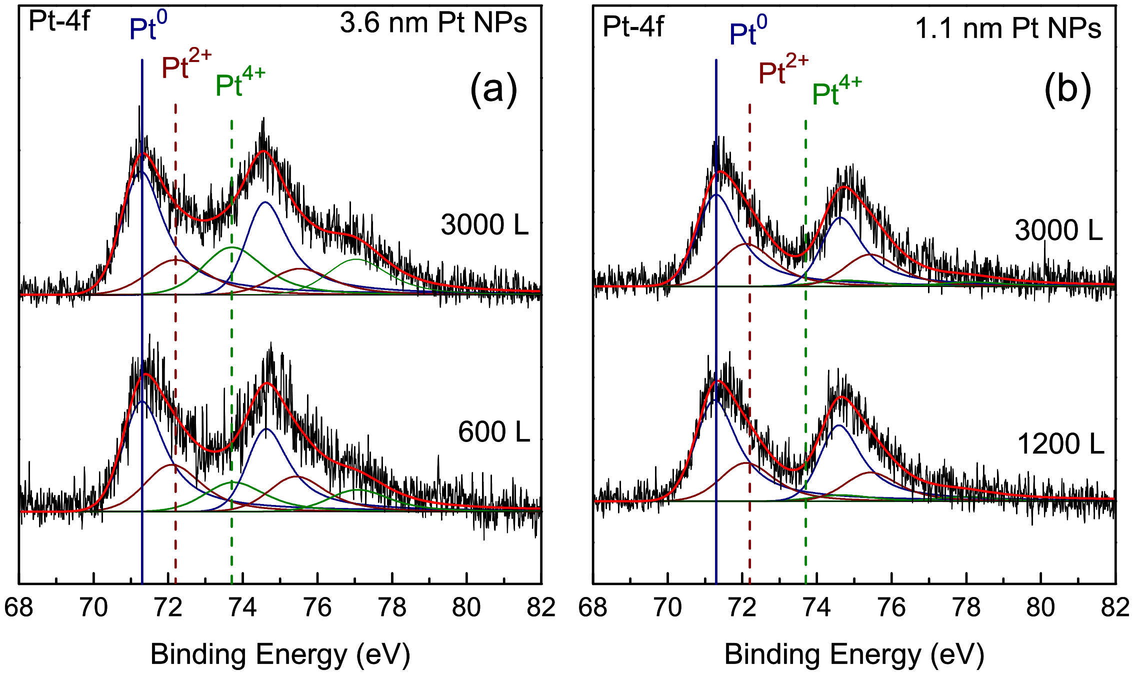

Figure 64 – XPS spectra of sample #4 (a) and sample #5 (b) after oxygen plasma exposures, as given in Langmuir (L), and before TPD.

preferred over PtO. However, the author's don't rule out the formation of PtO, which also favors the formation of (100) surfaces. Similar to the study by Nolte et al. [20], where the total area of (100) facets increased, while (111) facets decreased, after surface oxidation of Rh NPs, the small Pt NPs of our sample #5 could undergo significant surface restructuring upon oxygen exposure. Subsequent oxygen adsorption on the surface might then proceed with lower binding strength, bringing about shifts in the TPD spectrum to low temperatures. The XPS of Figure 64 also reveals almost no difference in the oxidation state of the small NPs (b) from 1200 to 3000 L, although TPD clearly shows increasing coverages in this range. This reveals that doses higher than 3000 L are necessary for substantial Pt-oxide formation on these NPs, and that a significant amount of $O_2$ observed in TPD is likely from multilayer desorption. For the larger particles (sample #4), the formation of $PtO_2$ is evident in the high

BE XPS peak observed after the 3000 L exposure [Figure 64(a)], revealing that these particles can more easily form bulk-like oxide phases, similar to the bulk Pt(111). The idea of surface restructuring may lend some insight into our observation that repeated exposures are necessary before any $O_2$-evolution from our NPs can be seen in the TPD. As seen in Figure 59, the as-prepared, fresh NP samples start out completely oxidized by the plasma treatment that is used to remove the encapsulating polymers. It is possible that these NPs have little or no crystalline order and the first few cycles of oxygen exposure and annealing bring about structures ($PtO_x$ "skin" layers) capable of the extensive oxygen uptake needed to observe TPD spectra from these small NPs. Perhaps annealing alone would facilitate the same restructuring, however, at the end of each TPD ramp the sample is held at $T_R$ for 2 min before cooling and even 10 such cycles (20 min at 913 K) reveal little oxygen uptake (Figure 60). In addition, 913 K is far below the estimated melting temperature of our 3.6 nm NPs. Therefore, we believe it is likely that exposure to oxygen is key to this process, after which, the TPD ramp effectively anneals the sample in the presence of that oxygen. Techniques such as cross-sectional TEM may be of use in determining the structure of our small particles, before and after oxidation, however, the possible amorphous nature of the oxides formed will limit TEM observations and exposure to the atmosphere may also induce changes. More extensive, *in-situ* spectroscopic studies are needed to understand the microscopic origin of the effects observed.

As a final note, we should keep in mind the conditions of the two studies described in this chapter (XPS and TPD). For the XPS study samples were exposed to long $O_2$-plasma treatments (2 hours) amounting to ~50,000 L in order to create completely oxidized particles, after which, annealing steps lasted for 10 min at each temperature up to 1000 K. For the

TPD studies, the samples were exposed to a maximum of 3000 L and subjected to a heating ramp up to 913 K, where they remained for only 2 minutes. Therefore, the TPD study is more dynamic in nature as compared to the XPS data. For samples in the XPS study we may desorb/decompose more oxygen species at a certain temperature than what we find with TPD simply because of the longer annealing times. Similarly, very high exposures in the XPS study allow us to form in a sense an equilibrium or maximum coverage of oxygen/oxides on our NPs, while the short exposures of the TPD study are much more limiting in their effect.

## 9.3 Conclusions

In summary, we have conducted an extensive study on the evolution of oxide species on size-selected Pt NPs supported on $SiO_2$/Si(100). We have used AFM, XPS, and TPD experiments to gain insights into this complex problem, the results of which are listed below.

1) The thermal stability of Pt-oxides as studied by XPS reveal that NPs in the range of ~1-7 nm, prepared by micelle encapsulation, may be fully oxidized throughout their volume by exposure to a RT oxygen plasma in UHV. AFM also revealed that the initial arrangement of the NPs on the $SiO_2$ was preserved after the different TPD cycles.

2) XPS fittings show that at least three separate species of Pt are found in all samples which we have assigned as $PtO_2$, PtO, and metallic $Pt^0$; keeping in mind the possibility of other species, more specifically, $Pt_3O_4$, which cannot be unambiguously distinguished from PtO by XPS. In the O1-s region we have evidence of a chemisorbed layer of atomic oxygen and two, more weakly bound molecular states of oxygen on Pt(111).

3) The thermal decomposition of these oxides goes as $PtO_2 \rightarrow PtO \rightarrow Pt^0$ for all samples, including bulk Pt(111) with PtO and $PtO_2$ species coexisting

4) The fresh, completely oxidized Pt NPs, prepared by micelle encapsulation, show no oxygen uptake initially. Only after several cycles of oxygen exposure and annealing in UHV is an $O_2$ signal seen to appear in the TPD spectra. This is tentatively ascribed to the poorly ordered initial condition of the micellar NPs and subsequent restructuring under oxygen annealing.

5) For low oxygen exposures during TPD experiments, the smallest NPs (1.1 nm) formed predominantly PtO, while the larger NPs (3.6 nm) formed substantial amounts of $PtO_2$. However, the relative stability appears different upon annealing with easier decomposition of $PtO_2$ taking place on the larger NPs.

6) $O_2$-desorption spectra reveal that both small (1.1 nm) and large (3.6 nm) Pt NPs show trends similar to $O_2$ TPD from bulk Pt(111). Low coverage peaks appear at high temperatures and increase in intensity while shifting to lower temperatures with increasing coverage. However, $O_2$-desorption from the NPs takes place at higher temperatures than the bulk Pt, suggesting stronger O-binding to the NPs.

7) The NP samples were very sensitive to oxygen dosing and necessitated "conditioning" with high doses, after which, dosing was kept low. Subsequently, stable oxides were formed. This indicates that our Pt NPs are extremely dynamic systems with restructuring due to oxygen annealing likely taking place for each TPD cycle.

# PART II – VIBRATIONAL PROPERTIES OF NANOSCALE SYSTEMS

## Motivation

The vibrational density of states (VDOS) of materials is of great importance because of the thermodynamic information contained therein. The VDOS is key to understanding processes such as thermal conductivity [362], NP diffusion [363], and phase stability and transitions in NPs [165, 364]. Furthermore, the possibility of tailoring the VDOS of materials, through phonon engineering, has attracted attention for controlling the thermal properties of nano-electronic devices [365]. Phonons may also be significant in the tailoring of catalytic surfaces. Because many reactions involve surface diffusion of reactants, energy dissipation through coupling to substrate phonons may be an important mechanism [366]. In such cases adsorption and desorption processes will be greatly affected by the substrate phonon modes [367, 368]. For example, in Ref [366] the authors found that $CO_2$ molecules desorbing from the Pd(111) surface lose as much as 34 % of their initial energy to the substrate.

Although much work has been done [211], experimentally [369-375] and theoretically [376-378] on bulk and nanocrystalline materials, experimental work done on isolated NP-systems is very rare. This represents a shortcoming in the field because distinct differences in the VDOS are expected for bulk materials and their nano-counterparts [379, 380]. For example, enhancements in the VDOS at low and high energies, a broadening of the VDOS, and Debye as well as non-Debye behavior of the low-energy modes have been reported; attributed to phonon lifetime broadening, under-coordinated surface atoms, oxides, and atoms located at boundaries (i.e. grains) [369, 374, 376, 377, 381]. These effects are directly related to the unique bonding and interatomic potential which arise in nanostructures [382]. For example, the loss of neighboring atoms can decrease (soften) the strength of interatomic force constants, thereby increasing contributions to the low energy VDOS. However, this depends on the local surface structure, as it has been shown [383] that on vicinal surfaces interatomic force constants can increase, also due to under-coordination. This will result in an enhancement of the VDOS at high energies. Calculations for 2-3 nm Ag NPs [379] also show low and high energy enhancements in the VDOS. In Ref [379], under-coordinated surface atoms were found to be responsible for the low energy modes, while an overall decrease in bond length created high energy modes above those of the bulk metal [379]. Sun et al. [380] have also calculated that surface modes are responsible for low energy enhancements while a "stiff" transition layer was responsible for enhanced modes at high energies in (Au, Pb, Ag, and Cu)-NPs containing ~500-1000 atoms. In these studies, neither oxidation effects nor grain-boundaries can account for the increase of the free NP's VDOS, since the calculations were performed for pure defect-free particles. In addition, linear [11], non-linear [15-17], and Debye-like (quadratic) [6-10,12-14] behavior of the low-E VDOS has been reported. As such the physical nature of the low-E excess modes in nanocrystalline materials is still a topic of interest and the exact mechanism leading to the VDOS enhancement in free NPs is still under investigation. This being the case, the first step towards a greater understanding of the vibrational properties of NPs is a more thorough experimental investigation on true NP-systems.

# CHAPTER 10: PHONON DENSITY OF STATES OF Fe NPs: SIZE, SURFACE COATING, AND ADSORBATE EFFECTS

B. Roldan Cuenya, A. Naitabdi, J. R. Croy, W. Sturhahn, J. Y. Zhao, E. E. Alp, R. Meyer, and D. Sudfeld. Physical Review B 76 (2007) 195422

## 10.1 Experimental

Monolayer-thick films of size-selected, isolated $^{57}$Fe NPs uniformly spaced over large surface areas were prepared using micelle encapsulation [236] with PS(x)-P2VP(y) diblock copolymers (molecular weights: x = 81000, y = 14200 for sample #1 and x = 27700 and y = 4300 for sample #2 and #2b) loaded with an $^{57}$FeCl$_3$ salt. The distinct molecular weights of the two polymers resulted in samples with different average NP diameters, d, and interparticle distances l [24].

The NPs were deposited on SiO$_2$/Si(111) wafers and C-coated Ni grids and their morphological and structural properties were investigated by AFM and HR-TEM. NRIXS measurements on the SiO$_2$/Si(111)-supported particles (samples #1, #2, #2b), were performed at room temperature in air at beamline 3-ID of the APS (ANL, Chicago). The synchrotron-beam energy was scanned around the resonant energy of 14.413 keV of the $^{57}$Fe nucleus with an energy resolution of 1.3 meV. The measurement time per sample was two days. The spectra have been decomposed into single-phonon [$\propto$ g(E)] and multi-phonon contributions using the PHOENIX software [384]. The method is described in detail in Chapter 2.

## 10.2 Results and Discussion

Figure 65 shows AFM images of $^{57}$Fe NPs deposited on $SiO_2$/Si(111) obtained after polymer removal by annealing in UHV at 773 K [(a) sample #1b, (c) sample #2b] and subsequent *in-situ* $Ar^+$-etching (1 keV) and air exposure [(b) sample #1, (d) sample #2]. Isolated, monodispersed NPs with local hexagonal arrangement can be observed. On the $Ar^+$-etched samples, a minimum residual C-signal, comparable to the one obtained upon annealing a polymer-free Si substrate (coated by adventitious carbon) under UHV, was observed by XPS, Figure 66(a). ). Here we can see that after annealing, the C-signal from the encapsulating polymer is strongly suppressed. A subsequent sputtering treatment results in a negligible residual C-signal shifted with respect to the original binding energy of the polymeric C-1s. In (b), the evolution of the Si and $SiO_2$ signals can be followed after the different treatments. The final sputtering results in a nearly $SiO_2$-free substrate. However, since all the NRIXS measurements were conducted in the air, the native $SiO_2$ is always present. The $Ar^+$-etching did not result in distortions of the NP's spatial arrangement. It did, however, provide a partial, ultra thin Si coating, presumably along the NP's rim, that minimized the oxidation of the NPs upon air exposure, as evidenced by XPS, Figure 66(b). The $Ar^+$ etched samples appeared to be more resistant to oxidation as after seven months in air, the XPS spectra from sample #2 showed 30.5 % $Fe^0$ and 69.5 % $Fe^{3+}$ [Figure 67(b), curve (vi)]. On a similarly synthesized sample (sample #1), after sputtering and a long air exposure (7 months), 16 % $Fe^0$ and 84 % $Fe^{3+}$ were detected [Figure 67(a), curve (vi)]. These results indicate that sample #2 has the lowest concentration of $Fe^{3+}$ (or the thinnest oxide shell). STM images were also acquired on these samples as shown in Figure 68. However, it should be taken into account that tip effects may also contribute to an artificial enhancement

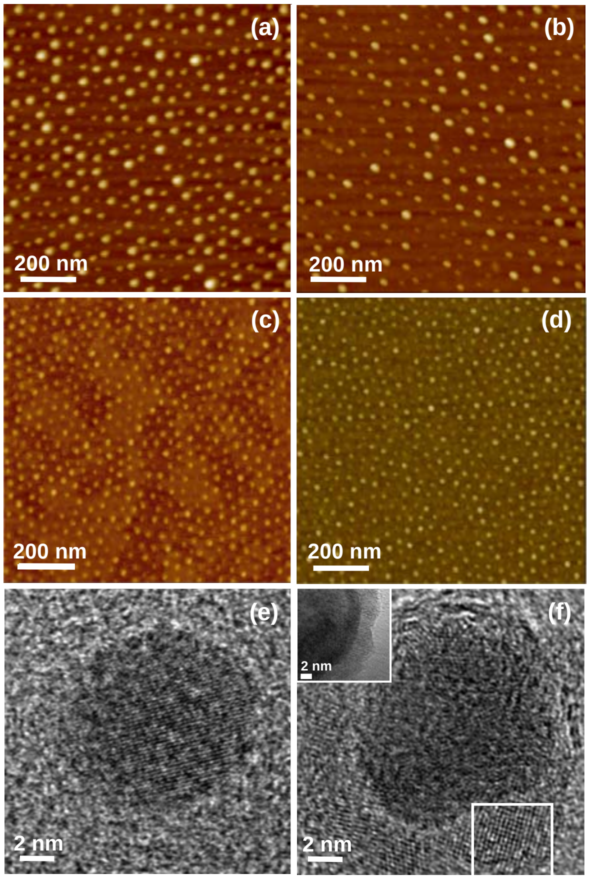

Figure 65 – AFM (a-d) and HR-TEM images (e,f) of $^{57}$Fe NPs synthesized by encapsulation in PS(81000)-P2VP(14200) [top row and (e)] and PS(27700)-P2VP(4300) [center row and (f)]. The NPs were deposited on $SiO_2$/Si(111) (for AFM) and on C-coated Ni grids (for TEM). The images were obtained after polymer removal by annealing in UHV to 773 K for 30 min [(a) and (c),(f) sample #2b], and after *in-situ* sputtering [(b),(e) sample #1 and (d) sample #2]. The top inset in the TEM image (f) demonstrates the core-shell structure of the nanoparticles in sample #2b. Both shell and core are crystalline. A FFT analysis from the region marked in Fig. 65(f) with a square frame (bottom right corner) has been conducted. TEM images acquired by D. Sudfeld (University of Duisburg-Essen)

of the measured STM diameters. We found values of d = 9.8 ± 0.6 nm and 8.2 ± 0.6 nm (STM), and l = 70 ± 11 nm and 37 ± 3 nm (AFM) for samples #1 and #2, respectively. The NPs were found to be non-spherical, with a diameter (STM) to height (AFM) ratio ranging from 2.5 to 5.5. HR-TEM measurements reveal that all NPs have a crystalline core, Figure 65(e),(f). The oxide shell could not be detected by HR-TEM, probably because it is

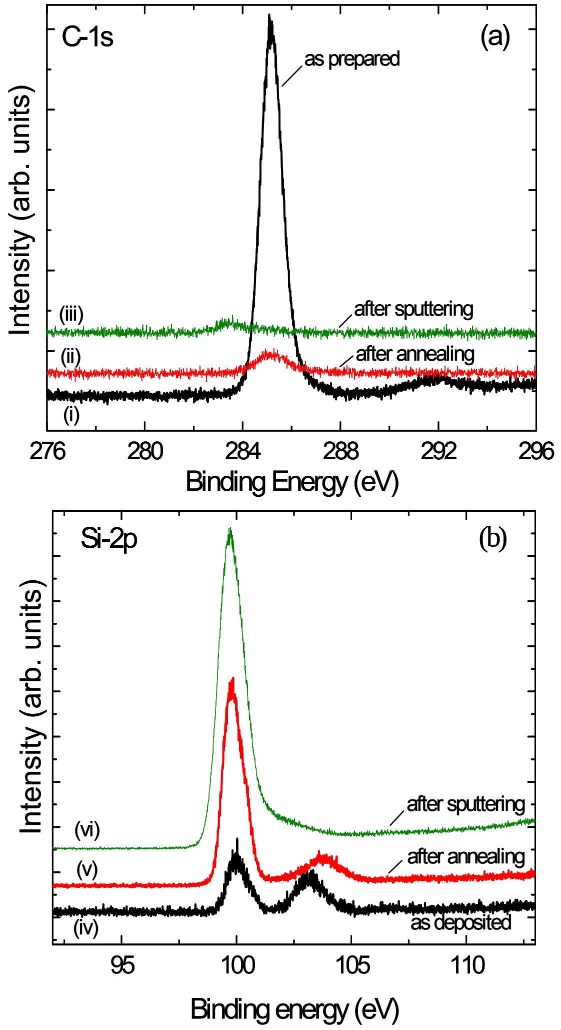

Figure 66 – XPS spectra (Al Kα = 1486.6 eV) from a sample containing size-selected $^{57}$Fe nanoparticles synthesized by encapsulation on PS(27700)-P2VP(4300) and supported on $SiO_2$/Si(111). The C-1s (a) and Si-2p core levels (b) are shown before (i, iv), after (ii, v) UHV annealing at 500°C and after $Ar^+$ sputtering (1 keV, 1 hour) (iii, vi

amorphous and rather thin. From the fast Fourier transform (FFT) analysis of the TEM image of sample #1, Figure 65(e), a lattice parameter of $a = 0.289 \pm 0.024$ nm corresponding to bcc iron was determined. A third sample (#2b) (with $d = 8.5 \pm 0.6$ nm and $l = 32 \pm 4$ nm), prepared in a similar way as sample #2 but without $Ar^+$ etching after UHV annealing,

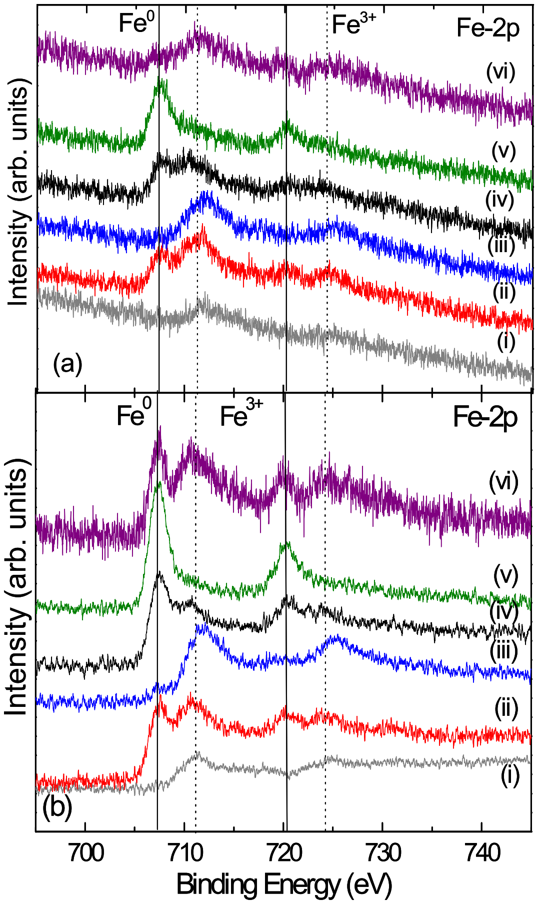

Figure 67 – XPS spectra from the Fe-2p core level of size selected $^{57}$Fe NPs deposited on $SiO_2$/Si(111). The particles were synthesized by encapsulation on (a) PS(81000)-P2VP(14200), (b) PS(27700)-P2VP(4300), and measured as deposited (i), after annealing in UHV at 773 K, 30 min (ii), and after subsequent air exposure (one day) [sample #2b (b)] (iii), followed by $Ar^+$ sputter-etching at 1 keV, 20 min (iv), and additional $Ar^+$ sputter-etching at 1 keV, 60 min (v). After seven months of air exposure of the $Ar^+$-etched samples, the spectra (vi) were measured [sample #1 (a) and sample #2 (b)].

revealed a crystalline bcc-Fe core/shell structure by HR-TEM [Figure 65(f)], with a ~2-5 nm thick crystalline shell. According to the lattice spacing of the shell it is most likely $Fe_3C$. The lattice constant of a = 0.293 ± 0.024 nm, measured for the core region of the particle in sample #2b, belongs to the bcc phase of iron [Figure 65(f)]. The thick shell (between 2 to 5nm) [Figure 65(f), top inset] has a cubic structure. A FFT pattern analysis taken from the

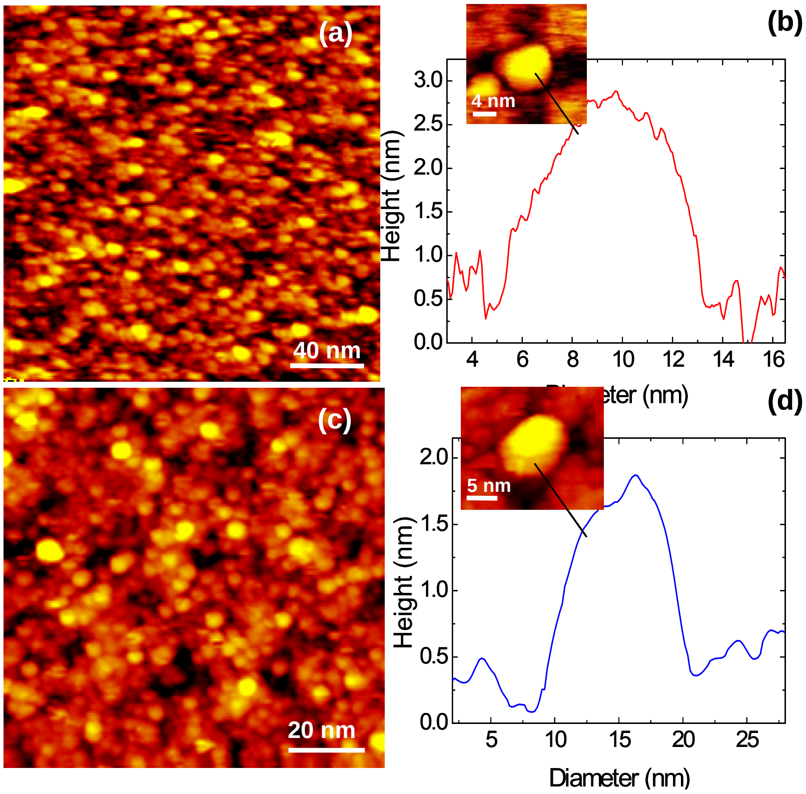

Figure 68 – Scanning tunneling microscopy images of $^{57}$Fe nanoparticles supported on $SiO_2$/Si(111) and synthesized by encapsulation in PS(27700)-P2VP(4300) (a)(b)(sample #2), and PS(81000)-P2VP(14200) (c)(d)(sample #1). In the right column, 2D profiles and STM images (inset) of an isolated $^{57}$Fe NP in sample #2 (b) and sample #1 (d) are displayed. In (b),(d), the height scales are underestimated due to the low conductivity of our naturally oxidized $SiO_2$/Si(111) substrates. The tunneling parameters were: (a),(b) Vt = 2.5 V, It = 0.23 nA, and (c),(d) Vt = 1.53 V, It = 0.15 nA. STM images acquired by Dr. A. Naitabdi (UCF).

bright-field image [FFT region of interest is marked in Figure 65(f), bottom insert] revealed lattice spacings of $d_{hkl}$ = 0.252 ± 0.017 nm and $d_{hkl}$ = 0.263 ± 0.017 nm, respectively. It is most probable that these lattice spacings belong to the (311) orientation of $Fe_2O_3$ or $Fe_3O_4$, or to the (020) orientation of $Fe_3C$. Since none of the other samples showed this type of shell after similar air exposure, the shell seems to originate from residual polymer that was not removed during the *in-situ* annealing of sample #2b, and, most likely, is $Fe_3C$.

Figure 69(b) shows g(E) of samples #1, #2, #2b, and of a bulk bcc $^{57}$Fe foil reference, obtained from the measured data shown in Figure 69(a). The results reveal three clear differences between g(E) of supported, isolated Fe NPs and that of the bulk bcc-Fe reference sample: (i) the strong suppression of the sharp phonon peaks, in particular, of the strong longitudinal acoustic phonon peak at 36 meV; this effect may originate from phonon damping due to confinement [370, 381, 385], (ii) the significant enhancement of g(E) at low and high energies, where excitations extend beyond the cut-off energy of ~40 meV of bulk bcc-Fe, and (iii) the striking, non-Debye-like behavior of g(E) [with $g(E)/E^2 \neq$ constant] of the NPs at low energies [see also Figure 70]. Samples #1 and #2 show a distinct shoulder in the VDOS at low E with a plateau between 6.5-14 meV, and a common peak at ~41-43 meV. It is worthwhile mentioning that bulk hematite ($\alpha$-$^{57}Fe_2O_3$) also shows a peak near ~41 meV [213]. However, since the strong VDOS peaks of bulk hematite around ~20 meV are missing in the VDOS of our NPs [Figure 69(b)], we cannot positively identify the oxide shell of our NPs with $\alpha$-$Fe_2O_3$. Oxidized nanocrystalline Fe does not exhibit such a distinct peak near 41-43 meV [374]. Although the nature of the 41-43 meV peak is unknown, it seems to be related to some vibrational state of Fe in our NP oxide shell that is similar to the 41 meV vibrational mode in bulk $\alpha$-$Fe_2O_3$. In contrast to samples #1 and #2, for sample #2b a low-E region with a nearly linear E-dependence and no distinct high-E peaks are observed [Figure 69(b), insert].

MD simulations were carried out by our collaborator Prof. Ralf Meyer (Laurentian University, Sudbury, Canada) on spherical Fe NP, with diameters of 3.1 and 7.3 nm, deposited on Ag(001) [386]. In agreement with our experimental observations, an increase in g(E) was obtained for both NPs at low and high E. However, particularly in the low-E regime, the increase was less pronounced than in the experiments. We attribute this

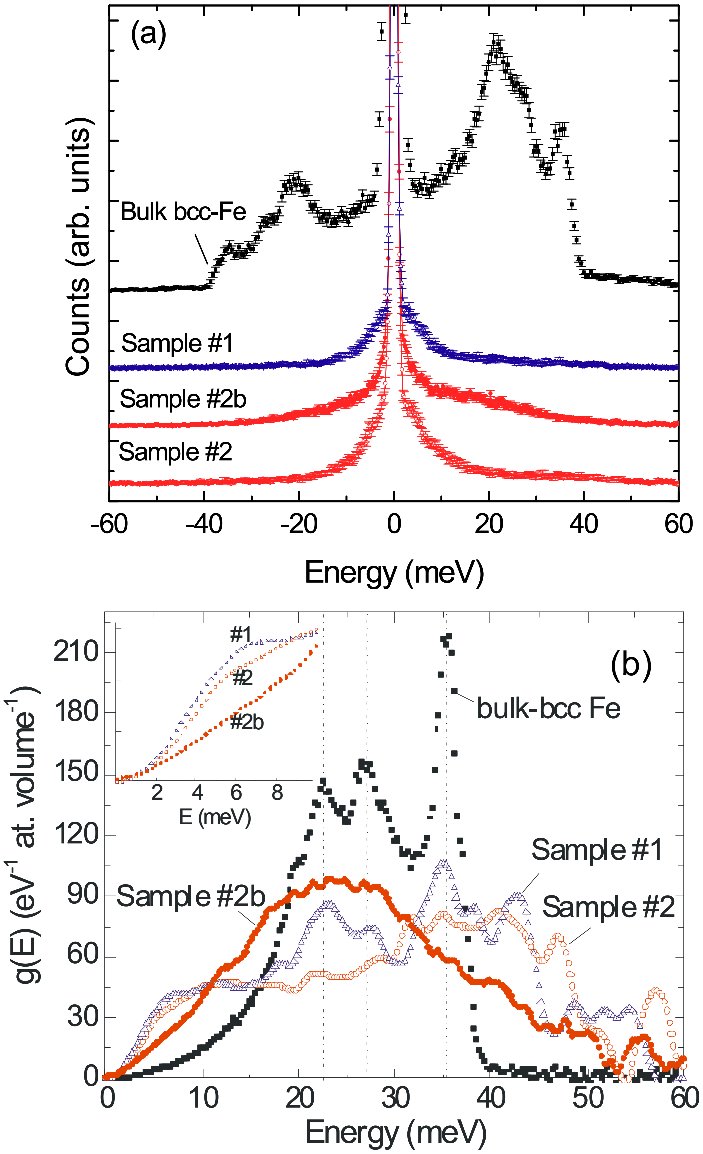

Figure 69 – (a) Experimental NRIXS spectra from size-selected $^{57}$Fe nanoparticles supported on $SiO_2$/Si(111) and synthesized by encapsulation on PS(27700)-P2VP(4300)

difference to the oxide shell (samples #1 and #2) or $Fe_3C$ shell (sample #2b) of the experimental NPs, and in particular to differences in the low-coordinated interfacial core/shell or shell surface states [363, 387]. Since the MD-simulated NPs were free from Fe-oxide and/or carbide shells. In addition, an apparent suppression of the sharp phonon peaks demonstrated a size-dependent phonon confinement in the simulated NPs, as is also observed for the experimental NPs.

MD-calculated contributions to the VDOS of atoms with different coordination showed that the largest contribution to the VDOS enhancements, at high and low E, originates from surface and interface atoms, whereas the perfect bcc core of the NPs behaves nearly bulk-like, except for E < ~4-5 meV (see below). The simulations of our collaborator, with Fe NPs(bcc-core)/Ag, also show that surface layers contribute significantly to the observed differences from the bulk Fe-foil and that the NP core behaves in a bulk-like fashion (above ~5 meV).Yildirim et al. [388] have recently calculated the surface dynamics of Ag, Cu, Au, Pd, and Pt (100) considering interactions up to 20th nearest neighbor. The authors find an overall enhancement at low energies with a corresponding decrease in high energy modes, relative to the bulk metals. Theses differences were also found to originate mainly from the first few surface layers with lower layers showing bulk-like behavior.

A striking feature measured for our supported, isolated $^{57}$Fe NPs is the anomalous non-quadratic behavior in the VDOS at low E, Figure 70. The log-log plot of $g(E) \propto E^n$ provides $n = 1.86 \pm 0.03$ ($E \leq 4.8$ meV, sample #1), $n = 1.84 \pm 0.02$ ($E \leq 5.0$ meV, sample #2) and $n = 1.33 \pm 0.01$ ($E \leq 10$ meV, sample #2b), Figure 70 (insert). These values are all below $n = 2$, and sample #2b is closer to 2D behavior ($n=1$) than to Debye behavior ($n=2$). The VDOS derived from our MD simulations also show non-Debye behavior, not only for Fe atoms at the surface but also in the core. However, the effect is much less pronounced than in the experimental systems of Figure 70. Again, this difference can be attributed to the oxide shell (samples #1, #2) or $Fe_3C$ shell (sample #2b). We therefore conclude, in agreement with Ref. [380], that the formation of an outer particle shell leads to a significant enhancement of the anomalous VDOS behavior at low energies. This is further confirmed by the fact that, for a given shell, the number of observed low-E phonon modes scales with the NP's shell thickness, Figure 70 (insert). The samples with the thickest (sample #1) and thinnest (sample #2) oxide shells (according to our XPS data) show the highest and lowest g(E) enhancements, respectively. Obviously, the nature of the shell (oxide or carbide) affects the type of non-Debye behavior at low E, presumably via differences in low-coordinated interfacial or surface Fe atoms [363, 387].

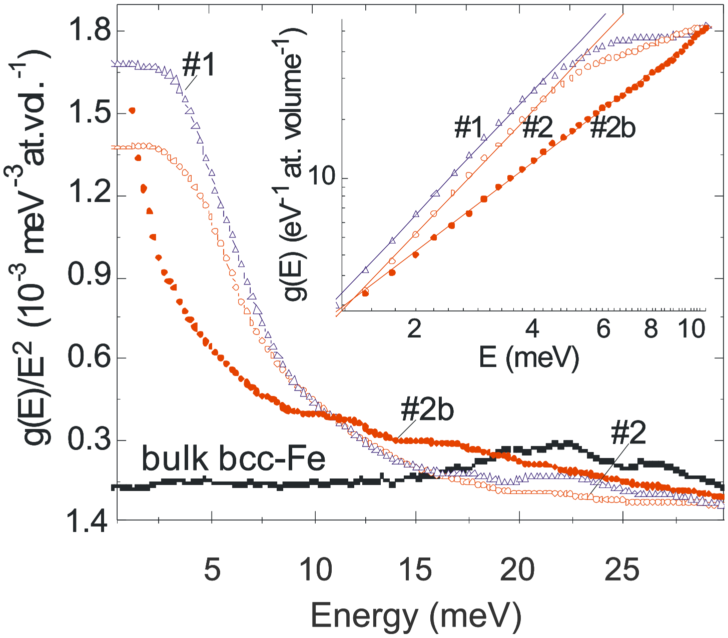

Figure 70 - (a) Measured reduced VDOS, $g(E)/E^2$, for samples #1, #2, #2b, and bulk bcc Fe.

We would like to emphasize that Debye behavior ($n \approx 2$) was reported for partially oxidized, compacted nanocrystalline Fe [369, 370, 372-375, 381, 389]. This is not surprising, because such a compacted powder material is inherently a 3D system, contrary to the case of our self-organized arrays of isolated NPs with their large surface-to-volume ratio. The latter property implies low-coordinated interfacial core/shell and/or shell surface states, which, according to theory [363, 379, 380, 387], lead to the tendency of 2D behavior in isolated NPs.

## 10.3 Conclusions

In summary, our measured VDOS of supported, isolated, single-grain $^{57}$Fe NPs reveal an enhancement of the low- and high-E phonon modes and non-Debye behavior in the low-E region. Experimentally, the non-Debye behavior was found to depend on the nature of the NP's surface shell. It reveals a tendency towards 2D vibrational behavior, very likely due to the high number of low-coordinated interfacial core/shell and/or shell surface states. We suppose that our conclusions are not limited to Fe NPs, but are valid for metal NPs in general. The modified VDOS observed for NPs is expected to affect their thermal stability and other temperature-related properties such as chemical order-disorder transitions and the pre-exponential factor in Arrhenius-type surface phenomena.

# CHAPTER 11: PHONON DENSITY OF STATES OF Fe-Pt ALLOY NPs: SEGREGATION PHENOMENA

B. Roldan Cuenya, J. R. Croy, L. K. Ono, A. Naitabdi, H. Heinrich, W. Keune, J. Zhao, W. Sturhahn, E. E. Alp, and M. Hu. Physical Review B 80 (2009) 125412

## 11.1 Experimental

Monolayer-thick films of size-selected, isolated $^{57}Fe_{1-x}Pt_x$ NPs uniformly spaced over large surface areas were prepared by micelle encapsulation [243, 283, 331, 390] of $^{57}FeCl_3$ and $H_2PtCl_6$ salts in PS(27700)-P2VP(4300) diblock copolymers. Samples of bimetallic particles with two different nominal compositions of $^{57}Fe_{0.8}Pt_{0.2}$ (sample #1) and $^{57}Fe_{0.3}Pt_{0.7}$ (sample #2) were obtained by tuning the relative concentration ratio of the two metal salts.

NRIXS on the $SiO_2$/Si(111) supported $^{57}$Fe-Pt NPs was performed at RT in air at beamlines 3-ID and HP-CAT16 of the APS (ANL, Chicago) by tuning the synchrotron beam energy around the resonant energy of 14.4125 keV of the $^{57}$Fe nucleus with an energy resolution of 2.3 meV (1.0 meV) for sample #1 (sample #2).

Figure 71 shows atomic force microscopy (AFM) images from (a) sample #1 (nominal $^{57}Fe_{0.8}Pt_{0.2}$) and (b) sample #2 (nominal $^{57}Fe_{0.3}Pt_{0.7}$) containing NPs deposited on $SiO_2$/Si(111). The average NP height before $Ar^+$ etching for these samples is 2.1 ± 0.4 nm. The etching did not result in distortions of the NP's spatial arrangement. It did, however, provide an ultra thin Si coating due to sputtering of Si atoms from the Si(111) substrate that prevented the NPs from oxidation upon air exposure, as evidenced by our cross sectional TEM [Figure 71(c)] and XPS data (see below).

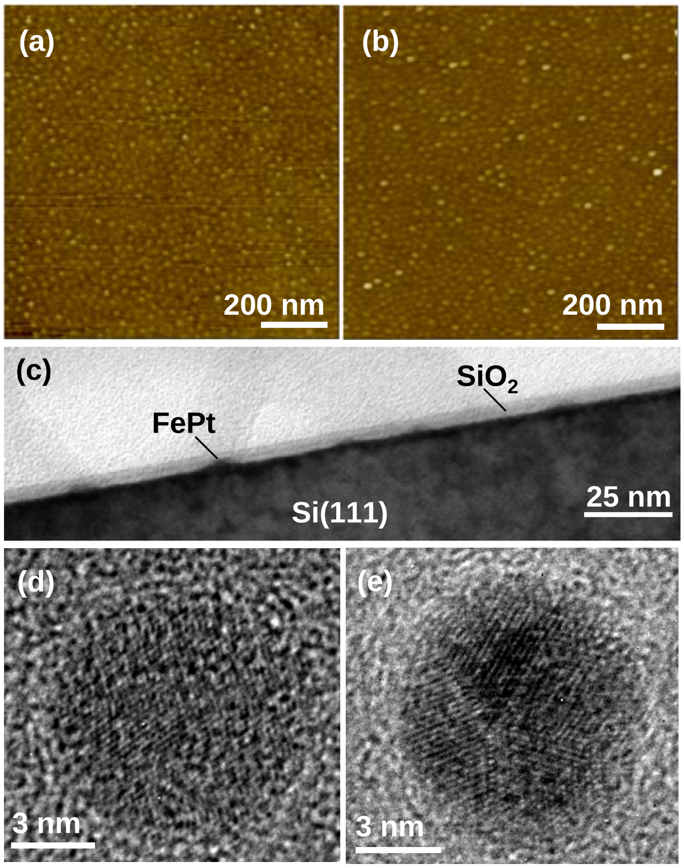

Figure 71 – AFM and HR-TEM images of sample #1 (a),(d) and sample #2 (b),(e), with Fe-Pt alloy NPs (NPs) synthesized as described in the text. (c) Cross sectional TEM image of NPs similar to those in sample #2, but synthesized using PS(81000)-P2VP(14200) and deposited on SiO$_2$/Si(111). All images were taken after polymer removal by annealing in UHV at 500°C and subsequent Ar$^+$-sputter etching (0.5 keV, 20 min) at room temperature. TEM images acquired by H. Heinrich (UCF).

HR-TEM images from samples #1 and #2 (NPs deposited on C-coated Cu grids) are shown in Figure 71(d) and (e), respectively. Single-grain NPs were observed in the case of sample #1, while multifaceted grains were detected in sample #2. The resolution of our TEM was not sufficient to detect a shell around the NP core. From these images, the typical particle diameters are ~8.2 nm. According to our TEM and AFM data the aspect ratio (diameter/height) of our NPs is ~4. From the FFT analysis of the TEM images in Figure 71(d), (e), a lattice parameter of a = 0.309 ± 0.007 nm (0.379 ± 0.007 nm) was determined for sample #1 (sample #2), assuming the bcc (fcc) phase. Our NRIXS results (see below) support the bcc (fcc) structure for sample #1 (sample #2). As a reference, the lattice parameters of bulk alloys with composition $Fe_{0.8}Pt_{0.2}$ (bcc) and $Fe_{0.75}Pt_{0.25}$ (fcc, $Fe_3Pt$) are given by 0.297 nm (extrapolated from data in Ref. [391] ), and 0.375 nm [305], respectively. Comparison indicates that the NPs in sample #1 are close to bcc $Fe_{0.8}Pt_{0.2}$, i.e., close to the nominal composition, while the NPs in sample #2 are close to fcc $Fe_{0.75}Pt_{0.25}$, which differs significantly from the nominal particle composition of $Fe_{0.3}Pt_{0.7}$. As will be discussed later, this is attributed to the segregation of Pt to the NP surface leaving an Fe-rich core.

Figure 72 displays XPS spectra from the Fe-2p (a) and Pt-4f (b) core level regions of NPs in sample #2 (i), (ii), and sample #1 (iii),(iv), deposited on $SiO_2$/Si(111). $Ar^+$ etching resulted in an ultra thin Si-coating on the samples that largely protected the NPs against oxidation, since no $Fe^{3+}$ signal (e.g., $Fe^{3+}$-$2p_{3/2}$ in $Fe_2O_3$: at 711 eV) [202] was detected on these samples by XPS after air exposure. The BE of Fe in these bimetallic particles ($2p_{3/2}$, 707.3 eV) is in agreement with that of metallic iron (707.0-707.3 eV) [202] or $Fe_{0.48}Pt_{0.52}$ films (707.5 eV) [392]. By contrast, a very large BE was measured for Pt in our NP samples ($4f_{7/2}$, 73.0-73.1 eV) before and after air exposure. These BEs are up to +2.0 eV larger than for bulk $Pt^0$ ($4f_{7/2}$, 71.1 eV) [202] and are attributed to the formation of PtSi ($4f_{7/2}$, 73 eV) [359]. Our annealing treatment in vacuum (at 500°C) resulted in preferential segregation of Pt to the NP surface, which readily reacted with Si during the subsequent $Ar^+$-etching procedure. This trend for Pt segregation is in agreement with calculations and experimental results on Fe-Pt systems [314, 319, 323]. We infer that our NPs carry a thin PtSi shell, which is much thinner for the NPs in sample #1 because of its weaker Pt-4f signal (20 % Pt content) as

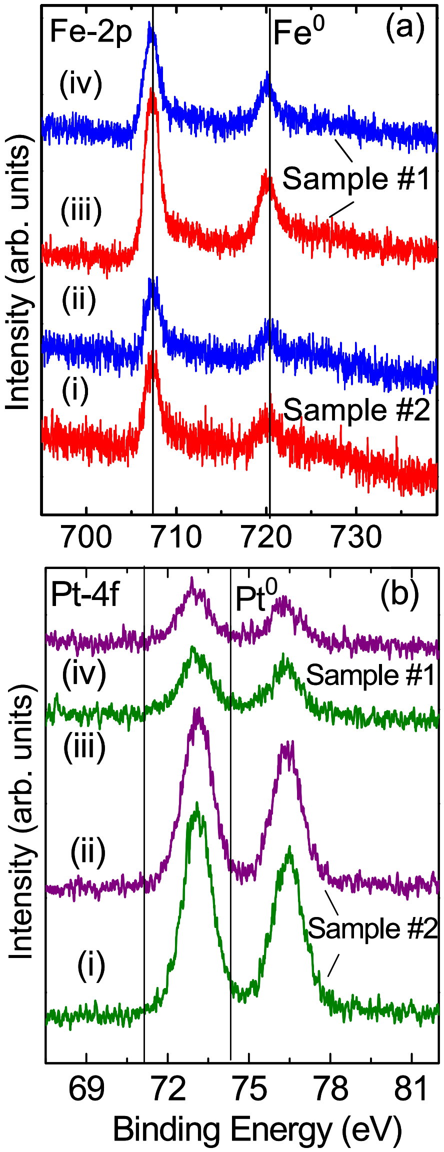

Figure 72 – XPS spectra (Al Kα = 1486.6 eV) of the Fe-2p (a) and Pt-4f (b) core levels of similarly sized Fe-Pt alloy NPs in sample #1 and sample #2 and deposited on $SiO_2$/Si(111). The spectra were measured after polymer removal by annealing in UHV at 500°C followed by $Ar^+$-sputter-etch (i),(iii), and after subsequent air exposure for 4 days (ii),(iv).

compared to sample #2 (70 % Pt content), and because the nominal and actual compositions of the NP core ($Fe_{\sim 0.8}Pt_{\sim 0.2}$) agree fairly well with each other, contrary to the case of sample #2. We expect that the observed Pt surface segregation and PtSi shell formation will influence the VDOS of the NPs (see below).

## 11.2 Results and Discussion

Figure 73 displays NRIXS spectra (raw data) of (a) sample #1 (NP core: bcc $^{57}Fe_{0.8}Pt_{0.2}$) and (b) sample #2 (NP core: fcc $^{57}Fe_{0.75}Pt_{0.25}$). The main features of these spectra are an intense elastic peak at E = 0 meV (Mössbauer or zero-phonon line) and side bands at higher and lower excitation energies E corresponding to phonon-assisted excitation of the nuclear resonance by photons via phonon creation (E>0) and annihilation (E<0). A broad and nearly structureless phonon excitation spectrum is observed for sample #1 [Figure 73(a)], while sharper phonon features near ~31 meV and ~13 meV and a cut-off near 40 meV are noticed for sample #2, Figure 73(b).

Figure 74(a) presents the Fe-projected (partial) VDOS, g(E), of sample #1 (bcc $^{57}Fe_{0.8}Pt_{0.2}$) (full squares) and of a reference bulk bcc $^{57}$Fe foil (full-drawn line), obtained from measured data. Also shown is the VDOS of a reference NP sample (reproduced from Ref. [386], full circles) containing similarly-sized, isolated, elemental bcc $^{57}$Fe NPs (of ~2.3 nm average AFM height), subjected to an identical preparation technique and carrying an Fe oxide shell [386], sample #3. Clear differences between g(E) of sample #1 and bulk bcc Fe are observed: (i) the strong suppression of the longitudinal acoustic (LA) phonon peak at ~36 meV and of the transverse acoustic (TA) modes near ~27 and ~22 meV, an effect that may be attributed to phonon damping due to confinement [370, 393]. However, a residue of the 36-meV phonon peak is visible in the g(E) of sample #1, which proves the existence of the bcc structure in the $^{57}Fe_{0.8}Pt_{0.2}$ NPs, in agreement with our TEM results. (ii) The enhancement of g(E) at low and high energies, where excitations extend beyond the cut-off energy of ~40 meV of bulk bcc Fe. This effect is less pronounced than for sample #3 [386]. According to theory, the low-E enhancement is attributed to low-coordinated vibrational

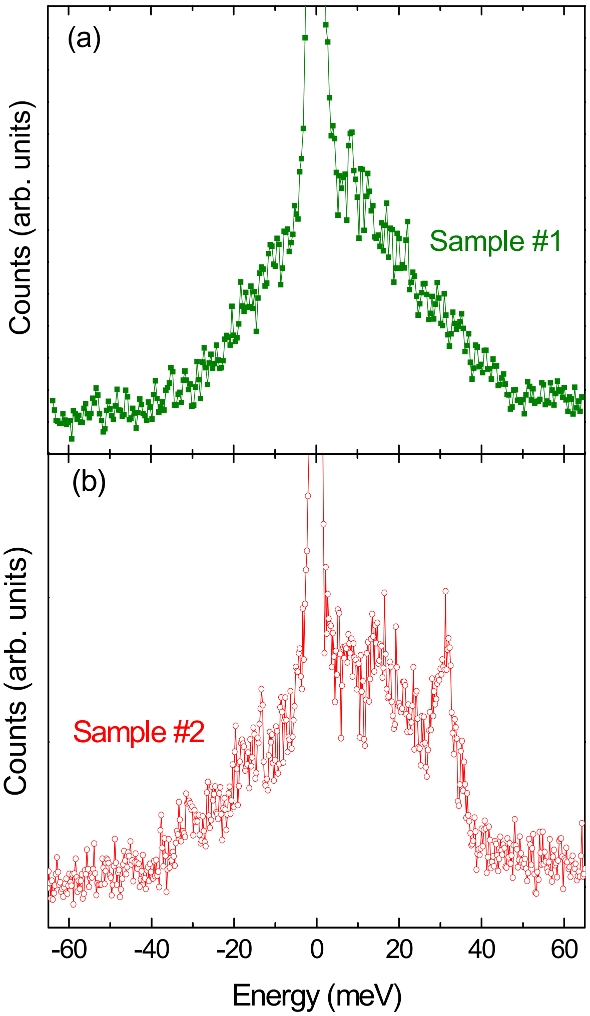

Figure 73 – Experimental NRIXS spectra (raw data) taken at RT from Fe-Pt alloy NPs supported on $SiO_2$/Si(111): (a) sample #1 (bcc alloy), (b) sample #2 (fcc alloy).

surface states [363, 377, 382, 387, 388, 390, 394, 395], while the high-E enhancement has been predicted to depend on compressive stress due to enhanced capillary forces in the NPs [377, 396] or to shrinkage of near neighbor atomic bond lengths of specific atoms relative to bulk [363, 382, 387, 394, 395]. In fact, it was observed experimentally in isolated $^{57}$Fe NPs (Chapter 10) that the low- and high-E enhancement in g(E) depends on the thickness and type of the Fe-containing shell around the $^{57}$Fe NPs (i.e. $Fe_2O_3$ or $Fe_3C$ [386]). Therefore, the

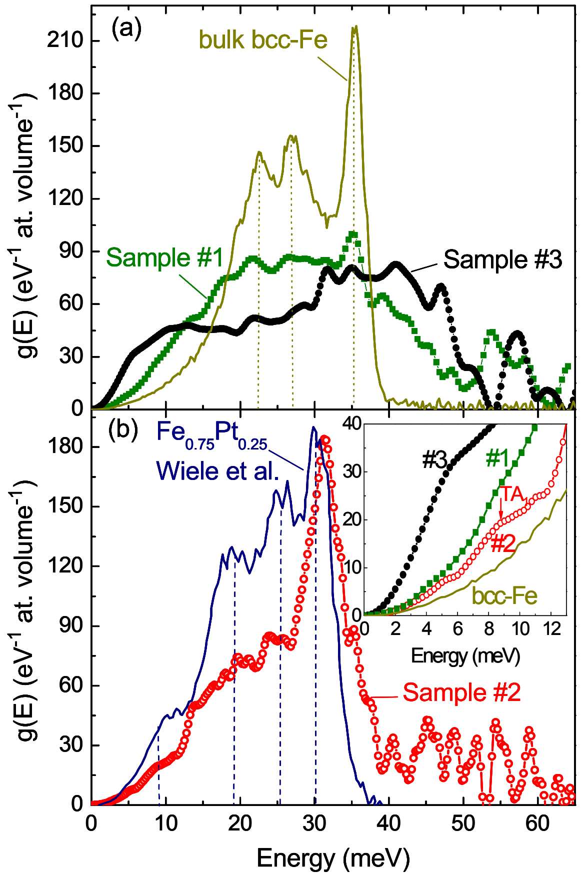

Figure 74 – VDOS, g(E), of Fe-Pt NPs, obtained from the data in Figure 73: (a) sample #1 (bcc $^{57}$Fe$_{0.8}$Pt$_{0.2}$) (full squares). Also shown: measured g(E) of bulk bcc $^{57}$Fe (full-drawn curve) and of elemental bcc $^{57}$Fe NPs (sample #3) from Ref. [386] (full circles). (b) sample #2 (fcc $^{57}$Fe$_{0.75}$Pt$_{0.25}$) (open circles). Also shown: measured g(E) of a bulk L1$_2$-ordered Fe$_{0.75}$Pt$_{0.25}$ Invar alloy [397, 398] (full-drawn curve). Inset in (b): low energy part of g(E).

remarkable decrease in the low-E and high-E regions of the VDOS of sample #1, as compared to that of sample #3 [Figure 74(a)], can be attributed to the different shell structures (PtSi versus $^{57}$Fe$_2$O$_3$). Since we measure the $^{57}$Fe-projected VDOS, the presence of Pt and Si atoms (and the decrease in the number of $^{57}$Fe atoms) at the NP surface of our sample #1 is expected to reduce the low-E part of g(E) as compared to pure $^{57}$Fe NPs.

The striking features of the Fe-projected VDOS of sample #2 (fcc $^{57}$Fe$_{0.75}$Pt$_{0.25}$) (open circles) are a strong and dominant peak at ~31 meV and relatively weak VDOS in the medium- and low-E regime of g(E), with weak bands near ~20 meV and ~25 meV, Figure 74(b). The ~31 meV peak lies at significantly lower energy than the main 36 meV peak of bulk bcc-Fe, Figure 74(a). The cut-off energy of sample #2 is at ~40 meV, as is also revealed by the NRIXS raw data, Figure 73(b) [399].

For comparison, we have reproduced in Figure 74(b) (full-drawn line) the g(E) curve of $L1_2$ -ordered bulk $Fe_{0.75}Pt_{0.25}$ Invar alloy (with a long-range order parameter S = 0.8) measured also by NRIXS by Wiele et al. [397, 398]. A comparison of these two g(E) curves reveals distinct differences, but also similarities: (i) both g(E) curves span roughly the same energy range; (ii) the strong VDOS peak at ~31 meV in sample #2 almost coincides with the most intense peak in g(E) at ~30 meV (optical phonon modes [400, 401]) in the bulk Invar sample; (iii) the weak peaks near ~20 meV and ~25 meV for sample #2 coincide with phonon bands (other optical phonons [400, 401]) at analogous positions in the bulk Invar sample; however, these phonon bands are considerably reduced in their g(E) intensity (by about 50 %) in the NPs of sample #2 as compared to g(E) of the bulk Invar alloy; (iv) a small blue-shift of the cut-off energy from ~38 meV in the bulk Invar sample to ~40 meV in sample #2 exists, and, most importantly, (v) a shoulder at ~9 meV is visible in the g(E) of both samples, although g(E) at the shoulder of sample #2 is reduced (by ~50 %) relative to that of the bulk Invar sample [Figure 74(b) and insert]. Its energy (~9 meV) agrees well with the energy (at the Brillouin zone boundary) of the [110] $TA_1$ mode in bulk ordered $Fe_3Pt$ at RT [397, 398, 400-403]. This can be seen in the inelastic neutron scattering (INS) results by Noda and Endoh [401]. In Figure 1 (panel for $\Sigma_4$) of Ref. [401] (not shown), the [110] $TA_1$ dispersion curve of bulk ordered $Fe_3Pt$ Invar alloy at 295 K can be observed to merge horizontally at the zone boundary (at a reduced wave vector ζ[110] = 0.5) at a phonon energy of ~9 meV. This implies zero group velocity and enhanced g(E) at that energy. Similar features (and, moreover, the mode softening upon cooling) can be seen in the [110] $TA_1$ dispersion curve of $L1_2$-ordered $Fe_{72}Pt_{28}$ Invar alloy, obtained by Kästner et al. [403] from INS (see Figure 1 of Ref. [403]). Wiele et al. and Wiele [397, 398], in their NRIXS work, identified the shoulder near 9 meV in g(E) of bulk ordered Fe-Pt Invar alloys with the [110] $TA_1$ mode and, in fact, observed a red shift (phonon softening) of this mode upon decreasing the temperature, in qualitative agreement with the INS results [401, 403]. Therefore, by analogy with the literature reports just described, we attribute the g(E) shoulder at ~9 meV, observed in our Figure 74(b) for sample #2, to the [110] $TA_1$ phonon mode responsible for the soft-mode behavior in bulk $Fe_3Pt$ Invar alloys and for the martensitic transition at low temperature [364, 397, 398, 402-404].

The appearance of the [110] $TA_1$ phonon mode in g(E) of sample #2 unambiguously proves that Pt atoms are dissolved in the fcc Fe lattice of the core of these NPs, and that the average alloy composition in the core is on the Fe-rich side, in agreement with our TEM results. This follows from the fact that at the Brillouin zone boundary of the [110] $TA_1$ phonon mode only Fe atoms vibrate in a rigid cubic lattice of heavy Pt atoms ($M_2$ and $M_4$ modes in ordered $Fe_3Pt$ [400-403]. Also important in this context is the observation by Fultz et al. [405] that on the Pt-rich alloy side, $L1_2$-ordered bulk $FePt_3$ alloys exhibit a dominant sharp peak (optical phonons) in g(E) at 25 meV, i.e. at significantly lower energy than our ~31 meV peak, mainly caused by the higher average mass of $FePt_3$ as compared to $Fe_3Pt$. Further, no significant feature of the $TA_1$ mode near ~7-9 meV is observed in g(E) of Pt-rich $L1_2$-ordered bulk $FePt_3$ [405]. From these considerations and from observations (i)-(iii) and (v) above, we conclude that the core of the alloy NPs in our sample #2 is close to the

$Fe_3Pt$ Invar composition and is highly $L1_2$ ordered due to the relatively high annealing temperature of 500°C. Since the presence of the [110] $TA_1$ phonon mode is an intrinsic property of bulk Fe-based ordered Invar alloys [397, 398, 400-404], the existence of this mode observed in our ordered $Fe_{0.75}Pt_{0.25}$ alloy NPs is a pre-requisite for the existence of intrinsic Invar related properties of these NPs. Therefore, the observation of the [110] $TA_1$ mode provides strong indirect evidence for the persistence of Invar-related properties in $Fe_3Pt$ NPs.

The remarkable reduction of the g(E) intensity observed in the ~20-meV and ~25-meV (optical) phonon bands of the NPs [item (iii) above and Figure 74(b)] may be due to one or more of the following reasons: (a) higher $L1_2$ ordering in the NPs than in the bulk ordered $Fe_3Pt$ alloys of Ref. [397, 398] Wiele et al. [397, 398, 404] have observed that, with increasing $L1_2$ ordering, the g(E) contributions of these medium-energy bands decrease relative to that of the dominant ~30-meV peak [406], and, moreover, that the ~30-meV peak shifts (by ~1 meV) to higher energy [397, 398, 404]. A similar blue-shift is observed for our NPs [item (iv) above]. (b) In-plane projected g(E); since our NRIXS experiment is performed at grazing incidence of the X-ray beam relative to the $SiO_2$/Si(111) wafer (substrate), it is the in-plane projected VDOS of our NPs that is measured. Any structural anisotropy, induced, for instance, by mechanical stress between NP and substrate, could result in changes in the VDOS, where certain phonon modes can be enhanced or suppressed relative to the isotropic case. Since Wiele et al. [397, 398, 404] used a polycrystalline bulk $Fe_3Pt$ sample in their NRIXS experiment, their measured g(E) is the isotropic case. (c) Phonon conversion at the NP interface; it is known that the presence of interfaces may change the character of optical phonons from pure LO (longitudinal optical) or TO (transverse optical) to a mixture involving LO, TO and interface modes [407]. Since mixing results in larger dispersion, the VDOS in NPs can be modified.

It is worthwhile mentioning that g(E) of our sample #2 (fcc $^{57}Fe_{0.75}Pt_{0.25}$) presents some resemblances with data previously measured by Tanaka et al. [408] on fcc-Fe precipitates (80 nm in diameter) using NRIXS. In particular, a dominant 31-meV peak (LA phonons), relatively strong TA bands near ~18 meV and ~23 meV, and a cut-off at ~37 meV was measured by Tanaka et al. [408], but no feature near ~7-9 meV (typical for Fe-rich Fe-Pt alloys) was observed, contrary to the case of our fcc $^{57}Fe_{0.75}Pt_{0.25}$ NPs, Figure 74(b)(inset). We would like to emphasize that for our ordered $^{57}Fe_{0.75}Pt_{0.25}$ NPs [sample #2, Figure 74(b)], we do not observe the low- and high-E enhancement of g(E) that appears for the bcc $^{57}Fe_{0.8}Pt_{0.2}$ NPs in sample #1 [Figure 74(a)]. As we discussed above, the low- and high-E enhancement of g(E) is attributed to the specific core/shell structure of these NPs (bcc $^{57}Fe_{0.8}Pt_{0.2}$ core and PtSi shell). For sample #2, due to strong Pt surface segregation, a rather thick PtSi shell exists, (as indicated by our XPS data), preventing low- and high-E enhancements of g(E), as expected.

Several important thermodynamic quantities can be derived from the measured VDOS [213, 384, 409-411], such as the Lamb-Mössbauer (Debye-Waller) factor, kinetic energy, and the vibrational entropy and specific heat (all per atom).

Table 8 displays the values obtained for the NPs in our samples #1-3, nanocrystalline Fe [370], fcc-Fe precipitates in Cu [408], and bulk bcc-Fe [412] for comparison. These quantities, together with the measured partial DOS, should allow a good test of the Fe-Fe, Fe-Pt, and Pt-Pt pair potentials in theoretical work. Generally, according to

Table 8 and independent of the structure, all values given for the NPs are smaller than for bulk bcc Fe, except the kinetic energy per atom, which appears enhanced. The values for bcc $Fe_{0.8}Pt_{0.2}$ NPs are comparable to those of nanocrystalline Fe.

Table 8 - Thermodynamic parameters derived from NRIXS measurements.

| **Sample** | **Lamb-Mössbauer Factor** | **Kinetic Energy (meV/atom)** | **Vibrational Entropy ($k_B$/atom)** | **Vibrational Specific Heat ($k_B$/atom)** |
|---|---|---|---|---|
| **$Fe_{0.8}Pt_{0.2}$ NPs (bcc), sample #1** | 0.742 (4) | 43.8 (6) | 3.00 (6) | 2.63 (8) |
| **$Fe_{0.75}Pt_{0.25}$ NPs (fcc), sample #2** | 0.773 (4) | 44.1 (8) | 2.91 (6) | 2.61 (9) |
| **Fe NPs (bcc), sample #3** (Roldan et al. [386]) | 0.612 (3) | 45.0 (9) | 2.95 (7) | 2.6 (1) |
| **Fe Nanocrystalline** (Fultz et al. [370]) | 0.755 (1) | 43.2 (1) | 3.17 (2) | 2.68 (2) |
| **Fe NPs (fcc) in Cu** (Tanaka et al. [408]) | 0.734 (4) | | | |
| **bcc-Fe (bulk)** [412] | 0.7951 (6) | 42.54 (6) | 3.133 (9) | 2.723 (9) |

## 11.3 Conclusions

Pronounced modifications (relative to the bulk) in the Fe-projected VDOS, g(E), of isolated bcc $^{57}Fe_{0.8}Pt_{0.2}$ and fcc $^{57}Fe_{0.75}Pt_{0.25}$ (Invar type) NPs on a $SiO_2$/Si(111) support have been measured by NRIXS. Segregation of Pt atoms to the NP surface was observed by XPS upon annealing and $Ar^+$ sputter etching, leading to core/shell structures with Fe-rich particle cores and PtSi particle surfaces. The enhancement of the low- and high-E regions of g(E) observed for the bcc NPs is in qualitative agreement with theoretical predictions. By contrast, due to their different shell structure, no such enhancement was observed for the fcc Fe NPs, which show characteristic phonon features of bulk ordered $Fe_3Pt$ Invar alloys. Our observation of the Invar-typical [110] $TA_1$ phonon mode in $^{57}Fe_{0.75}Pt_{0.25}$ NPs provides indirect evidence for the persistence of Invar-related effects in NPs. The obtained modified VDOS will affect the thermal stability and thermodynamic properties of the NPs relative to bulk materials. Moreover, our work demonstrates the power of NRIXS for the non-destructive metallurgical phase analysis of alloy NPs.

# Summary

In the preceding chapters we have looked in detail at the physical, electronic, and chemical properties of supported mono and bimetallic Pt and Fe NPs. We have utilized a broad array of laboratory techniques (AFM, TEM, XPS, TPD) as well as two synchrotron facilities (APS, NSLS) to reveal the complex and dynamic nature of these nanocatalytic systems. Our use of micelle encapsulation as a synthesis technique for nanocatalysts has allowed us a high level of control over NP size distributions, which is critical when dealing with the ensemble averages obtained from most common experimental techniques. With the aid of a packed-bed reactor, QMS, XPS, and TEM we have fine-tuned the pretreatment conditions for obtaining clean, catalytically active, and mono-dispersed NP catalysts supported on a variety of nanocrystalline metal-oxides. Using EXAFS we have discerned the unique structures which result from our synthesis methods, revealing the possibility of pre-determining the shape of NP catalysts. Environmentally and economically relevant reactions (MeOH decomposition and oxidation) were used to probe the catalytic performance of our supported NPs. It was seen that a size-dependence exists for the decomposition of MeOH with decreasing NP size corresponding with increasing activity. For this reaction (MeOH decomposition) the support plays a major role, not only in the activity but also in the stability of Pt-oxide species. Less reducible supports ($ZrO_2$, $\alpha$-$Al_2O_3$) enhanced activity and stability of Pt NPs while the most reducible support ($CeO_2$) promoted agglomeration (and/or diffusion into $CeO_2$) of Pt, hindering its activity for MeOH decomposition. Parallel MeOH decomposition and oxidation experiments in conjunction with XPS data reveal that the oxides of Pt play no role in the decomposition of MeOH. However, the oxides of Pt likely play an active and dynamic role in MeOH oxidation, participating in a Mars-van Krevelen-like process, continually exchanging place with gas phase oxygen in the feed. We have also seen that oxygen in the feed, or annealing environment, can have a dominating effect in the segregation of secondary metals in Pt-M NPs. Metals with a high affinity for gas phase reactants (or adsorbates) may overcome common thermodynamic considerations (volume, surface energy, heats of sublimation) and contradict expected segregation trends. This is of great importance when designing bimetallic nanocatalysts, as the nature of the chemical environment under reaction conditions will dictate the working state of the catalyst.

The nature of the gas/adsorbate environment was reiterated in Chapter 9 where AFM, XPS, and TPD revealed the dynamic properties of supported Pt NPs. Here we saw that the oxygen uptake of our micelle-synthesized Pt NPs, supported on $SiO_2$/Si(100), continually changed when exposed to repeated cycles of atomic oxygen and annealing by TPD ramps, suggesting the restructuring of our NPs under the influence of oxidation. In addition, the possible formation of volatile Pt-oxide species, accompanied by a loss of Pt, was evidenced by AFM and XPS. This is of significant environmental importance considering the amount of Pt currently used in the oxygen rich environments of automotive catalytic converters. TPD experiments also showed evidence of stronger binding of oxygen to Pt NPs than on bulk Pt(111).

In part II of our work we studied the vibrational properties (VDOS) of supported $^{57}$Fe and $^{57}$FePt NPs. Experimentally we have seen enhancements in the low and high energy regions of the VDOS with non-Debye behavior in the low energy region. The low-energy enhancement was correlated to the core/shell structures that were created during our synthesis process leading to 2D-like vibrational behavior. The effect was related to low-coordinated atoms at the NP's surface. In addition, the nature and thickness of the shell in the core/shell NPs was shown to influence these enhancements and non-Debye behavior. The increase in the number of high-energy phonon modes appeared to be correlated to the presence of surface oxides, as well as to enhanced capillary pressures predicted in theory for such confined systems.

For $^{57}Fe_{0.8}Pt_{0.2}$ bcc NPs the same enhancements in the VDOS states have been observed as in the cased of monometallic $^{57}Fe$ NPs. For $^{57}Fe_{0.75}Pt_{0.25}$ NPs a thick PtSi shell surrounding an fcc Fe-rich core was formed during NP synthesis, resulting in no enhancements in the low-energy region of the VDOS. However, our experimental data show that characteristics of ordered $Fe_3Pt$ Invar alloys persist in these NPs. The VDOS obtained for these NPs contains thermodynamic information important for understanding the thermal transport and stability of nanoscale systems.

## Outlook

The continuation of the work described in this thesis should focus on the dynamic nature of NP catalysts as revealed in the preceding chapters. More specifically, *in-situ* spectroscopic techniques capable of following the morphological changes which occur in NPs, under realistic reaction environments, should be employed. Most suitable for these studies are *in-situ* EXAFS and environmental TEM experiments where reactant gases, temperature, and pressure can be controlled while acquiring detailed morphological and structural data. The focus should be on industrially relevant reactions which happen under both oxidizing and reducing conditions. For example, CO oxidation and/or $NO_x$ reduction, where the feed gas can be cycled from oxygen-lean to oxygen-rich while monitoring NP structure and surface oxidation/reduction. In addition, the micelle encapsulation technique should be further explored with the goal of a detailed knowledge of how NPs are formed inside the micelles and how such NPs might evolve under reaction conditions. For Example, further work on the optimum pretreatment conditions which can minimize NP sintering or non-thermal methods of polymer removal and metal-salt reduction is needed.

# LIST OF PUBLICATIONS

1) Size Dependent Study of MeOH Decomposition Over Size-selected Pt Nanoparticles Synthesized via Micelle Encapsulation. Jason R. Croy, S. Mostafa, J. Liu, Yong-ho Sohn, and B. Roldan Cuenya, Catal. Lett. 118 (2007) 1.

2) Support Dependence of MeOH Decomposition Over Size-selected Pt Nanoparticles. Jason R. Croy, S. Mostafa, J. Liu, Yong-ho Sohn, H. Heinrich, and B. Roldan Cuenya, Catal. Lett. 119 (2007) 209.

3) Atomic Vibrations in Iron Nanoclusters: Nuclear Resonant Inelastic X-ray Scattering and Molecular Dynamics Simulations. B. Roldan Cuenya, A. Naitabdi, Jason R. Croy, W. Sturhahn, J. Y. Zhao, E. E. Alp, R. Meyer, D. Sudfeld, E. Schuster, and W. Keune, Phys. Rev. B 76 (2007) 195422.

4) Bimetallic Pt-Metal Catalysts for the Decomposition of Methanol: Effect of Secondary Metal on the Oxidation State, Activity, and Selectivity of Pt. Jason R. Croy, S. Mostafa, L. Hickman, H. Heinrich, and B. Roldan Cuenya, Appl. Catal. A 350 (2008) 207.

5) Size-selected Pt Nanoparticles Synthesized via Micelle Encapsulation: Effect of Pretreatment and Oxidation State on the Activity for Methanol Decomposition and Oxidation. Jason R. Croy, S. Mostafa, H. Heinrich, and B. Roldan Cuenya, Catal. Lett. 131 (2009) 21.

6) Catalytic Decomposition of Alcohols Over Size-selected Pt Nanoparticles Supported on $ZrO_2$: A Study of Activity, Selectivity, and Stability. S. Mostafa, Jason R. Croy, H. Heinrich, B. Roldan Cuenya, Appl. Cat. A 366 (2009) 353.

7) Phonon Density of States of Self-assembled Isolated Fe-rich Fe-Pt Alloy Nanoclusters. B. Roldan Cuenya, Jason R. Croy, L. K. Ono, A. Naitabdi, H. Heinrich, W. Keune, J. Zhao, W. Sturhahn, E. E. Alp, and M. Hu, Phys. Rev. B 80 (2009) 125412.

8) Structure and Phonon Density of States of Supported Size-selected $^{57}$FeAu Nanoclusters: A Nuclear Resonant Inelastic X-ray Scattering Study. B. Roldan Cuenya, L. K. Ono, Jason R. Croy, A. Naitabdi, H. Heinrich, J. Zhao, E. E. Alp, W. Sturhahn, and W. Keune, App. Phys. Lett. 95 (2009) 143103.

9) Solving the Structure of Size-Selected Pt nanocatalysts Synthesized by Inverse Micelle Encapsulation. B. Roldan Cuenya, Jason R. Croy, S. Mostafa, F. Behafarid, L. Li, Z. Zhang, J.C. Yang, Q. Wang, and A.I. Frenkel, (2010) submitted.

# REFERENCES

[1] M. E. Elvira, ed. *The Discovery of the Elements*, Mack Printing Co., Easton, PA, 1935.

[2] H. Connor, Platinum Metals Rev. 11 (1967) 2.

[3] M. A. Barakat, and M. H. H. Mahmoud, Hydrometallurgy 72 (2004) 179.

[4] R. F. D. Bradshaw, Platinum Metals Rev. 21 (1977) 129.

[5] F. Garin, Catal. Today 89 (2004) 255.

[6] C. C. Peavy, Platinum Metals Rev. 2 (1958) 48.

[7] A. L. Harris, X. H. Yang, A. Hegmans, L. Povirk, J. J. Ryan, L. Kelland, and N. P. Farrell, Inorg. Chem. 44 (2005) 9598.

[8] *Platinum Metals Review*, http://www.platinummetalsreview.com, 2009.

[9] G. A. Somorjai, and K. McCrea, Appl. Catal. A 222 (2001) 3.

[10] E. J. Carlson, P. Kopf, J. Sinha, S. Sriramulu, and Y. Yang, National Renewable Energy Laboratory, Cost Analysis of PEM Fuel Cell Systems for Transportation, (2005).

[11] *Energy Information Adminsistration*, http://www.eia.doe.gov, 2009.

[12] B. Grzybowska-Swierkosz, Catal. Today 112 (2006) 3.

[13] J. A. Rodriguez, J. Evans, J. Graciani, J. B. Park, P. Liu, J. Hrbek, and J. F. Sanz, J. Phys. Chem. C 113 (2009) 7364.

[14] K. M. Parida, N. Sahu, P. Mohapatra, and M. S. Scurrell, J. Mol. Catal. A 319 (2010) 92.

[15] G. C. Bond, and D. T. Thompson, Catal. Rev. 41 (1999) 319.

[16] M. Haruta, Chem. Rec. 3 (2003) 75.

[17] F. Vila, J. J. Rehr, J. Kas, R. G. Nuzzo, and A. I. Frenkel, Phys. Rev. B 78 (2008) 121404(R).

[18] S. Giorgio, M. Cabie, and C. R. Henry, Gold Bull. 41 (2008) 167.

[19] S. Giorgio, S. S. Joao, S. Nitsche, D. Chaudanson, G. Sitja, and C. R. Henry, Ultramicroscopy 106 (2006) 503.

[20] P. Nolte, A. Stierle, N. Y. Jin-Phillipp, N. Kasper, T. U. Schulli, and H. Dosch, Science 321 (2008) 1654.

[21] M. Haruta, J. New Mat. Electr. Sys. 7 (2004) 163.

[22] M. Haruta, T. Kobayashi, H. Sano, and N. Yamada, Chem. Lett. 16 (1987) 405.

[23] M. Haruta, CATTECH 6 (2002) 102.

[24] J. Schwank, Gold Bull. 16 (1983) 103.

[25] A. Cho, Science 299 (2003) 1684.

[26] B. Roldan Cuenya, Thin Solid Films 518 (2010) 3127.

[27] M. Valden, X. Lai, and D. W. Goodman, Science 281 (1998) 1647.

[28] C. R. Henry, Prog. Surf. Sci. 80 (2005) 92.

[29] K. Asakura, W. J. Chun, M. Shirai, K. Tomishige, and Y. Iwasawa, J. Phys. Chem B 101 (1997) 5549.

[30] S. N. Reifsnyder, M. M. Otten, D. E. Sayers, and H. H. Lamb, J. Phys. Chem. B 101 (1997) 4972.

[31] Z. Xu, F. S. Xiao, S. K. Purnell, O. Alexeev, S. Kawi, S. E. Deutsch, and B. C. Gates, 372 (1994) 346.

[32] V. Komanicky, H. Iddir, K. C. Chang, A. Menzel, G. Karapetrov, D. Hennessy, P. Zapol, and H. You, J. Am. Chem. Soc. 131 (2009) 5732.

[33] L. M. Falicov, and G. A. Somorjai, Proc. Natl. Acad. Sci. USA 82 (1985) 2207.

[34] M. Mavrikakis, P. Stoltze, and J. Norskov, Catal. Lett. 64 (2000) 101.

[35] M. Haruta, Catal. Today 36 (1997) 153.

[36] N. Lopez, T. V. W. Janssens, B. S. Clausen, Y. Xu, M. Mavrikakis, T. Bligaard, and J. K. Norskov, J. Catal. 223 (2004) 232.

[37] A. Schneider, M. Wenderoth, K. J. Engel, M. A. Rosentreter, A. J. Heinrich, and R. G. Ulbrich, Appl. Phys. A Mater. 66 (1998) S161.

[38] F. Mehmood, A. Kara, T. S. Rahman, and K. P. Bohnen, Phys. Rev. B 74 (2006) 155439.

[39] F. Mehmood, A. Kara, T. S. Rahman, and C. R. Henry, Phys. Rev. B 79 (2009) 075422.

[40] P. S. Bagus, C. R. Brundle, G. Pacchioni, and F. Parmigiani, Surf. Sci. Rep. 19 (1993) 265.

[41] P. S. Bagus, F. Illas, G. Pacchioni, and F. Parmigiani, J. Electron. Spectrosc. 100 (1999) 215.

[42] Z. X. Yang, and R. Q. Wu, Phys. Rev. B 67 (2003) 081403(R).

[43] S. J. Tauster, Accounts Chem. Res. 20 (1987) 389.

[44] D. R. Rainer, and D. W. Goodman, J. Mol. Catal. A 131 (1998) 259.

[45] T. Dellwig, J. Hartmann, J. Libuda, I. Meusel, G. Rupprechter, H. Unterhalt, and H. J. Freund, J. Mol. Catal. A 162 (2000) 51.

[46] T. Schalow, B. Brandt, M. Laurin, S. Schauermann, S. Guilmond, H. Kuhlenbeck, J. Libuda, and H. J. Freund, Surf. Sci. 600 (2006) 2528.

[47] X. L. Tang, B. C. Zhang, Y. Li, Y. D. Xu, Q. Xin, and W. J. Shen, Catal. Lett. 97 (2004) 163.

[48] J. Zhou, Y. C. Kang, and D. A. Chen, Surf Sci 537 (2003) L429.

[49] L. Giordano, J. Goniakowski, and G. Pacchioni, Phys Rev B 64 (2001) 075417.

[50] E. Wahlstrom, N. Lopez, R. Schaub, P. Thostrup, A. Ronnau, C. Africh, E. Laegsgaard, J. K. Norskov, and F. Besenbacher, Phys Rev Lett 90 (2003) 026101.

[51] S. Laursen, and S. Linic, Phys. Rev. Lett. 97 (2006) 026101.

[52] J. A. Rodriguez, F. Vines, F. Illas, P. Liu, Y. Takahashi, and K. Nakamura, J. Chem. Phys. 127 (2007) 211102.

[53] J. H. Kang, L. D. Menard, R. G. Nuzzo, and A. I. Frenkel, JACS 128 (2006) 12068.

[54] S. I. Sanchez, L. D. Menard, A. Bram, J. H. Kang, M. W. Small, R. G. Nuzzo, and A. I. Frenkel, JACS 131 (2009) 7040.

[55] Y. Matsumura, M. Okumura, Y. Usami, K. Kagawa, H. Yamashita, M. Anpo, and M. Haruta, Catal. Lett. 44 (1997) 189.

[56] A. V. Ivanov, and L. M. Kustov, Russ Chem B+ 47 (1998) 1061.

[57] C. Hardacre, R. M. Ormerod, and R. M. Lambert, J. Phys. Chem. 98 (1994) 10901.

[58] A. Badri, C. Binet, and J. C. Lavalley, J. Chem. Soc. Faraday Trans. 92 (1996) 1603.

[59] B. R. Powell, and S. E. Whittington, J. Catal. 81 (1983) 382.

[60] H. P. Sun, X. P. Pan, G. W. Graham, H. W. Jen, R. W. McCabe, S. Thevuthasan, and C. H. F. Peden, Appl. Phys. Lett. 87 (2005) 201915.

[61] P. Wynblatt, and N. A. Gjostein, Prog. Solid State Chem. 9 (1975) 21.

[62] S. C. Parker, and C. T. Campbell, Phys. Rev. B 75 (2007).

[63] R. S. Goeke, and A. K. Datye, Top. Catal. 46 (2007) 3.

[64] A. Naitabdi, F. Behafarid, and B. R. Cuenya, Appl. Phys. Lett. 94 (2009) 083102.

[65] Q. Fu, H. Saltsburg, and M. Flytzani-Stephanopoulos, Science 301 (2003) 935.

[66] J. Tang, J. M. Lawrence, and J. C. Hemminger, Phys. Rev. B 47 (1993) 16477.

[67] X. L. Zhu, T. Hoang, L. L. Lobban, and R. G. Mallinson, Catal. Lett. 129 (2009) 135.

[68] L. Khelifi, and A. Ghorbel, J. Sol-Gel Sci. Tech. 19 (2000) 643.

[69] M. Vaarkamp, J. T. Miller, F. S. Modica, and D. C. Koningsberger, J. Catal. 163 (1996) 294.

[70] Y. Men, H. Gnaser, R. Zapf, V. Hessel, and C. Ziegler, Catal. Commun. 5 (2004) 671.

[71] A. B. Boffa, C. Lin, A. T. Bell, and G. A. Somorjai, Catal. Lett. 27 (1994) 243.

[72] R. J. Farrauto, and C. H. Bartholomew, *Fundamentals of Industrial Catalytic Processes*, First ed., Blackie Academic and Professional, London, 1997.

[73] *Platinum 2009 Interim Review*, Johnson Matthey, London (2009).

[74] C. R. Parkinson, M. Walker, and C. F. McConville, Surf. Sci. 545 (2003) 19.

[75] J. F. Weaver, H. H. Kan, and R. B. Shumbera, J. Phys-Condens. Matter 20 (2008).

[76] N. Saliba, Y. L. Tsai, C. Panja, and B. E. Koel, Surf. Sci. 419 (1999) 79.

[77] J. L. Gland, Surf. Sci. 93 (1980) 487.

[78] J. Wintterlin, S. Volkening, T. V. W. Janssens, T. Zambelli, and G. Ertl, Science 278 (1997) 1931.

[79] D. H. Parker, M. E. Bartram, and B. E. Koel, Surf. Sci. 217 (1989) 489.

[80] A. Eichler, F. Mittendorfer, and J. Hafner, Phys. Rev. B 62 (2000) 4744.

[81] S. P. Devarajan, J. A. Hinojosa, and J. F. Weaver, Surf. Sci. 602 (2008) 3116.

[82] J. F. Weaver, J. J. Chen, and A. L. Gerard, Surf. Sci. 592 (2005) 83.

[83] M. Todorova, W. X. Li, M. V. Ganduglia-Pirovano, C. Stampfl, K. Reuter, and M. Scheffler, Phys. Rev. Lett. 89 (2002).

[84] P. J. Ferreira, G. J. la O', Y. Shao-Horn, D. Morgan, R. Makharia, S. Kocha, and H. A. Gasteiger, J. Electrochem. Soc. 152 (2005) A2256.

[85] H. Over, and A. P. Seitsonen, Science 297 (2002) 2003.

[86] K. Thurmer, E. Williams, and J. Reutt-Robey, Science 297 (2002) 2033.

[87] N. Seriani, Z. Jin, W. Pompe, and L. C. Ciacchi, Phys. Rev. B 76 (2007) 14860.

[88] M. Arenz, K. J. J. Mayrhofer, V. Stamenkovic, B. B. Blizanac, T. Tomoyuki, P. N. Ross, and N. M. Markovic, J. Am. Chem. Soc. 127 (2005) 6819.

[89] F. Mittendorfer, N. Seriani, O. Dubay, and G. Kresse, Phys. Rev. B 76 (2007) 233413.

[90] P. Nolte, A. Stierle, N. Y. Jin-Phillip, N. Kasper, T. U. Schulli, and H. Dosch, Science 321 (2008) 1654.

[91] S. Giorgio, M. Cabie, and C. R. Henry, Gold Bull. 41 (2008) 167.

[92] S. Giorgio, S. Sao Joao, S. Nitsche, D. Chaudenson, G. Sitja, and C. R. Henry, Ultramicroscopy 106 (2006) 503.

[93] C. B. Wang, and C. T. Yeh, J. Catal. 178 (1998) 450.

[94] T. Li, and P. B. Balbuena, J. Phys. Chem. B 105 (2001) 9943.

[95] N. Seriani, W. Pompe, and L. C. Ciacchi, J. Phys. Chem. B 110 (2006) 14860.

[96] L. Olsson, and E. Fridell, J. Catal. 210 (2002) 340.

[97] H. J. Bi, W. P. Cai, C. X. Kan, L. D. Zhang, D. Martin, and F. Trager, J. Appl. Phys. 92 (2002) 7491.

[98] P. A. Chernavskii, N. V. Peskov, A. V. Mugtasimov, and V. V. Lunin, Russ. J. Phys. Chem. B 1 (2007) 394.

[99] Y. Xu, J. Greeley, and M. Mavrikakis, J. Am. Chem. Soc. 127 (2005) 12823.

[100] X. Wang, W.-K. Chen, and C.-H. Lu, Appl. Surf. Sci. 254 (2008) 4421.

[101] I. E. Wachs, and R. J. Madix, J. Catal. 53 (1978) 208.

[102] L. K. Ono, and B. Roldan Cuenya, J. Phys. Chem. C 112 (2008) 4676.

[103] D. R. Rolison, P. L. Hagans, K. E. Swider, and J. W. Long, Langmuir 15 (1999) 774.

[104] J. Gustafson, R. Westerstrom, O. Balmes, A. Resta, R. van Rijn, X. Torrelles, C. T. Herbschleb, J. W. M. Frenken, and E. lundgren, J. Chem. Phys. C 114 (2010) 4580.

[105] Y. Xie, F. Dong, S. Heinbuch, J. J. Rocca, and E. R. Bernstein, Phys. Chem. Chem. Phys. 12 (2010) 947.

[106] A. F. Carley, A. W. Owens, M. K. Rajumon, M. W. Roberts, and S. D. Jackson, Catal. Lett. 37 (1996) 79.

[107] S. T. Yong, K. Hidajat, and S. Kawi, Catal. Today 131 (2008) 188.

[108] H. Over, Y. D. Kim, A. P. Seitsonen, S. Wendt, E. Lundgren, M. Schmid, P. Varga, A. Morgante, and G. Ertl, Science 287 (2000) 1474.

[109] K. Lasch, L. Jorissen, K. A. Friedrich, and J. Garche, J. Solid State Electrochem. 7 (2003) 619.

[110] B. L. M. Hendriksen, and J. W. M. Frenken, Phys. Rev. Lett. 89 (2002) 046101.

[111] X. Q. Gong, Z. P. Liu, R. Raval, and P. Hu, J. Am. Chem. Soc. 126 (2004) 8.

[112] X. Y. Deng, B. K. Min, X. Y. Liu, and C. M. Friend, J. Phys. Chem. B 110 (2006) 15982.

[113] K. K. Bando, T. Kawai, K. Asakura, T. Matsui, L. Le Bihan, H. Yasuda, Y. Yoshimura, and S. T. Oyarna, Catal. Today 111 (2006) 199.

[114] H. A. Gasteiger, S. S. Kocha, B. Sompalli, and F. T. Wagner, Appl. Catal. B 56 (2005) 9.

[115] V. A. T. Dam, and F. A. de Bruijn, J. Electrochem. Soc. 154 (2007) B494.

[116] R. V. Hull, L. Li, Y. C. Xing, and C. C. Chusuei, Chem. Mater. 18 (2006) 1780.

[117] T. Ruhle, H. Schneider, J. Find, D. Herein, N. Pfander, U. Wild, R. Schlogl, D. Nachtigall, S. Artelt, and U. Heinrich, Appl. Catal. B 14 (1997) 69.

[118] D. Fliegel, Z. Berner, D. Eckhardt, and D. Stuben, Anal. Bioanal. Chem. 379 (2004) 131.

[119] M. Peuckert, and H. P. Bonzel, Surf. Sci. 145 (1984) 239.

[120] M. Schmid, S. Zimmermann, H. F. Krug, and B. Sures, Environ. Int. 33 (2007) 385.

[121] N. M. Markovic, T. J. Scmidt, V. Stamenkovic, and P. N. Ross, Fuel Cells 1 (2001) 105.

[122] F. Wu, H. Murakami, Y. Yamabe-Mitarai, H. Harada, H. Katayama, and Y. Yamamoto, Surf. Coat. Tech. 184 (2004) 24.

[123] J. R. Rostrup-Nielsen, Phys. Chem. Chem. Phys. 3 (2001) 283.

[124] Y. Xu, A. V. Ruban, and M. Mavrikakis, J. Am. Chem. Soc. 126 (2004) 4717.

[125] U. A. Paulus, A. Wokaun, G. G. Scherer, T. J. Schmidt, V. Stamenkovic, N. M. Markovic, and P. N. Ross, Electrochim. Acta. 47 (2002) 3787.

[126] S. Mukerjee, S. Srinivasan, M. P. Soriaga, and J. Mcbreen, J. Electrochem. Soc. 142 (1995) 1409.

[127] V. A. Lubarda, Mech. Mater. 35 (2003) 53.

[128] P. L. Hansen, A. M. Molenbroek, and A. V. Ruban, J. Phys. Chem. B. 101 (1997) 1861.

[129] S. Shukla, and S. Seal, Nanostructured Materials 11 (1999) 1181.

[130] J. Zhang, F. H. B. Lima, M. H. Shao, K. Sasaki, J. X. Wang, J. Hanson, and R. R. Adzic, J. Phys. Chem. B 109 (2005) 22701.

[131] G. F. Wang, M. A. Van Hove, P. N. Ross, and M. I. Baskes, Prog. Surf. Sci. 79 (2005) 28.

[132] Z. H. Gu, and P. B. Balbuena, J. Phys. Chem. C 112 (2008) 5057.

[133] G. E. Ramirez-Caballero, and P. B. Balbuena, Chem. Phys. Lett. 456 (2008) 64.

[134] C. A. Menning, and J. G. Chen, Topics in Catalysis (2010) DOI 10.1007/s11244.

[135] P. Liu, and J. K. Norskov, Phys. Chem. Chem. Phys. 3 (2001) 3814.

[136] J. G. Chen, C. A. Menning, and M. B. Zellner, Surf. Sci. Rep. 63 (2008) 201.

[137] T. Toda, H. Igarashi, and M. Watanabe, J. Electroanal. Chem. 460 (1999) 258.

[138] H. Igarashi, T. Fujino, Y. M. Zhu, H. Uchida, and M. Watanabe, Phys. Chem. Chem. Phys. 3 (2001) 306.

[139] S. Desai, and M. Neurock, Electrochim. Acta. 48 (2003) 3759.

[140] S. Stolbov, M. A. Ortigoza, R. Adzic, and T. S. Rahman, J. Chem. Phys. 130 (2009) 124714.

[141] Q. Yi, A. Chen, W. Huang, J. Zhang, X. Liu, G. Xu, and Z. Zhou, 9 (2007) 1513.

[142] A. Morlang, U. Neuhausen, K. V. Klementiev, F. W. Schutze, G. Miehe, H. Fuess, and E. S. Lox, Appl. Catal. B 60 (2005) 191.

[143] W. Rachmady, and M. A. Vannice, J. Catal. 209 (2002) 87.

[144] M. Bowker, T. Aslam, M. Roebuck, and M. Moser, Appl. Catal. A 257 (2004) 57.

[145] S. E. Maisuls, K. Seshan, S. Feast, and J. A. Lercher, Appl. Catal. B 29 (2001) 69.

[146] J. R. Kitchin, N. A. Khan, M. A. Barteau, J. G. Chen, B. Yakshinksiy, and T. E. Madey, Surf. Sci. 544 (2003) 295.

[147] K. Endo, K. Nakamura, Y. Katayama, and T. Miura, Electrochim. Acta 49 (2004) 2503.

[148] A. Niquille-Rothlisberger, and R. Prins, Catal. Today 123 (2007) 198.

[149] D. A. Simonetti, E. L. Kunkes, and J. A. Dumesic, J. Catal. 247 (2007) 298.

[150] O. S. Alexeev, G. W. Graham, M. Shelef, and B. C. Gates, J. Catal. 190 (2000) 157.

[151] F. Donsi, K. A. Williams, and L. D. Schmidt, Ind. Eng. Chem. Res. 44 (2005) 3453.

[152] R. D. Cortright, P. E. Levin, and J. A. Dumesic, Ind. Eng. Chem. Res. 37 (1998) 1717.

[153] W. Huang, J. R. McCormick, R. F. Lobo, and J. G. Chen, J. Catal. 246 (2007) 40.

[154] M. Englisch, V. S. Ranade, and J. A. Lercher, J. Mol. Catal. A 121 (1997) 69.

[155] R. W. J. Scott, A. K. Datye, and R. M. Crooks, J. Am. Chem. Soc. 125 (2003) 3708.

[156] N. Taylor, H. Kim, and J. E. Greene, Surf. Sci. 475 (2001) 171.

[157] T. N. Taylor, and C. T. Campbell, Surf. Sci. 280 (1993) 277.

[158] J. A. Rodriguez, C. M. Truong, and D. W. Goodman, Surf. Sci. 271 (1992) L331.

[159] R. Zeis, A. Mathur, G. Fritz, J. Lee, and J. Erlebacher, J. Power Sources 165 (2007) 65.

[160] Y. H. Niu, and R. M. Crooks, C.R. Chim. 6 (2003) 1049.

[161] Y. Shu, L. E. Murillo, J. P. Bosco, W. Huang, A. I. Frenkel, and J. G. Chen, Appl. Catal. A 339 (2008) 169.

[162] J. C. Serrano-Ruiz, G. W. Huber, M. A. Sanchez-Castillo, J. A. Dumesic, F. Rodriguez-Reinoso, and A. Sepulveda-Escribano, J. Catal. 241 (2006) 378.

[163] O. Ozturk, J. B. Park, S. Ma, J. S. Ratliff, J. Zhou, D. R. Mullins, and D. A. Chen, Surf. Sci. 601 (2007) 3099.

[164] H. B. Zhao, and B. E. Koel, J. Catal. 234 (2005) 24.

[165] N. A. Zarkevich, T. L. Tan, and D. D. Johnson, Phys. Rev. B 75 (2007) 104203.

[166] A. L. Bonivardi, F. H. Ribeiro, and G. A. Somorjai, J. Catal. 160 (1996) 269.

[167] *Basic Research Needs for Solar Energy Utilization*, D.O.E., U.S. (2003).

[168] J. K. Norskov, and C. H. Christensen, Science 312 (2006) 1322.

[169] G. A. Olah, Catal Lett 93 (2004) 1.

[170] L. Spector, PCWorld.com (April 2003).

[171] M. Haruta, Y, Souma, Catal. Today 36 (1997) 1.

[172] M. S. Spencer, Topics in Catalysis 22 (2003) 135.

[173] X. H. Zhang, L. T. Luo, and Z. H. Duan, React. Kinet. Catal. Lett. 87 (2005) 43.

[174] J. Tabatabaei, B. H. Sakakini, and K. C. Waugh, Catal. Lett. 110 (2006) 77.

[175] M. Kurtz, J. Strunk, O. Hinrichsen, M. Muhler, K. Fink, B. Meyer, and C. Wöll, Angew. Chem. Int. Edit. 44 (2005) 2790.

[176] H. Wilmer, M. Kurtz, K. V. Klementiev, O. P. Tkachenko, W. Grunert, O. Hinrichsen, A. Birkner, S. Rabe, K. Merz, M. Driess, C. Woll, and M. Muhler, Phys. Chem. Chem. Phys. 5 (2003) 4736.

[177] www.methanol.org.

[178] R. Garcia, and R. Perez, Surf. Sci. Rep. 47 (2002) 197.

[179] N. C. Santos, and M. A. R. B. Castanho, Biophys. Chem. 107 (2004) 133.

[180] F. J. Giessibl, Rev. Mod. Phys. 75 (2003) 949.

[181] *MultiMode$^{TM}$ SPM Instruction Manual*, Digital Instruments Veeco Metrology Group, (1999).

[182] A. V. Pokropivnyi, V. V. Pokropivnyi, and V. V. Skorokhod, Tech. Phys. 42 (1997) 1435.

[183] P. Neuzil, and R. Nagarajan, J. Micromech. Microeng. 16 (2006) 1298.

[184] Veeco Probes, http://www.veecoprobes.com, 2010.

[185] Y. Gan, Surf. Sci. Rep. 64 (2009) 99.

[186] M. von Heimendahl, *Electron Microscopy of Materials An Introduction*, Academic Press, New York, 1980.

[187] C. B. Lioutas, G. Zoulis, S. Konidaris, E. K. Polychroniadis, and D. Stroz, Micron 40 (2009) 6.

[188] Z. L. Zhang, and U. Kaiser, Ultramicroscopy 109 (2009) 1114.

[189] L. Miao, S. Tanemura, T. Jiang, M. Tanemura, K. Yoshida, N. Tanaka, and G. Xu, Superlattice Microst. 46 (2009) 357.

[190] N. Tanaka, Sci. Technol. Adv. Mat. 9 (2008) 014111.

[191] P. J. Goodhew, J. Humphreys, and R. Beanland, *Electron Microscopy and Analysis*, 3rd ed., Taylor and Francis, London, 2001.

[192] F. Ernst, and M. Ruhle, Curr. Opin. Solid St. Mat. Sci. 2 (1997) 469.

[193] P. L. Hansen, S. Helveg, and A. K. Datye, Adv. Catal. 50 (2006) 77.

[194] P. A. Crozier, R. G. Wang, and R. Sharma, Ultramicroscopy 108 (2008) 1432.

[195] H. H. Rose, Sci. Technol. Adv. Mat. 9 (2008) 014107.

[196] A. Cimino, D. Gazzoli, and M. Valigi, J. Electron. Spectrosc. 104 (1999) 1.

[197] A. M. Venezia, Catal. Today 77 (2003) 359.

[198] P. Beccat, P. Da Silva, Y. Huiban, and S. Kasztelan, Oil Gas Sci. Technol. 54 (1999) 487.

[199] J. W. Niemantsverdriet, *Spectroscopy in Catalysis*, VCH Publishers, New York, 1993.

[200] H. Rosner, J. Gegner, D. Regesch, W. Schnelle, R. Gumeniuk, A. Leithe-Jasper, H. Fujiwara, T. Haupricht, T. C. Koethe, H. H. Hsieh, H. J. Lin, C. T. Chen, A. Ormeci, Y. Grin, and L. H. Tjeng, Phys. Rev. B 80 (2009) 075114.

[201] A. Howard, D. N. S. Clark, C. E. J. Mitchell, R. G. Egdell, and V. R. Dhanak, Surf. Sci. 518 (2002) 210.

[202] NIST, X-ray Photoelectron spectroscopy Database, Version 3.4 (Web Version), http://srdata.nist.gov/xps/index.htm

[203] J. B. Miller, H. R. Siddiqui, S. M. Gates, J. N. Russell, J. T. Yates, J. C. Tully, and M. J. Cardillo, J. Chem. Phys. 87 (1987) 6725.

[204] A. M. Dejong, and J. W. Niemantsverdriet, Surf. Sci. 233 (1990) 355.

[205] L. K. Ono, and B. Roldan Cuenya, J. Phys. Chem. C 112 (2008) 18543.

[206] D. L. S. Nieskens, A. P. van Bavel, and J. W. Niemantsverdriet, 546 (2003) 159.

[207] B. Mayer, C. C. Collins, and M. Walton, J. Vac. Sci. Technol. A 19 (2001) 329.

[208] R. Talman, *Accelerator X-ray Sources*, Wiley-VCH, Weinheim, 2006.

[209] W. Sturhahn, E. E. Alp, T. S. Toellner, P. Hession, M. Hu, and J. Sutter, Hyperfine Interact. 113 (1998) 47.

[210] G. Schatz, and A. Weidinger, *Condensed Nuclear Matter Physics Nuclear Methods and Applications*, 2nd ed., John Wiley and Sons Ltd, West Sussex, 1996.

[211] R. Rolhsberger, *Nuclear Condensed Matter Physics with Synchrotron Radiation: basic principles, methodology and applications*, Springer, New York, 2004.

[212] E. E. Alp, W. Sturhahn, and T. S. Toellner, Hyperfine Interact. 135 (2001) 295.

[213] A. I. Chumakov, and W. Sturhahn, Hyperfine Interact. 123 (1999) 781.

[214] E. E. Alp, W. Sturhahn, T. S. Toellner, J. Zhao, M. Hu, and D. E. Brown, Hyp. Interact. 144 (2002) 3.

[215] D. E. Sayers, E. A. Stern, and F. W. Lytle, Phys. Rev. Lett. 27 (1971) 1204.

[216] J. J. Rehr, and R. C. Albers, Rev. Mod. Phys. 72 (2000) 621.

[217] M. Newville, J. Synch. Rad. 8 (2001) 96.

[218] D. C. Koningsberger, and R. Prins, ed. *X-Ray Absorption: Principles, Applications, Techniques of EXAFS, SEXAFS and XANES* Vol. Wiley-Interscience, New York, 1988.

[219] G. Meitzner, G. H. Via, F. W. Lytle, and J. H. Sinfelt, J. Phys. Chem. 96 (1992) 4960.

[220] A. L. Ankudinov, J. J. Rehr, J. J. Low, and S. R. Bare, J. Chem. Phys. 116 (2002) 1911.

[221] M. Azar, V. Caps, F. Morfin, J. L. Rousset, A. Piednoir, J. C. Bertolini, and L. Piccolo, J. Catal. 239 (2006) 307.

[222] B. Roldan Cuenya, S. H. Baeck, T. F. Jaramillo, and E. W. McFarland, J. Am. Chem. Soc. 125 (2003) 12929.

[223] H. G. Boyen, G. Kastle, F. Weigl, B. Koslowski, C. Dietrich, P. Ziemann, J. P. Spatz, S. Riethmuller, C. Hartmann, M. Moller, G. Schmid, M. G. Garnier, and P. Oelhafen, Science 297 (2002) 1533.

[224] S. Altwasser, R. Glaser, and J. Weitkamp, Micropor. Mesopor. Mat. 104 (2007) 281.

[225] J. Weitkamp, Solid State Ionics 131 (2000) 175.

[226] J. Libuda, S. Schauermann, M. Laurin, T. Schalow, and H. J. Freund, Monatshefte Fur Chemie 136 (2005) 59.

[227] J. A. Schwarz, C. Contescu, and A. Contescu, Chem. Rev. 95 (1995) 477.

[228] U. Heiz, and U. Landman, ed. *Nanocatalysis*, Vol. Springer, Heidelberg, 2007.

[229] B. Kasemo, S. Johansson, H. Persson, P. Thormahlen, and V. P. Zhdanov, Top. Catal. 13 (2000) 43.

[230] J. Regalbuto, ed. *Catalyst Preparation*, Vol. CRC Press, Boca Raton, 2007.

[231] M. S. Spencer, and M. V. Twigg, Annu. Rev. Mater. Res. 35 (2005) 427.

[232] N. Zheng, J. Fan, and G. D. Stucky, J. Am. Chem. Soc. 128 (2006) 6550.

[233] G. M. Whitesides, J. P. Mathias, and C. T. Seto, Science 254 (1991) 1312.

[234] Z. S. Gao, S. K. Varshney, S. Wong, and A. Eisenberg, Macromolecules 27 (1994) 7923.

[235] S. K. Varshney, X. F. Zhong, and A. Eisenberg, Macromolecules 26 (1993) 701.

[236] J. P. Spatz, S. Mossmer, C. Hartmann, M. Moller, T. Herzog, M. Krieger, H. G. Boyen, P. Ziemann, and B. Kabius, Langmuir 16 (2000) 407.

[237] J. P. Spatz, A. Roescher, and M. Möller, Adv. Mater. 8 (1996) 337.

[238] J. P. Spatz, S. S. Sheiko, and M. Moller, Macromolecules 29 (1996) 3220.

[239] G. Kästle, H. G. Boyen, F. Weigl, G. Lengl, T. Herzog, P. Ziemann, S. Riethmuller, O. Mayer, C. Hartmann, J. P. Spatz, M. Moller, M. Ozawa, F. Banhart, M. G. Garnier, and P. Oelhafen, Adv. Func. Mater. 13 (2003) 853.

[240] L. K. Ono, and B. Roldan-Cuenya, Catal. Lett. 113 (2007) 86.

[241] A. Naitabdi and B. Roldan Cuenya, Appl. Phys. Lett. 91 (2007) 113110.

[242] R. Glass, M. Arnold, J. Blummel, A. Kuller, M. Moller, and J. P. Spatz, Adv. Func. Mater. 13 (2003) 569.

[243] A. Naitabdi, L. K. Ono, F. Behafarid, and B. Roldan Cuenya, J. Phys. Chem. C 113 (2009) 1433.

[244] S. D. Jackson, J. Willis, G. D. Mclellan, G. Webb, M. B. T. Keegan, R. B. Moyes, S. Simpson, P. B. Wells, and R. Whyman, J. Catal. 139 (1993) 191.

[245] G. Kästle, H. G. Boyen, F. Weigl, P. Ziemann, S. Riethmuller, C. H. Hartmann, J. P. Spatz, M. Moller, M. G. Garnier, and P. Oelhafen, Phase Transitions 76 (2003) 307.

[246] A. I. Frenkel, C. W. Hills, and R. G. Nuzzo, J. Phys. Chem. B 105 (2001) 12689.

[247] M. Vaarkamp, J. T. Miller, F. S. Modica, G. S. Lane, and D. C. Koningsberger, Japan. J. Appl. Phys. 32 (1993) 454.

[248] F. W. Lytle, R. B. Greegor, E. C. Marques, D. R. Sandstrom, G. H. Via, and J. H. Sinfelt, J. Catal. 95 (1985) 546.

[249] M. G. Samant, and M. Boudart, J. Phys. Chem. B 95 (1991) 4070.

[250] N. Ichikuni, and Y. Iwasawa, Catal. Lett. 20 (1993) 87.

[251] P. G. Allen, S. D. Conradson, M. S. Wilson, S. Gottesfeld, I. D. Raistrick, J. Valerio, and M. Lovato, Electrochim. Acta 39 (1994) 2415.

[252] K. Asakura, T. Kubota, W. J. Chun, Y. Iwasawa, K. Ohtani, and T. Fujikawa, J. Synchrotron Rad. 6 (1999) 439.

[253] T. Kubota, K. Asakura, N. Ichikuni, and Y. Iwasawa, Chem. Phys. Lett. 256 (1996) 445.

[254] H. Yoshitake, T. Mochizuki, O. Yamazaki, and K. Ota, J. Electroanal. Chem. 361 (1993) 229.

[255] M. Vaarkamp, F. S. Modica, J. T. Miller, and D. C. Koningsberger, J. Catal. 144 (1993) 611.

[256] M. M. Otten, M. J. Clayton, and H. H. Lamb, J. Catal. 149 (1994) 211.

[257] M. Vaarkamp, B. L. Mojet, M. J. Kappers, J. T. Miller, and D. C. Koningsberger, J. Phys. Chem. B 99 (1995) 16067.

[258] A. L. Ankudinov, J. J. Rehr, J. J. Low, and S. R. Bare, J. Synchrotron Rad. 8 (2001) 578.

[259] A. L. Ankudinov, J. J. Rehr, J. J. Low, and S. R. Bare, Topics in Catalys. 18 (2002) 3.

[260] A. V. Soldatov, S. Della Longa, and A. Bianconi, Solid State Commun. 85 (1993) 863.

[261] A. T. Matsuura, T. Fujikawa, and H. Kuroda, J. Phys. Soc. Japan 52 (1983) 3275.

[262] D. Glasner, and A. I. Frenkel, AIP Conf. Proc. 882 (2007) 746.

[263] J. H. Kwak, J. Hu, D. Mei, C.-W. Yi, D. H. Kim, C. H. F. Peden, L. F. Allard, and J. Szanyi, Science 325 (2009) 1670.

[264] L. L. Wang, and D. D. Johnson, J. Am. Chem. Soc. 129 (2007) 3658.

[265] A. Karim, V. Prasad, G. Mpourmpakis, W. W. Lonergan, A. I. Frenkel, J. G. Chen, and D. G. Vlachos, JACS 131 (2009) 12230.

[266] C. M. Chang, and M. Y. Chou, Phys. Rev. Lett. 93 (2004) 133401.

[267] B. Roldan Cuenya, J. R. Croy, S. Mostafa, F. Behafarid, L. Li, Z. Zhang, J. C. Yang, Q. Wang, and A. I. Frenkel, Submitted (2010).

[268] S. J. L. Billinge, and I. Levin, Science 316 (2007) 561.

[269] G. C. Bond, and S. Flamerz, Appl. Catal. 46 (1989) 89.

[270] K. Duckers, and H. P. Bonzel, Surf. Sci. 213 (1989) 25.

[271] G. M. Bancroft, I. Adams, L. L. Coatsworth, C. D. Bennewitz, J. D. Brown, and W. D. Westwood, Anal. Chem. 47 (1975) 586.

[272] K. S. Kim, N. Winograd, and R. E. Davis, J. Am. Chem. Soc. 93 (1971) 6296.

[273] M. Zhao, and R. M. Crooks, Adv. Mater. 11 (1999) 217.

[274] J. Silvestre-Albero, A. Sepulveda-Escribano, F. Rodriguez-Reinoso, and J. A. Anderson, J. Catal. 223 (2004) 179.

[275] J. L. G. Fierro, J. M. Palacios, and F. Tomas, Surf. Interface Anal. 13 (1988) 25.

[276] O. Bjorneholm, F. Federmann, F. Fossing, and T. Moller, Phys. Rev. Lett. 74 (1995) 3017.

[277] *Catalysis Looks to the Future*, National Research Council, Washington D.C. (1992).

[278] Y. Usami, K. Kagawa, M. Kawazoe, Y. Matsumura, H. Sakurai, and M. Haruta, Appl. Catal. A 171 (1998) 123.

[279] W. J. Shen, and Y. Matsumura, Phys. Chem. Chem. Phys. 2 (2000) 1519.

[280] M. P. Kapoor, Y. Ichihashi, K. Kuraoka, W. J. Shen, and Y. Matsumura, Catal. Lett. 88 (2003) 83.

[281] Y. Matsumura, K. Tanaka, N. Tode, T. Yazawa, and M. Haruta, J. Mol. Catal. A 152 (2000) 157.

[282] Y. Y. Liu, K. Suzuki, S. Hamakawa, T. Hayakawa, K. Murata, T. Ishii, and M. Kumagai, Catal. Lett. 66 (2000) 205.

[283] L. K. Ono, D. Sudfeld, and B. Roldan Cuenya, Surf. Sci. 600 (2006) 5041.

[284] X. F. Lai, and D. W. Goodman, J. Mol. Catal. A. 162 (2000) 33.

[285] S. N. Antonyuk, A. L. Lapidus, V. B. Kazanskii, V. I. Yakerson, A. A. Khanumyan, E. Z. Golosman, A. I. Nechugovskii, and O. Y. Pesin, Kinetics and Catalysis 41 (2000) 753.

[286] J. Chou, N. R. Franklin, S. H. Baeck, T. F. Jaramillo, and E. W. McFarland, Catal. Lett. 95 (2004) 107.

[287] C. T. Campbell, and C. H. F. Peden, Science 309 (2005) 713.

[288] F. Esch, S. Fabris, L. Zhou, T. Montini, C. Africh, P. Fornasiero, G. Comelli, and R. Rosei, Science 309 (2005) 752.

[289] V. I. Nefedov, D. Gati, B. F. Dzhurinskii, N. P. Sergushin, and Y. V. Salyn, Zh. Neorg. Khimii 20 (1975) 2307.

[290] G. Corro, J. L. G. Fierro, and V. C. Odilon, Catal. Commun. 4 (2003) 371.

[291] M. L. Miller, and R. W. Linton, Anal. Chem. 57 (1985) 2314.

[292] A. E. Hughes, and B. A. Sexton, J. Electron Spectrosc. 50 (1990) C15.

[293] S. Oswald, W. Hassler, R. Reiche, J. Lindner, and F. Weiss, Mikrochim. Acta. 133 (2000) 303.

[294] D. D. Sarma, and C. N. R. Rao, J. Electron. Spectrosc. 20 (1980) 25.

[295] S. A. Lee, K. W. Park, J. H. Choi, B. K. Kwon, and Y. E. Sung, J. Electrochem. Soc. 149 (2002) A1299.

[296] L. M. Plyasova, V. V. Aver'yanov, A. A. Khassin, A. V. Kulikova, and V. N. Parmon, Dokl. Phys. Chem. 401 (2005) 23.

[297] V. Perrichon, L. Retailleau, P. Bazin, M. Daturi, and J. C. Lavalley, Appl. Catal. A 260 (2004) 1.

[298] S. Penner, D. Wang, R. Podloucky, R. Schlogl, and K. Hayek, Phys. Chem. Chem. Phys. 6 (2004) 5244.

[299] M. Chen, and L. D. Schmidt, J. Catal. 55 (1978) 348.

[300] J. R. Croy, S. Mostafa, J. Liu, Y. H. Sohn, and B. Roldan Cuenya, Catal. Lett. 118 (2007) 1.

[301] N. Lopez, T. V. W. Janssens, B. S. Clausen, Y. Xu, M. Mavrikakis, T. Bligaard, and J. K. Norskov, J. Catal. 223 (2004) 232.

[302] S. Imamura, T. Hagashihara, Y. Saito, H. Aritani, H. Kanai, Y. Matsumura, and N. Tsuda, Catal. Today 50 (1999) 369.

[303] B. V. Crist, On-Screen PDF Handbook of Monochromatic XPS Spectra - Commercially Pure Binary Oxides, XPS International, Inc., 2005, Vol.2, p. 828.

[304] W. B. Pearson, ed. *A Handbook of Lattice Spacings and Structures of Metals and Alloys*, Vol. 1, Pergamon, Oxford, 1964.

[305] W. B. Pearson, ed. *A Handbook of Lattice Spacings and Structures of Metals and Alloys*, Vol. 2, Pergamon, Oxford, 1967.

[306] A. S. Arico, A. K. Shukla, H. Kim, S. Park, M. Min, and V. Antonucci, Appl. Surf. Sci. 172 (2001) 33.

[307] A. K. Shukla, M. Neergat, P. Bera, V. Jayaram, and M. S. Hegde, J. Electroanal. Chem. 504 (2001) 111.

[308] J. L. G. Fierro, J.M. Palacios, F. Tomas, Surf. Interface Anal. 13 (1988) 25.

[309] R. Symanski, and H. Charcosset, Platinum Metals Rev. 30 (1986) 23.

[310] P. Oelhafen, J. Phys. F: Metal Phys. 11 (1981) L41.

[311] G. V. Samsonov, ed. *The Oxide Handbook*, Vol. Plenum Publishing Corporation, New York, 1982.

[312] E. Antolini, T. Lopes, and E. R. Gonzalez, J. Alloys and Compounds 461 (2008) 253.

[313] J. W. Arblaster, Platinum Metals Rev. 51 (2007) 130.

[314] C. Creemers, and P. Deurinck, Surf. Interface Anal. 25 (1997) 177.

[315] K. F. Wojciechowski, Surf. Sci. 437 (1999) 285.

[316] D. S. Mainardi, and P. B. Balbuena, Langmuir 17 (2001) 2047.

[317] B. E. Nieuwenhuys, Adv. Catal. 44 (2000) 259.

[318] L. Guczi, Catal. Today 101 (2005) 53.

[319] Y. G. Ma, and P. B. Balbuena, Surf. Sci. 602 (2008) 107.

[320] E. Irissou, M. C. Denis, M. Chaker, and D. Guay, Thin Solid Films 472 (2005) 49.

[321] Z. Bastl, and T. P. Pick, Surf. Sci. 566 (2004) 832.

[322] J. Zhang, K. Sasaki, E. Sutter, and R. R. Adzic, Science 315 (2007) 220.

[323] U. B. Demirci, J. Power Sources 173 (2007) 11.

[324] J. W. Niemantsverdriet, J. A. C. van Kaam, C. F. J. Flipse, and A. M. van der Kraan, J. Catal. 96 (1985) 58.

[325] G. W. Graham, H. W. Jen, O. Ezekoye, R. J. Kudla, W. Chun, X. Q. Pan, and R. W. McCabe, Catal. Lett. 116 (2007) 1.

[326] R. Lopez, R. Romero, F. Martin, J. R. Ramos-Barrado, and D. Leinen, Surf. Interface Anal. 38 (2006) 277.

[327] P. Waszczuk, G. Q. Lu, A. Wieckowski, C. Lu, C. Rice, and R. I. Masel, Electrochim. Acta 47 (2002) 3637.

[328] J. Greeley, J. K. Norskov, and M. Mavrikakis, Annu. Rev. Phys. Chem. 53 (2002) 319.

[329] R. Blume, M. Havecker, S. Zafeiratos, D. Teschner, A. Knop-Gericke, R. Schlogl, P. Dudin, A. Barinov, and M. Kiskinova, Catal. Today 124 (2007) 71.

[330] E. Antolini, T. Lopes, and E. R. Gonzalez, J. Alloy Compounds 461 (2008) 253.

[331] J. R. Croy, S. Mostafa, H. Heinrich, and B. Roldan Cuenya, Catal. Lett. 131 (2009) 21.

[332] H. Iida, and A. Igarashi, Appl. Catal. A 303 (2006) 192.

[333] P. Bera, S. Malwadkar, A. Gayen, C. V. V. Satyanarayana, B. S. Rao, and M. S. Hegde, Catal. Lett. 96 (2004) 213.

[334] J. R. Croy, S. Mostafa, J. Liu, Y. H. Sohn, H. Heinrich, and B. Roldan Cuenya, Catal. Lett. 119 (2007) 209.

[335] J. M. Petroski, Z. L. Wang, T. C. Green, and M. A. El-Sayed, J. Phys. Chem. B 102 (1998) 3316.

[336] N. Seriani, and F. Mittendorfer, J Phys-Condens. Mat. 20 (2008) 184023.

[337] Y. Abe, M. Kawamura, and K. Sasaki, Jpn. J. Appl. Phys. 1 38 (1999) 2092.

[338] J. G. Wang, W. X. Li, M. Borg, J. Gustafson, A. Mikkelsen, T. M. Pedersen, E. Lundgren, J. Weissenrieder, J. Klikovits, M. Schmid, B. Hammer, and J. N. Andersen, Phys. Rev. Lett. 95 (2005) 256102.

[339] W. Wen, J. Rodriguez, J. Croy, S. Mostafa, and B. Roldan Cuenya, Unpublished (2008).

[340] W. Li, and B. Hammer, Chem. Phys. Lett. 409 (2005) 1.

[341] S. Tougaard, and A. Ignatiev, Surf. Sci. 124 (1983) 451.

[342] C. H. Jung, R. Ishimoto, H. Tsuboi, M. Koyama, A. Endou, M. Kubo, C. A. Del Carpio, and A. Miyamoto, Appl. Catal. A 305 (2006) 102.

[343] K. Schubert, S. Bhan, T. K. Biswas, K. Frank, and P. K. Panday, Naturwiss. 55 (1968) 542.

[344] J. R. Croy, S. Mostafa, L. Hickman, H. Heinrich, and B. Roldan Cuenya, Appl. Catal. A 350 (2008) 207.

[345] Y. Nagai, K. Dohmae, Y. Ikeda, N. Takagi, T. Tanabe, N. Hara, G. Guilera, S. Pascarelli, M. A. Newton, O. Kuno, H. Y. Jiang, H. Shinjoh, and S. Matsumoto, Angew. Chem. Int. Ed. 47 (2008) 9303.

[346] Y. Yazawa, N. Kagi, S. Komai, A. Satsuma, Y. Murakami, and T. Hattori, Catal. Lett. 72 (2001) 157.

[347] C. T. Williams, C. G. Takoudis, and M. J. Weaver, J. Phys. Chem. B 102 (1998) 406.

[348] C. B. Wang, G. Deo, and I. E. Wachs, J. Phys. Chem. B 103 (1999) 5645.

[349] O. Pozdnyakova, D. Teschner, A. Wootsch, J. Krohnert, B. Steinhauer, H. Sauer, L. Toth, F. C. Jentoft, A. Knop-Gericke, Z. Paal, and R. Schlogl, J. Catal. 237 (2006) 1.

[350] S. Shiizaki, I. Nagashima, Y. Matsumura, and M. Haruta, Catal. Lett. 56 (1998) 227.

[351] Y. H. Zhou, P. H. Lv, and G. C. Wang, J. Mol. Catal. A 258 (2006) 203.

[352] J. Greeley, and M. Mavrikakis, J. Catal. 208 (2002) 291.

[353] H. C. Hu, and I. E. Wachs, J. Phys. Chem. 99 (1995) 10911.

[354] J. M. Tatibouet, Appl. Catal. A 148 (1997) 213.

[355] H. Over, A. P. Seitsonen, E. Lundgren, M. Schmid, and P. Varga, Surf. Sci. 515 (2002) 143.

[356] K. Kuribayashi, and S. Kitamura, Thin Solid Films 400 (2001) 160.

[357] C. B. Wang, H. K. Lin, S. N. Hsu, T. H. Huang, and H. C. Chiu, J. Mol. Catal. A 188 (2002) 201.

[358] C. Puglia, A. Nilsson, B. Hernnas, O. Karis, P. Bennich, and N. Martensson, Surf. Sci. 342 (1995) 119.

[359] P. J. Grunthaner, F. J. Grunthaner, and A. Madhukar, J. Vac. Sci. Technol. 20 (1982) 680.

[360] B. H. Morrow, and A. Striolo, Nanotechnology 19 (2008) 195711.

[361] Y. H. Wen, H. Fang, Z. Z. Zhu, and S. G. Sun, Phys. Lett. A 373 (2009) 272.

[362] I. F. I. Mikhail, J. Phys. C. Solid St. Phys. 13 (1980) 335.

[363] H. Yildirim, A. Kara, S. Durukanoglu, and T. S. Rahman, Surf. Sci. 600 (2006) 484.

[364] For a review see: E.F. Wassermann, in: Ferromagnetic Materials, vol. VI, edited by K.H. Buschow and E.P. Wohlfarth (North Holland, Amsterdam, 1990), p. 240ff.

[365] D. L. Nika, N. D. Zincenco, and E. P. Pokatilov, J Nanoelectron. Optoe. 4 (2009) 180.

[366] B. Gumhalter, and T. Matsushima, Surf. Sci. 561 (2004) 183.

[367] B. Bendow, and S. C. Ying, Phys. Rev. B 7 (1973) 622.

[368] S. C. Ying, and B. Bendow, Phys. Rev. B 7 (1973) 637.

[369] E. Bonetti, L. Pasquini, E. Sampaolesi, A. Deriu, and G. Cicognani, J. Appl. Phys. 88 (2000) 4571.

[370] B. Fultz, C. C. Ahn, E. E. Alp, W. Sturhahn, and T. S. Toellner, Phys. Rev. Lett. 79 (1997) 937.

[371] B. Fultz, L. Anthony, J. L. Robertson, R. M. Nicklow, S. Spooner, and M. Mostoller, Phys. Rev. B 52 (1995) 3280.

[372] B. Fultz, J. L. Robertson, T. A. Stephens, L. J. Nagel, and S. Spooner, J. Appl. Phys. 79 (1996) 8318.

[373] A. B. Papandrew, A. F. Yue, B. Fultz, I. Halevy, W. Sturhahn, T. S. Toellner, E. E. Alp, and H. K. Mao, Phys. Rev. B 69 (2004) 144301.

[374] L. Pasquini, A. Barla, A. I. Chumakov, O. Leupold, R. Ruffer, A. Deriu, and E. Bonetti, Phys. Rev. B 66 (2002) 073410.

[375] J. Trampenau, K. Bauszus, W. Petry, and U. Herr, Nanostruct. Mater. 6 (1995) 551.

[376] P. M. Derlet, R. Meyer, L. J. Lewis, U. Stuhr, and H. Van Swygenhoven, Phys. Rev. Lett. 87 (2001) 205501.

[377] R. Meyer, L. J. Lewis, S. Prakash, and P. Entel, Phys. Rev. B 68 (2003) 104303.

[378] R. Singh, and S. Prakash, Surf. Sci. 532 (2003) 272.

[379] A. Kara, and T. S. Rahman, Phys. Rev. Lett. 81 (1998) 1453.

[380] D. Y. Sun, X. G. Gong, and X. Q. Wang, Phys. Rev. B 63 (2001) 193412.

[381] H. Frase, B. Fultz, and J. L. Robertson, Phys. Rev. B 57 (1998) 898.

[382] A. Kara, and T. S. Rahman, Surf. Sci. Rep. 56 (2005) 159.

[383] T. S. Rahman, A. Kara, and S. Durukanoglu, J. Phys-Condens. Mat. 15 (2003) S3197.

[384] W. Sturhahn, Hyperf. Interact. 125 (2000) 149.

[385] U. Stuhr, H. Wipf, K. H. Andersen, and H. Hahn, Phys. Rev. Lett. 81 (1998) 1449.

[386] B. Roldan Cuenya, A. Naitabdi, J. Croy, W. Sturhahn, J. Y. Zhao, E. E. Alp, R. Meyer, D. Sudfeld, E. Schuster, and W. Keune, Phys. Rev. B 76 (2007) 195422.

[387] S. Durukanoglu, A. Kara, and T. S. Rahman, Phys. Rev. B 67 (2003) 235405.

[388] H. Yildirim, A. Kara, T. S. Rahman, R. Heid, and K. P. Bohnen, Surf. Sci. 604 (2010) 308.

[389] B. Fultz, L. Anthony, L. J. Nagel, R. M. Nicklow, and S. Spooner, Phys. Rev. B 52 (1995) 3315.

[390] B. R. Cuenya, A. Naitabdi, J. Croy, W. Sturhahn, J. Y. Zhao, E. E. Alp, R. Meyer, D. Sudfeld, E. Schuster, and W. Keune, Phys. Rev. B 76 (2007) 195422.

[391] L. Zwell, G. R. Speich, and W. C. Leslie, Metallurgical Transactions 4 (1973) 1990.

[392] A. Ethirajan, U. Wiedwald, H. G. Boyen, B. Kern, L. Y. Han, A. Klimmer, F. Weigl, G. Kastle, P. Ziemann, K. Fauth, J. Cai, R. J. Behm, A. Romanyuk, P. Oelhafen, P. Walther, J. Biskupek, and U. Kaiser, Adv. Mater. 19 (2007) 406.

[393] B. Roldan Cuenya, W. Keune, R. Peters, E. Schuster, B. Sahoo, U. von Horsten, W. Sturhahn, J. Zhao, T. S. Toellner, E. E. Alp, and S. D. Bader, Phys. Rev. B 77 (2008) 165410.

[394] H. Yildirim, A. Kara, and T. S. Rahman, J. Phys. Condens. Matter 21 (2009) 084220.

[395] S. R. Calvo, and P. B. Balbuena, Surf. Sci. 581 (2005) 213.

[396] R. Meyer, S. Prakash, and P. Entel, Phase Trans. 75 (2002) 51.

[397] N. Wiele, H. Franz, T. Ansthalten, and W. Petry, Annual Report from the Advanced Photon Source, (1999).

[398] N. Wiele, PhD Dissertation, Technische Universitat Munchen (Munich), 2001.

[399] The high-energy oscillations above ~40 meV in Fig. 74(b) are believed to be an artifact due to the low count-rate in that energy regime and the slightly higher background count-rate for E > ~40 meV as compared to E < ~ -40 meV in Fig. 73(b), combined with the mathematical Fourier-log procedure employed in the PHOENIX software used for data evaluation (W. Sturhan, Hyperfine Int. 125 (2000) 149).

[400] K. Tajima, Y. Endoh, Y. Ishikawa, and W. G. Stirling, Phys. Rev. Lett. 37 (1976) 519.

[401] Y. Noda, and Y. Endoh, J. Phys. Soc. Jap. 57 (1988) 4225.

[402] J. Kastner, J. Neuhaus, E. F. Wassermann, W. Petry, B. Hennion, and H. Bach, Eur. Phys. J. B 11 (1999) 75.

[403] J. Kastner, W. Petry, S. M. Shapiro, A. Zheludev, J. Neuhaus, T. Roessel, E. F. Wassermann, and H. Bach, Eur. Phys. J. B 10 (1999) 641.

[404] N. Wiele, H. Franz, and W. Petry, Physica B 263 (1999) 716.

[405] B. Fultz, T. A. Stephens, E. E. Alp, M. Y. Hu, J. P. Sutter, T. S. Toellner, and W. Sturhahn, Phys. Rev. B 61 (2000) 14517.

[406] In a recent molecular dynamics simulation of the PDOS of $Cu_{3-x}Au_x$ alloy NPs, a suppression of the low-E phonon bands relative to the high-E peak height and a blue-shift of the high-E peak with increasing L12 ordering was predicted by R. Meyer, Laurentian University, Sudbury, Canada, (private communication).

[407] B. Jusser, and M. Cardona, *Light Scattering in Solids V, Topics in Applied Physics, Vol. 66*, Springer, Heidelberg, 1989.

[408] T. Tanaka, A. Tajima, R. Moriizumi, C. Oshima, Y. Tsunoda, M. Seto, S. Kitao, and T. Mitsui, J. Phys. Soc. Jap. 74 (2005) 1762.

[409] A. I. Chumakov, R. Ruffer, H. Grunsteudel, H. F. Grunsteudel, G. Grubel, J. Metge, O. Leupold, and H. A. Goodwin, Europhys. Lett. 30 (1995) 427.

[410] M. Seto, Y. Yoda, S. Kikuta, X. W. Zhang, and M. Ando, Phys. Rev. Lett. 74 (1995) 3828.

[411] W. Sturhahn, T. S. Toellner, E. E. Alp, X. Zhang, M. Ando, Y. Yoda, S. Kikuta, M. Seto, C. W. Kimball, and B. Dabrowski, Phys. Rev. Lett. 74 (1995) 3832.

[412] G. Shen, W. Sturhahn, E. E. Alp, J. Zhao, T. S. Toellner, V. B. Prakapenka, Y. Meng, and H. R. Mao, Phys. Chem. Minerals 31 (2004) 353.